INFORMATION TO USERS

This manuscript has been reproduced from the microfilm master. UMI films the text directly from the original or copy submitted. Thus, some thesis and dissertation copies are in typewriter face, while others may be from any type of computer printer.

The quality of this reproduction is dependent upon the quality of the copy submitted. Broken or indistinct print, colored or poor quality illustrations and photographs, print bleedthrough, substandard margins, and improper alignment can adversely affect reproduction.

In the unlikely event that the author did not send UMI a complete manuscript and there are missing pages, these will be noted. Also, if unauthorized copyright material had to be removed, a note will indicate the deletion.

Oversize materials (e.g., maps, drawings, charts) are reproduced by sectioning the original, beginning at the upper left-hand corner and continuing from left to right in equal sections with small overlaps.

Photographs included in the original manuscript have been reproduced xerographically in this copy. Higher quality 6" x 9" black and white photographic prints are available for any photographs or illustrations appearing in this copy for an additional charge. Contact UMI directly to order.

UMI®

SEISMOLOGICAL CONSTRAINTS ON TECTONICS OF

SOUTHERN AND CENTRAL ALASKA:

EARTHQUAKES LOCATIONS AND SOURCE MECHANISMS

A

THESIS

Presented to the Faculty

of the University of Alaska Fairbanks

in Partial Fulfillment of the Requirements

for the Degree of

DOCTOR OF PHILOSOPHY

By

Natalia Anatolievna Ratchkovski

Fairbanks, Alaska

May 2001

UMI Number: 3004676

UMI®

UMI Microform 3004676

SEISMOLOGICAL CONSTRAINTS ON TECTONICS OF

SOUTHERN AND CENTRAL ALASKA:

EARTHQUAKES LOCATIONS AND SOURCE MECHANISMS
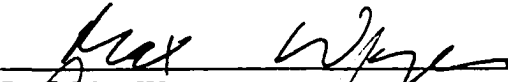
By

Natalia Anatolievna Ratchkovski

RECOMMENDED:

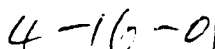Prof. Douglas Christensen

Prof. Steven McNutt

Prof. Max Wyss

Prof. Roger Hansen, Advisory Committee Chair

Prof. Paul Layer
Head, Department of Geology and Geophysics

APPROVED:

Prof. David Woodall
Dean, College of Science, Engineering and Mathematics

Prof. Joseph Kan, Dean of the Graduate School

4 -16 -01

Date

Abstract

The major emphasis of this thesis is on investigations of earthquake locations and source mechanisms and what we can learn about Earth structure from them. I used a Joint Hypocenter Determination (JHD) method to improve the earthquake locations obtained after routine data processing. Over 15,000 subduction zone earthquakes in southern Alaska and over 3,600 crustal earthquakes in central Alaska with magnitudes $M_L \geq 2$ that occurred from 1988 to 2000 were relocated. I found that the relative earthquake locations can be improved with the use of the JHD relocation technique (30-60% reduction in RMS residuals). Thus, many details of the subduction zone geometry and crustal structure can be mapped.

To constrain source characteristics, I use a moment tensor inversion method that simultaneously inverts for the source parameters and velocity structure. First, I apply this technique to the sequence of strong earthquakes in the Kodiak Island region, including December 6, 1999 and January 10, 2001 M_W 7 events. Next, I expand this approach to moderate-sized ($M_L \geq 4$) crustal earthquakes in central Alaska and calculate 38 moment tensors. I demonstrate that the moment tensor inversion of regional waveforms provides reliable results even when recordings from a single broadband station are used. A catalog of the moment tensors together with the focal mechanisms obtained using conventional P-wave first motion analysis is used to calculate principal stress directions in central Alaska. I find that the stress state in the crust is inhomogeneous and that the orientation of the maximum compressive stress changes from a SE-NW to SSW-NNE orientation from west to east across interior Alaska.

One more topic of this thesis is the application of the array analysis to understanding characteristics of anomalous seismic phases observed in the records of the intermediate-depth Alaskan subduction zone earthquakes. I identified two secondary phases arriving with 1-3 s and 7-12 s delays after the first P-wave arrival. They are interpreted as S-to-P and P-to-S converted phases at the upper/lower surface of the subducted slab.

Table of Contents

List of Figures

List of Tables

Acknowledgments

While this thesis includes work done in the past 6 years, my journey towards a Ph.D. degree started much earlier than that. First of all, I would like to express my deepest gratitude to my mother and to my late father, who while not having a chance to pursue a higher degree education themselves, made sure, that both of their daughters did.

I would like to thank my first mentors and advisors Dr. George Mitrofanov and Academician Sergei Goldin from the Novosibirsk State University for showing me not only great research opportunities in geophysical sciences, but also a fun side of being a geophysicist, such as meeting interesting people and visiting new places.

I am grateful to my Master's degree advisor Dr. Niren Biswas for inviting me to study in the U.S. Many thanks go to my Ph.D. program advisor Dr. Roger Hansen, who was very patient when progress in my studies slowed down and was very understanding after the birth of my first child to let me slowly adjust to my new role of being a mother and a student. I am also thankful to the members of my advisory committee Dr. Doug Christensen, Dr. Steve McNutt, and Dr. Max Wyss for their advice and support throughout these years and to Dr. Jeff Freymueller for substituting Max Wyss at my thesis defense.

I would like to thank all my fellow students from the Geophysical Institute and other UAF departments for making the work environment fun and enjoyable. To name a few, they are John Benoit, Hilary Fletcher, Pavel Izbekov, Art Jolly, George Minassian, Elena Suleimani, Stefan Wiemer, and many others. I also appreciate help and support of administration of the Geology and Geophysics Department.

I feel this thesis would have been delayed for another year or two, if it was not for the technical support of our system administrator Mitch Robinson. I should also thank people working for AEIC and AVO - Steve Estes, Kent Lindquist, Scott Stihler, Guy Tytgat, Lalitha Rao, who kept the earthquake dataflow coming with minimal interruptions.

And last, but not least, I would like to express my sincere gratitude to my husband of 10 years, Artem, for his unconditional support and love and, of course, to my 2-year-old son Daneel, the greatest joy of my life.

Chapter 1: Introduction.

Alaska spans 4,800 km of the active boundary between the Pacific and North American plates and is the site of three of the world's ten largest earthquakes ever recorded. Most of the seismic energy in Alaska is released in great earthquakes that rupture the megathrust zone between the two plates, such as the great 1964 Prince William Sound earthquake (M_W 9.2). Many small and intermediate-sized earthquakes occur in the down-going plate and form the Wadati-Benioff zone (WBZ), that extends to a maximum depth of about 220 km. Upper plate crustal seismicity is also abundant and pervades practically the entire state of Alaska (Figure 1.1). In the last century, interior and southern Alaska was the site of several major earthquakes with 7+ magnitude. A regional seismograph network was established in Alaska in the 1960's and greatly expanded in recent years. Now, there are over 300 seismograph stations operating in Alaska (Figure 1.1) with additional data exchange established with Japan and Canada.

One of the primary tasks of seismologists is the accurate determination of an earthquake magnitude and location. These parameters are of a great value and interest for both the public and the scientific community. Regional distance analysis is extremely important in the study of small and moderate-sized earthquakes, which are rarely well recorded at teleseismic distances. Instrumental and computational advances of the past decade allow a near-real-time processing of the earthquake data and automatic identification of the earthquake locations and magnitudes (Lindquist and Hansen, 2001). The earthquake locations, however, determined during routine processing may have a high uncertainty, especially in areas with heterogeneous Earth structure and sparse station coverage. Therefore, one of the major topics of this thesis is accurate determination of the hypocentral parameters. I apply a joint hypocenter determination method to calculate new locations for the crustal

| △ station | ○ 0-25 km | ● 50-75 km | ● 100-125 km | ● 150-175 km |
| ◆ volcano | ● 25-50 km | ● 75-100 km | ○ 125-150 km | ● 175-200 km |
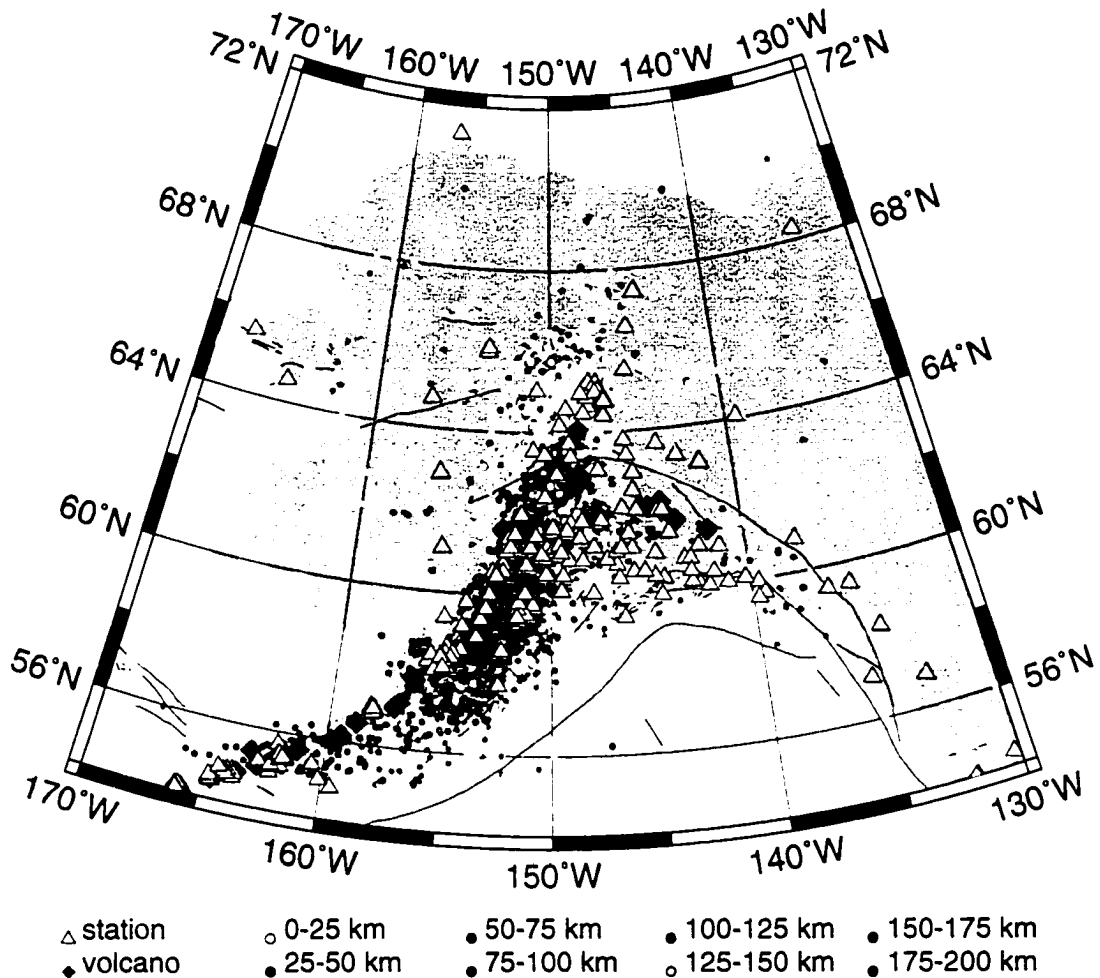
Figure 1.1. Map of Alaska with epicenters of the earthquakes with magnitude greater than 2 that occurred from 1990 to 1999 (from the AEIC catalog). Major faults are shown by red lines. Open triangles are seismic station operated in 2000. Red diamonds are the subduction zone volcanoes.

and subduction zone earthquakes in southern and central Alaska. Results of the relocation of the subduction zone earthquakes are presented in Chapters 2 and 3. I will demonstrate, that the relocated hypocenters provide more detail on the WBZ structure therefore allowing us to interpret the observations with greater confidence. Also, the joint relocation method has been applied successfully to crustal earthquakes in central Alaska (Chapter 4).

Another task of equal importance is the determination of the earthquake source parameters. Traditionally, the earthquake source is described in terms of a fault plane solu-

tion, which gives the orientation of the fault and auxiliary planes. A conventional approach is to use P-wave first motions for obtaining the focal mechanism. This approach, however, suffers from a number of drawbacks. Inaccuracies in the velocity model can lead to poorly determined take-off angles, and therefore to inaccurate faulting parameters. Sparse seismic networks, such as in Alaska, cause large uncertainties in the fault plane solutions.

With more powerful computers and better recording instruments, modern seismology is attacking problems of describing detailed processes of earthquake faulting using waveform modeling. I apply a waveform inversion approach to calculate moment tensor solutions for crustal and shallow subduction zone earthquakes. Seismic moment tensors provide full characterization of the earthquake source, such as size of the earthquake (seismic moment) and faulting parameters (Figure 1.2). The waveform inversion for subduction zone earthquakes is demonstrated with the example of the 1999 Kodiak Island M_W 7
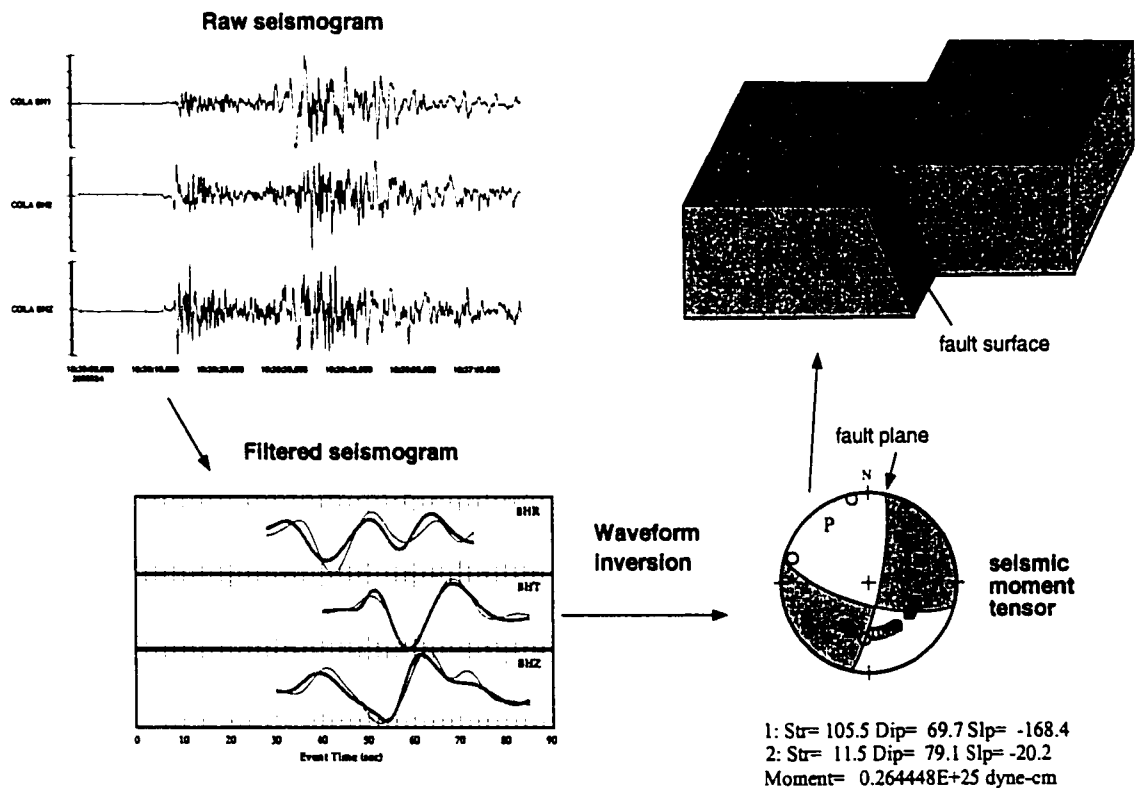
Figure 1.2. A flow-diagram of the waveform inversion procedure.

earthquake (Chapter 3). Results of moment tensor inversions for crustal earthquakes in central Alaska are presented in Chapter 4. Applications of the moment tensor inversion procedure to crustal earthquakes in central Alaska demonstrates that it is possible to obtain a reliable solution for intermediate-sized earthquakes using records from a single broadband station within 50-300 km distance. I also test different velocity models to identify the best structure for calculating Green's functions for crustal earthquakes in central Alaska.

Faulting characteristics of the earthquakes are one of the major information sources used to constrain details of the regional tectonics. I use the catalog of the focal mechanisms for crustal earthquakes in central Alaska obtained with the conventional P-wave first motion analysis and waveform inversion to calculate principal stress orientations in the crust. These data are presented in Chapter 4.

Dense arrays of seismometers (seismic arrays) is another instrumentation development of modern seismology. Array data allow for a better understanding of the propagating wave field, as well as help focus on seismicity in remote areas and small seismic events by enhancing the signal to noise ratio. I use seismic array data to estimate apparent velocities and back azimuths of the anomalous phases observed in the records of the intermediate depth Alaskan subduction zone earthquakes. These observations are discussed in Chapter 5.

Methods that I used for the data processing, such as joint hypocenter determination method, moment tensor inversion and array data processing, are described in detail in Appendices A, B, and D, respectively.

In summary, in my thesis I demonstrate that with the help of modern instrumentation and new earthquake data processing techniques seismologists are able to obtain detailed information about earthquake source processes. This information allows researchers to refine existing tectonic models and to propose new ones.

Chapter 2: Segmentation of the subducted plate beneath southern and central Alaska.[1]

2.1. INTRODUCTION.

The Alaska-Aleutian subduction zone extends along the Aleutian arc and terminates in the Alaskan Interior around 64°N latitude. The subducting Pacific plate moves at a rate of 5-7 cm per year with respect to the North American plate. The direction of the subduction changes from normal in the central Aleutians to oblique beneath Alaska. The WBZ (Wadati-Benioff zone) beneath Alaska is characterized by intense seismic activity down to a maximum depth of 220 km (Figure 2.1). The WBZ strike undergoes a 20° counterclockwise rotation at about 59°N latitude and a 35° clockwise change farther north at about 63°N.

Seismicity of the WBZ in southern and central Alaska has been extensively studied over the past twenty five years (e.g., van Wormer et al., 1974; Davies, 1975; Lahr, 1975; Davies and House, 1979; Pulpan and Frohlich, 1985; Gedney and Davies, 1986; Page et al., 1989; Page et al., 1991). A number of researchers (van Wormer et al., 1975; Kienle et al., 1983; Pulpan and Frohlich, 1985) proposed segmentation of the subducting Pacific plate on the basis of earthquake locations, geometry and composition of the volcanic arc, and a variety of other data. The identified blocks within the Alaska subduction zone are the southwestern (Kodiak), central (Kenai) and northeastern (McKinley) segments.

The purpose of this work is to provide additional evidence for the segmentation of the subducted plate in southern and central Alaska and to introduce a catalog of the relo-

---

1. This work has been submitted for publication in Bull. Seism. Soc. Am. (2001).
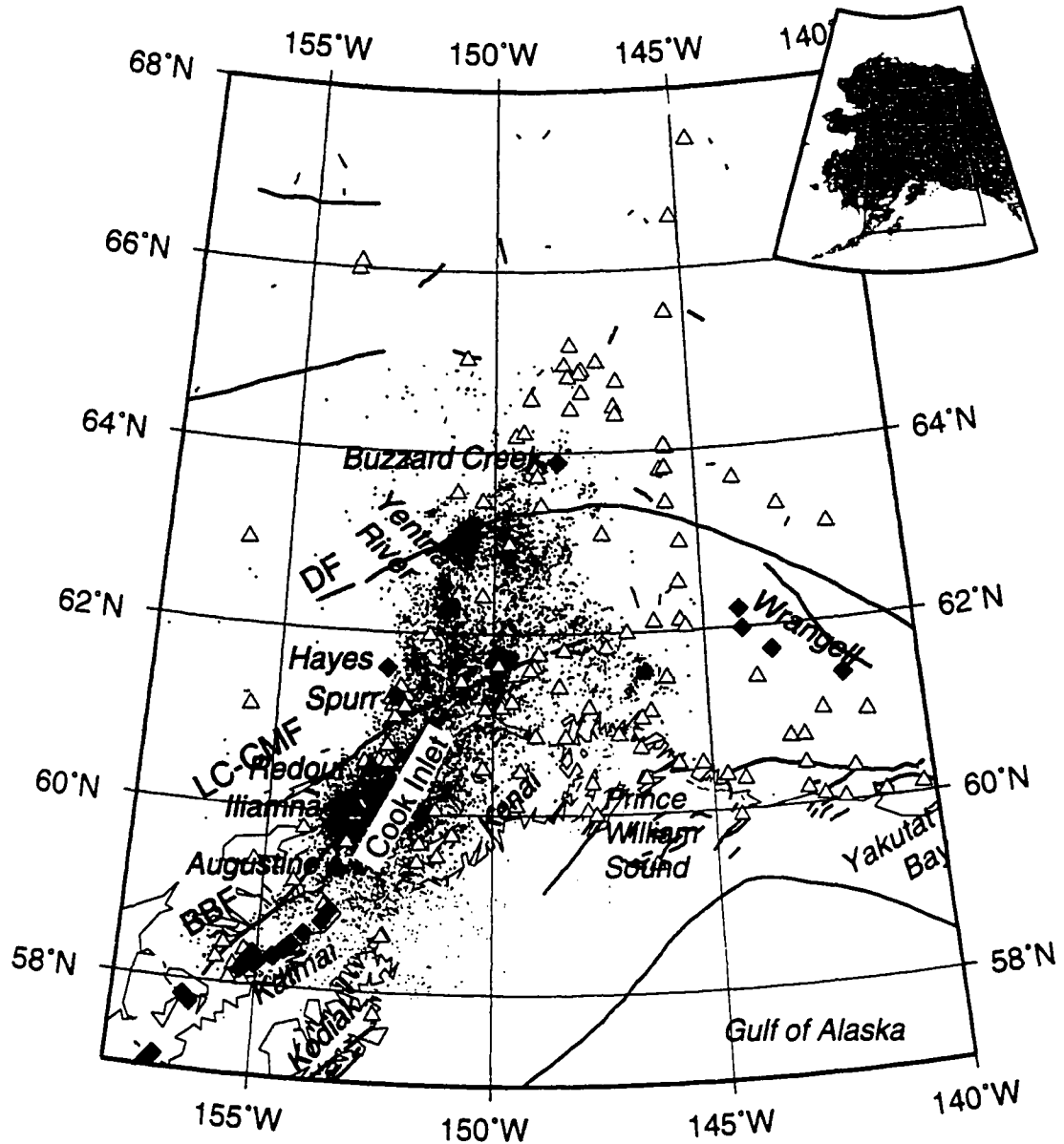
Figure 2.1. Map of the study area with locations of 15,552 subduction zone earthquakes selected for the joint relocation. Open triangles are locations of the seismic stations used in the relocation. Grey diamonds denote active volcanoes. Solid lines are mapped surface traces of the faults: DF - Denali fault, LC-CMF - Lake Clark - Castle Mountain fault system, BBF - Bruin Bay fault.

cated earthquakes for future studies. The relocation effort was part of a study of anomalous phases observed in the records of Alaskan subduction zone earthquakes (Ratchkovsky et al., 1999; see also Chapter 5). To determine the nature of the observed phases it is important to know precisely where the earthquakes are located in the WBZ.

The Alaska Earthquake Information Center (AEIC) records and locates several thousand subduction zone earthquakes each year. The earthquakes are routinely located using a single event location algorithm with different regional velocity models (Lahr, 1989). Previous relocation studies of the AEIC catalog using the joint hypocenter determination method (Ratchkovsky et al., 1997; Ratchkovsky et al., 1998) showed that the relocated hypocenters have more accurate relative locations and, therefore, can provide more detail on the structure of the Alaskan WBZ.

2.2. DATA AND THE RELOCATION METHOD.

The goal of this relocation effort is to relocate as many earthquakes as possible and at the same time to assure reliability of the relocation results. The earthquakes were selected from the AEIC catalog according to the following criteria: 1) occurrence between July, 1988 and July, 1998; 2) local magnitude M_L no less than 2.0; 3) focal depth greater than 25 km; 4) epicenters located between 58°N and 65°N latitude; and 5) number of P and S phases no less than 8 and 4, respectively. A total of 15,552 earthquakes satisfied the above criteria (Figure 2.1). The phase readings from 164 seismic stations which operated during any time from 1988 to 1998 and located within 3 degrees epicentral distance are used (Figure 2.1). Also, a quality weight from 0 (good) to 4 (too uncertain to be used) is assigned to each phase reading. These are the quality weights assigned during the standard data processing at AEIC; 0, 1, 2, and 3 weight codes are assigned to readings with standard errors ranging up to 0.1, 0.5, 1.0, and 2.0 seconds, respectively.

To relocate the selected earthquakes, I used a joint hypocenter determination method. Originally, the method was developed by Douglas (1967) to determine hypocentral parameters and station corrections using a least-squares inversion method. Variations of this method have been widely applied in determining earthquake locations. Many stud-

ies (e.g., Engdahl et al., 1982; Pujol, 1992; Ratchkovsky et al., 1997) have shown that the relative locations of hypocenters can be improved significantly by the use of the JHD method in areas with complicated three-dimensional velocity structure and in areas where the velocity structure is poorly known. In general, negative and positive JHD station corrections correspond to raypaths through high and low velocity zones, respectively. They compensate for lateral variations of velocity, which improves the accuracy of the hypocenter locations.

The JHD algorithm (Appendix A) used in the present study was developed by Pujol (1988). The relocation process is iterative, with each iteration consisting of two loops. First, station corrections are determined for the current hypocenter parameters and a given plane-layer velocity model. Then, these corrections are used to adjust the earthquake location parameters. In general, with each iteration the overall root-mean-square residual of the events decreases and convergence is achieved in about five to seven iterations. In the last iteration, the JHD station corrections calculated in the previous step are used to compute the final earthquake locations. This particular algorithm has been used in a variety of tectonic settings and proved to be reliable and computationally effective (Pujol et al., 1989; Pujol et al., 1991; Ratchkovsky et al., 1997; Ratchkovsky et al., 1998).

The selected earthquakes occupy a large volume (700 km by 700 km by 200 km). To assure that the station corrections are determined for similar ray paths, the selected earthquakes were subdivided into blocks on the basis of their hypocentral locations and each block was relocated separately. We used three depth intervals: 25 to 50 km, 50 to 100 km, and below 100 km; geographic parallels served as the boundaries between the blocks within each depth interval. For each group, we tested different relocation parameters, including the velocity model, to assure the most reliable relocation results. In this way, all earthquakes were relocated in 17 separate blocks with the number of events in each block ranging from 77 to 1,677 (Figure 2.2(a)). In the final relocation we used two velocity models: one for the earthquakes located to the south of 62°N and another for those located to the north of 62°N (Figure 2.2(b)). These velocity models are the standard structures used by AEIC for routine processing of the earthquake data.

(a)

(b)
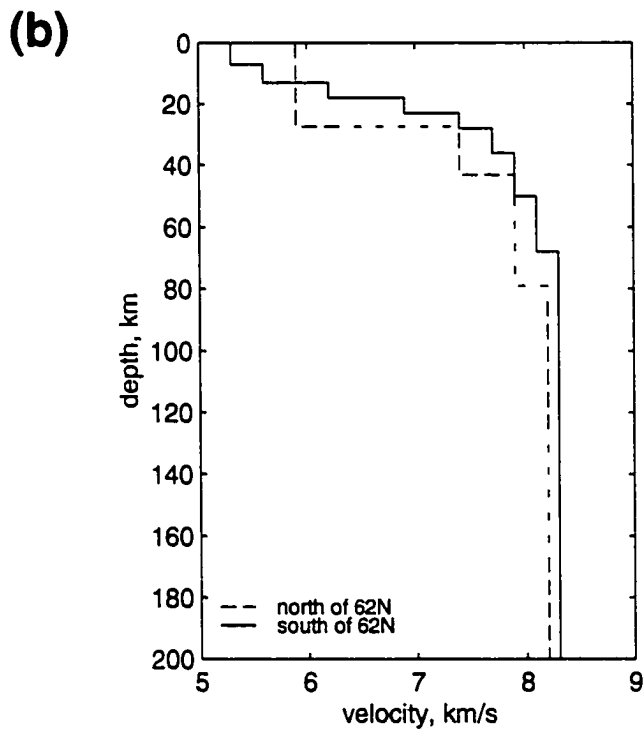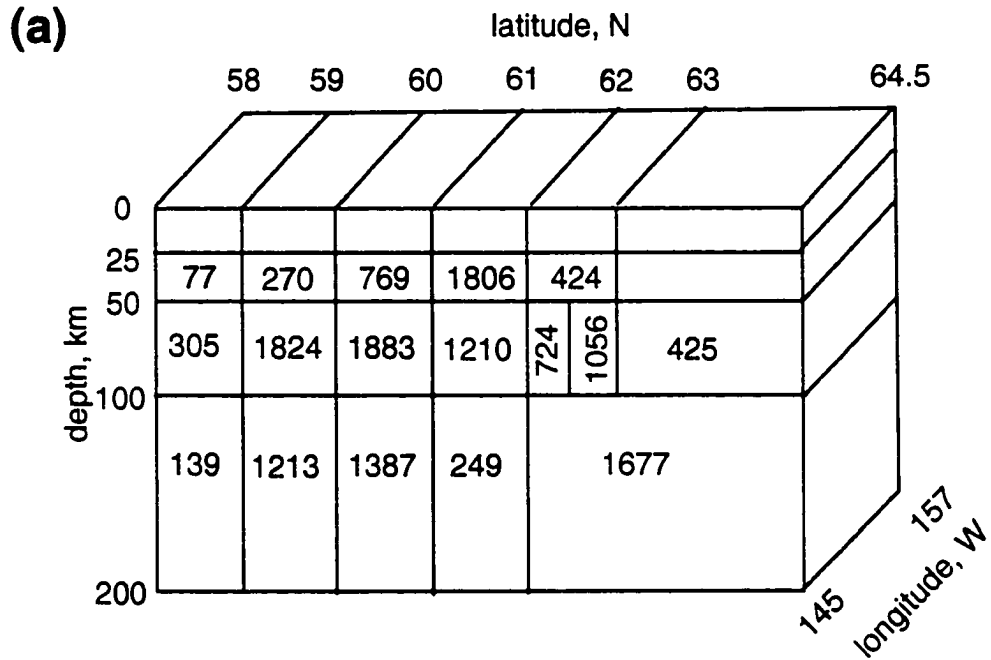
Figure 2.2. (a) Relocation blocks with the number of earthquakes inside each block. (b) Two velocity models used in the relocation: solid line - for the blocks located south of 62°N, dashed line - for the blocks located north of 62°N.

2.3. RELOCATION RESULTS AND DISCUSSION.

A total of 14,102 events were relocated. The maximum hypocentral shifts reach values of 20 km in a few extreme cases. The average epicenter shift is 3.7 km and the average upward and downward depth shifts are 4.0 and 4.1 km, respectively; roughly the same number of earthquakes shifted upwards (47%) and downwards (53%) (Figure 2.3(a)). Figure 2.3(b) illustrates change in the hypocentral locations after the relocation. Figures 2.4 and 2.5 show relocated data in map and cross-sectional views, respectively. Figure 2.6 shows the same data in depth slices of 25 and 50 km. The following discussion will concentrate on the structure and segmentation of the WBZ as evidenced by the JHD hypocentral locations.

First, I will discuss the transition between the Kodiak and Kenai blocks. Cross-section C1 in Figure 2.5(a) includes events from the Kodiak block as identified in Pulpan and Frohlich (1985). Cross-section C2 represents events beneath the lower and central Cook Inlet. Among the major differences between the Kodiak and Kenai blocks are the changes in the thickness and strike orientation of the WBZ. Maximum thickness of the WBZ within the Kodiak block is about 20 km, while beneath the central Cook Inlet it reaches 30 km. The WBZ becomes much more active immediately north of the Kodiak block. In particular, intermediate-depth earthquake cluster beneath Iliamna volcano is the most active part of the WBZ beneath southern Alaska. Also, volcanoes of the Kodiak group are located above 70-90 km isobath of the leading edge of the WBZ, while the Cook Inlet volcanoes are located above the 100 km depth isobath. These facts lead Pulpan and Frohlich to the conclusion that the Kodiak and Kenai blocks are separate segments of the subducted plate. The new JHD hypocentral locations support their findings. There is no evidence, however, that the subducted plate is tearing along the transition between the blocks.

The segment of the Alaska WBZ north of 62°N latitude (cross-sections C6 and C5 in Figure 2.5(a)) is its most complex part. Van Wormer et al. (1974) pointed to a possible break in the subducting Pacific plate which separates two independent blocks: the McKinley block to the northeast of the break and Kenai block to the south of it. The boundary
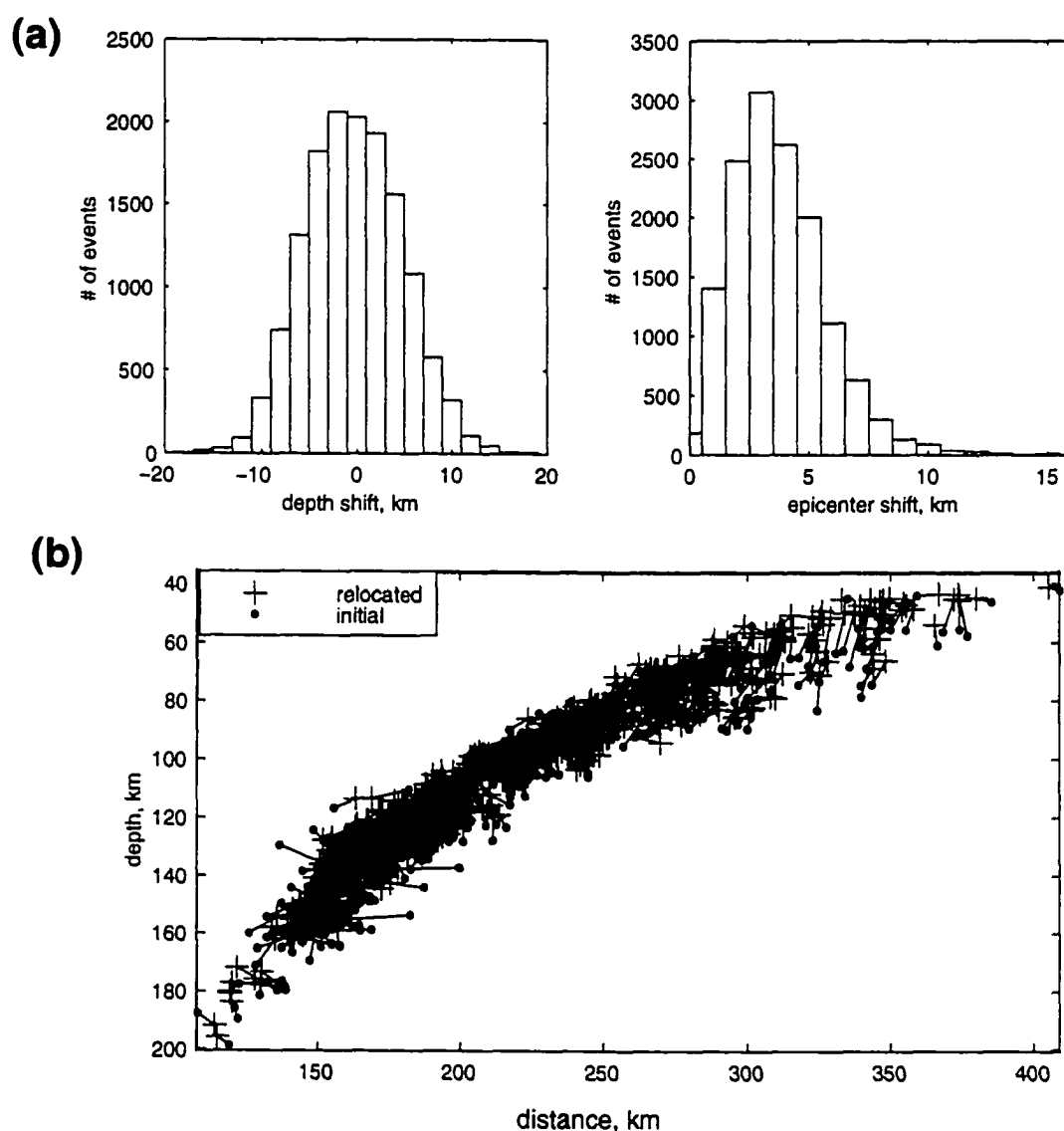
Figure 2.3. (a) Histogram of changes in the focal depths and epicenter locations of 14,102 earthquakes after the JHD relocation. (b) Representative cross-section of the initial (points) and relocated (crosses) hypocenters. The cross-section is 20 km wide and includes events beneath central Cook Inlet.

between the blocks was identified as extending from the Yentna river through Prince William Sound perhaps as far as Yakutat Bay (Figure 2.1). Later, Pulpan and Frohlich (1985) proposed a segmentation model for the subducting plate beneath Cook Inlet with three independent segments: southwestern, central and northeastern. However, the nature of the
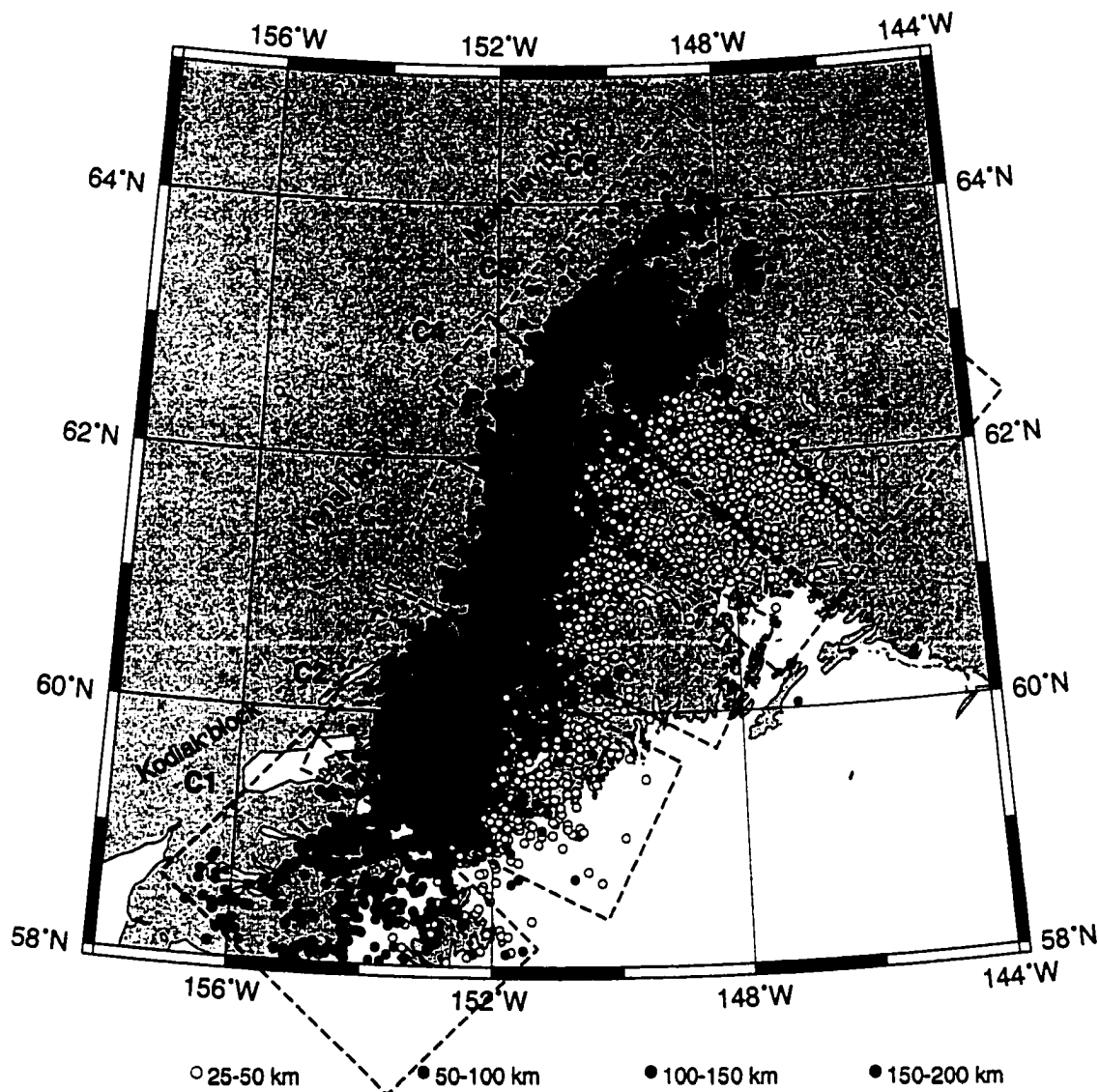
Figure 2.4. Epicentral locations of 14,102 earthquakes after the JHD relocation. Dashed rectangles marked C1 through C6 delineate locations of the cross-sections shown in Figure 2.5.

boundary between the central (Kenai) and northeastern (McKinley) blocks was not explored by the authors in detail. Using lateral strain estimates for the subducted lithosphere in the Circum-Pacific region, Burbach and Frohlich (1986) identified the plate segment boundary at the northern end of Cook Inlet and characterized it as "strong", i.e. that it is accompanied by a significant lateral strain. Recent study of the stress directions in the
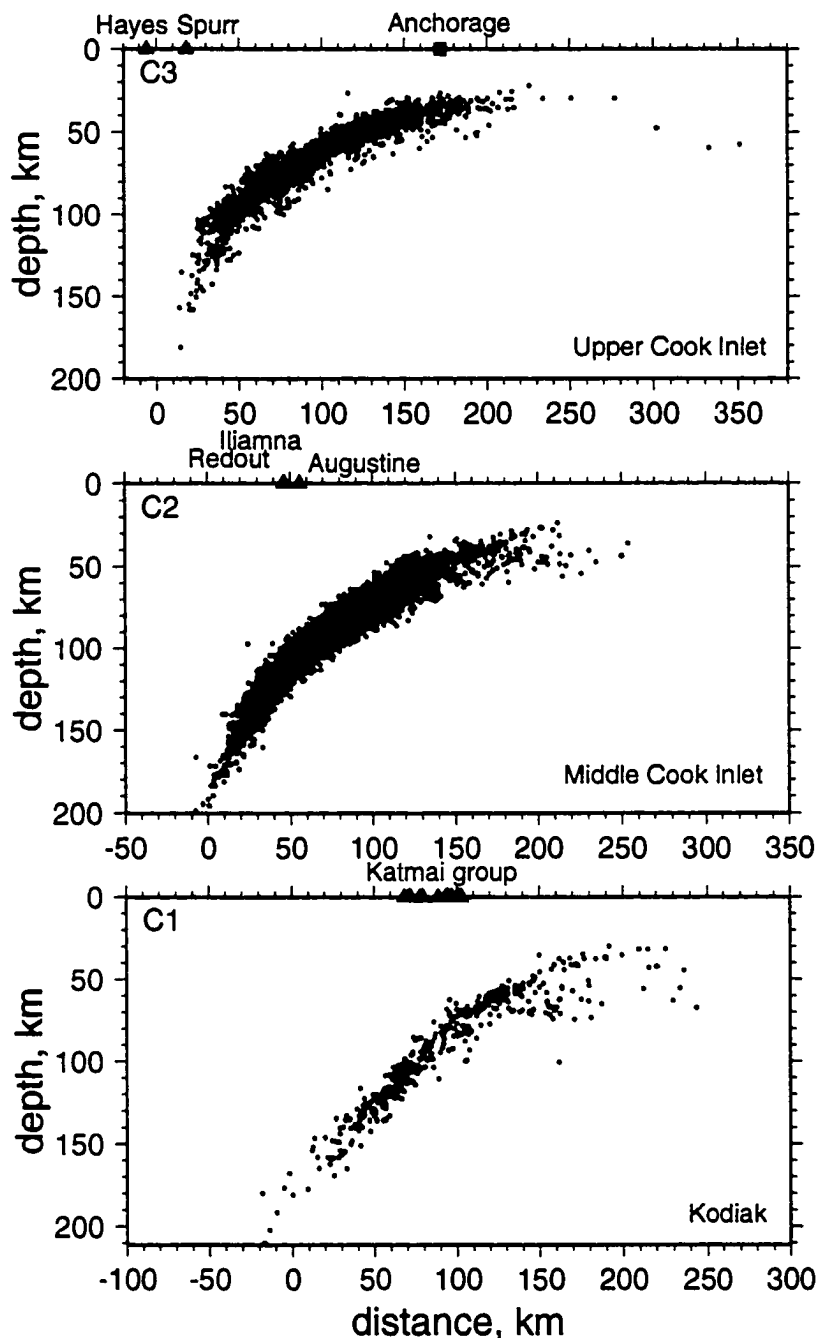
Figure 2.5. (a) Cross-sections of the JHD relocated events as shown in Figure 2.4. Triangles are volcano locations. Square shows location of the city of Anchorage. Cross-section C1 includes events from the Kodiak block; C2, C3 and C4 include events from the Kenai block; and cross-sections C5 and C6 include events from the McKinley block. In cross-sections C5 and C6 we illustrate segmentation of the McKinley block. Segments are marked by letters A thought D and by the arrows.
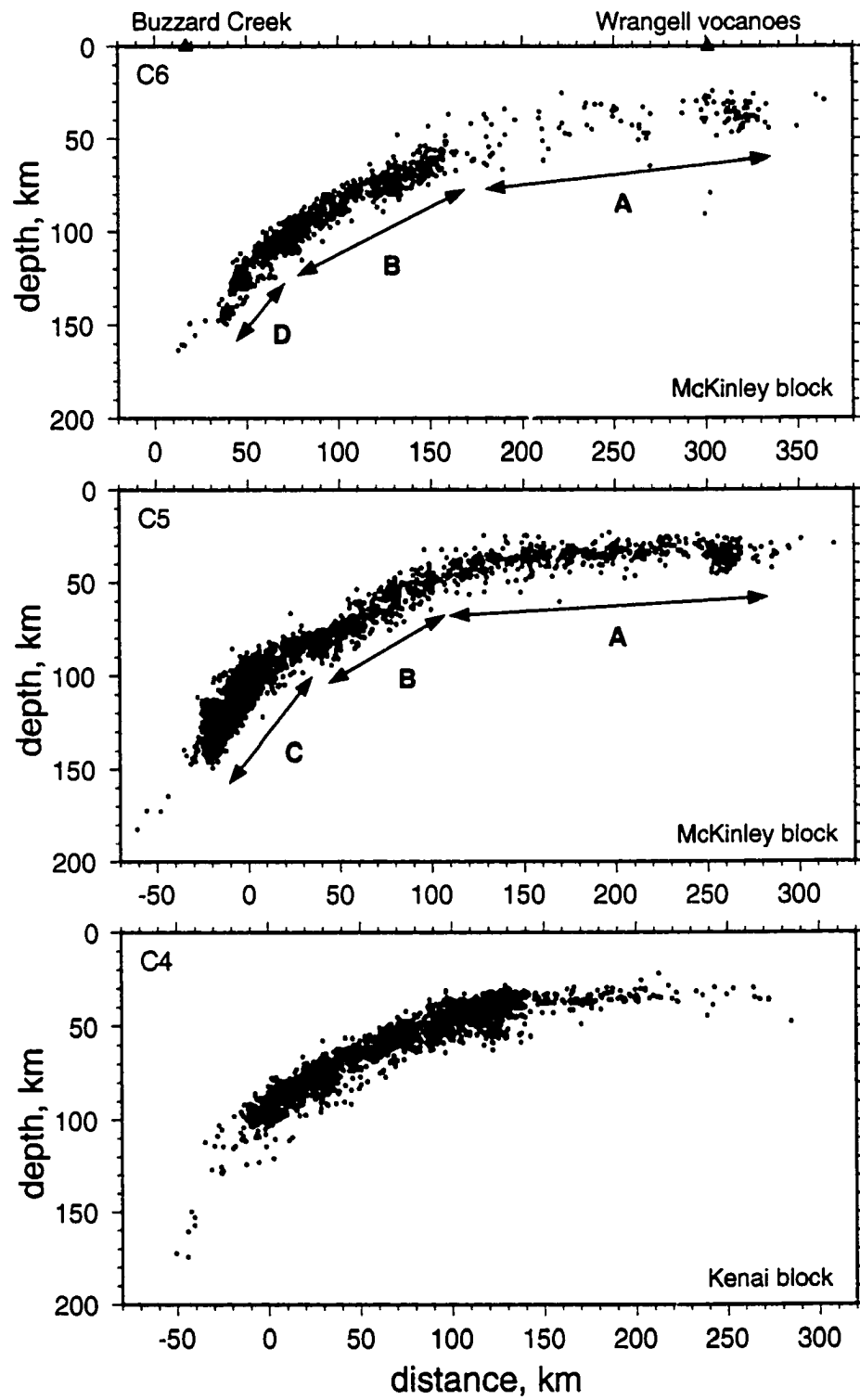
Figure 2.5. (a) (continued).
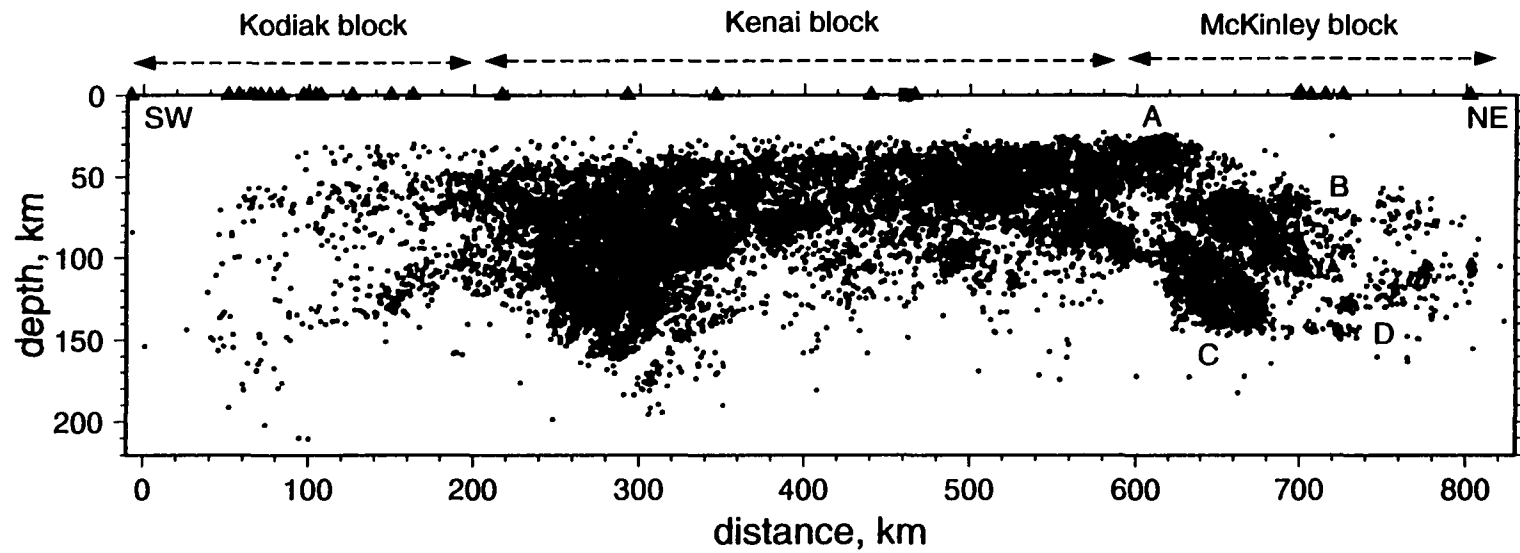
Figure 2.5. (b) Along-strike cross-section of the relocated events (N20°). Segmentation of the McKinley block is illustrated with the segments marked A through D.

Alaskan WBZ by Lu et al. (1997) concluded that there are rapid stress changes in the bent portion of the WBZ at around 63°N.

The new JHD earthquake locations support the hypothesis of the existence of a break in the subducting plate between the Kenai and McKinley blocks. This break is indicated by a change in the strike orientation and by the seismicity offsets that are illustrated in Figure 2.6, where 25- and 50-km-thick depth slices of the relocated hypocenters are shown. Some of the offsets are very significant (see 50-75 km and 75-100 km depth slices) and could not be explained by a model of a smooth transitional bend without a tear.

In addition, hypocentral locations indicate, that the McKinley block itself is segmented into independent blocks. Close examination of the seismicity in the McKinley block leads us to the conclusion that it consists of at least 4 separate segments (marked A through D in Figure 2.5). Segment A is the shallowest part of the McKinley block and is still in contact with the overlying North American plate. Segment B extends from approximately 50 to 110 km depth and is remarkably planar with a slope of about 30° (cross-section C6 in Figure 2.5(a)). Segment C is the most active in the McKinley block and extends from about 90 to 150 km depth. It has a triangular shape in map view and dips more steeply (about 65°) than the adjacent segment B. Segment D is the northernmost part of the McKinley block and the smallest of all segments discussed above. It starts at about 100 km and reaches 150 km depth, dipping at an angle of nearly 80°. In contrast to the other segments, its seismicity is concentrated in small clusters (see Figure 2.5(b)). There are few earthquakes below 150 km depth (see cross-sections C5 and C6 in Figure 2.5(a)). None of the identified segment boundaries coincide with the boundaries of the relocation blocks.

Next, we analyzed the Harvard CMT moment tensor solutions for the subduction zone earthquakes in Alaska. There are 48 solutions available from the CMT catalog for the earthquakes that occurred between 1977 and 2000. In Figure 2.7 orientations of the P and T principal moment tensor axes are shown. In Figure 2.8 the same data are summarized in a plot of P- and T-axes on a lower hemispheric projection and in a triangular diagram, which classifies the types of faulting. The earthquakes above 100 km depth are character-
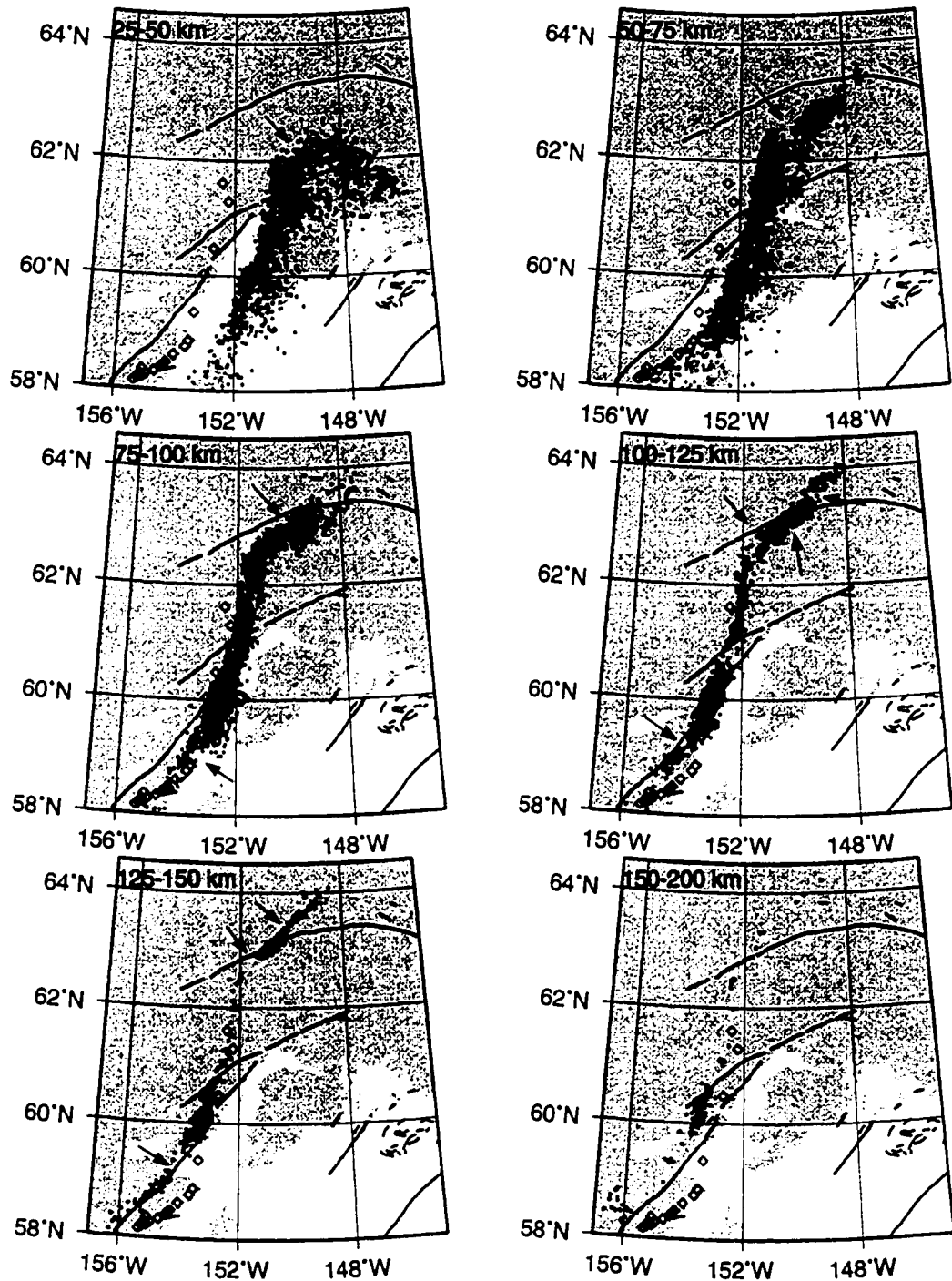
Figure 2.6. Depth slices of the JHD relocated events. Each slice is 25 km thick with the exception of the 50-km-thick slice that includes events below 150 km depth. Solid arrows illustrate segmentation of the plate, based on both the seismicity off-sets and gaps. Open diamonds are locations of the volcanos.
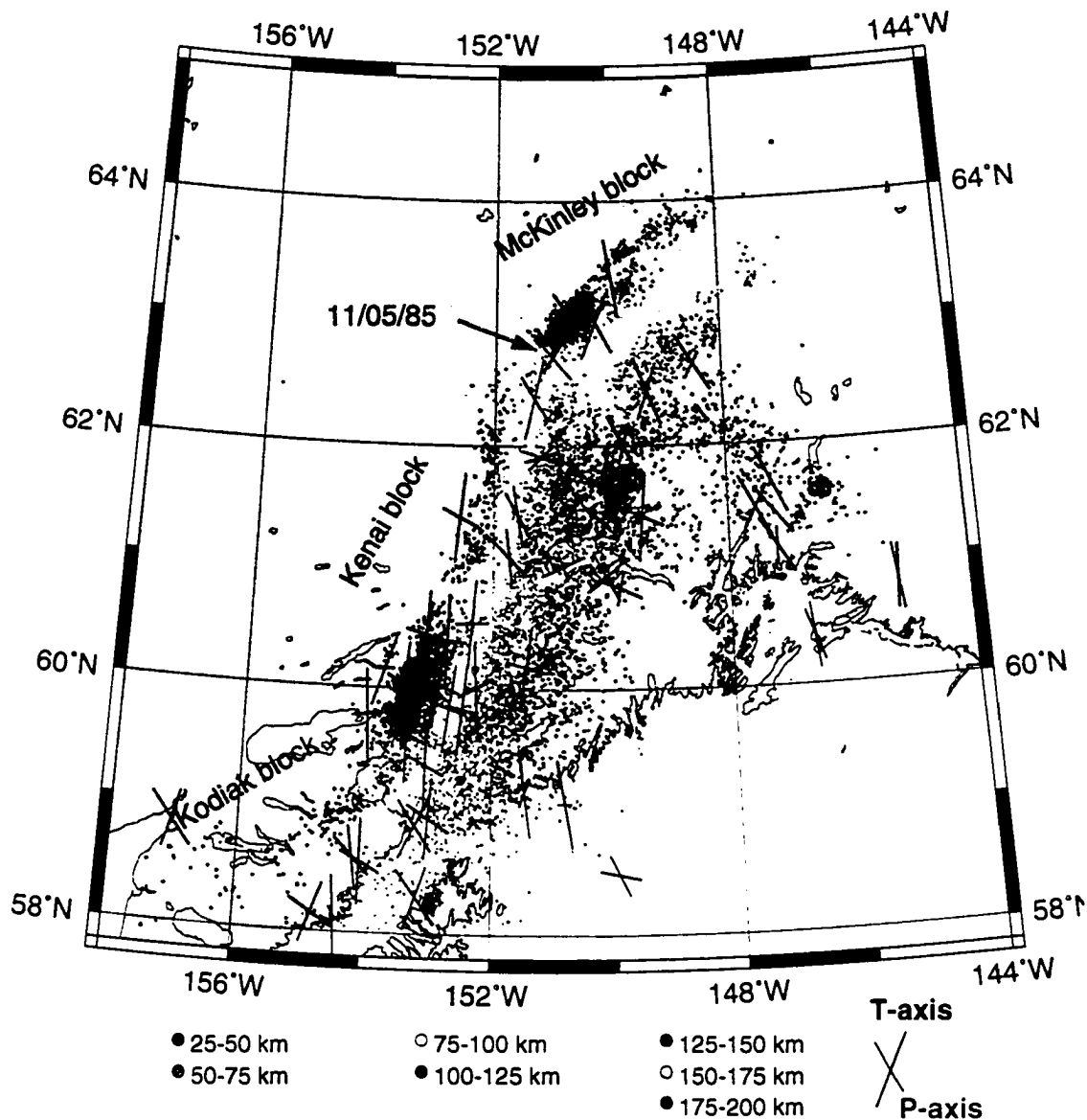
Figure 2.7. The JHD relocated earthquakes and directions of the maximum and minimum principal axes of 48 Harvard CMT moment tensor solutions for the subduction zone earthquakes that occurred from 1977 to 2000. A common feature among the moment tensor solutions is the down-dip orientation of the T principal axes, which is consistent with the extensional regime caused by the gravitational pull of the subducted slab. One earthquake, that occurred in 1985 and located in the boundary zone between the McKinley and Kenai blocks (pointed to by the arrow), however, has along-strike T-axis orientation.
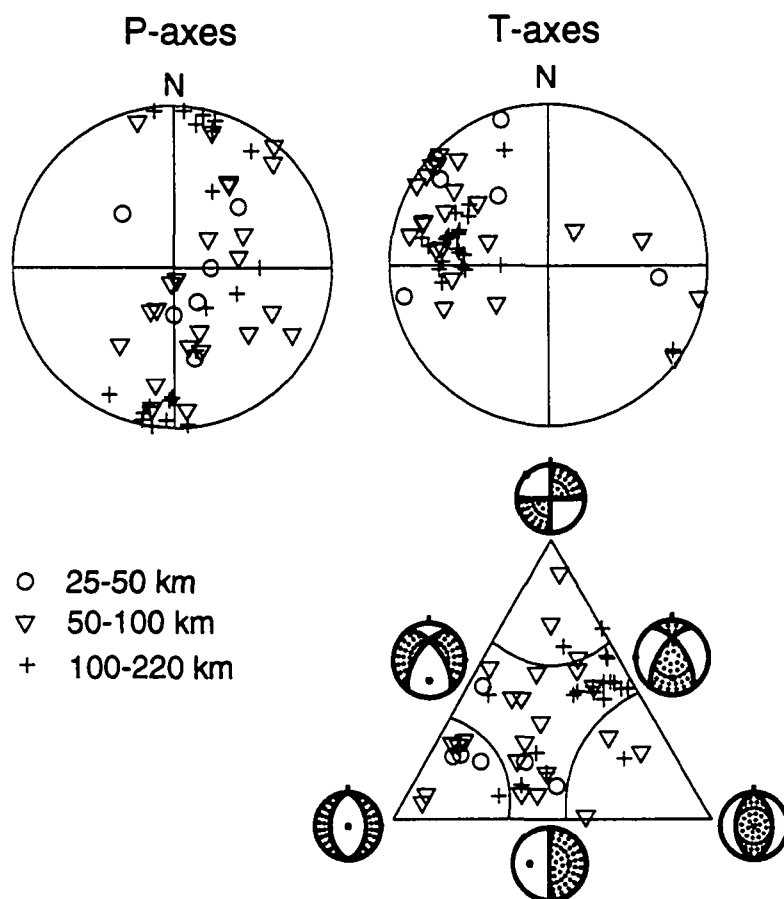
Figure 2.8. Upper panel shows lower hemispheric projection of the minimum and maximum principal axes of 48 Harvard CMT moment tensor solutions for the Alaskan subduction zone earthquakes that occurred from 1977 to 2000. Triangular diagram representing types of the focal mechanisms (Frohlich, 1992) is shown on the lower panel. The vertices of the triangle correspond to pure trust (right), pure normal (left) and pure strike-slip (top) mechanisms. The curved lines inside the triangle correspond to mechanisms with 60° dip of N- and T-axes and with 50° dip of P-axis. Different symbols indicate depth range of the earthquakes: circles - 25-50 km depth, triangles - 50-100 km depth, crosses - below 100 km depth.

ized by predominantly normal and oblique-normal type of faulting, while the earthquakes below 100 km depth are represented by mostly reverse type mechanisms (see triangular diagram in Figure 2.8). The common feature among all available moment tensor solutions for the earthquakes below 50 km depth is the down-dip orientation of the T-axes, which is consistent with the down-dip extensional regime caused by the gravitational pull of the

subducting slab. The down-dip extensional regime is also indicated by the stress tensor inversion results of Lu et al. (1997) for the subducting slab beneath Alaska.

There is one earthquake, however, that does not fit this pattern. It is located within the boundary zone between the McKinley and Kenai blocks at 88 km depth. In contrast with the solutions available for the neighboring earthquakes, its T-axis is oriented parallel to the strike direction. The JHD location is not available for this 1985 earthquake because it predates our study period. Therefore, it is not possible to identify exactly on which side of the boundary between the blocks this earthquake is located. However, its location near the boundary and its difference from the other neighboring earthquakes may indicate the complex conditions present near the edges of the individual blocks within the subducting plate.

2.4. CONCLUSIONS.

A total of 14,102 subduction zone earthquakes from the AEIC catalog that occurred from July, 1988 to July, 1998 and were located between 58°N and 65°N latitude were relocated using the joint hypocenter determination method. The selected earthquakes were divided into 17 blocks on the basis of their hypocentral locations and each block was relocated separately. Maximum hypocentral shifts reach values of 20 km in a few extreme cases. Average epicenter shift is 3.7 km and average upward and downward depth shifts are 4.0 and 4.1 km, respectively (roughly the same number of earthquakes shifted upwards (47%) and downwards (53%)). The relocated subduction zone earthquakes have more accurate relative locations and provide more detail on the structure of the Alaskan Wadati-Benioff zone. In particular, we were able to identify more precisely the boundaries between the southwestern (Kodiak), central (Kenai) and northeastern (McKinley) blocks of the Alaskan WBZ. The boundary between the Kodiak and Kenai blocks seems to be represented by a smooth bend, with no evidence for the tear in the subducted plate. The boundary between the Kenai and McKinley blocks, however, is represented by a tear in the plate that can be traced as far as Prince William Sound (Figure 2.9). In addition, there is
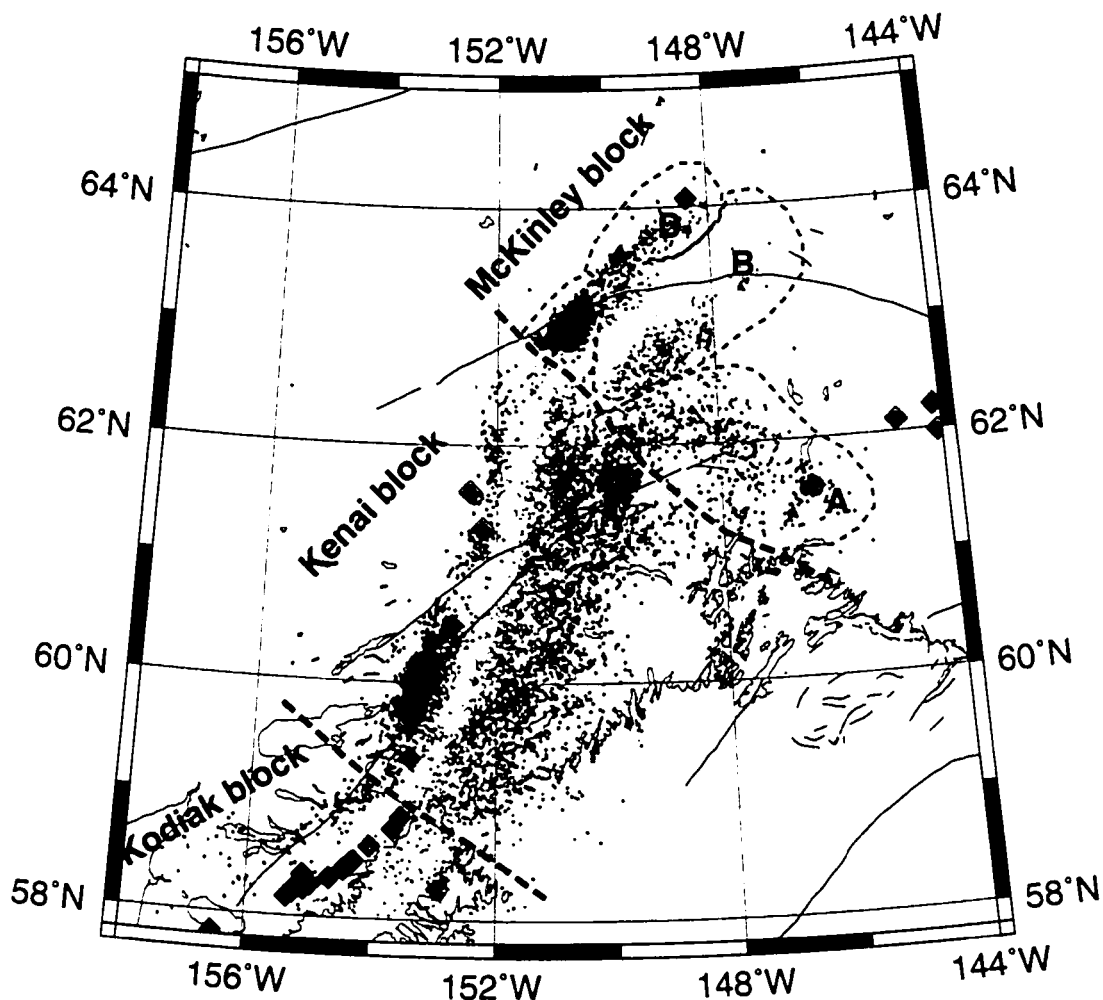
Figure 2.9. Interpretation of the plate segmentation in southern and central Alaska based on the new locations of the subduction zone earthquakes (each color corresponds to a 25 km depth interval, starting from 25 km depth). Thick dashed lines are the boundaries between the three plate segments: southwestern (Kodiak), central (Kenai), and northeastern (McKinley). Thin dashed lines and letters A through D show segmentation of the McKinley block. Red diamonds are the volcano locations. Solid red lines are the mapped traces of faults.

evidence for plate segmentation within the McKinley block. The boundaries between the segments are marked by seismicity gaps and offsets and abrupt dip changes across them.

We suggest, that the new catalog of relocated Alaska subduction zone earthquakes should be incorporated into future studies of the Alaskan subduction zone, such as analy-

sis of the effect of heterogeneous slab structure on generation of the anomalous wave phases, relationship between the Alaska and Wrangell subduction zones, investigations of the subduction zone volcanism and/or absence of such, GPS studies of the crustal movements above the subducting slab, etc. The JHD earthquake catalog is available from the AEIC website (http://www.aeic.alaska.edu/Seis/).

Chapter 3: The Kodiak Island M_W 7 earthquake

of 6 December 1999.[1]

3.1. INTRODUCTION.

An M_W 7 earthquake occurred on December 6, 1999 at 2:12 pm AKST in the Kodiak Island region of Alaska. This event was felt strongly in the towns of Kodiak and Old Harbor as well as surrounding communities. It caused some minor damage including power and phone outages in Kodiak. Felt reports were received from as far as Fairbanks, 900 km away. The earthquake was located by the Alaska Earthquake Information Center (AEIC) at 57.51°N and 154.67°W at 45.8 km depth. Aftershocks of M_L 5.4 and M_W 6.4 followed the main shock by ten minutes and one hour, respectively. Aftershock activity decreased rapidly from about 25 events per hour in the first few hours after the main shock to 5 events a day 10 days later. It appears that the main shock triggered a swarm of earthquakes in the Katmai volcano field that subsided after a few hours (Power et al., 2001).

Convergence of the Pacific and North American plates dominates the tectonic framework of the Kodiak region (Figure 3.1). The plate boundary lies along the Aleutian trench about 100 km seaward of Kodiak Island. A typical volcanic arc accompanying subduction is located on the Alaska Peninsula and the west coast of Cook Inlet. Most of the seismic energy in southern Alaska is released in major earthquakes that rupture the shallow part of the megathrust. The Great 1964 Prince William Sound earthquake (M_W 9.2) ruptured a 800-km-long portion of the megathrust including the Kodiak Island segment (Christensen and Beck, 1994). In 1938, an M_W 8.2 earthquake ruptured the segment of the

1. This Chapter has been published as an article in Seism. Res. Lett. v.72, pp. 22-32, 2001.
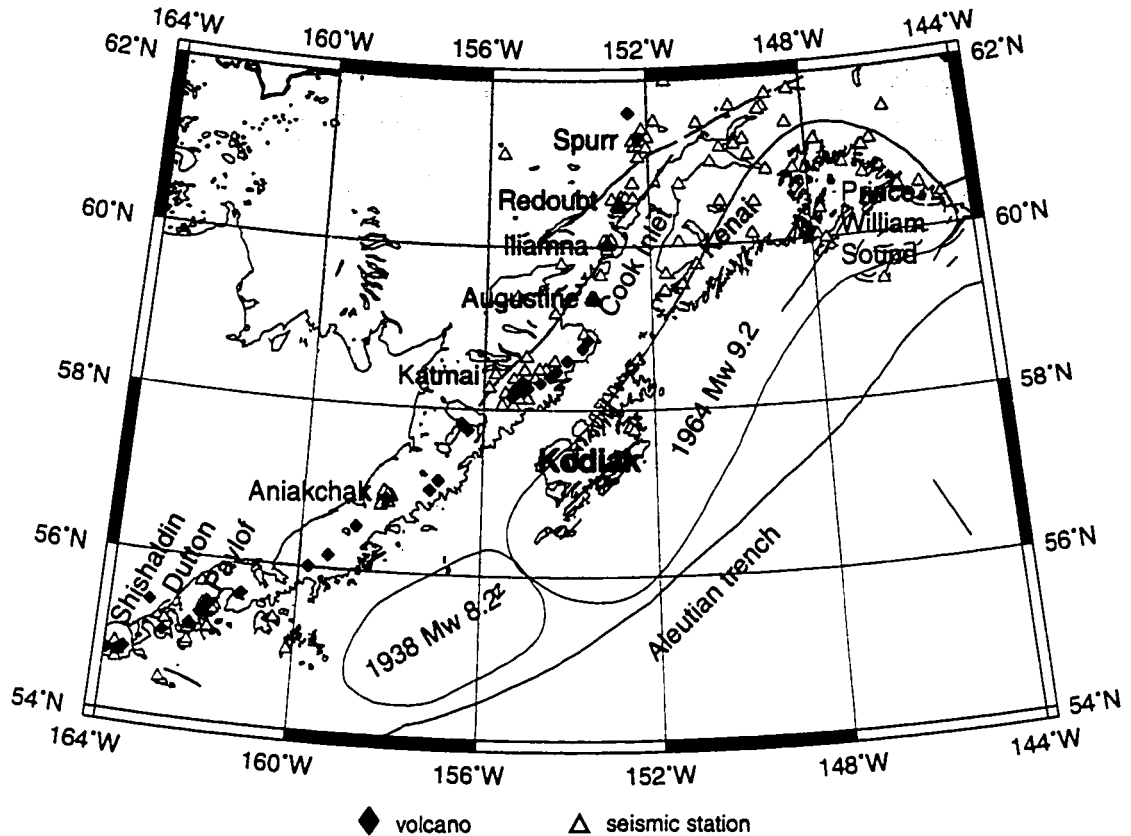
Figure 3.1. Map of the study area and surrounding regions. Rupture zones of the 1964 (M_W 9.2) and 1938 (M_W 8.2) earthquakes, major faults and the Aleutian trench are shown. Open triangles are seismic stations used in the earthquake relocations. Solid diamonds are active volcanoes.

boundary south of Kodiak Island. Recent GPS studies of the deformation processes near Kodiak showed that the down-dip width of the locked portion of the megathrust could be as much as 158 km (Savage et al., 1999).

A number of significant earthquakes occurred beneath the Kodiak Island region in the 1900s, including seven earthquakes with magnitude 6.8 or larger (Figure 3.2 and Table 3.1). While the majority of these shocks are associated with the megathrust ruptures, two earthquakes in 1912, an m_b 7.3 and an m_b 6.9, occurred at a depth of 90 km within a 20 km radius of the 1999 Kodiak Island earthquake. Allowing for some uncertainty in their locations, it is safe to suggest that both earthquakes occurred within the subducting plate.

Table 3.1: Earthquakes in the Kodiak region with magnitude 6.8 or greater.

#	date	time	lat, N	lon, W	depth, km	M_W	M_L	M_S	m_b	reference
1	10/09/1900	12:28:17.6	57.09°	153.48°	0.0	7.9		7.7		Boyd & Lerner-Lam (1988)
2	12/23/1906	17:22:00.0	56.85°	153.90°	0.0			7.3		Boyd & Lerner-Lam (1988)
3	06/10/1912	16:06:06.0	59.00°	153.00°	25.0		7.0	6.9	6.8	Gutenberg & Richter (1954)
4	11/07/1912	07:40:24.0	57.50°	155.00°	90.0		7.5		7.3	Gutenberg & Richter (1954)
5	12/05/1912	12:27:36.0	57.50°	154.00°	90.0		7.0		6.9	Abe (1981)
6	09/04/1965	14:32:50.2	58.29°	152.50°	30.0		7.1	6.8	7.0	NEIC, Abe (1981)
7	12/22/1965	19:41:21.6	58.35°	153.13°	38.0		6.8			NEIC
8	12/06/1999	23:12:34.0	57.31°	154.29°	35.8	7.0	7.0			this study
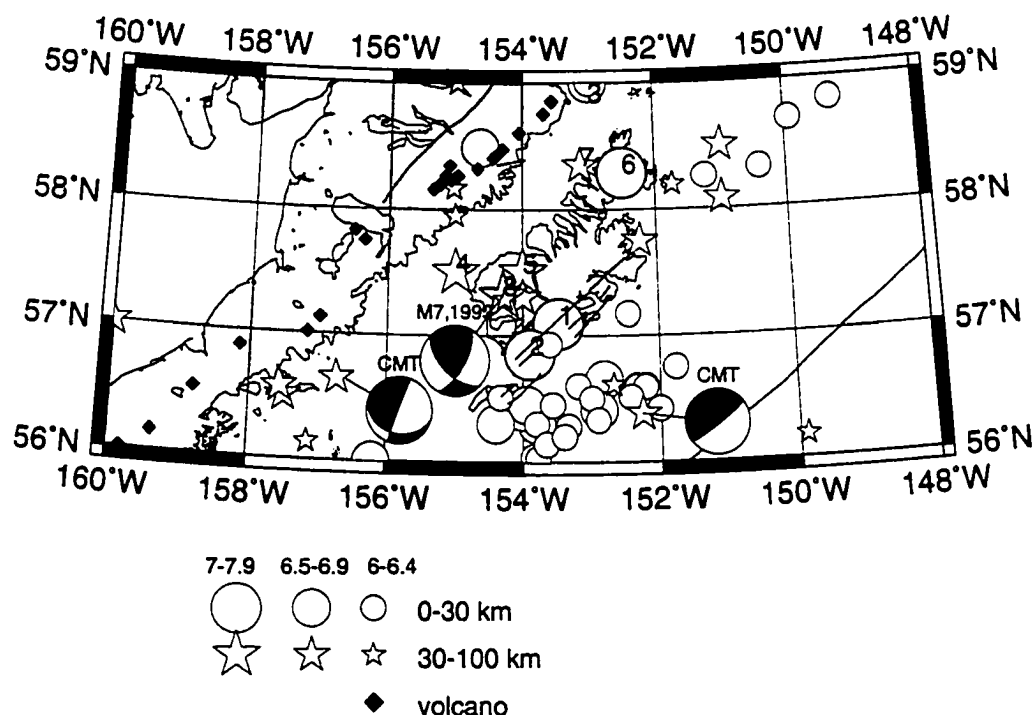
Figure 3.2. Location of significant earthquakes (magnitude 6 and greater) that occurred in the Kodiak region since 1900. Two Harvard CMT moment tensors are shown (lower hemispheric projection) as well as moment tensor solution for the 1999 Kodiak Island M_W 7 earthquake determined in this study. Numbers refer to the earthquakes listed in Table 3.1.

Therefore, strong earthquakes in the Kodiak region are known to have originated inside the subducting plate and not only on the interplate contact.

The 1999 M_W 7 event and its aftershocks recorded by the regional seismic network were relocated using the Joint Hypocenter Determination (JHD) method. Regional broadband data have been used to calculate moment tensors for the main shock and its largest aftershock. This Chapter discusses the aftershock distribution of the M_W 7 event and its source mechanism.

3.2. RELOCATION OF REGIONAL EARTHQUAKES AND AFTERSHOCKS.

3.2.1. Earthquake data, velocity structure and relocation method.

Over 400 aftershocks of the M_W 7 event were located by AEIC throughout the month of December. The aftershock locations, however, had a rather large uncertainty. The major difficulty in locating earthquakes in the Kodiak Island region is that the area lies on the edge of the Alaskan regional seismic network. The majority of the stations are located to the north and northwest of Kodiak Island with a few stations on the Alaska Peninsula and in the Aleutians (Figure 3.1). A broadband seismometer was installed by IRIS near the city of Kodiak in 1997. Unfortunately, this instrument was not recording on December 6, 1999. An additional difficulty in locating earthquakes in the Kodiak Island vicinity is that the velocity structure in the region is highly heterogeneous and poorly known.

Therefore, a Joint Hypocenter Determination method (Appendix A) was used to relocate the recorded aftershocks. Many studies have shown (Engdahl et al., 1982; Pujol, 1992; Ratchkovsky et al., 1997) that the relative locations of hypocenters can be improved significantly by the use of the JHD method in areas with complex three-dimensional velocity structure and in areas in which the velocity structure is poorly known. Originally, the method was developed by Douglas (1967) to determine epicenter parameters and station corrections using a least-squares inversion method. Variations of this method have

been widely applied in determining earthquake locations. In general, negative and positive JHD station corrections correspond to raypaths through high and low velocity zones, respectively. They compensate for lateral variations of velocity, which improves the accuracy of the hypocenter locations. The JHD algorithm used in the present study was developed by Pujol (1988). It has been used in a variety of tectonic settings and has proved to be reliable and computationally effective (Pujol et al., 1989; Pujol et al., 1991; Ratchkovsky et al., 1997; Ratchkovsky et al., 1998).

To tie locations of the aftershocks to the regional seismicity, all earthquakes that occurred in the area extending from $148°$ to $160°W$ longitude and from $56°$ to $59°N$ latitude were included into the relocation. Since 1988, the number of earthquakes AEIC has located in this region has grown from under 100 events per year to over 300 events in 1998. The increasing number of located earthquakes in the area over the past 5 years is due mainly to the installation of seismic networks by the Alaska Volcano Observatory for monitoring volcanoes on the Alaska Peninsula (e.g., Katmai, Aniakchak, Pavlof, Dutton and Shishaldin volcano networks).

Firstly, all available earthquakes from the AEIC catalog that occurred in the Kodiak region from July 1988 throughout the end of 1999 were selected. The search resulted in 2,129 events, including over 400 aftershocks of the M_W 7 earthquake of December 6, 1999. Since seismotectonic events were our major interest, events associated with the volcanic activity were removed from the dataset, including a swarm of earthquakes beneath the Katmai volcano field triggered by the M_W 7 earthquake. Events with the number of P and S phases less than 5 and 2, respectively were also excluded. With these criteria, 1,391 earthquakes were available for the joint relocation, including 310 aftershocks of the M_W 7 earthquake. Stations used in the relocation are shown in Figure 3.1.

The JHD station corrections strongly depend on the ray path. Therefore, to ensure the best relocation results we subdivided the selected events into five datasets on the basis of their epicentral location and depth and relocated each dataset separately. The datasets are:

(I) - 56°-58°N, 0-50 km, 385 events including M_W 7 event and most of its aftershocks;

(II) - 58°-59°N, 0-50 km, 201 events;

(III) - 56°-58°N, 50-100 km, 224 events;

(IV) - 58°-59°N, 50-100 km, 380 events; and

(V) - 56°-59°N, 100-210 km, 201 events.

Few details are known about the velocity structure beneath Kodiak Island and the surrounding areas. A velocity model for the Shumagin Islands (south-west of Kodiak Island) was determined by Rowlett and Jacob from travel time studies of nuclear explosions (Reyners and Coles, 1982). Berg et al. (1967) used seismic and gravity observations in the Katmai volcanic field to produce velocity models for the Katmai area and Kodiak Island. Shor and von Huene (1972) constructed a cross-section of the crustal structure from the eastern end of Kodiak Island towards the Aleutian trench based on seismic refraction profiles. This cross-section suggests that the depth to the top of the oceanic crust immediately east of Kodiak Island is near 19 km and the depth to the Moho in the subducting plate is 23 km. The deep seismic reflection transect EDGE (Moore et al., 1991) extended from Augustine volcano towards the trench. It revealed a number of prominent reflectors, including the top of the oceanic crust and the Moho. Several velocity models have been proposed for Cook Inlet and the Kenai Peninsula (e.g., Woollard et al., 1960; Matumoto and Page, 1969; Lahr et al., 1978; Stephens et al., 1990).

Although the velocity models differ considerably in detail, the choice of the particular structure should not significantly influence the relative hypocenter locations. This is due to the fact that the JHD station corrections determined for a given set of hypocenters and a flat-layer velocity model should account for inaccuracies of the model. After having tested a number of velocity structures in the joint relocation, we chose the standard AEIC model used for locating earthquakes in south-central Alaska because it produces minimum average RMS residuals for the events, therefore allowing relocation of the maximum number of earthquakes. Although the JHD locations may still be systematically offset, relative JHD locations are more accurate than the initial ones.

3.2.2. Relocation results.

A total of 933 events were relocated, including 97 aftershocks of the 1999 Kodiak Island earthquake. Maps and a cross-section of the relocated earthquakes are shown in Figures 3.3 and 3.4. The earthquakes located beneath Kodiak Island and the Alaska Peninsula define a Wadati-Benioff zone (WBZ) with an average thickness of about 25 km and a maximum depth of 203 km. The dip angle gradually increases from 25° in the upper part of the section to 50° below 150 km depth

From over 400 aftershocks of the M_W 7 earthquake located by AEIC, we were able to relocate only 97. This is due to the poor quality of the initial locations resulting from a small number of picks available for each aftershock. Clearly, the small number of picks

◆ volcano	○ 0-50 km	+ 12/06-12/31 aftershocks
	● 50-100 km	○ Mw 7, 12/06/99
	● 100-150 km	○ Mw 6.4, 12/07/99
	● 150-200 km	○ Ml 5.4, 12/06/99
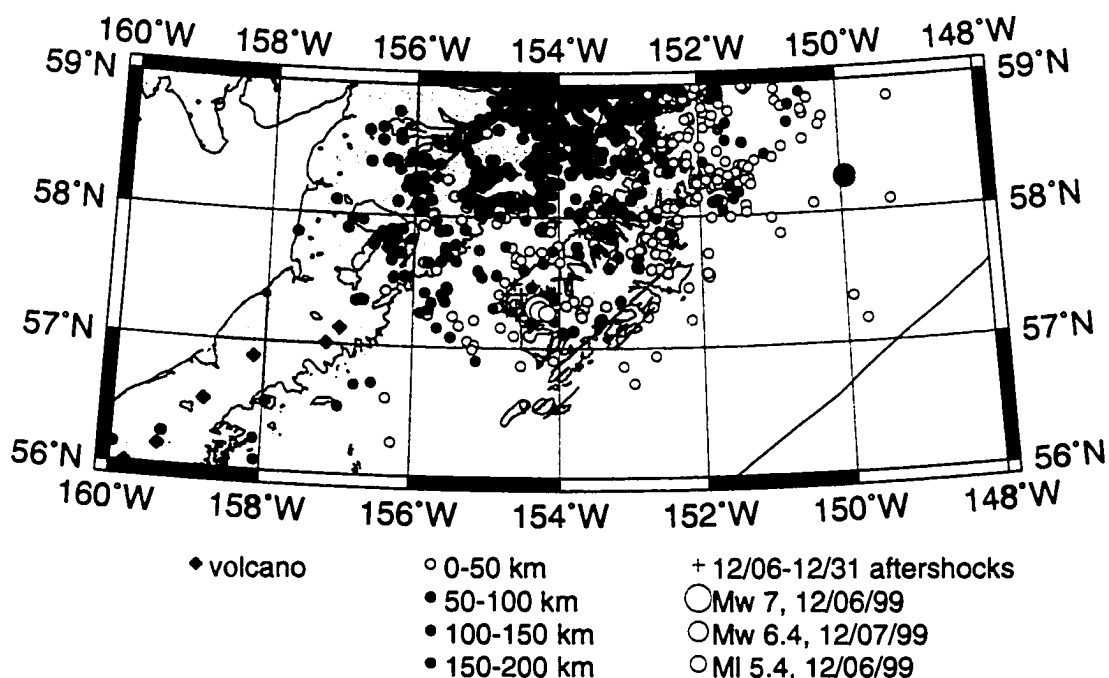
Figure 3.3. Map of the JHD relocated earthquakes in the Kodiak region, including the 1999 Kodiak Island M_W 7 earthquake and its aftershocks (crosses). The main shock and the two largest aftershocks (M_W 6.4 on December 7 and M_L 5.4 on December 6, 1999) are shown by open circles, size of the circle is proportional to the magnitude of the event.
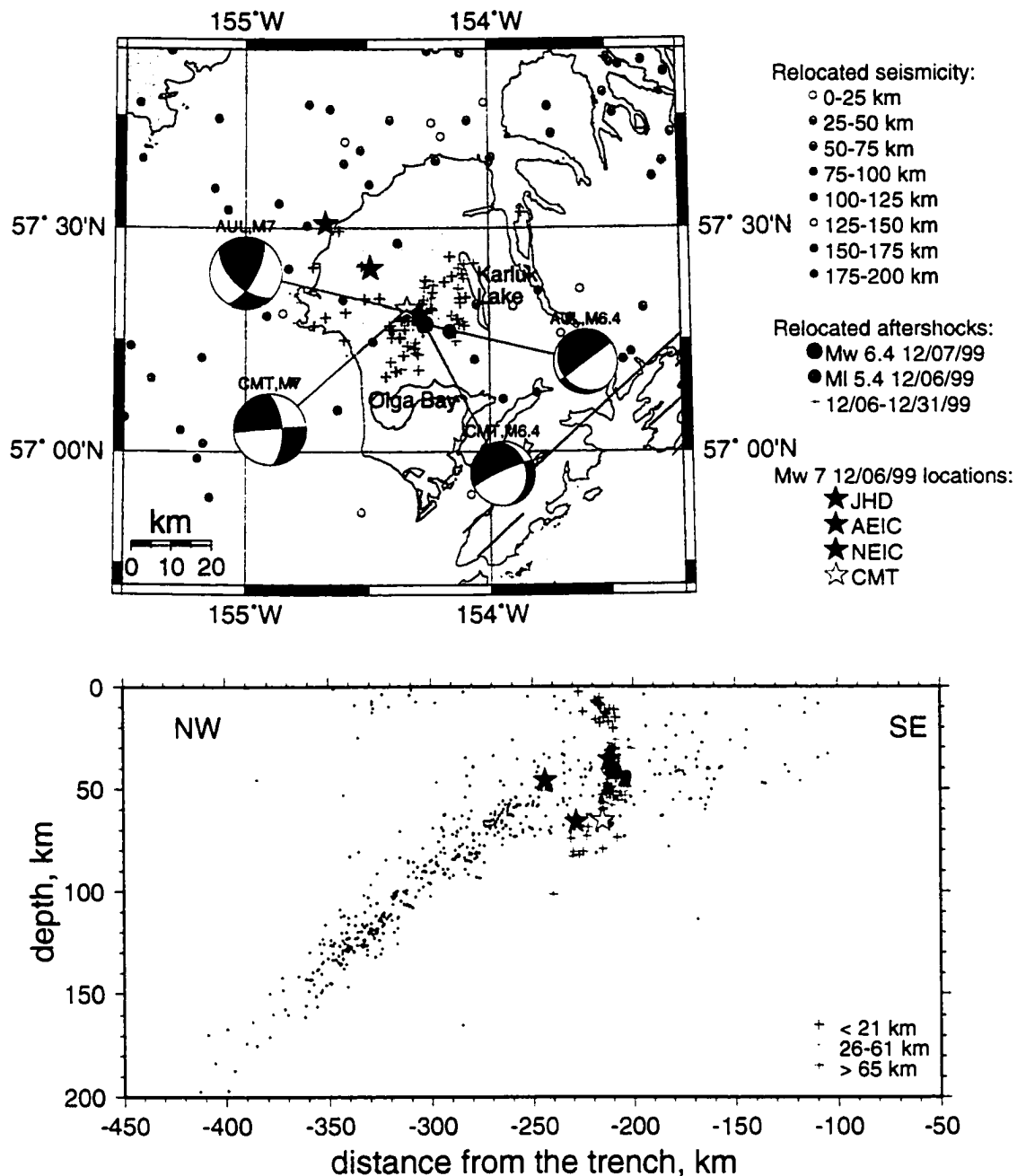
Figure 3.4. Detailed view of the relocated aftershocks of the 1999 Kodiak Island M_W 7 earthquake. Aftershocks delineate a nearly vertical 36-km-long southwest-to-northeast striking surface. Locations of the main shock provided by different agencies are also shown (Table 3.2). Moment tensor solutions from the Harvard CMT Catalog and from this study are shown for both the main shock and the M_W 6.4 aftershock (lower hemispheric projection).

Table 3.2: Locations of the December 6, 1999 Kodiak Island M$_W$ 7 earthquake reported by different agencies.

Catalog	lat, N	lon, W	depth, km
JHD relocation, this study	57.3076°	154.2896°	35.75
AEIC	57.5102°	154.6735°	45.82
NEIC	57.41°	154.49°	66
Harvard CMT solution	57.32°	154.34°	65.4

caused large uncertainties in the earthquake locations, resulting in large RMS residuals for the majority of the aftershocks.

Figure 3.4 shows a detailed view of the relocated aftershocks. Three clusters can be identified. The first (shallow) cluster is located in the overriding plate between 3 and 21 km depth and represents induced seismicity. The second (intermediate) group contains most of the relocated aftershocks and defines a southwest to northeast striking surface that extends from Olga Bay to Karluk Lake. The surface is nearly vertical and extends from 26 to 61 km depth, i.e. through almost the entire thickness of the subducting plate. The surface projection of this cluster is 36 km long. We interpret these aftershocks as those located on or near the fault plane of the main shock. The third (deep) cluster is rather diffuse, with the majority of the shocks located between 65 and 83 km depth. The deepest aftershock (at 101.6 km depth) is located below the main WBZ. This earthquake has the maximum allowable RMS in the relocation with a residual of 0.39 sec. We think that the bias in its location is caused by the erroneous phase picking.

The relocated hypocenter of the M$_W$ 7 earthquake is positioned at 57.31°N and 154.29°W at 35.8 km depth. This location is 30 km southeast of the preliminary AEIC location and almost 10 km shallower. The M$_W$ 6.4 aftershock is located at 57.29°N and 154.27°W at 41.4 km depth. Therefore, the distribution of the relocated aftershocks strongly suggests that the M$_W$ 7 earthquake is an intraplate event.

3.3. MOMENT TENSOR INVERSION.

A technique for inverting waveform data for both the source and structure parameters is utilized here (Hansen and Harvey, 1989; Appendix B). Synthetic seismograms are computed using the Locked Mode Approximation method (Harvey, 1981). This algorithm is in particular very suitable for use in Alaska because of the complexity of the crustal and upper mantle structure and relatively poor coverage in terms of broadband instruments. It has been shown that the inversion provides stable results even when data from only one station are used (Hansen et al., 1989).

We used waveform data recorded at the broadband station located on Augustine Island, 230 km northeast of the M_W 7 earthquake epicenter (station code AUL). In addition, we utilized data recorded by instruments of the BEAAR experiment, which is a three-year PASSCAL deployment aimed at imaging crustal and mantle structure beneath interior Alaska (Meyers et al., 1999).

Due to the complexity of the crustal and upper mantle structure in Alaska, it was necessary to explore the effect of the assumed velocity structure on the inversion results. Since the waves modeled have the wavelengths on the order of 10 km and longer, the waveforms reflect the averaged properties along the travel path. After having tested a number of velocity models in the inversion, we came to the conclusion that a three-layer velocity model adequately describes the structure and allows us to compute synthetic seismograms with a satisfactory fit to the recorded long-period data. Variations in the compressional and tensional axes of the moment tensor due to changes in velocity models were insignificant. The locations of the main shock and the M_W 6.4 aftershock in the inversion were fixed to those obtained in the joint relocation.

Inversion results for the main shock and M_W 6.4 aftershock using the Augustine station data are shown in Figure 3.5. The moment tensor solution for the main shock indicates a fault plane striking at 29° azimuth and dipping at 66°. The inversion for the aftershock resulted in nearly pure dip-slip faulting on a plane striking at 234° azimuth and

(a) **Mw 7, 12/06/99, AUL**

(b) **Mw 6.4, 12/07/99, AUL**

1: Str= 134.8 Dip= 57.8 Slp= 28.3
2: Str= 28.7 Dip= 66.3 Slp= 144.4

dc= 93.19% dp= 6.81%

1: Str= 142.5 Dip= 18.2 Slp= -1.5
2: Str= 233.9 Dip= 89.5 Slp= -108.2

dc= 91.69% dp= 8.31%
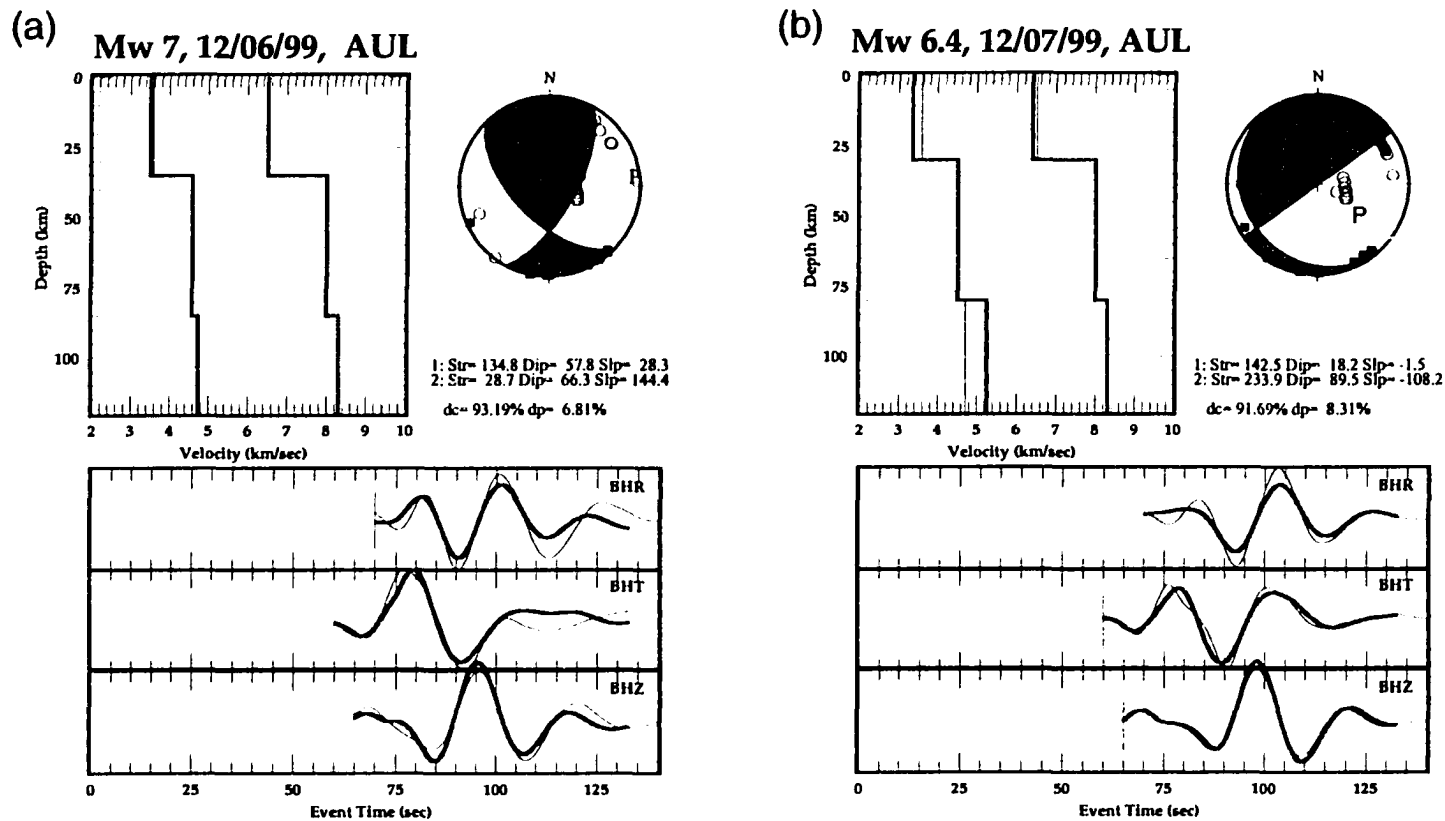
Figure 3.5. Results of the moment tensor inversion using data from the broadband station AUL located on Augustine Island for (a) 1999 Kodiak Island M_W 7 earthquake and (b) M_W 6.4 aftershock. Upper left panel shows velocity model with thin and thick lines representing the initial and modified structures, respectively. Bottom panel displays recorded (thin) and synthetic (thick) waveform data filtered with 0.01-0.05 Hz band-pass filter. Lower hemispheric projection of the focal sphere with the compressional quadrants shaded grey is shown in the upper right corner. First motion data are indicated by the closed squares (compression) and open circles (dilation). Strike, dip and slip values of the fault planes are printed below the focal sphere, as well as percentage of the double couple and CLVD components in the solution.

33

dipping at 89°. These results are in agreement with the fault plane delineated by the after-shock locations and with the teleseismic and regional P-wave first motions.

In addition, for the main shock we inverted waveform data recorded at the four BEAAR sites (Figure 3.6). The calculated strike of the fault plane ranges between 14° and 40°. The dip angle is between 66° and 88°. The major difference between the inversion results obtained with AUL and BEAAR data is a larger CLVD component in the BEAAR data inversion results (up to 36%). Also, velocity structures that best fit the observations at BEAAR stations have thicker crust than that required to fit the Augustine data (40 km versus 30-35 km).The change in the velocity model required to fit the data as well as the increased percentage of CLVD component in the moment tensor together point toward a difficulty in representing a complex three-dimensional structure with a suite of changing one-dimensional velocity models. To improve this problem of characterizing complex 3-D Alaska structure with 1-D Green's functions, we are researching an iterative technique that balances the trade-offs between frequency bandwidth, velocity model parameters, and source estimates for defining the proper parameters to use for calculating a grid of appropriate regional Green's functions.

Finally, the Harvard centroid moment tensor (CMT) solution for the main shock is inconsistent with the aftershock distribution and with the regional and teleseismic P-wave first-motion data. Relocation of the aftershocks and moment tensor inversion of the regional data indicate a fault plane aligned in a southwest to northeast direction, while the two fault planes of the CMT solution are oriented almost exactly north-to-south and east-to-west, respectively (Figure 3.4 and Table 3.3). The inconsistency between our results from regional broadband data and the CMT illustrates that the CMT solutions can be useful for general indications but cannot be taken as the ground truth for the purpose of improving the regional velocity models. A large effort is still needed for improving region-alized Green's functions for fast and accurate moment tensor calculations. The CMT solution for the M_W 6.4 aftershock has the fault plane striking at 246° azimuth and dipping at 82° angle, which is in agreement with the inversion results obtained in this work.
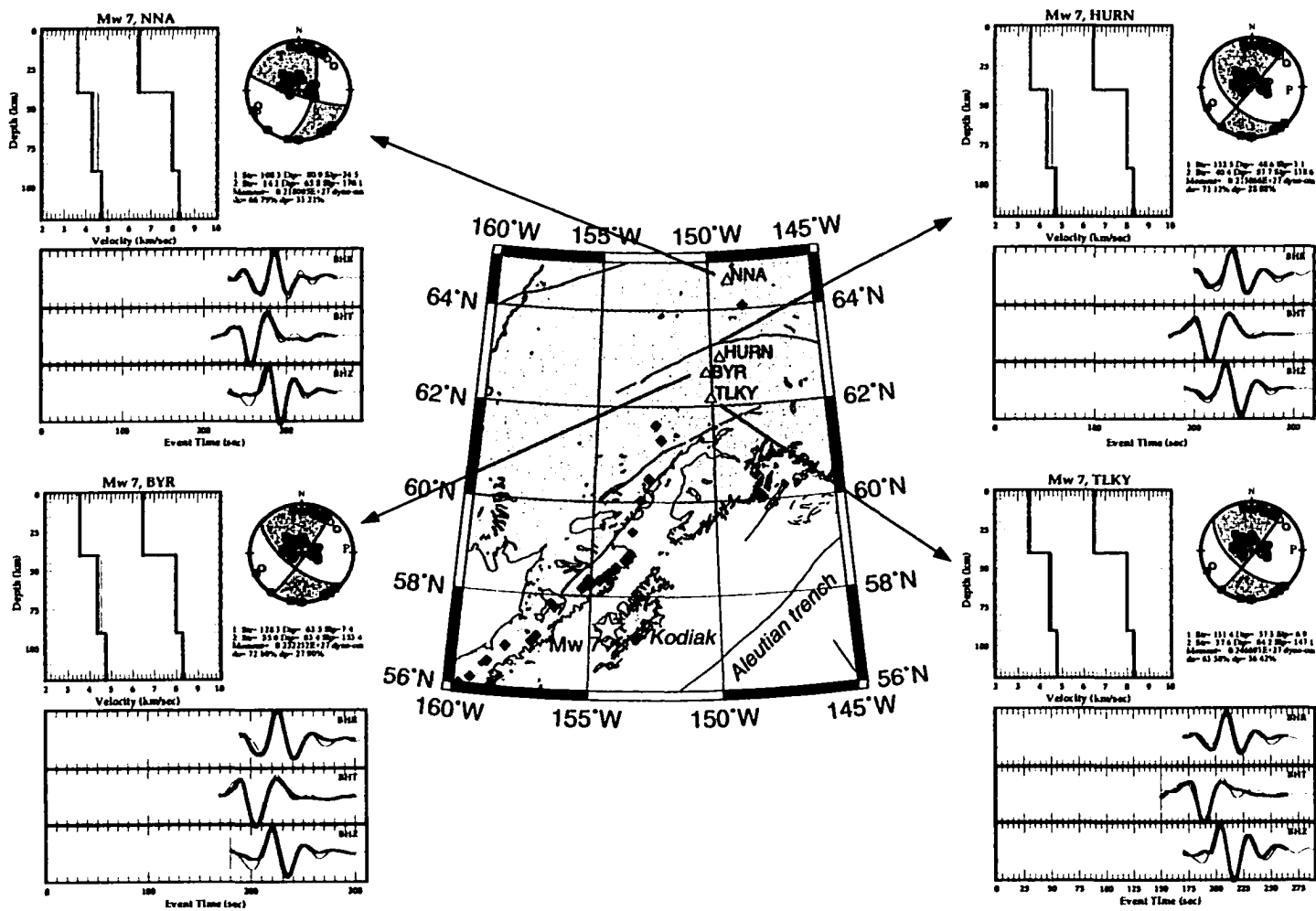
Figure 3.6. Results of the moment tensor inversion for the 1999 Kodiak Island M_W 7 earthquake using data recorded by the four PASSCAL instruments in interior Alaska (see map in the center). Inversion results for all four stations show nearly vertical SSW-to-NNE striking fault plane. See Figure 3.5 for panel explanations.

Table 3.3: Fault plane parameters for selected earthquakes (referred to in the text).

earthquake	solution	1st plane			2nd plane		
		strike	dip	slip	strike	dip	slip
05/20/1979, M_W 6.6	CMT	102°	10°	8°	199°	86°	119°
12/06/1999, M_W 7	CMT	357°	63°	-177°	266°	88°	-27°
	this study	29°	66°	144°	135°	58°	28°
12/07/1999, M_W 6.4	CMT	351°	28°	-163°	246°	82°	-63°
	this study	143°	18°	-2°	234°	89°	-108°
03/08/2000, M_L 5.2	NEIC	354°	28°	-146°	234°	75°	-66°
05/08/2000, M_W 5.1	CMT	113°	18°	-44°	246°	78°	-103°
07/11/2000, M_W 6.5	CMT	357°	43°	-161°	252°	77°	-49°

3.4. LATE AFTERSHOCK M_W 6.5 OF JULY 11, 2000.

On July 11, 2000, a M_W 6.5 earthquake occurred in the aftershock zone of the M_W 7 earthquake of December 6, 1999. The AEIC located the earthquake at 57.36°N and 154.21°W at 43.6 km depth. Thirty aftershocks have been recorded in the first five days after the earthquake including a M_L 5.5 event on July 11th. In addition, there were three magnitude 5.0-5.2 earthquakes within the aftershock zone of the December, 1999 M_W 7 earthquake that occurred between January and May, 2000. To tie locations of these earthquakes to the December aftershock sequence, we added the new earthquakes to the datasets I and III and ran the JHD relocation once again (Figure 3.7). The resulting JHD location of the M_W 6.5 earthquake is 41.5 km deep and positioned at the northern end of the December aftershock zone (namely, at 57.41°N and 154.21°W). Most of its 23 relocated aftershocks are concentrated to the north of the main shock location and the December aftershock sequence. Similar to the aftershocks of the December earthquake, several July aftershocks are located in the overriding plate and represent induced seismicity. The aftershocks in the subducting plate are located between 30 and 65 km depth and delineate
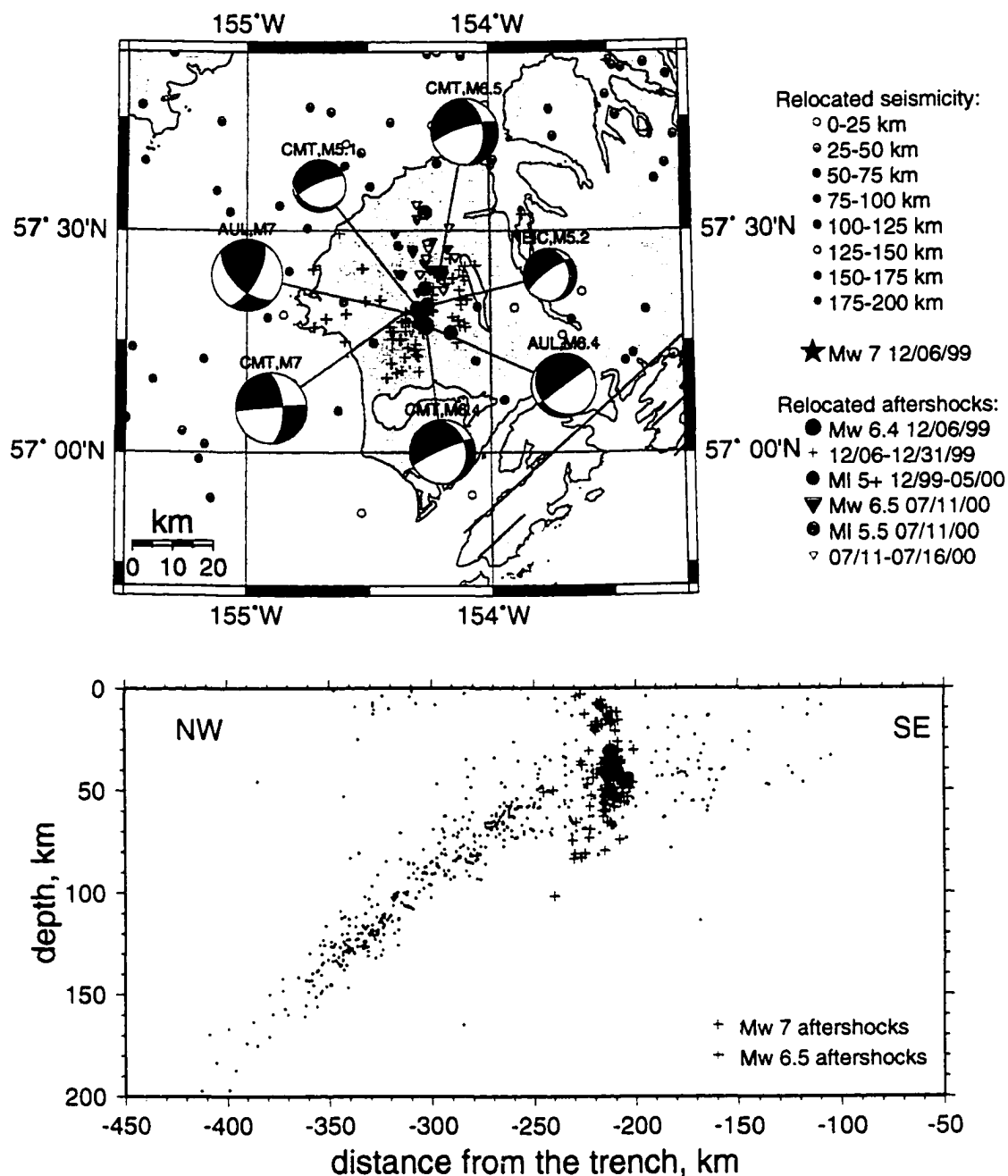
Figure 3.7. Detailed view of the relocated aftershocks of the 1999 M_W 7 earthquake and of the M_W 6.5 earthquake of July 11, 2000. Epicenter of the July earthquake is located at the northern end of the December aftershock zone. Also shown are the moment tensor solutions for the M_W 7 earthquake and its aftershocks (lower hemispheric projection): CMT - Harvard CMT Catalog, NEIC - National Earthquake Information Center, AUL - this study.

a roughly south-to-north striking surface. It is interesting to note that the three M_L 5+ aftershocks that occurred between January and May, 2000 are all located between the December M_W 7 and July M_W 6.5 epicenters. Therefore, it may be that the 1999 Kodiak Island M_W 7 earthquake triggered the July 11, 2000 M_W 6.5 earthquake. Both earthquakes ruptured the subducting Pacific plate; the fault surface of the July earthquake, as delineated by the aftershocks, is adjacent to and located north of the December aftershock zone.

3.5. CONCLUSIONS.

The relocated hypocenter of the 1999 Kodiak Island M_W 7 earthquake is positioned at 57.31°N and 154.29°W at 35.8 km depth. The majority of the relocated aftershocks are distributed between 26 and 83 km depth along a steeply dipping plane with a southwest-to-northeast orientation. The moment tensor inversion for the main shock results indicate a fault plane trending at 29° azimuth and dipping at 66°. The moment tensor inversion for the M_W 6.4 aftershock shows a nearly pure dip-slip mechanism with the fault plane striking at 234° azimuth. The moment tensor solutions for the main shock and four of its aftershocks are consistent with the stress regime in the slab beneath the Kodiak Island region, which is characterized by along-arc compression and down-dip extension (Lu and Wyss, 1996).

Therefore, the aftershock relocation and moment tensor inversion results indicate that the 1999 Kodiak Island M_W 7 earthquake was located within the subducting Pacific plate down-dip of the locked portion of the megathrust (Savage et al., 1999). The fault plane is parallel to the strike direction and cuts across the plate through nearly its entire thickness (Figure 3.8). The 1999 Kodiak Island earthquake is the first well documented large intraplate event in the Alaska-Aleutian subduction zone.The strong intraplate subduction zone events, such as 1970 M_S 7.8 Peru (Dewey and Spence, 1979), 1994 M_W 8.3 Kurile (Katsumata et al., 1995) and 1999 M_W 7.5 Oaxaca (Singh et al., 2000) earthquakes are less commonly observed than the megathrust ruptures. It appears that the stress
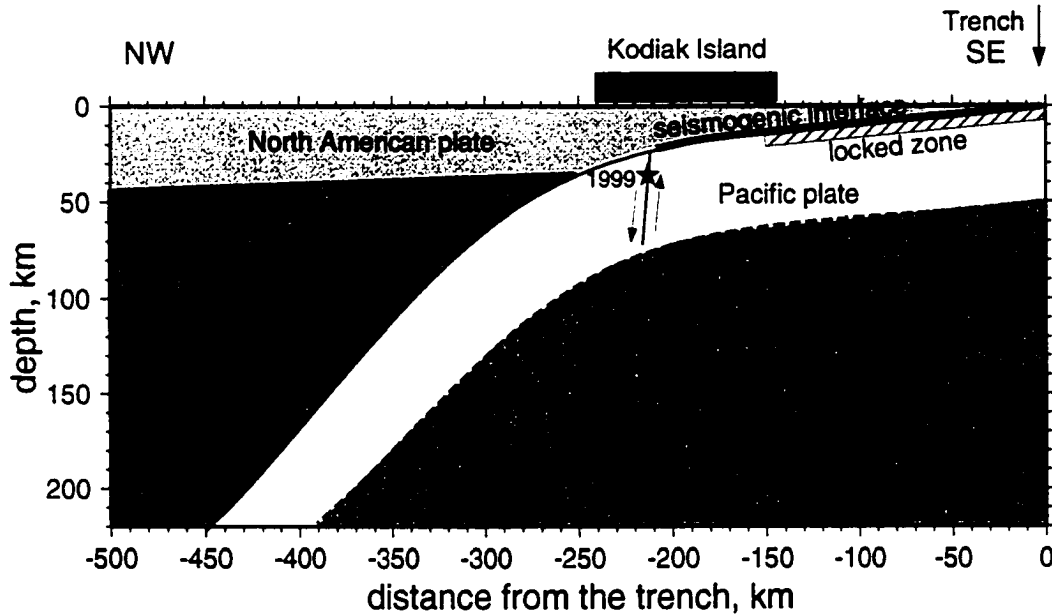
Figure 3.8. Schematic representation of the subduction beneath the Kodiak Island region. Location of the 1999 Kodiak Island M_W 7 earthquake and its mechanism are from this study. Position of the upper surface of the subducting slab is constrained using the relocated seismicity. Width of the seismogenic interface is a down-dip extension of the rupture zone of the Great 1964 Prince William Sound earthquake from Christensen and Beck (1994). Down-dip extent of the locked zone is from Savage et al. (1999).

changes caused by the M_W 7 earthquake triggered a M_W 6.5 earthquake, which occurred seven months later north of the December earthquake aftershock zone (Figure 3.7).

It has been observed that strong intraplate earthquakes in the subducted slabs display a temporal behavior (Lay et al., 1989). Prior to large thrust earthquakes the events in the down-dip subducted slab are tensional; following the rupture of the interface either the down-dip events became compressional or the tensional ones become less frequent. However, only tensional down-dip intraplate events were found in the Kodiak Island region (Lay et al., 1989) including the time period after the Great 1964 Prince William Sound earthquake. Tensional mechanism of the 1999 Kodiak Island earthquake and its location close to the down-dip end of the rupture zone of the 1964 earthquake (Christensen and Beck, 1994) is consistent with the slab-pull concentrating stress at the edge of a coupled interplate contact.

3.6. ADDENDUM: M_W 7 EARTHQUAKE OF 10 JANUARY 2001 - ANOTHER INTRAPLATE EVENT IN THE KODIAK REGION?[1]

Another strong earthquake occurred in the Kodiak Island region on January 10, 2001. Its magnitude estimates vary from M_L 6.8 (AEIC) to M_W 7.0 (Harvard CMT). The earthquake is located about 100 km southeast of the 1999 M_W 7 earthquake at 29.69 km depth (AEIC location). Four M_L 4+ aftershocks followed the main shock within two days (Table 3.4). Off-shore location of this sequence makes it difficult to obtain reliable hypocentral locations, especially for the small aftershocks. Figure 3.9 shows error ellipsoids for the main shock and 20 aftershocks that occurred throughout the end of January.

Table 3.4: Locations of M_W 7 earthquake of January 10, 2001 and its largest aftershocks.

date	magnitude	location	lat, °N	lon, °W	depth, km
01/10/01 16:02:40.8	M_W 7.0	AEIC	56.69	153.15	29.69
		JHD	56.66	153.27	30.36
01/10/01 16:11:54.4	M_L 4.1	AEIC	56.61	153.20	38.56
		JHD	56.67	153.23	32.88
01/10/01 20:12:23.3	M_L 4.5	AEIC	56.76	153.38	36.97
		JHD	56.74	153.40	31.86
01/10/01 20:19:10.3	M_L 4.4	AEIC	56.93	153.48	42.63
		JHD	57.02	153.51	40.08
01/11/01 3:29:02.2	M_L 4.1	AEIC	56.34	153.20	63.66
		JHD[a]	56.79	153.22	50.17

a. relocated using single event location program with JHD station corrections

Again, we attempted to relocate recorded aftershocks using the JHD method. We were able to obtain JHD locations for 7 aftershocks only (Figure 3.10). Location of the main shock has not changed significantly (Table 3.4). Three of M_L 4+ aftershocks moved closer to the main shock and align along a vertical plane. The deepest of them located initially at 63.66 km depth moved to a much shallower depth of 50.17 km (01/11/01 event).

---

1. This section was not part of the original publication.
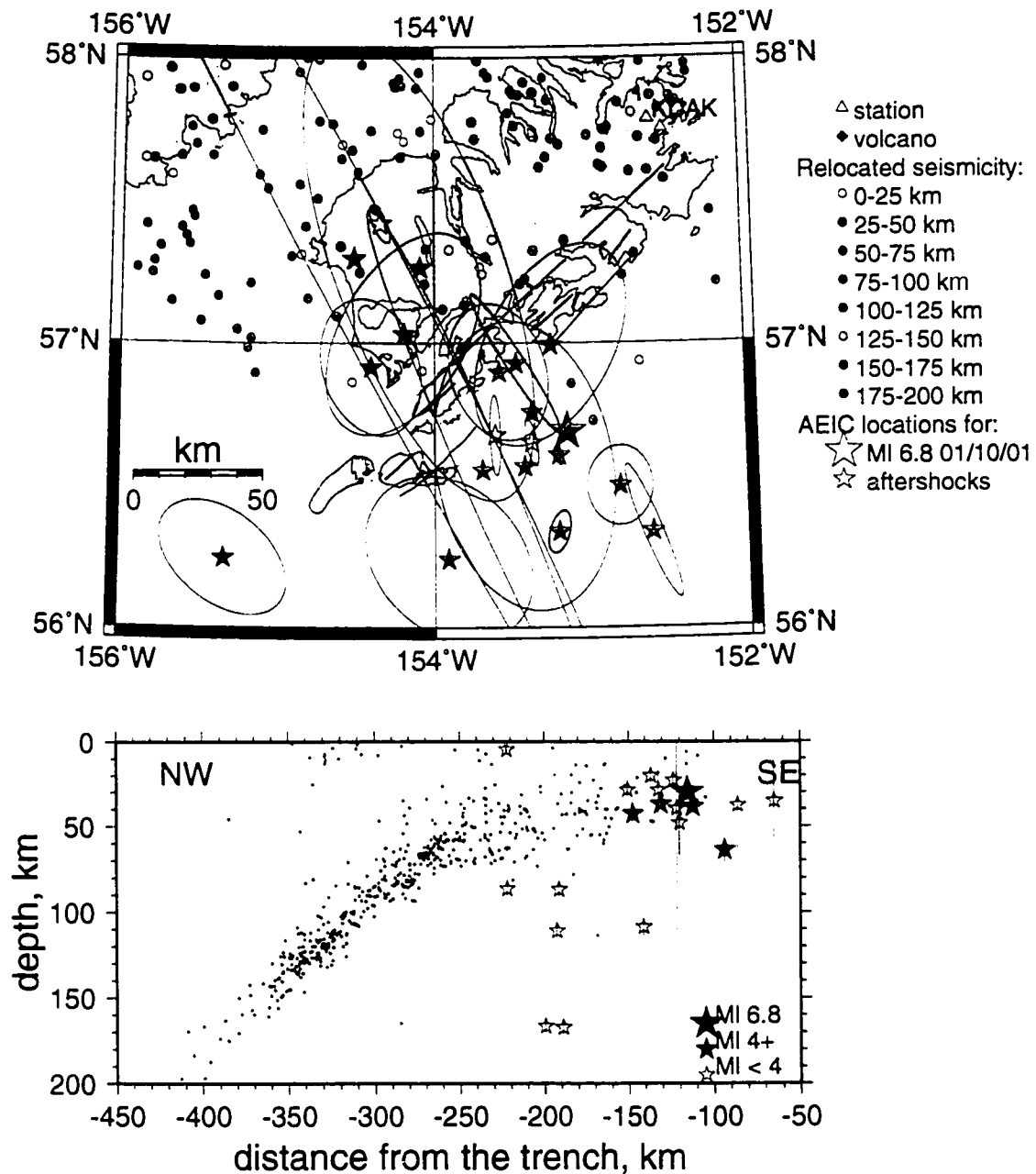
Figure 3.9. Locations of the regional earthquakes (JHD relocated), M_W 7 earthquake of January 10, 2001 and its aftershocks (AEIC locations). Error ellipsoids for the 68% confidence level are shown: red - main shock, blue - M_L 4+ aftershocks, black - M_L <4 aftershocks. Cross-section shows depth error bars of the aftershocks (68% confidence level).
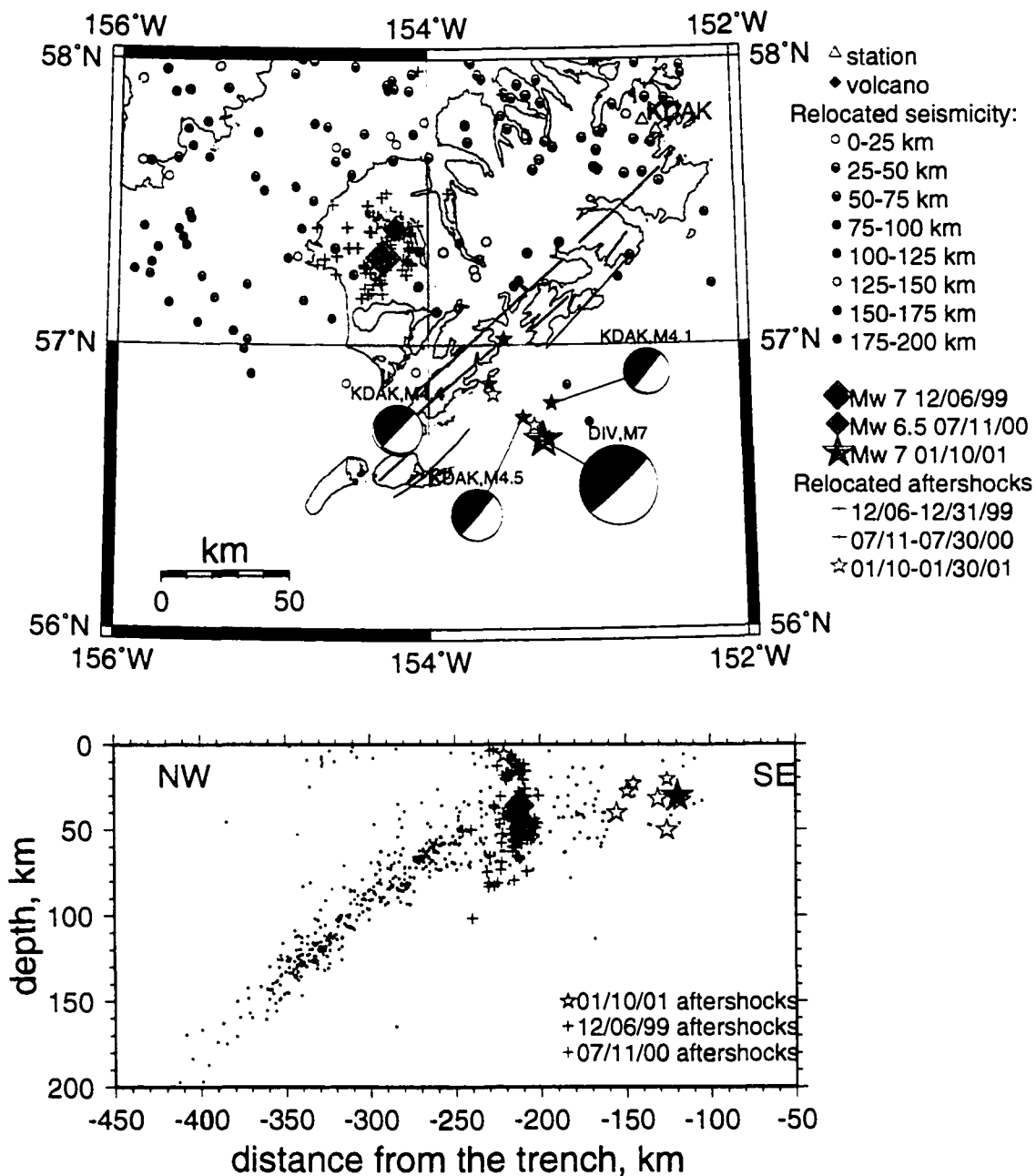
Figure 3.10. JHD locations of the regional earthquakes, 1999 M_W 7, 2000 M_W 6.5, and 2001 M_W 7 earthquakes and their aftershocks. Focal mechanisms of the 2001 M_W 7 event and three of its aftershocks obtained using regional broadband data are shown (lower hemispheric projection).

M_L 4.4 event of 01/10/01 is located off this axis, but its error ellipsoid allows us to suggest that it could be located closer to the main shock.

Next, we calculated moment tensor solutions for the main shock and three of the aftershocks using regional broadband records (see Table 3.5 and Figure 3.11). Faulting parameters of the main shock are similar to those reported by the Harvard group (CMT solution). While we were unable to obtain a better waveform fit for the main shock, agreement with the regional and teleseismic P-wave first motions is satisfactory (Figure 3.11(a)). Again, the closest broadband station KDAK was malfunctioning at the time of M_W 7 earthquake and the record could not be used in the moment tensor inversion.

Table 3.5: Faulting parameters of M_W 7 earthquake of January 10, 2001 and its largest aftershocks.

date	M_W	solution	plane 1			plane 2		
			strike, deg.	dip, deg.	slip, deg.	strike, deg.	dip, deg.	slip, deg.
01/10/01 16:02:40.8	7.0	CMT	227	6	79	58	84	91
	7.0	this study	212	4	75	47	86	91
01/10/01 20:12:23.3	4.4	this study	158	4	27	41	88	94
01/10/01 20:19:10.3	4.3	this study	136	14	2	44	89	104
01/11/01 3:29:02.2	4.0	this study	143	10	14	39	88	100

Faulting parameters of the three M_L 4+ aftershocks are similar to each other and to the main shock (Figure 3.11(b-e)). The first plane has a shallow dip angle (between 4° and 14°). The second plane is nearly vertical and aligned in southwest-northeast direction, i.e parallel to the trench direction. For the deepest aftershock (occurred on 01/11/01), we were able to match the waveforms with a higher accuracy when assuming a shallower depth (compare Figure 3.11(d) for the source depth of 50.17 km with Figure3.11(e) for the source depth of 30 km).

According to a marine seismic refraction study near Kodiak Island (Shor and von Huene, 1972) the depth to the top of the subducting plate in the epicentral area of the 2001

(a)

010110.DIV

1: Str= 212.0 Dip= 3.8 Slp=75.1 Moment= 0.452546E+27 dyne-cm
2: Str= 46.9 Dip= 86.3 Slp= 91.0 dc= 54.59% dp= 45.41%

(b)

0101102012.KDAK

1: Str= 157.5 Dip= 3.9 Slp=26.9 Moment= 0.271209E+24 dyne-cm
2: Str= 40.7 Dip= 88.3 Slp=93.5 dc= 76.84% dp= 23.16%
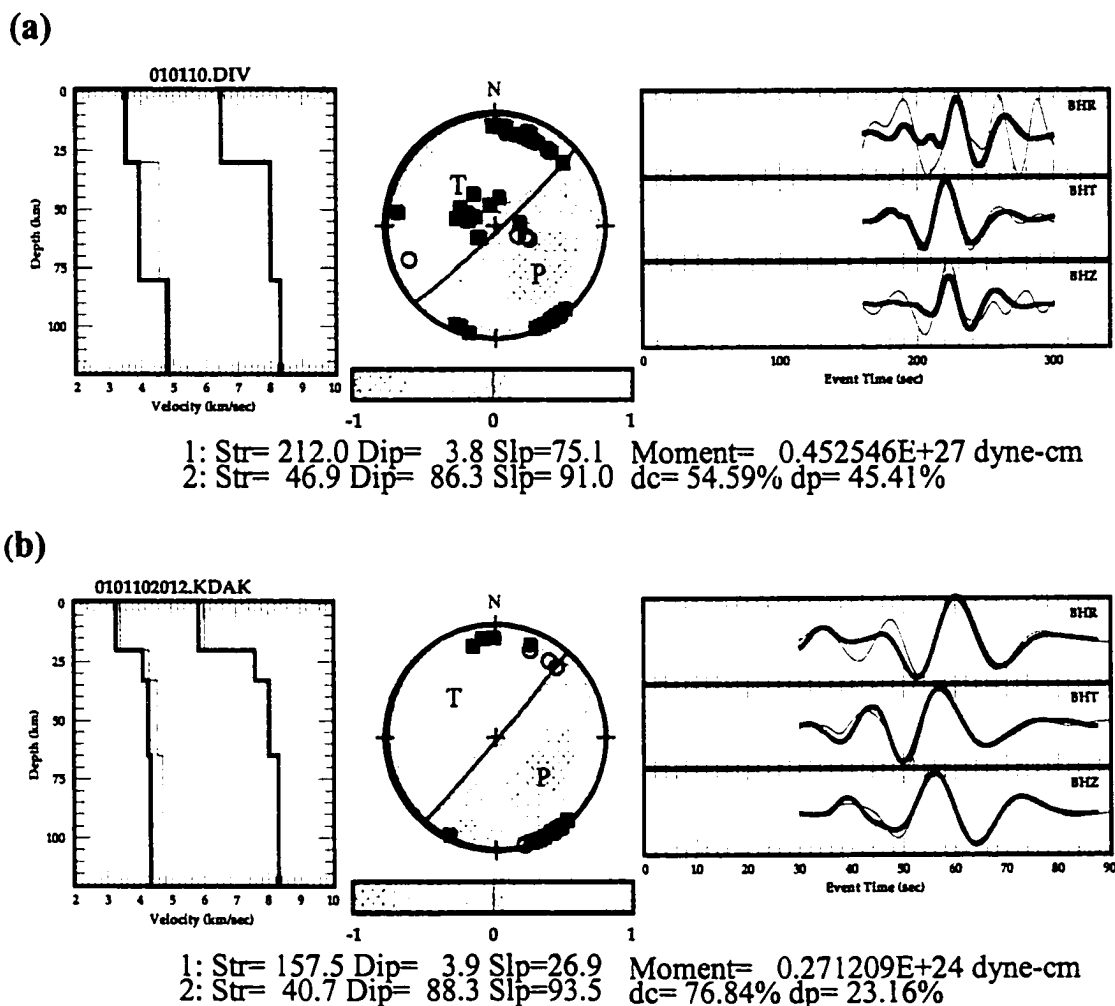
Figure 3.11. Moment tensor inversion results: (a) M_W 7 earthquake of January 10, 2001 (station DIV is located at 61.13°N and 145.77°W); (b) M_L 4.5 01/10/01 20:12:23.3 aftershock; (c) M_L 4.4 01/10/01 20:19:10.3 aftershock; (d) M_L 4.1 01/11/01 3:29:02.2 aftershock; and (e) same as (d) for the source at 30 km depth. Panel on the left displays initial (thin line) and final (thick line) P- and S-wave velocity models. Title above this panel indicates date of the earthquake and name of the station used in the inversion. Panel on the right displays recorded (thin) and synthetic (thick) filtered waveform data, time along the x-axis is from the origin time of earthquake. Lower hemispheric projection of the focal sphere is shown in the middle. First motion data is indicated by the closed squares (compression) and open circles (dilation). Strike, dip and slip values of the fault planes are printed below the focal sphere, as well as percentage of the double couple and CLVD components in the solution

(c)

1: Str= 136.2 Dip= 14.3 Slp=2.2   Moment= 0.209231E+24 dyne-cm
2: Str= 44.1 Dip= 89.4 Slp=104.3   dc= 91.10% dp= 8.90%

(d)

1: Str= 122.3 Dip= 16.5 Slp= 2.6   Moment= 0.885395E+23 dyne-cm
2: Str= 29.8 Dip= 89.3 Slp= 106.5   dc= 90.69% dp= 9.31%

(e)

1: Str= 141.1 Dip= 9.6 Slp=13.3   Moment= 0.266145E+23 dyne-cm
2: Str= 38.0 Dip= 87.8 Slp= 99.3   dc= 69.74% dp= 30.26%
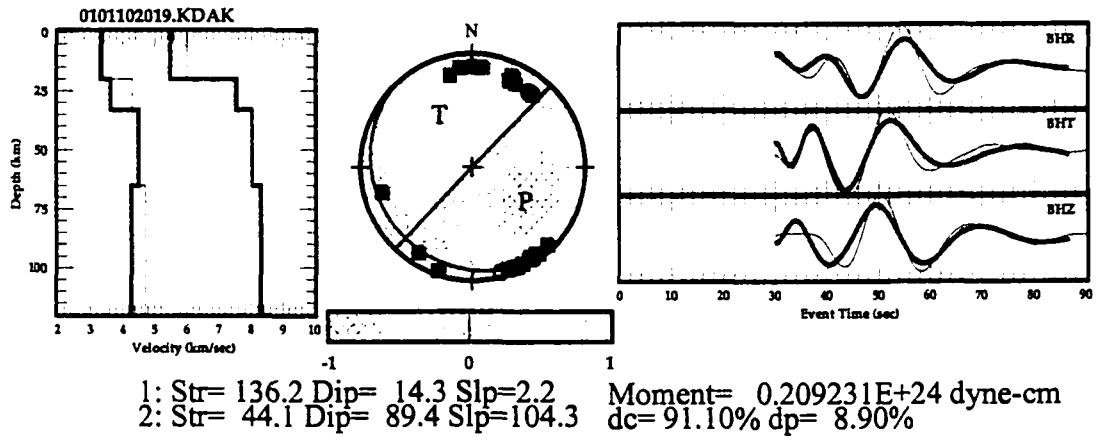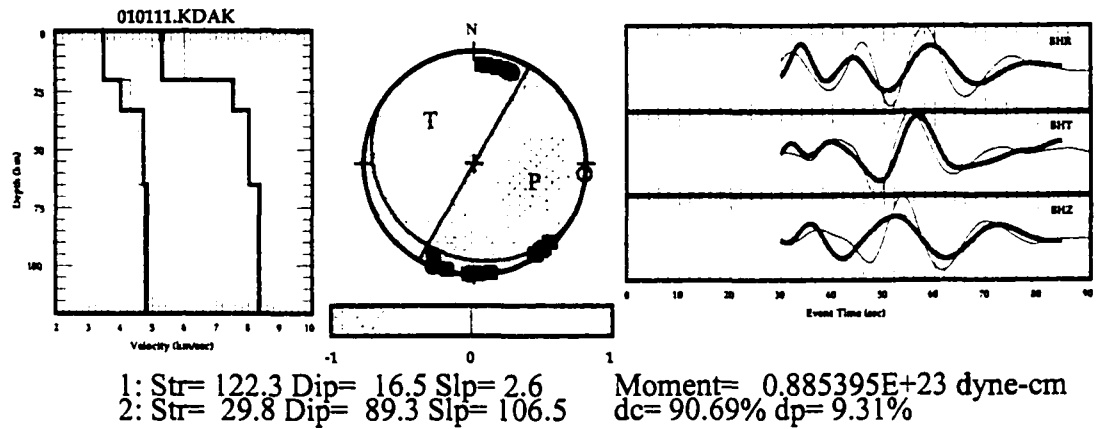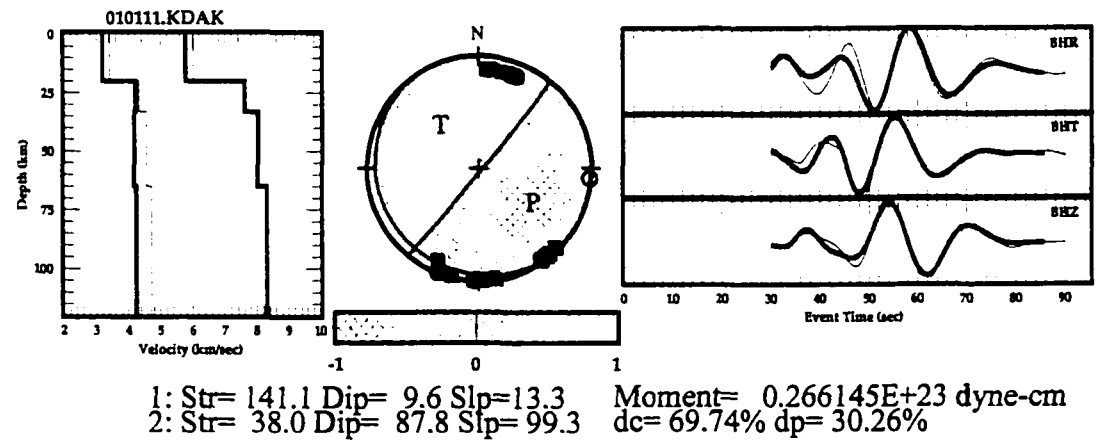
Figure 3.11 (continued).

M_W 7 earthquake is about 20 km. Therefore, we argue that the following evidence suggests that the M_W 7 earthquake of January 10, 2001 located beneath the continental shelf off-shore Kodiak Island is an intraplate event similar to the 1999 Kodiak Island M_W 7 earthquake: (1) the focal depths of the main shock (30 km) and well-located aftershocks (between 20 km and 50 km) are greater than estimates for a megathrust depth in the epicentral area, (2) a preferable alignment of the well-located aftershocks on a vertical plane rather than on horizontal, and (3) the dip of the shallow dipping focal plane is too small and of a wrong orientation for a megathrust event.

Chapter 4: New constraints on tectonics of interior Alaska: Earthquake locations, source mechanisms and stress regime.

4.1. INTRODUCTION.

The tectonic framework of Alaska is dominated by subduction of the Pacific plate underneath the North American plate. Stresses due to the plate convergence are transmitted across great distances (> 500 km) into interior Alaska where the deformation causes substantial crustal seismicity. While some of the earthquakes are clearly associated with the large-scale strike-slip fault systems of Denali in the south and Kaltag and Tintina in the north, the majority of the shocks are located in a zone of distributed shear deformation between the two fault systems (Figure 4.1). These earthquakes are aligned in three major north-northeast trending zones which are called Minto Flats (MFSZ), Fairbanks (FSZ) and Salcha (SSZ) seismic zones. Among the largest earthquakes in the interior are the 1904 M_S 7.3, 1929 M_S 6.2 and 6.5, 1937 M_S 7.3, 1947 M_S 7.2, and 1968 M_S 6.5 Rampart earthquakes. Locations for the three earlier shocks are rather uncertain, but can be generally identified with the area between the Denali and Tintina fault systems. The most recent event of note is the 1995 M_W 6.0 Minto Flats earthquake.

Little is known about geological structures that produce this broadly distributed seismicity. The area between the Tintina and Denali fault systems is occupied by the Yukon-Tanana terrane, an assemblage of Paleozoic and older metasedimentary, metavolcanic, and metaplutonic rocks that are multiply deformed and regionally metamorphosed (Foster et al., 1994). These rocks are cut by a suite of Cenozoic northeast-striking linea-

° 0-10 km	● 30-40 km	★ M>=7
● 10-20 km	● 40-50 km	★ 6.0-6.9
● 20-30 km	° 50-60 km	★5.0-5.9
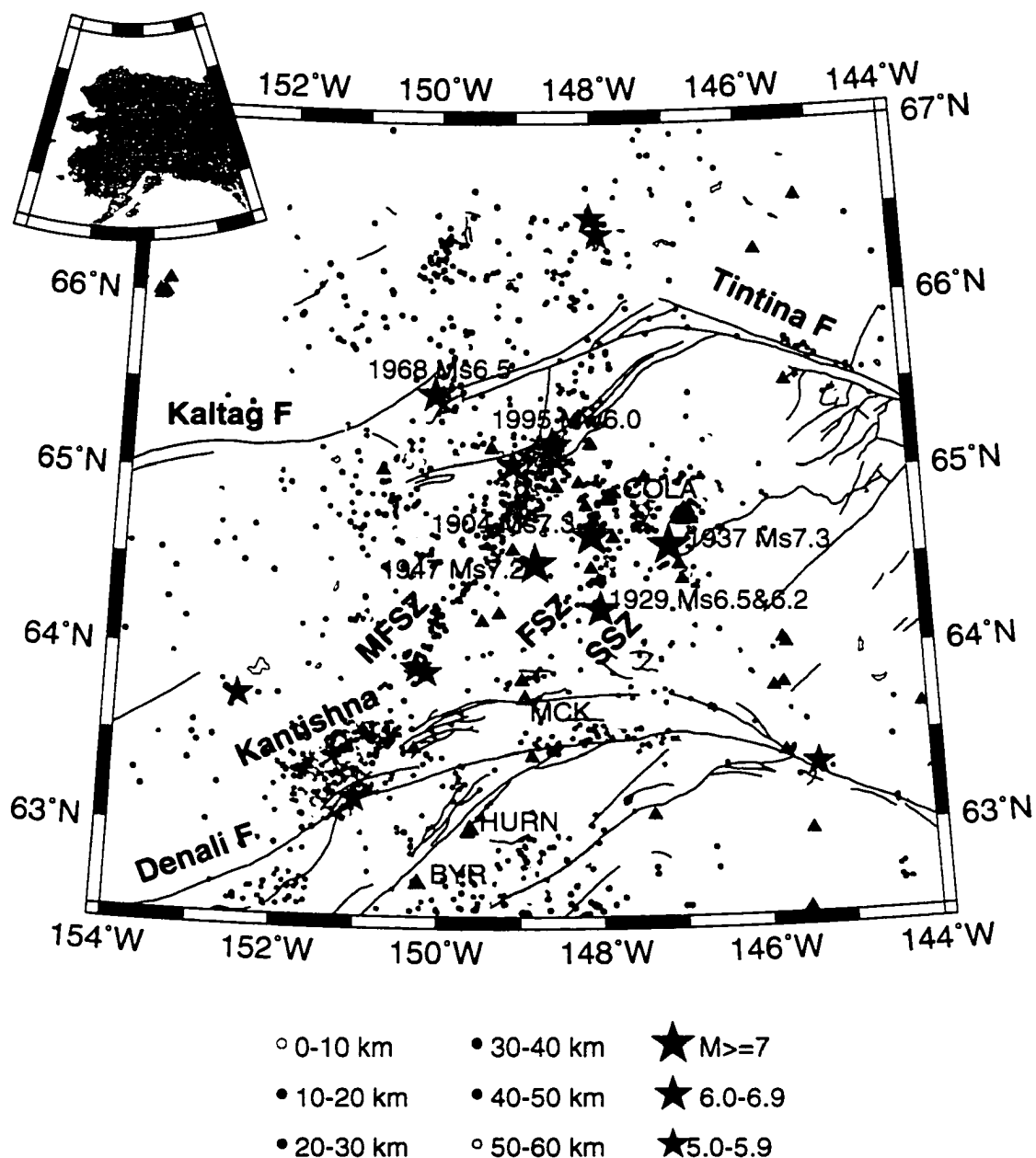
Figure 4.1. Map of the study area. Earthquakes with magnitude less than 5 are shown by the circles (1988-1999 time period, the AEIC catalog). Significant earthquakes along with the year of occurrence and magnitude are shown by the stars. Green triangles are the seismograph station locations, that were used in the joint relocation. Broadband sites records from which are used in this study are denoted by the station code names. Red lines are the major faults. Seismic zones: MFSZ - Minto Flats, FSZ - Fairbanks, SSZ - Salcha.

ments and sinistral-slip faults. Several of these faults show evidence suggestive of late Cenozoic displacement. Suggestive, but not definitive, evidence from trenching studies and geomorphic features suggests late Pleistocene displacements. None of the best exposed faults, however, displace late Holocene alluvium (Page et al., 1995).

The northeast-trending earthquake lineaments are diffuse which may indicate a presence of overlapping parallel faults, splays and cross faults. Page et al. (1995) suggested a block-rotation model to characterize the deformation in interior Alaska. In this model, the crustal blocks are rotating clockwise in a dextral shear zone between the Denali and Tintina fault systems. The deformation accommodates shortening across the region in response to north-northwest compression resulting from plate convergence.

According to the GPS studies of crustal movements in central Alaska conducted over the past 5 years (Fletcher and Freymueller, 2000), the region between the Denali and Tintina faults shows a relatively low rate of strain accumulation.

Analysis of seismic waves recorded at the local and regional distances is extremely important in the study of small or moderate-sized earthquakes, which are rarely well recorded at teleseismic distances. Advances in broadband instrumentation have made it possible to determine the seismic source parameters from a single seismic station. Recent improvements of the Alaska Seismic Network and installation of the broadband seismometers in Alaska offer us a new tool for evaluating the block-rotation model and seismic hazard in the interior. We use a Joint Hypocenter Determination (JHD) method to relocate over 3,600 crustal earthquakes that occurred from 1988 to 1999 in the area between 154°W and 144°W longitude and 62.5°N and 67°N latitude. New earthquake locations provide more details on the structure of seismic clusters in the area, such as the Kantishna cluster. Next, for the relocated earthquakes with magnitudes 3.4 or above we calculate focal mechanisms using the P-wave first motions. In addition, we utilize a moment tensor inversion technique to obtain constraints on the source mechanisms of the earthquakes with magnitudes 4 and above using waveform data recorded at the broadband stations in the interior. The combined dataset of the focal solutions from the first motions and moment tensor inversions is then used to calculate principal stress orientations in the crust.

An additional goal of this study is to evaluate the potential for implementing a near-real-time moment tensor inversion within the scope of operations of the AEIC. In particular, the first task is to characterize the velocity structure for calculating the Green's functions used in the moment tensor inversion procedure.

4.2. DATA AND METHODS.

4.2.1. Earthquake relocations.

The earthquake location is an important factor in identifying faulting parameters. To obtain more accurate locations for the interior Alaska earthquakes we used the JHD method (Pujol, 1988; Appendix A). There are almost 4,200 earthquakes with depths above 60 km in the AEIC catalog that occurred from 1988 to 1999 in the region between 154°W and 144°W longitude and 62.5°N and 67°N latitude. Since this area is too large to process as a single block in the joint relocation, the selected earthquakes were subdivided into 6 subsets based on their epicentral locations:

(1) 62.5-64°N, 154-150°W, 1682 events, includes Kantishna cluster;

(2) 62.5-64°N, 150-144°W, 835 events, including $10/22/1996$ M_W 5.7 earthquake;

(3) 64-65.5°N, 154-150°W, 193 events;

(4) 64-65.5°N, 150-144°W, 947 events, including 1995 Minto Flats earthquake;

(5) 65.5-67°N, 154-149°W, 167 events;

(6) 65.5-67°N, 149-144°W, 157 events.

These datasets were subdivided further into three depth intervals (0-10 km, 10-20 km and below 20 km) and each of the 18 subsets was relocated separately. Events in each dataset are not restricted by their locations and are allowed to migrate across the boundaries.

Only arrivals with an epicentral distance less than 4° were used. In addition, quality weights assigned to the phase readings during the routine earthquake processing were applied. Events with the number of P- and S-phases less than 5 and 2, respectively, were excluded from the relocations.

A total of 3,611 earthquakes have been relocated (Figure 4.2). Average depth and epicenter shifts are 3 km and 3.8 km, respectively (Figure 4.3). Relative mislocations between the neighboring datasets are on the order of 1-2 km.

○ 0-10 km	● 30-40 km
● 10-20 km	● 40-50 km
● 20-30 km	○ 50-60 km
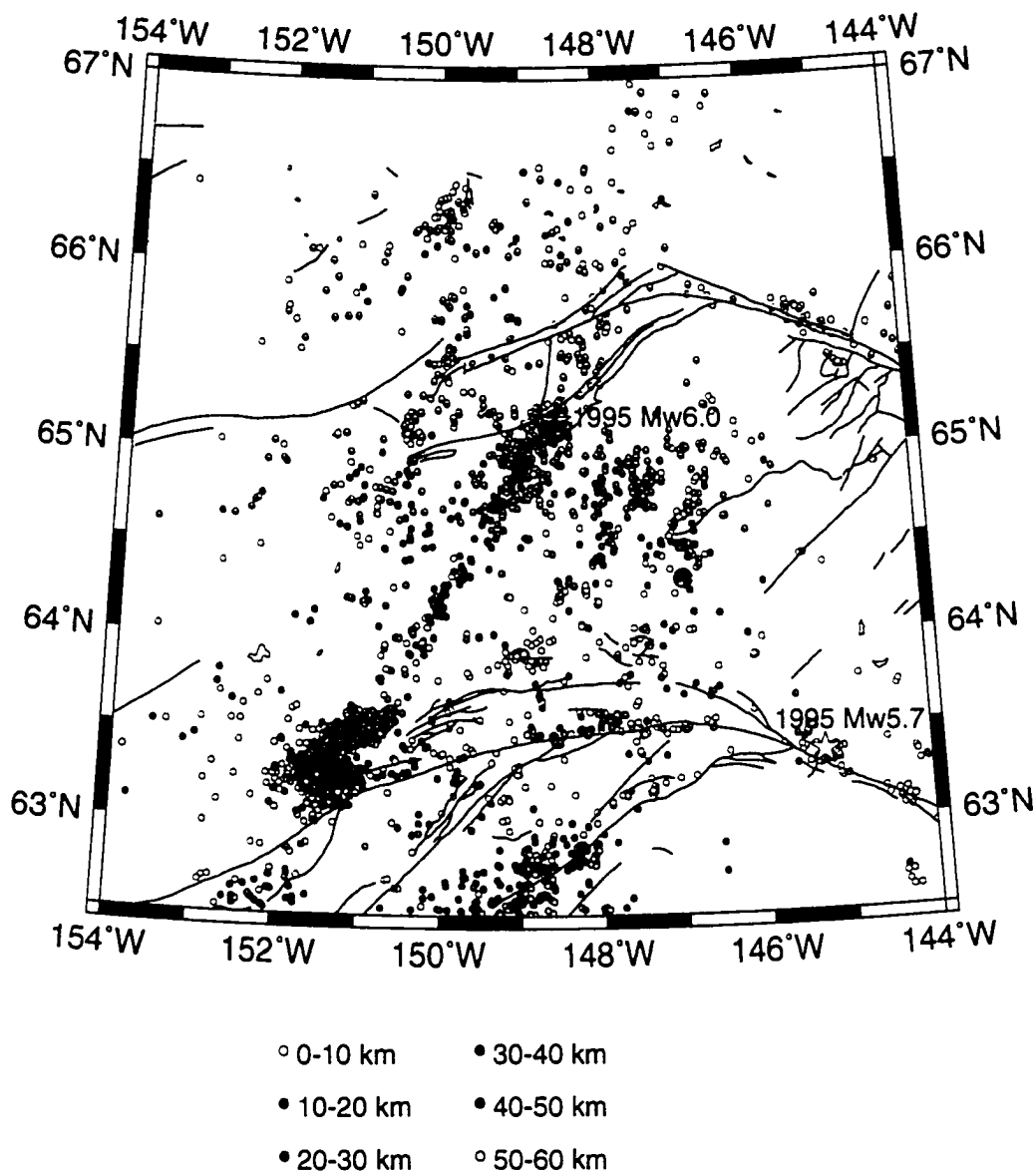
Figure 4.2. Map of 3,611 JHD relocated earthquakes. Earthquakes occurred from 1988 to 1999. Two significant earthquakes are shown by the stars.
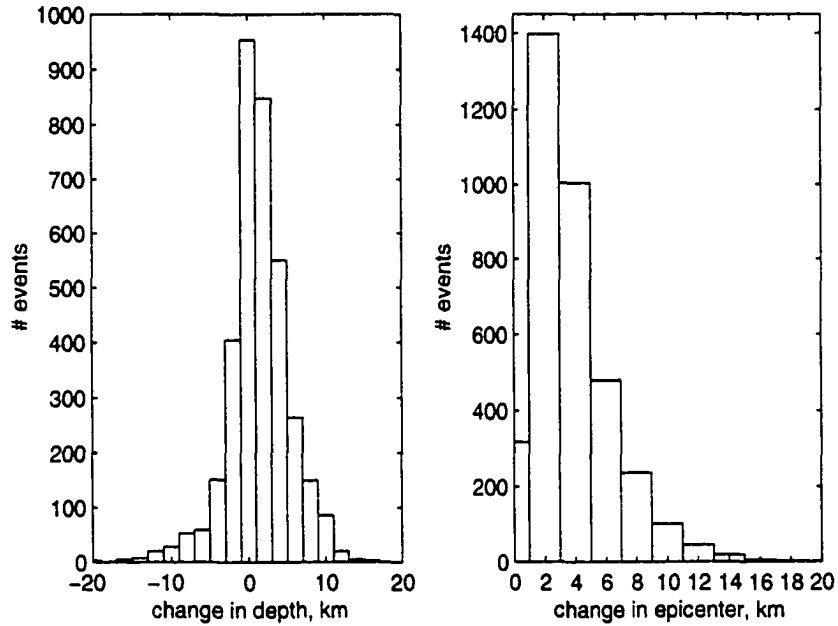
Figure 4.3. Change in depth and epicenter locations od 3,611 earthquakes after the joint relocation procedure.

4.2.2. Earthquakes source parameters.

The next step after the relocation is to identify source characteristics of the earthquakes. The most complete information about the earthquake source is given by its moment tensor. To estimate the moment tensor, however, one needs at least one three-component broadband recording of an earthquake. The broadband seismometer at the College Observatory in Fairbanks has been operational continuously throughout the period of the study. The site was equipped with a Streckeisen STS seismometer from 1988 until the middle of 1996 (station code COL). Then, the Observatory was relocated and a new borehole Geotech KS-54000 instrument was installed (station code COLA). In October 1997, the AEIC installed a broadband seismometer at a site in McKinley park (station code MCK). Additional data recorded by BEAAR instruments became available beginning in the summer of 1999. BEAAR is a three-year PASSCAL project aimed at imaging the crustal and upper mantle structure across the Alaska Range (Meyers et al., 2000). There-

fore, the majority of the cataloged earthquakes have broadband data recorded only at College Observatory.

We use a moment tensor inversion technique that simultaneously inverts for the velocity structure and source parameters (Hansen and Harvey, 1989; Appendix B). This technique suits Alaskan conditions well, because the velocity structure is highly heterogeneous and poorly known. Synthetic waveforms are computed using the Locked Mode Approximation method (Harvey, 1981). It has been shown in previous studies that this method works reliably even when only one station is used in the inversion (Hansen et al., 1989). Findings from this study confirm this conclusion.

There were 53 earthquakes with magnitude 4 or larger that occurred in the study area from 1988 throughout the end of 2000. For six of these earthquakes broadband recording were unavailable. We were able to obtain moment tensor solutions for 38 of the 47 remaining earthquakes (Figure 4.4; Appendix C).

To complement the dataset of fault plane solutions obtained through the moment tensor inversion, we used the FPFIT computer program (Reasenberg and Oppenheimer, 1985) to calculate focal mechanisms for the earthquakes with magnitude 3.4 or larger using P-wave first motions. Available first motions were re-examined and additional first motions picked. In this way, 185 new fault plane solutions were obtained (Figure 4.5).

In addition, five moment tensor solutions for earthquakes that occurred between 1980 and 1986 were available from the Harvard CMT catalog, and were added to the catalog of focal mechanisms (Figure 4.5).

4.2.3. Stress tensor inversion.

All of the focal mechanisms obtained using P-wave first motions or moment tensor inversions were then used to calculate principal stress orientations in the crust. We apply a stress tensor inversion method developed by Gephart and Forsyth (1984) which is implemented as a part of ZMAP, a MATLAB based seismological software package (Wiemer and Zuniga, 1994; Wiemer, 1996). The method is based on finding a best fitting principal stress tensor for a group of earthquakes by a grid search over a range of possible models,
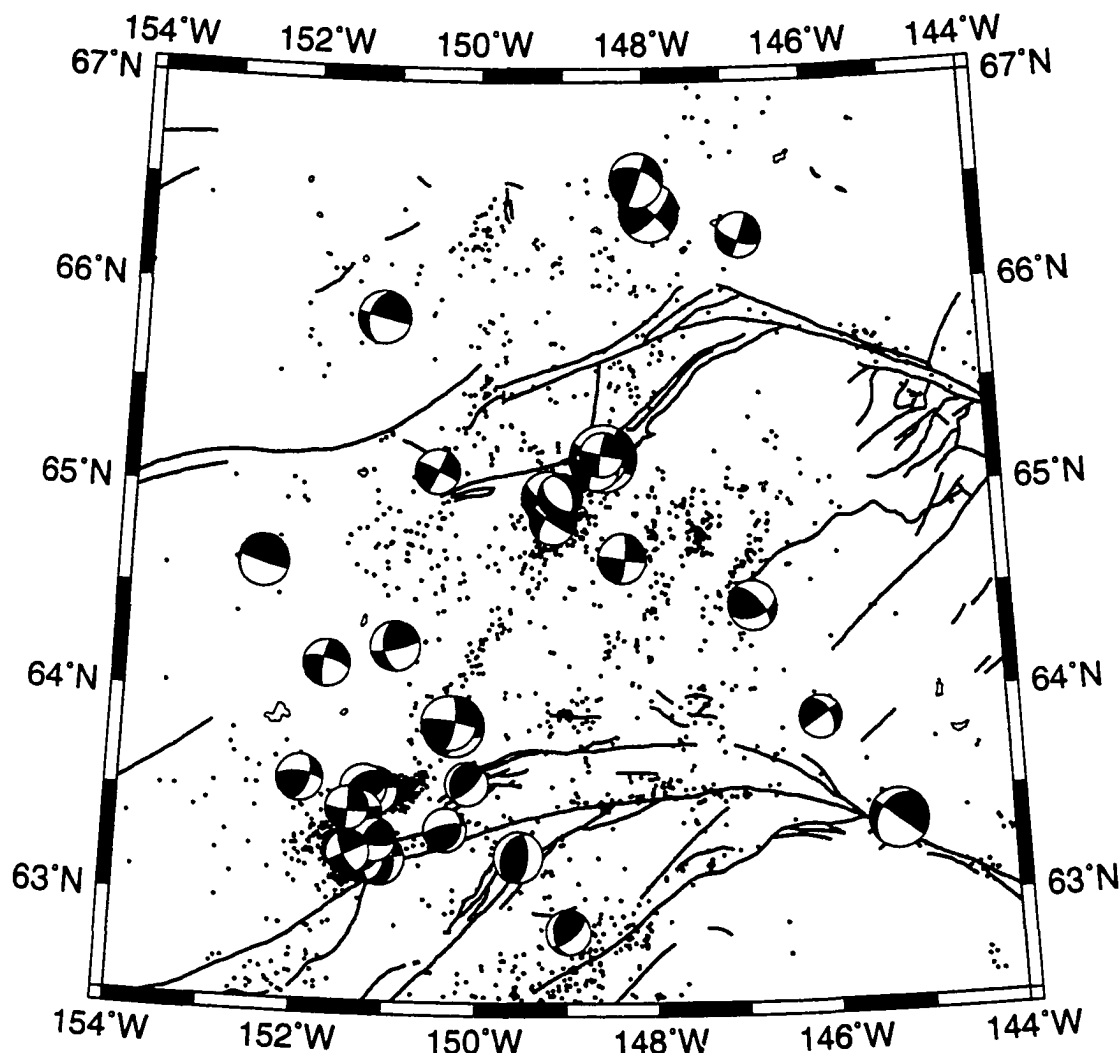
Figure 4.4. Map of the relocated earthquakes with 38 moment tensor solutions obtained using the regional broadband data (lower hemispheric projection).

under the assumptions that the slip on the fault plane occurs in the direction of the resolved shear stress and that the stress orientation is homogeneous in the selected volume. The degree of heterogeneity of the stress tensor in a given volume is measured by an average misfit value. The misfit for each earthquake is defined as the smallest rotation angle about an axis of any orientation that would bring the direction of slip on either of the two nodal planes into agreement with the direction of the slip predicted by the stress model. The misfit values of less than 6° are indicative of homogeneous stress conditions in
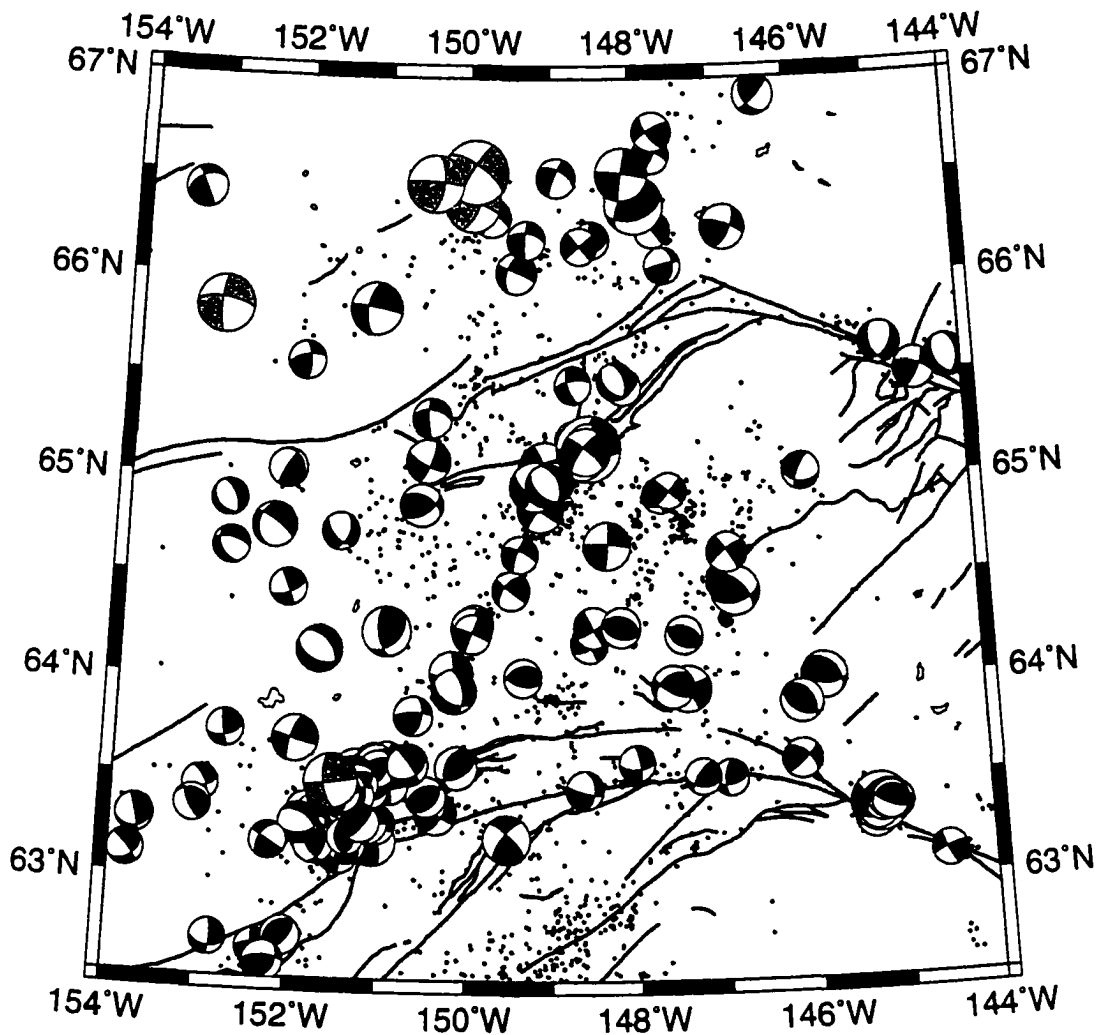
Figure 4.5. Map of the relocated earthquakes with 185 fault plane solutions obtained using the P-wave first motions and 5 CMT moment tensors, black and grey focal spheres, respectively (lower hemispheric projection).

a given volume, while the misfit values above 9° indicate that the stress field is heterogeneous or contaminated with large errors in the fault plane solutions (Wyss et al., 1992; Giampiccolo et al., 1999).

This method has been applied successfully in a variety of tectonic settings (e.g. in Alaska, Lu et al., 1997; Lu and Wyss, 1996; Sanchez, 2000). Recent work of Hardebeck and Hauksson (2001) on testing this method with the synthetic data shows that it provides

accurate estimates of stress orientations, especially in favorable conditions such as large datasets and high-quality focal mechanisms. The estimated confidence regions, however, are systematically too large. Stress tensor inversion results are discussed later in this Chapter.

4.3. MOMENT TENSOR INVERSION RESULTS.

The two important factors that influence moment tensor inversion results are the source location and the velocity model used to calculate Green's functions. This section discusses the influence of the latter factor on the inversion results for the interior Alaska earthquakes. In particular, four base velocity models have been tested in the moment tensor inversion (Figure 4.6):

(1) the standard AEIC velocity model used for locating earthquakes north of 62.5°N;

(2) the modified AEIC velocity model used for locating earthquakes south of 62.5°N (fewer layers than in the standard velocity model);

(3) the velocity model estimated using the receiver function analysis beneath College Seismic Observatory (Searcy et al., 1996); and

(4) the velocity profile constructed from Trans-Alaska Crustal Transect (TACT) refraction/ wide-angle reflection data (Beaudoin et al., 1992). In this model, the depth to the Moho changes from 29 km in the north (approximately 30 km southeast of Fairbanks) to 32 km in the south (approximately 30 km southeast of Delta Junction). We tested modifications of this model with Moho depths ranging from 29 to 35 km.

First of all, we used earthquakes which were recorded at several broadband stations to compare how stable the solution is when only one station is used in the inversion. There are only a few such earthquakes available. Figure 4.7 presents the comparison of the moment tensor inversion results for two earthquakes obtained using recordings from the MCK and COLA stations. Agreement between the two stations is good; fault plane parameters are within a few degrees of each other. Therefore, it is possible to obtain a satisfactory result with only one station. This was an encouraging finding because most of the
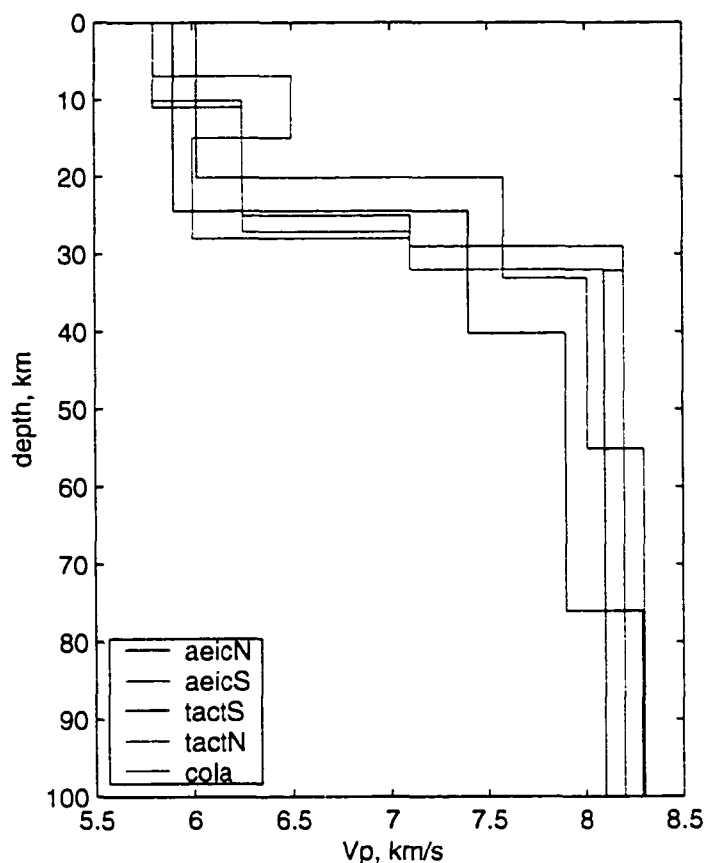
Figure 4.6. Velocity models tested in the moment tensor inversion procedure: aeicN - standard AEIC model for locating earthquakes north of 62.5°N; aeicS - modified standard AEIC model for locating earthquakes south of 62.5°N (fewer layers); tactS and tactN - velocity profiles constructed from Trans-Alaska Crustal Transect (TACT) refraction/wide-angle reflection data; cola - velocity structure beneath College Observatory obtained using receiver function analysis.

earthquakes available for the moment tensor inversion occurred before expansion of the broadband network in interior Alaska.

An additional constraint, and a quality control on the moment tensor inversion results, are the P-wave first motions. Only inversion results that were in agreement with the first motions were used in this work (all first motions were checked by the author). If more than 5% of the first motions did not fit the fault plane solution obtained in the inversion, the result was discarded.
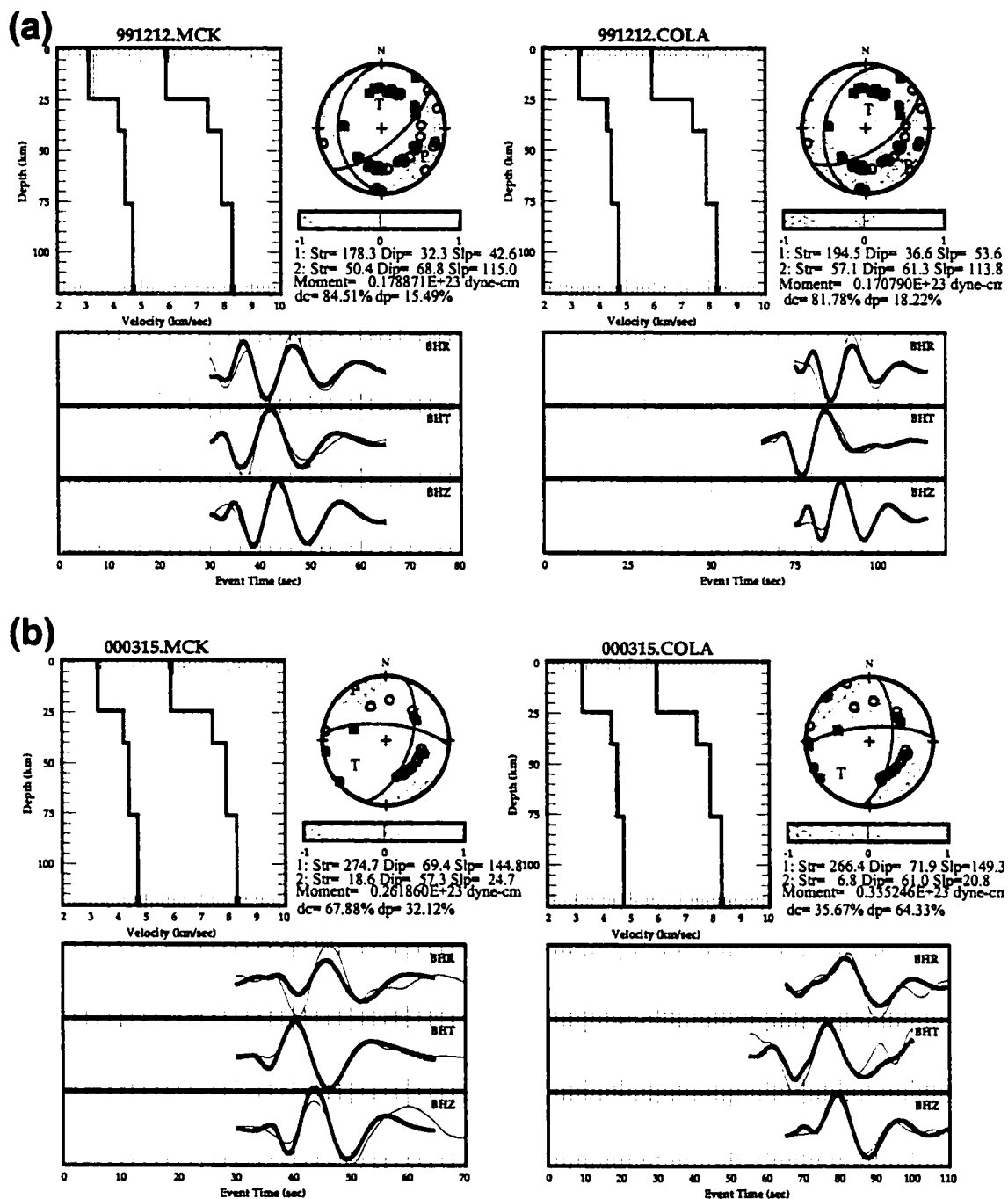
Figure 4.7. Comparison of the moment tensor inversion results obtained using recordings from stations MCK and COLA (see Appendix C for detailed legend). (a) 12/12/99 M_L 4.1 event located south of the Denali fault. (b) 3/15/00 M_L 4.3 event located in the Kantishna cluster.

All four velocity models were tested for each of the selected earthquakes. The best inversion result in terms of the waveform fit and agreement with the first motions was chosen in each case. From these tests it can be concluded that in general the TACT velocity model with varying crustal thickness works best for the interior Alaska earthquakes, when records from COLA or MCK stations are used. For the earthquakes located north of the Kaltag and Tintina fault system or within the Minto Flats seismic zone, the TACT model with the crustal thickness of 29-32 km gives the most satisfactory inversion results. For the region west of the MFSZ, the TACT model with the crustal thickness of 29 km works best. For the earthquakes located east of the MFSZ, the TACT velocity model with a thicker crust (32-35 km) gives the most stable inversion results. Finally, for the earthquakes located in the Kantishna cluster the TACT model with a 32-km-thick crust or the AEIC model for central Alaska work equally well.

The unique location of the Kantishna cluster allows us to look at differences in velocity characteristics north and south of the Denali fault. Clearly, two different velocity models are required to fit the waveforms recorded at the stations located north (e.g., MCK and COLA) and south (e.g., BYR and HURN) of the cluster, respectively (compare events 000315 (Figure C35) and 990625 (Figure C31) or 000225 (Figure C34) and 990805 (Figure C32)). The AEIC velocity model for locating earthquakes in southern Alaska gives better results for the stations located south of the Denali fault.

For the areas with poor station coverage, such as west of the Minto Flats seismic zone and north of the Kaltag and Tintina fault system, our ability to obtain moment tensor solutions is rather critical. For these regions, fault plane solutions calculated using a conventional P-wave first motion analysis have large uncertainties.

In summary, moment tensor solutions were calculated for 38 earthquakes (Figure 4.4; Appendix C). The most recent earthquakes are M_L 5.6 event of November 29, 2000 and two of its largest aftershocks of M_L 5.3 and 5.0.

4.4. SIGNIFICANT EARTHQUAKES AND SEISMIC CLUSTERS IN INTERIOR ALASKA.

4.4.1. 1995 Minto Flats M_W 6.0 earthquake.

On October 6, 1995 the most significant earthquake since the 1968 M_S 6.5 Rampart earthquake occurred in interior Alaska. It was located at the northern end of the Minto Flats seismic zone, approximately 50 km northwest of Fairbanks. This event was felt strongly in Fairbanks, items were knocked off the shelves, a minor property damage was reported. Locations of the main shock and the aftershocks, as well as fault plane solutions are shown in Figure 4.8.

The main shock was located by the AEIC at 65.17°N and 148.57°W at 9.09 km depth. The relocated hypocenter is centered at 65.16°N and 148.54°W at 12.18 km depth. The relocated aftershocks occupy a diffuse volume between 0 and 20 km depth with the majority located above the main shock. The fault plane solution for the main shock indicates a steeply dipping north-northeast striking fault plane. Assuming that this plane is the fault plane, the earthquake would be right-lateral strike-slip. Fault plane solutions for 11 aftershocks with magnitudes ranging from 3.4 to 4.5 are similar to that of the main shock. The aftershocks located above the main shock delineate a dipping plane consistent with the fault plane solution of the main shock while the aftershocks located below are spread over a larger volume. There is no systematic difference in focal mechanisms for the aftershocks located above and below the main shock. Distribution of the deeper aftershocks over a larger volume may reflect a more complex process of stress redistribution around the source, such as appearance of splay and/or parallel fractures.

In conclusion, the location and mechanism of the 1995 Minto Flats M_W 6.0 earthquake are consistent with a model of the clockwise block rotation in response to the shear deformation between the Denali fault to the south and the Kaltag and Tintina faults to the north.
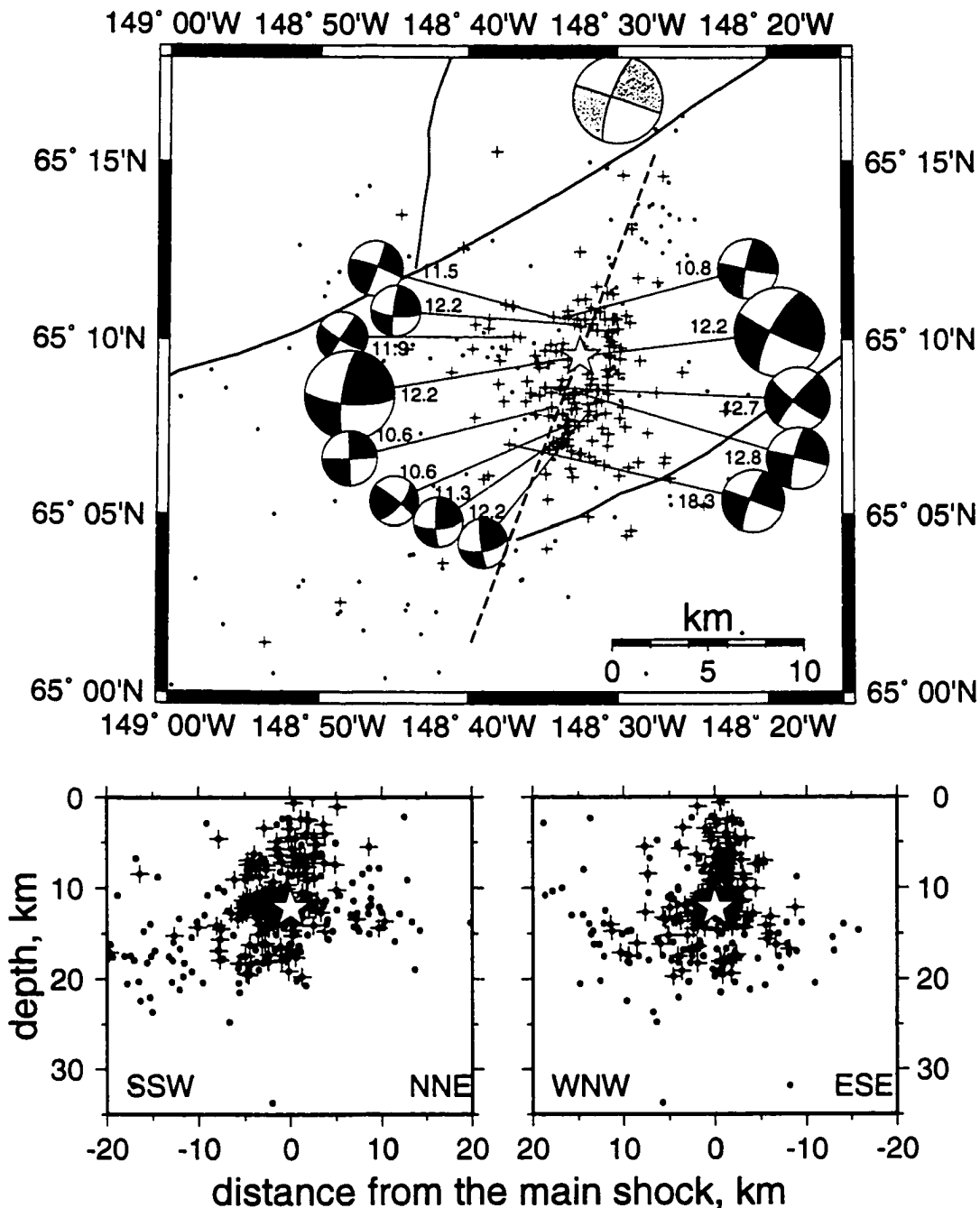
Figure 4.8. Detailed view of the aftershocks of the 1995 Minto Flats M_W 6.0 earthquake. The main shock and its aftershocks are shown by the star and crosses, respectively. Fault plane solutions obtained using P-wave first motions (black spheres), moment tensor inversion of COLA data (dark grey spheres) and CMT solution for the main shock (light grey sphere) are presented. Number next to the focal sphere is the focal depth in km. Dashed line indicates cross-section trend.

4.4.2. 1996 M_W 5.7 earthquake near the Denali fault.

On October 22, 1996 an M_W 5.7 earthquake occurred near the Denali fault (Figure 4.9). This event was felt in many communities across central Alaska, no property damage was reported. The AEIC located the earthquake at 63.35°N and 145.36°W at a depth of 3.91 km. The relocated position is at 63.36°N and 145.29°W at 2.76 km depth. The majority of the relocated aftershocks are located between the surface and 5 km depth and delineate a southwest-to-northeast striking surface approximately 7 km long.

The fault plane solution for the main shock calculated using P-wave first motions has one focal plane striking at 226° and dipping at 66°, which we interpret as the fault plane of the earthquake based on the aftershock distribution. The moment tensor solution obtained using COLA data underpredicts the dip angle of the fault plane. Fault plane solutions for 6 aftershocks that occurred through the end of 1996 are similar to the main shock mechanism. Three earthquakes which are located at the northeastern edge of the aftershock area and occurred 7 months and 2.5 years later have distinctly different mechanisms. They have a significant thrust component, which may indicate different faulting processes involved in a later stress redistribution around the source area of the M_W 5.7 earthquake, such as propagation of splay fractures.

This earthquake is unusual because it is located about 10 km north of the trace of the Denali fault in an area with no known mapped faults. There are, however, two fault structures on the opposite side of the Denali fault, one of which has an orientation similar to the fault plane of the M_W 5.7 event. Therefore, it could be postulated that this earthquake involved a similar fault structure on the northern side of the Denali fault. In conclusion, this earthquake, contrary to some people's beliefs, was not located on the Denali fault itself.
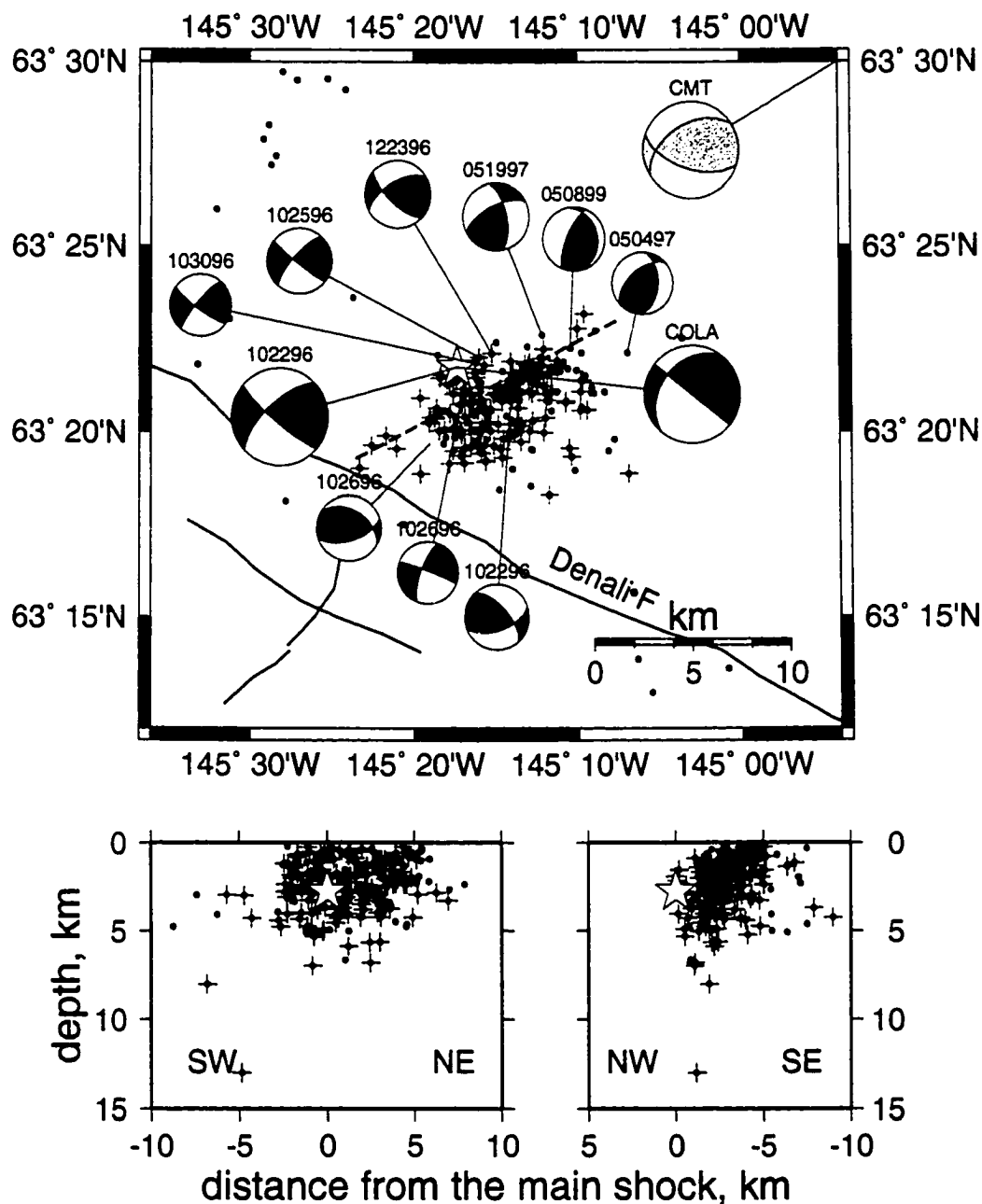
Figure 4.9. Detailed view of the aftershocks of 10/22/1996 M_W 5.7 earthquake. The main shock and its aftershocks are shown by the star and crosses, respectively. Fault plane solutions obtained using P-wave first motions (black spheres), moment tensor inversion of COLA data (dark grey sphere) and CMT solution for the main shock (light grey sphere) are presented. Dashed line indicates cross-section trend.

4.4.3. A sequence of M_L 5+ earthquakes in 2000 at the southern end of the Minto Flats seismic zone.

On November 29, 2000 people living in interior Alaska were awakened around 2 a.m. by the strong shaking caused by two magnitude 5+ earthquakes. The shocks occurred within 40 sec of each other, which made it impossible to obtain a reliable location for the second event. Analysis of the seismograms recorded at stations MCK and COLA indicates, however, that these shocks originated at the same location, given that the S-P times are identical for both of them. The magnitude of the first event was estimated between 5.6 (M_L AEIC) and 5.8 (M_W CMT). The second event was somewhat smaller at about magnitude 5.3. The AEIC located the main shock at 63.88°N and 150.15°W at 22.47 km depth. Another significant aftershock (M_L 5.0) occurred on December 6, 2000 and was located at 63.91°N and 150.28°W at a depth of 18.71 km.

The processing of the aftershocks was complicated by the fact that two critical stations located 40-50 km south and southwest of the source region had not been working since the fall of 2000. Therefore, due to a large azimuthal gap aftershock locations reported by the AEIC have a rather large uncertainty. To our advantage, however, BEAAR instruments (PASSCAL broadband experiment in the Alaska Range (Meyers et al., 2000)) are located strategically near the earthquake source region. Unfortunately, data from only two stations (GNR and RCK, Figure 4.10) were immediately available. The remainder of the BEAAR data will be retrieved in the summer of 2001.

Over 60 aftershocks of the M_L 5.6 earthquake were located through the end of December 2000 by the AEIC. To obtain better locations for the aftershocks, additional arrivals from BEAAR stations GNR and RCK were picked by the author and merged with the AEIC phase picks. These earthquakes were then added to an existing dataset of regional seismicity (see 4.2.1) and relocated using the JHD method. Only 32 aftershocks have been successfully relocated (Figure 4.10). The main shock has moved to a shallower depth of 19.6 km and is positioned at 63.85°N and 150.26°W. The JHD location of the M_L 5.0 aftershock is 63.86°N and 150.32°W, 13.77 km deep. Aftershocks align along a SSW-
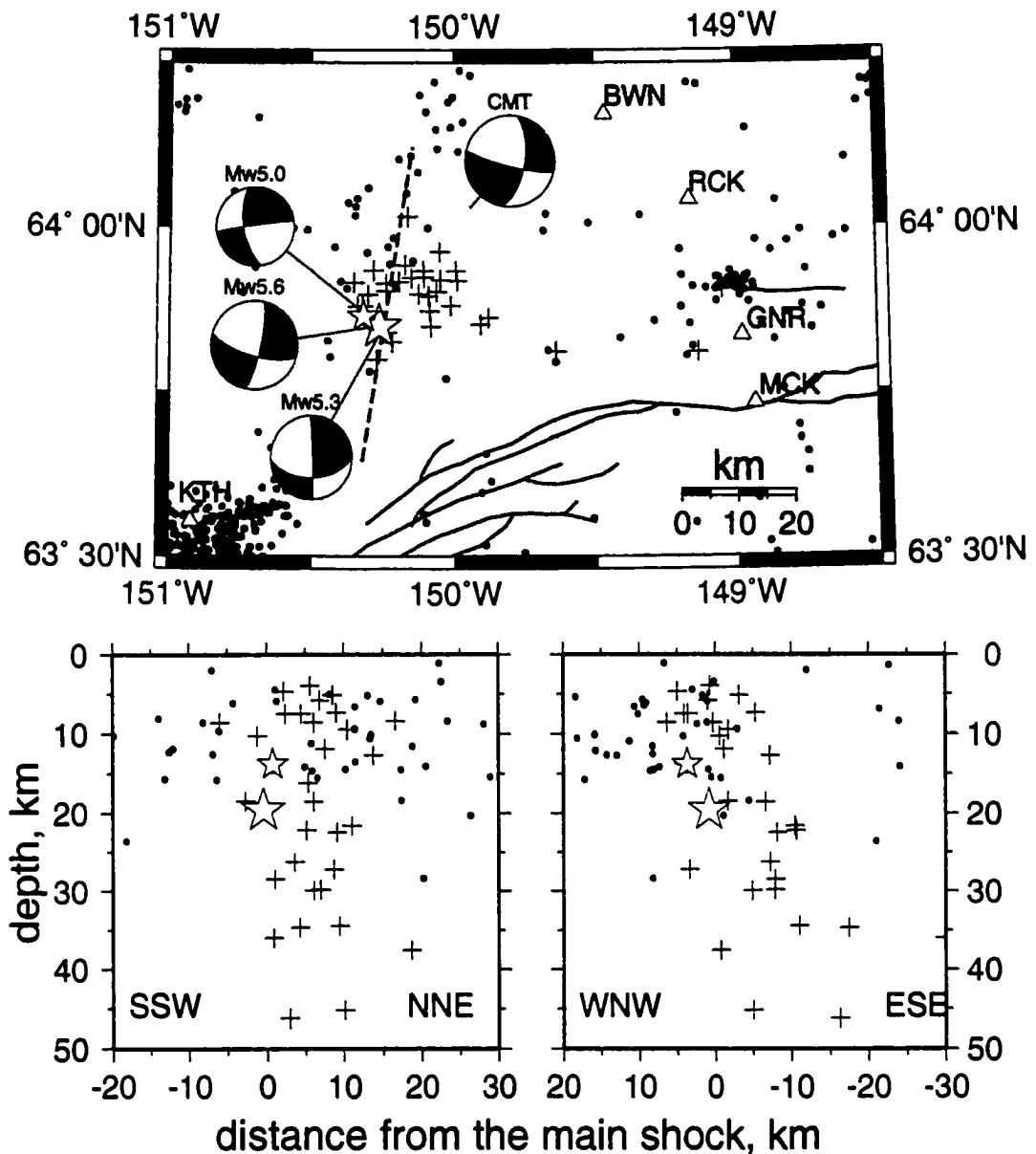
Figure 4.10. Detailed view of the source area of November 29, 2000 M_L 5.6 earthquake. The main shock and its 12/06/2000 M_L 5.0 aftershock are shown by the stars. Crosses are locations of the JHD relocated aftershocks. Moment tensor solutions for the main shock and two largest aftershocks obtained using the regional broadband data are presented as well as the CMT solution for the main shock. Dashed line indicates cross-section trend. Seismic stations with name codes are shown by open triangles.

NNE striking plane dipping to the east and are located between 5 and 45 km depth. There were no earthquakes below 20 km depth in the M_L 5.6 source region prior to this sequence. The main shock is located at the edge of the deepest crustal seismicity that have been previously recorded.

The moment tensor solutions for the main shock and two of its largest aftershocks were obtained using regional broadband data. Moment tensor inversion results for the M_L 5.6 and M_L 5.0 events are presented in Appendix C. One fault plane of the main shock solution is striking at $12°$ and dipping at $79°$, and the second plane's strike and dip are $106°$ and $70°$, respectively. The calculated M_W magnitude is 5.6.

Obtaining a moment tensor for the aftershock that immediately followed the main shock turned out to be difficult. Due to the small time separation between the two events, waveforms of the second shock are contaminated by the S-wave coda of the main shock. It is possible, however, to separate the second event from the first one in the MCK record, which is a broadband station located 62 km east of the earthquake. Assuming the same location for the second event as for the main shock, and an origin time of 42 sec later, a moment tensor solution was calculated (Figure 4.11). The estimated M_W magnitude is 5.3.

In summary, the sequence of magnitude 5+ earthquakes in the interior that occurred in November and December 2000 provides additional information for understanding of interior Alaska tectonics. These earthquakes are interesting in several ways. First of all, the main shock occurred at a depth of 20 km where no earthquakes were previously observed, while some of the aftershocks are located even deeper. Secondly, the north-south striking fault plane is rotated by about $20°$ from the general trend of seismicity that composes the Minto Flats seismic zone. Closer examination of the fault plane solutions available for the earthquakes within the MFSZ (Figures 4.4 and 4.5) shows, that the general trend of fault plane orientations changes from SW-NE to S-N north and south of $64°N$ latitude, respectively. It confirms the previous suggestion, that different faults have been developing as composite parts of the MFSZ (Page et al., 1995).

Future work on this earthquake sequence will include relocation of the aftershocks using BEAAR data, when these data become available.

001129.two.MCK

1: Str= 357.9 Dip= 88.5 Slp=-39.9
2: Str= 89.2 Dip= 50.1 Slp=-178.1
Moment= 0.928702E+24 dyne-cm
dc= 83.60% dp= 16.40%
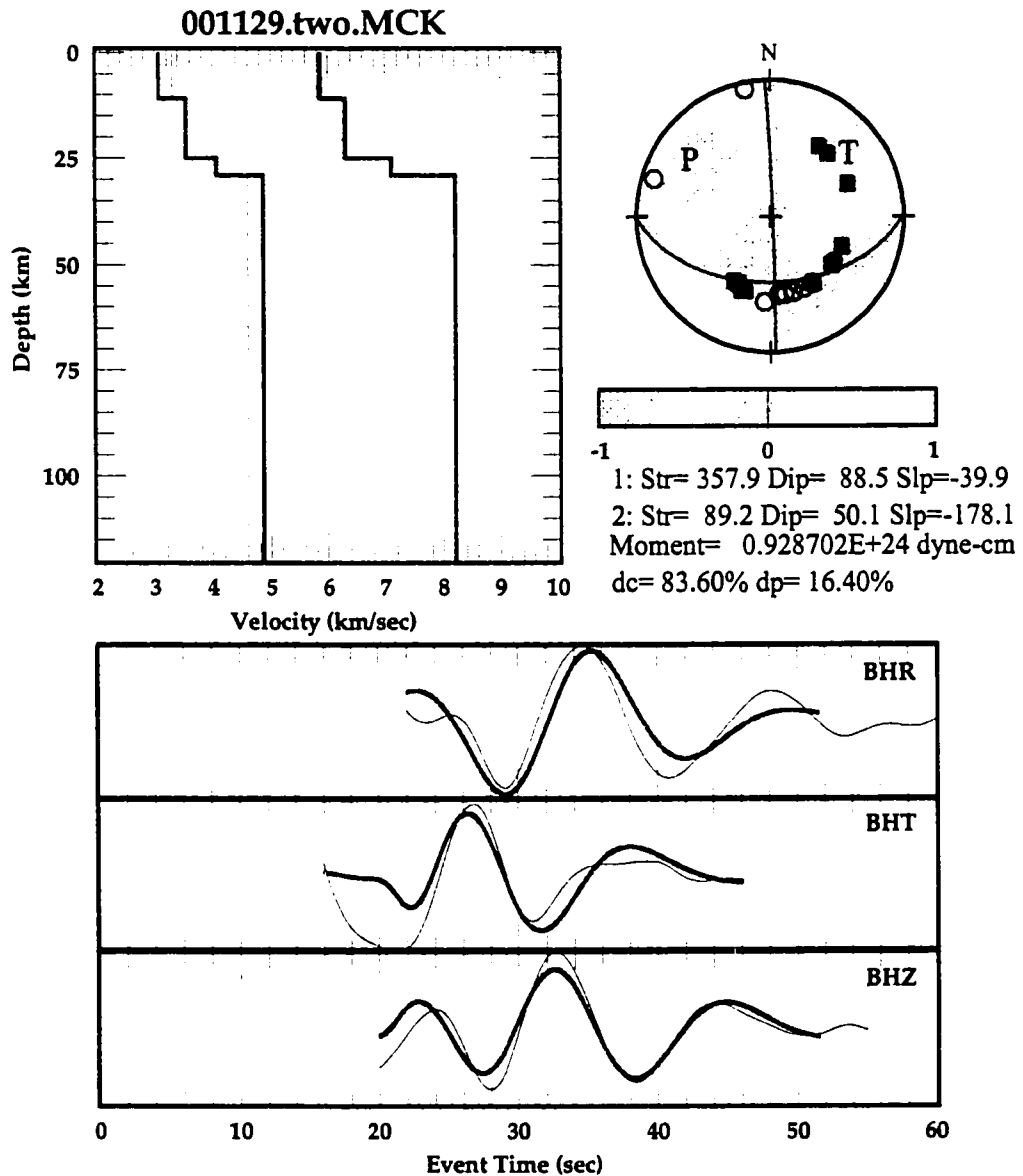
Figure 4.11. Moment tensor inversion results for M_W 5.3 aftershock of 11/29/00 M_L 5.6 earthquake. First motions shown are from the main shock. See Appendix C for the legend.

4.4.4. Kantishna cluster.

The Kantishna cluster is the most active crustal seismic source in the interior. It is located just north of the Denali fault and is composed of two distinct strands of seismicity aligned in a roughly southwest-northeast and east-west direction, respectively (Figure 4.12(a)). The distinct separation between these two strands is the major improvement after the joint relocation over the AEIC locations. The majority of the earthquakes are located above 20 km depth. There is, however, a lineation of the earthquakes in the western part of
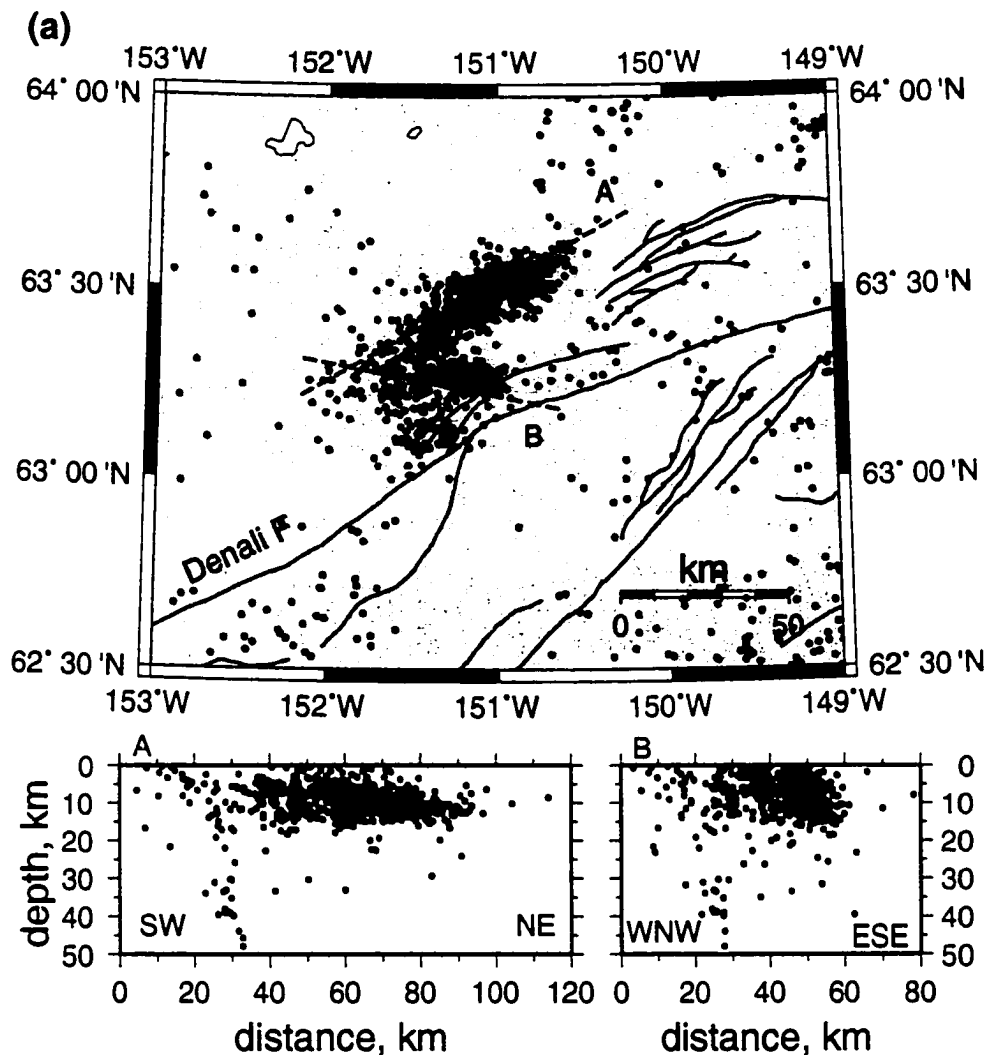
Figure 4.12. (a) Detailed view of the Kantishna seismic cluster. Two cross-section trends (A and B) are shown by dashed lines. Solid lines are the surface fault traces.
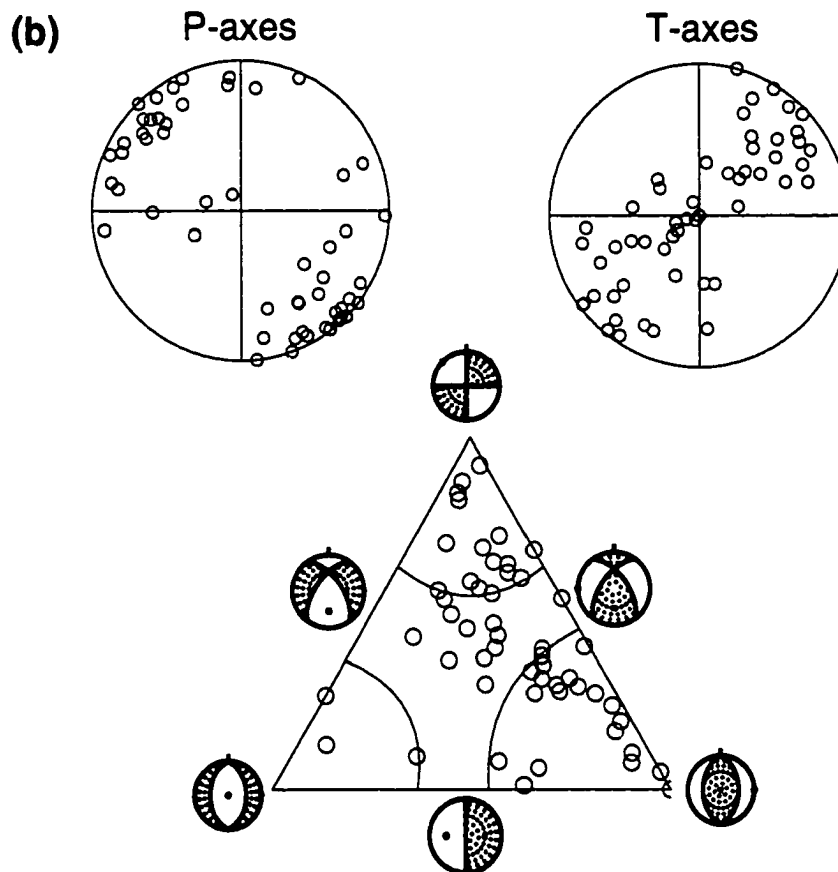
Figure 4.12. (b) Upper panel shows a lower hemispheric projection of P- and T-axes of the fault plane solutions for the Kantishna cluster earthquakes. Triangular diagram representing types of the focal mechanisms (Frohlich, 1992) is shown below. The vertices of the triangle correspond to pure trust (right), pure normal (left) and pure strike-slip (top) mechanisms. The curved lines inside the triangle correspond to mechanisms with 60° dip of N- and T-axes and with 50° dip of P-axis.

the cluster that extends to a depth of at least 50 km. This deeper seismicity is rather enigmatic, since the thickness of the crust in this area is believed to be about 40 km (Meyers et al., 2000).

Faulting characteristics of the Kantishna cluster earthquakes are presented in Figure 4.12(b). The triangle diagram presented here clearly demonstrates that most of the earthquakes are characterized by reverse type faulting. The solutions range from pure thrust to strike-slip mechanisms with a significant reverse component. Despite the seem-

ingly simple pattern in P- and T-axes orientation, the stress field within this area is complicated (see section 4.5).

4.5. STRESS TENSOR INVERSION RESULTS.

Our knowledge of the stress orientations in the crust is critical for understanding the regional tectonics. A total of 196 fault plane solutions for earthquakes in interior Alaska were available for a stress tensor inversion. Inversion of all earthquakes together resulted in a high misfit value (10.7°). This high value indicates that the whole area can not be characterized by a homogeneous stress field. Next, the study region was subdivided into separate volumes and the principal stress orientations were calculated for each of them. The areas are: (1) north of the Kaltag and Tintina fault system; (2) west of the MFSZ; (3) Minto Flats seismic zone; (4) east of the MFSZ; and (5) Kantishna cluster. This division is based on our knowledge and understanding of the interior tectonics. The Kantishna cluster was separated into an individual volume, because its inclusion into other volumes (e.g. (2) or (3)) resulted in high misfit values. The misfit values in each of the volumes except for the Kantishna cluster range from 4.5° to 5.5° with the number of events in each dataset between 19 and 31 (Figure 4.13(a) and Table 4.1).

The Kantishna cluster had to be subdivided into subvolumes since inversion of all its earthquakes (75 events) resulted in a misfit value of 9.2°. A well-constrained result was obtained for the northern half of the cluster with a small 95% confidence regions and misfit value of 5.5°. A more difficult task was to find a homogeneous stress tensor for earthquakes located in the southern half of the cluster. Eventually, we were able to find two volumes with misfit values of 6.4° and 5.7°, but the 95% confidence regions are rather large. According to Hardebeck and Hauksson (2001), however, the estimated confidence regions may be smaller.

The best fitting maximum (SH_{max}) and minimum (SH_{min}) horizontal stresses for seven target areas are shown in Figure 4.13(b). The major finding of this work is that the stress orientations change across the region in a systematic manner. In particular, the max-

Table 4.1: Stress tensor inversion parameters for 7 regions in central Alaska.

dataset	# of events	misfit, degree	σ_1 (max)		σ_2		σ_3 (min)		R^a
			pl.[b]	az.[c]	pl.	az.	pl.	az.	
north of Kaltag & Tintina faults	20	4.8	11	155	2	65	79	326	0.1
west of MFSZ	19	5.5	6	309	69	201	20	41	0.5
MFSZ	31	5.3	2	173	81	275	9	83	0.6
east of MFSZ	19	4.5	9	196	75	321	12	105	0.5
Kantishna north	36	5.5	6	113	12	204	77	357	0.5
Kantishna middle	18	6.4	16	316	35	215	51	66	0.5
Kantishna south	15	5.7	13	290	44	33	43	188	0.4

a. $R=(\sigma_1-\sigma_2)/(\sigma_1-\sigma_3)$
b. plunge, degrees
c. azimuth, degrees

imum compressive stress rotates clockwise from SE-NW to SSW-NNE from west to east of the Minto Flats seismic zone, respectively. Its orientation within the MFSZ is SSE-NNW, which is an intermediate state between the regions west and east of it. Confidence regions of SH_{max} do not overlap among these three areas, which suggests significant differences in the stress regimes. The same is observed for the minimum horizontal compressive stress. Its orientation changes from SW-NE through WSW-ENE to SES-WNW as one moves across the region from west to east, i.e. SH_{min} gradually rotates clockwise.

The region north of the Kaltag and Tintina fault system is characterized by SE-NW compression and SW-NE extension, i.e. an intermediate state between the area west of MFSZ and MFSZ itself. Its 95% confidence regions for SH_{max} and SH_{min}, however, overlap with the corresponding confidence intervals of the stress tensors for the above mentioned two areas to the south of it. Taking into account that these confidence regions may be overestimated (Hardebeck and Hauksson, 2001), the difference still might be significant.

(a)   North of Kaltag & Tintina F

$\sigma1>\sigma2>\sigma3$

West of MFSZ   MFSZ   East of MFSZ

Kantishna south   Kantishna middle   Kantishna north
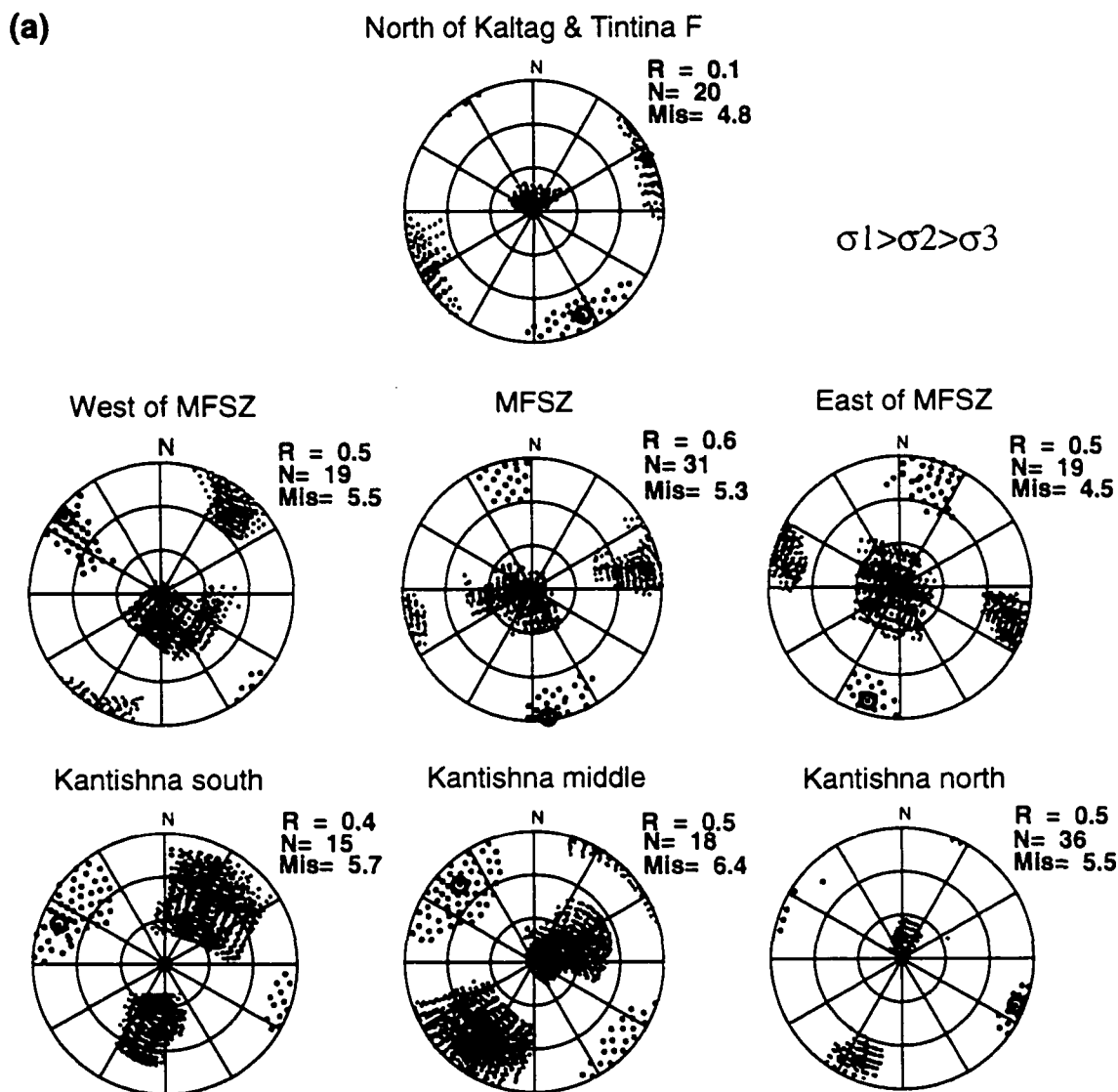
Figure 4.13. (a) Polar projection of the principal stresses for seven areas in central Alaska. Black circles, x's and crosses denote orientations of the maximum, intermediate and minimum stresses of the best fitting stress tensor, respectively. Green, blue and red areas are 95% confidence regions for the maximum, intermediate and minimum stresses, respectively.

The stress field within the Kantishna cluster is diverse with the major differences in orientations of the minimum principal stress. It is nearly vertical in the well-constrained inversion for the northern half of the cluster and changes to a south-north orientation with a 43° plunge in the southern part of the cluster. It is difficult, however, to judge the quality
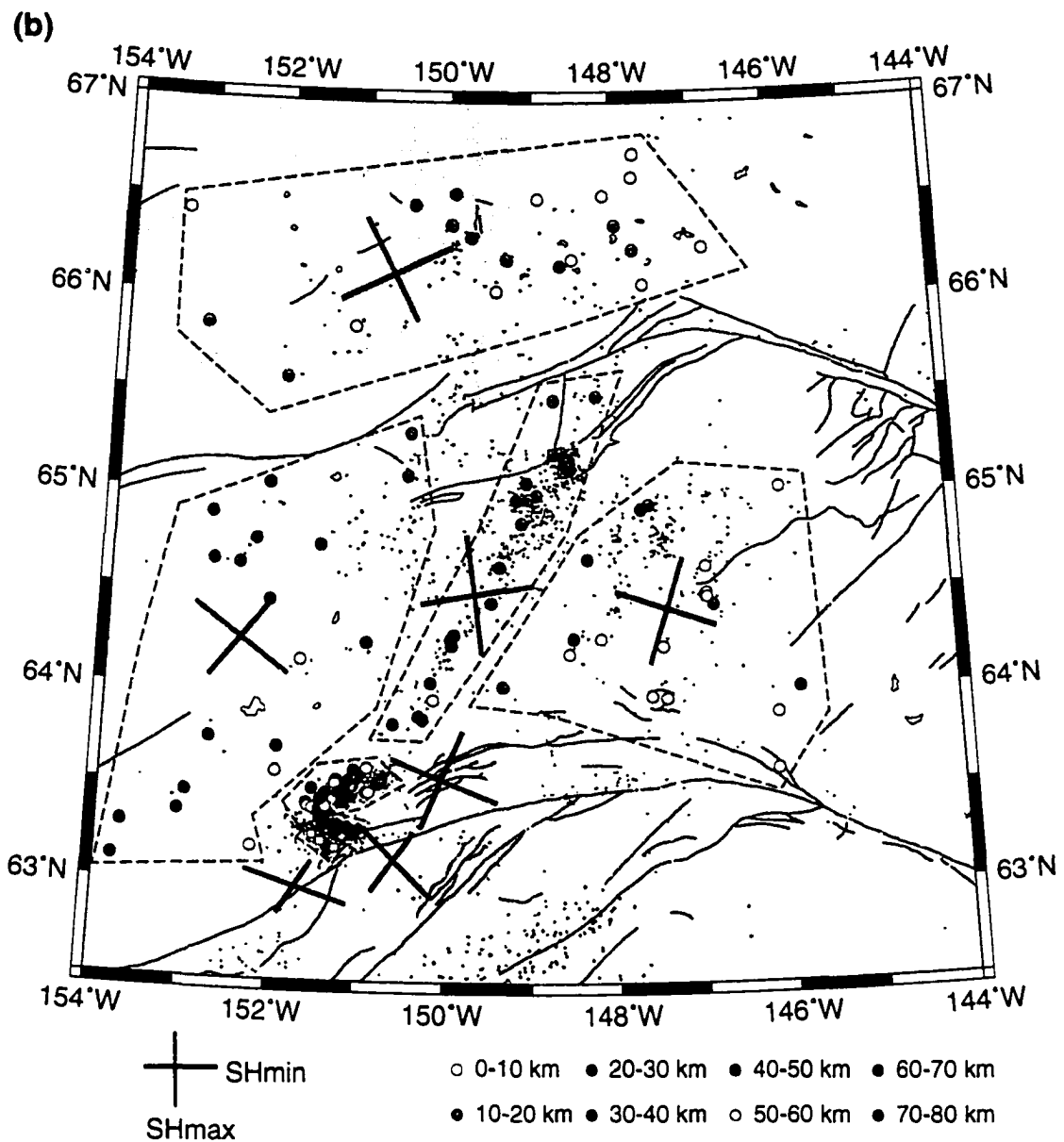
Figure 4.13. **(b)** Relocated earthquakes and orientations of the best fitting maximum (green) and minimum (blue) horizontal stresses for 7 target areas. Dashed polygons outline separate inversion regions with larger symbols representing earthquakes included into the inversion.

of the inversion for the southern part of the Kantishna cluster, since the misfit value is close to a maximum allowable limit of 6° for a homogeneous stress field and the number of events in the inversion is rather small. The definite conclusion, however, is that the stresses in this area change rapidly across relatively short distances.

In summary, stress orientations change in a systematic manner across central Alaska. The estimated maximum principal stress rotates clockwise from a SE-NW to a SSW-NNE direction from west to east. This general trend coincides with the stress indicators presented by Estabrook and Jacob (1991) and gives a more detailed representation of the stress field in central Alaska than any other source of information available up to now.

4.6. CONCLUSIONS.

In total 3,611 earthquakes that occurred from 1988 to 1999 are relocated using the Joint Hypocenter Determination method. The Minto Flats seismic zone has the most coherent structure among the three major seismic zones in the interior and extends from the Kaltag fault in the north to the Kantishna cluster in the south. The Fairbanks and Salcha seismic zones do not extend as far north and south as the MFSZ. If the block-rotation model of the deformation in central Alaska (Page et al., 1995) is valid, then the FSZ and SSZ may continue propagating farther north and/or south in a number of moderate- to large-sized earthquakes.

The new earthquake locations provide more detail on the structure of the Kantishna cluster and better locations for the aftershock sequence of the 11/29/2000 M_L 5.6 earthquake in the Minto Flats seismic zone. The Kantishna cluster is composed of two distinct earthquake lineations of SW-NE and WNW-SES orientations, respectively. The JHD locations for the aftershocks of the 1995 M_W 6.0 Minto Flats earthquake and 10/22/96 M_W 5.7 earthquake near the Denali fault are also available. Locations and mechanisms of the 1995 and 2000 Minto Flats seismic zone events are consistent with the block-rotation model.

A catalog of 196 fault plane solutions consisting of the moment tensor solutions for the earthquakes with magnitude 4.0 or above and P-wave first motion solutions for the earthquakes with magnitude 3.4 and above that occurred from 1988 to 2000 is composed for interior Alaska. Moment tensor solutions are calculated using regional broadband data. This catalog has been used to calculate principal stress orientations in the crust. The stress orientations change systematically across central Alaska. In particular, the maximum principal stress orientation rotates clockwise from SE-NW to SSW-NNE direction as one moves from west to east across central Alaska. These stress orientations agree with the stress trajectories inferred from the geological stress indicators and are consistent with a stress regime we would expect if the Pacific Plate were a rigid intrusion into a plastically deforming North American Plate (Nakamura and Uyeda, 1980; Estabrook and Jacob, 1991).

Stress orientations within the Kantishna cluster are complex showing rapid changes across short distances. Orientations of the maximum principal stresses are identical to those west of the MFSZ and range between ESE-WNW and SE-NW. The intermediate and minimum stresses, however, vary considerably. The predominant faulting mechanism within the cluster is thrusting or oblique with a significant reverse component. This complexity may be caused by the location of the Kantishna cluster at the junction of the major tectonic features in the region: the Denali fault in the south and the MFSZ in the northeast. Detailed GPS measurements of the crustal movements in the area could help to resolve this question.

Analysis of the fault plane solutions for the earthquakes within the Minto Flats seismic zone shows that the predominant orientations of the fault planes changes across 64°N latitude from a southwest-northeast orientation north of it to a south-southwest-north-northeast orientation south of it. This change coincides with a change in the earthquake alignment. The earthquakes form a coherent southwest-northeast oriented lineament north of 64°N latitude, while the seismicity is more diffused to the south. North of 64°N, the orientation of the maximum compressive stress is rotated approximately 35° from the prevailing seismicity trend. This angle is indicative of strong, less-well-devel-

oped faults (Provost and Houston, 2000) within the MFSZ, which is consistent with the assumption that the MFSZ is composed of a series of subparallel faults and fault splays.

Tests with different velocity structures in the moment tensor inversion procedure show that the TACT velocity model with varying crustal thickness is the best suitable for calculating Green's functions for the earthquakes that occurred in the interior. However, the area south of the Denali fault requires a different structure.

The moment tensor inversion study shows that it is possible to obtain a reliable moment tensor solution for moderate-sized earthquakes ($M_L \geq 4$) using three-component records from a single broadband station when the epicentral distances are between 50 and 300 km.

Chapter 5: Anomalous phases from the Alaskan subduction zone earthquakes, observed at seismic arrays.

5.1. INTRODUCTION.

Anomalous phases traveling within the slab have been recognized and used to investigate crustal and upper mantle structure in many subduction zone regions around the world. These phases include reflected (James and Snoke, 1990; Iidaka and Mizoue, 1991), converted (Mitronovas and Isacks, 1971; Matsuzawa et al., 1986, 1990; Iidaka et al., 1990), refracted (Chiu et al., 1985; Smith et al., 1994; van der Hilst and Snieder, 1996) and channel-guided waves (Hori et al., 1985; Oda et al., 1990; Abers and Sarker, 1996). The anomalous slab phases are interpreted as being generated at, or near, the top of the subducted plates, as well as at discontinuities within interiors of the plates. No subduction zone is an exact copy of the other and therefore, observations of the anomalous phases are different from place to place. However, some common observations can be found among the different subduction zones.

Anomalous phases arriving with 1-3 s delays after the first arrival were observed in the records of the subduction zone earthquakes in Tonga (Mitronovas and Isacks, 1971; Huppert and Frohlich, 1981), New Hebrides (Louat et al., 1979; Chiu et al., 1985), the Pacific plate in Japan (Suyehiro and Sacks, 1979; Matsuzawa et al., 1990; Iidaka and Mizoue, 1991), the Izu slab in Japan (Nakamura et al., 1992), the Nazca plate (James and Snoke, 1990), and New Zealand (van der Hilst and Snieder, 1996). Matsuzawa et al. (1990) and Nakamura et al. (1992) interpreted these phases as S-to-P converted waves at

the upper surface of the subducting slab. James and Snoke (1990) observed differences in back azimuths between the first arrival and secondary an anomalous arrivals of up to 20°. They interpreted anomalous secondary phase as a wide-angle reflection off the upper surface of the subducted slab. Chiu et al. (1985) interpreted anomalous earlier arrival as a P-wave refracted into a faster portion of the subducted slab. A somewhat different phenomenon was reported by van der Hilst and Snieder (1996) in the subduction zone beneath New Zealand. They observed high-frequency precursors to direct P-wave arrival, which were interpreted as diffractions in the high-velocity layer 8-10 km thick at the top of the subducted slab. The opposite effect was reported for the Alaska-Aleutian subduction zone by Abers and Sarker (1996). They observed normal dispersion of the arriving energy in the records of the intermediate-depth earthquakes. This dispersion was explained by the existence of a low-velocity layer at the top of the subducted slab which acted as a waveguide.

Later anomalous arrivals with delays of 7-13 s have been observed in Tonga (Mitronovas and Isacks, 1971), New Hebrides (Louat et al., 1979; Chiu et al., 1985), the Tohoku district in Japan (Matsuzawa et al., 1986, 1987), and the Izu slab in Japan (Nakamura et al., 1992). In these studies, the later anomalous phases most commonly were interpreted and modeled as P-to-S converted waves at the upper surface of the slab. Nakamura et al. (1992), however, proposed conversion at the lower boundary of the slab.

Alaska is in a good location with respect to the subducting slab for studying anomalous phases caused by the inhomogeneous subsurface structure. In south-central Alaska the Pacific plate underthrusts the North American plate at a rate of 5.6 cm/year. This process gives rise to intense seismicity down to a depth of about 200 km (Figure 5.1). However, the geometry of the subduction zone in southern and central Alaska is rather complex (Page et al., 1991; Chapter 2). The subducted slab undergoes a 20° counter-clockwise turn at about 59°N latitude and 35° clockwise turn farther north, at approximately 63°N latitude. The intermediate-depth seismicity terminates at about 64°N, which is associated with the edge of the subducted plate. In addition, several researchers (e.g., van Wormer et al., 1974; Pulpan and Frohlich, 1985) proposed segmentation of the subducted plate
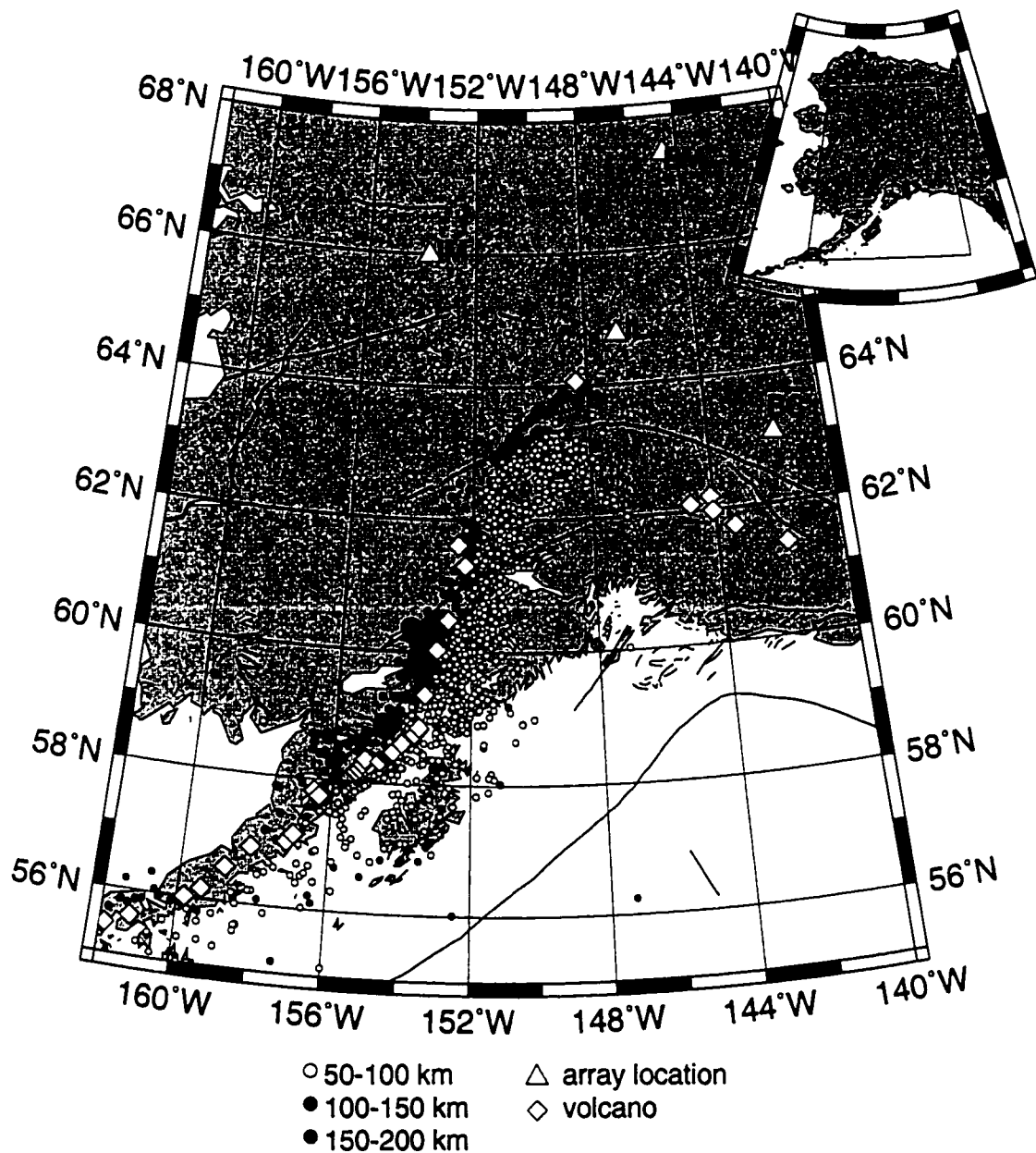
Figure 5.1. Map of the study area. Epicentral locations of the subduction zone earthquakes with $M_L \geq 3$ from the AEIC catalog from 1988 to 1998 are shown. Locations of the seismic arrays are indicated by open triangles. Open diamonds are the Alaska and Wrangell subduction zone volcanoes. Major faults and the Aleutian trench are shown by solid lines.

beneath Alaska into the three segments: Kodiak in the south, Kenai in the center and McKinley in the north. A tear in the subducted plate between the Kenai and McKinley blocks has been identified along its bend (Burbach and Frohlich, 1986; Ratchkovski and Hansen, 2000; see also Chapter 2). The tear may extend as far as Prince William Sound. In addition, the Wrangell subduction zone is located to the east of the Alaska subduction zone; it extends to a depth of 100 km and is 150 km long in the strike direction (Stephens et al., 1984). The nature of the relationship between the two subduction zones remains a topic of discussion. Page et al. (1989) suggested that the two zones are continuous at shallow depths of 20-40 km. Recently, it has been proposed, that these two zones are not connected at greater depths (Ratchkovski and Hansen, 2000).

Among the few studies of the anomalous slab phases in Alaska, the most recent one is by Abers and Sarker (1996) who investigated dispersion of the body waves travelling through the subducted slab beneath Alaska. They found that the high frequency energy is delayed with respect to the low frequency first arrival and suggested a 2-6 km thick low velocity waveguide that parallels the slab to explain their observations. Stephens et al. (1990) documented S-to-P converted waves generated near the top of the Wadati-Benioff zone (WBZ) within the shallow subduction zone in southern Kenai peninsula. Reyners and Coles (1982) observed secondary phases arriving between the direct P- and S-waves in the Shumagin Islands region of the eastern Aleutian subduction zone. Recently, Helffrich and Abers (1997) studied P-to-S converted phases in the same region of the Aleutian arc. They interpreted these phases as generated at the top of a low-velocity layer, which extends to a depth of 150 km and is 8% slower than the overlying mantle.

The purpose of this study is to search for, and identify, anomalous phases in the recordings of the Alaska subduction zone earthquakes. We used recordings from four seismic arrays located in interior Alaska (Figure 5.1). The arrays are equipped with vertical component short-period bore-hole sensors. Arrays BC, BM and IM are 5-element arrays and IL is a 19-element array with an additional 3-component seismometer. The aperture of each of the arrays is about 10 km. Two of the arrays are located on the continuation of the strike of the WBZ, one is located to the northwest of the subducted slab, and the last one is

to the north-east of the slab. Use of seismic array data has several advantages over data from single stations. First of all, bore-hole sensors provide higher signal-to-noise ratio than surface seismic stations. Moreover, the arrays provide information on apparent velocities and back azimuths of coherent seismic arrivals. Lindquist (1998) conducted a detailed study of detection capabilities of the Alaskan seismic arrays.

5.2. DATA SELECTION AND INITIAL ANALYSIS.

We have analyzed records of the intermediate-depth subduction zone earthquakes recorded and cataloged by the Alaska Earthquake Information Center (AEIC) during the period from July, 1997 to March, 1998. Initial earthquake selection criteria were: 1) local magnitude $M_L \geq 3$; 2) focal depths below 50 km; and 3) epicenters located between 55°N and 64°N. After this selection criteria we had 325 earthquakes for the waveform analysis. Due to poor signal-to-noise ratio and missing data at some arrays, the number of actual records available for the analysis was between 226 and 325 for each of the four arrays.

The initial data analysis consisted of visual examination of the waveforms and identification of the coherent phases, their arrival times and amplitudes. Next, frequency-wavenumber (FK) analysis (Capon, 1969; Fyen, 1996) was used to determine back azimuths and apparent velocities of the identified coherent arrivals (see Appendix D for description of the FK analysis). Further analysis included comparison and correlation of all available phase characteristics of the identified anomalous arrivals.

We determined the back azimuth and apparent velocity of the first arrival for all of the selected earthquakes. This allowed us to compare back azimuths of the AEIC hypocenter locations with those determined using the FK analysis of the array data. These results are presented in Figure 5.2. There are systematic trends in the residual data. In particular, for array BC, back azimuth residuals are consistently negative for the events located to the south of 59°N. The residuals range between -6° and 10° for events located north of 59°N with an average residual value of $0.8^o \pm 3.2^o$. The residuals at array BM are
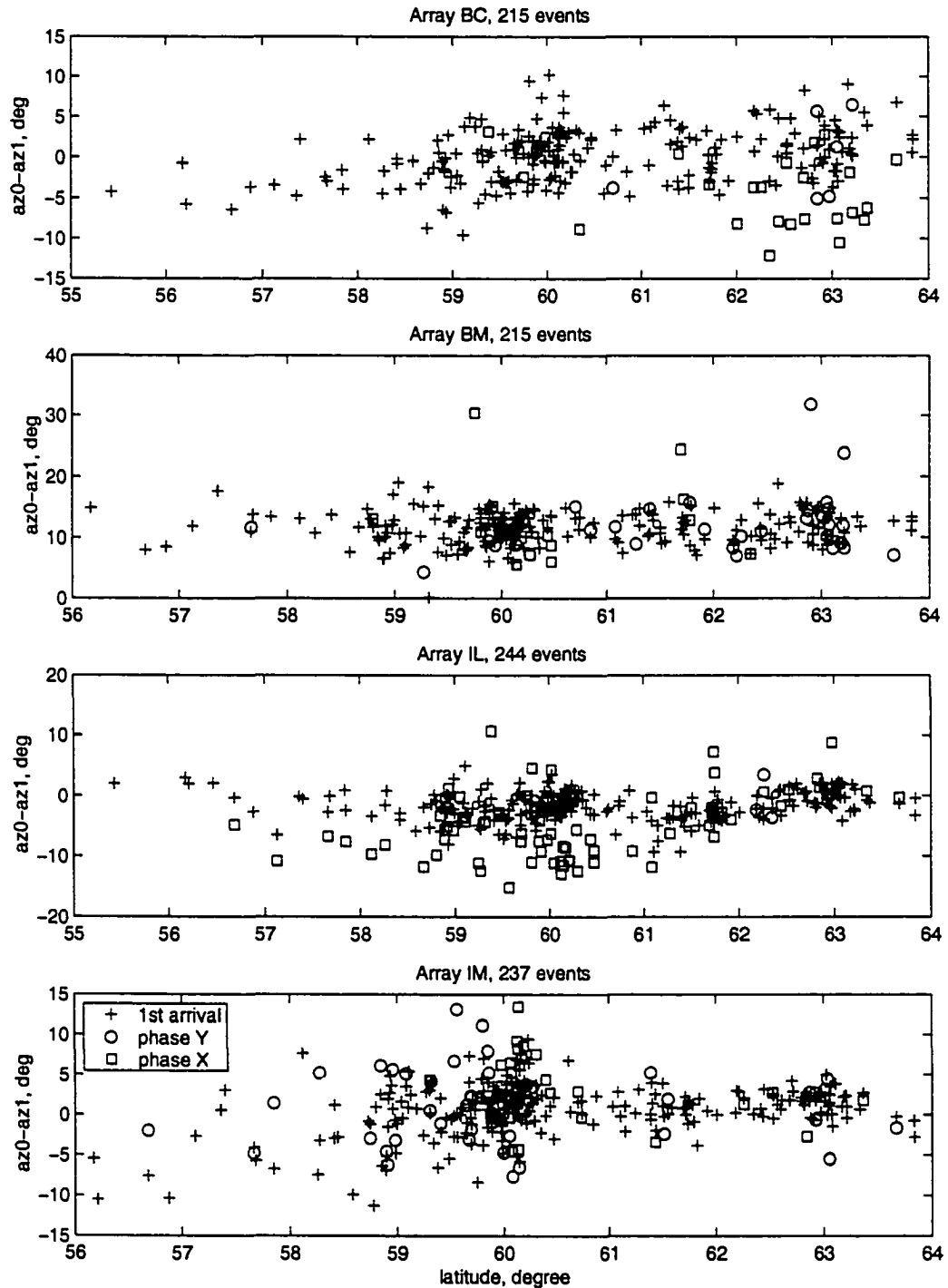
Figure 5.2. Difference between back azimuth for the AEIC epicenter location (az0) and back azimuth from FK analysis of the array data (az1) versus location of the earthquake along the strike of the WBZ. Crosses represent estimates for the first arrivals, circles and squares represent estimates for Y and X phases, respectively.

consistently positive with an average value of $11.6^o \pm 2.6^o$. There is an overall constant trend for azimuthal residuals at array IL with an average of $-1.7^o \pm 2.3^o$. On a smaller scale, however, some fine details can be noted, especially in the region between 61°N and 64°N. Lastly, at array IM the residuals for the events located north of 60.5°N show a constant trend with an average of $1.0^o \pm 2.9^o$; farther south, residuals become more negative and span a wider range.

Thus, the largest discrepancies between the AEIC epicentral locations and FK back azimuths are at array BM. Ray paths from the subduction zone earthquakes to arrays BC and IM exit the slab near the origins of the earthquakes, and therefore the ray paths are to a lesser degree affected by the three-dimensional structural inhomogeneities of the slab. Arrays IL and BM, on the other hand, are located on a continuation of the strike of the Alaska WBZ, and therefore ray paths from the subduction zone earthquakes are expected to be greatly affected by the presence of the slab.

5.3. CHARACTERISTICS OF THE OBSERVED ANOMALOUS PHASES.

Analysis of the selected earthquake records revealed two prominent anomalous phases between the first P- and S-wave arrivals for all four arrays. We determined back azimuths and apparent velocities of the anomalous phases for all selected earthquakes where these phases were represented by a coherent arrival with a satisfactory signal-to-noise ratio. Locations of the earthquakes with the observed phases are shown in Figures 5.3 and 5.4. Below is a detailed description of characteristics of the observed anomalous phases for each of the four arrays.

Array IL. Array IL is located on continuation of the strike of the WBZ and is about 90 km away from its northern termination. Most commonly at this array we observe a phase arriving with a 1-2 s delay after the first P-wave (herein referred to as phase X_{IL}). An example of this arrival is shown in Figure 5.5 (upper panel). Figure 5.6 illustrates the dif-
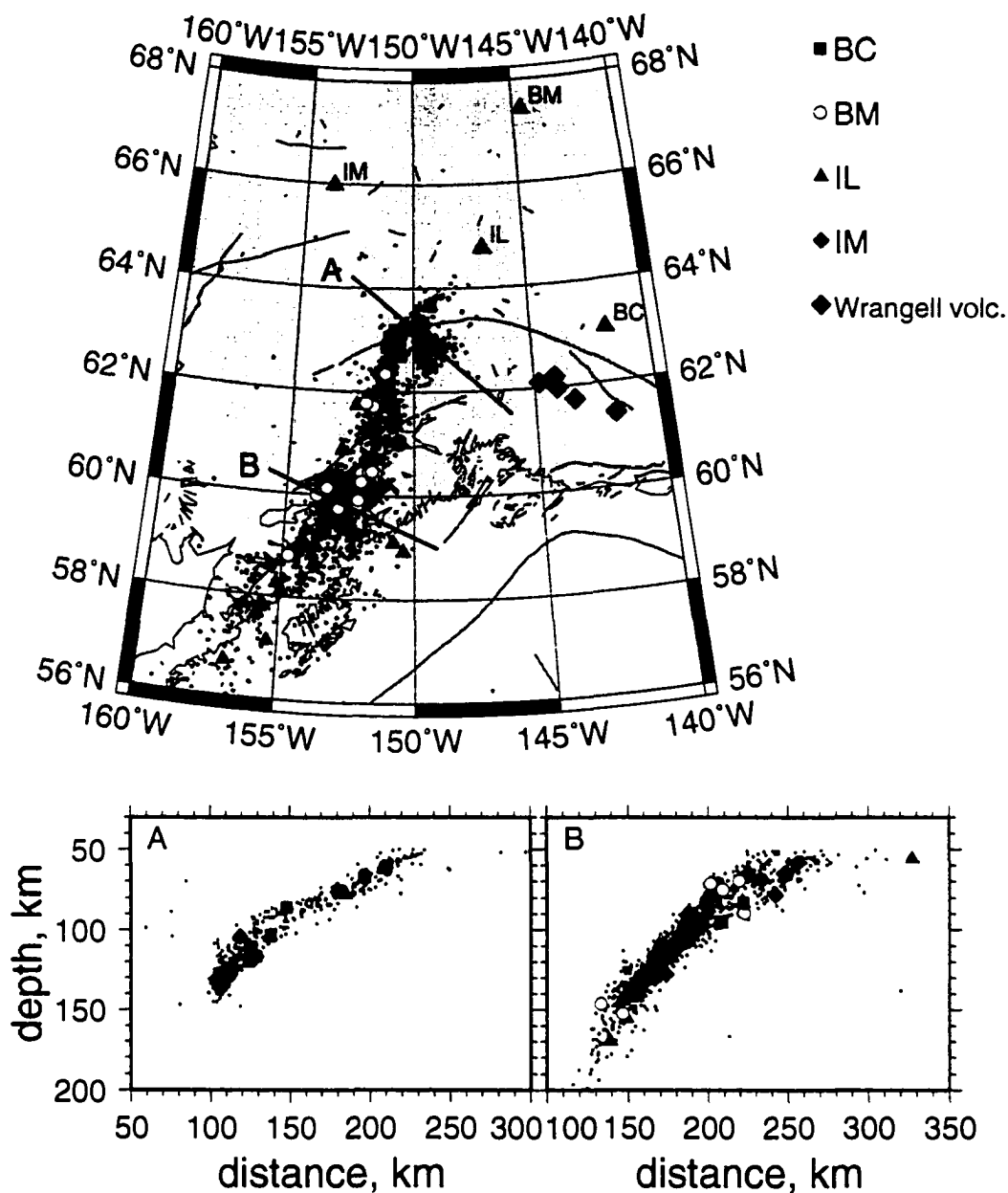
Figure 5.3. Location of the earthquakes with the observed anomalous phases X: blue squares at array BC, yellow circles at array BM, red triangles at array IL, and green diamonds at array IM. Two cross-sections are also shown, each is 150 km thick. Background seismicity includes earthquakes from 1988 to 1999 with $M_L \geq 3$ and depths greater than 50 km as cataloged by the Alaska Earthquake Information Center. Black triangles are locations of the seismic arrays. Major faults in the area and the Aleutian trench are shown by red lines.
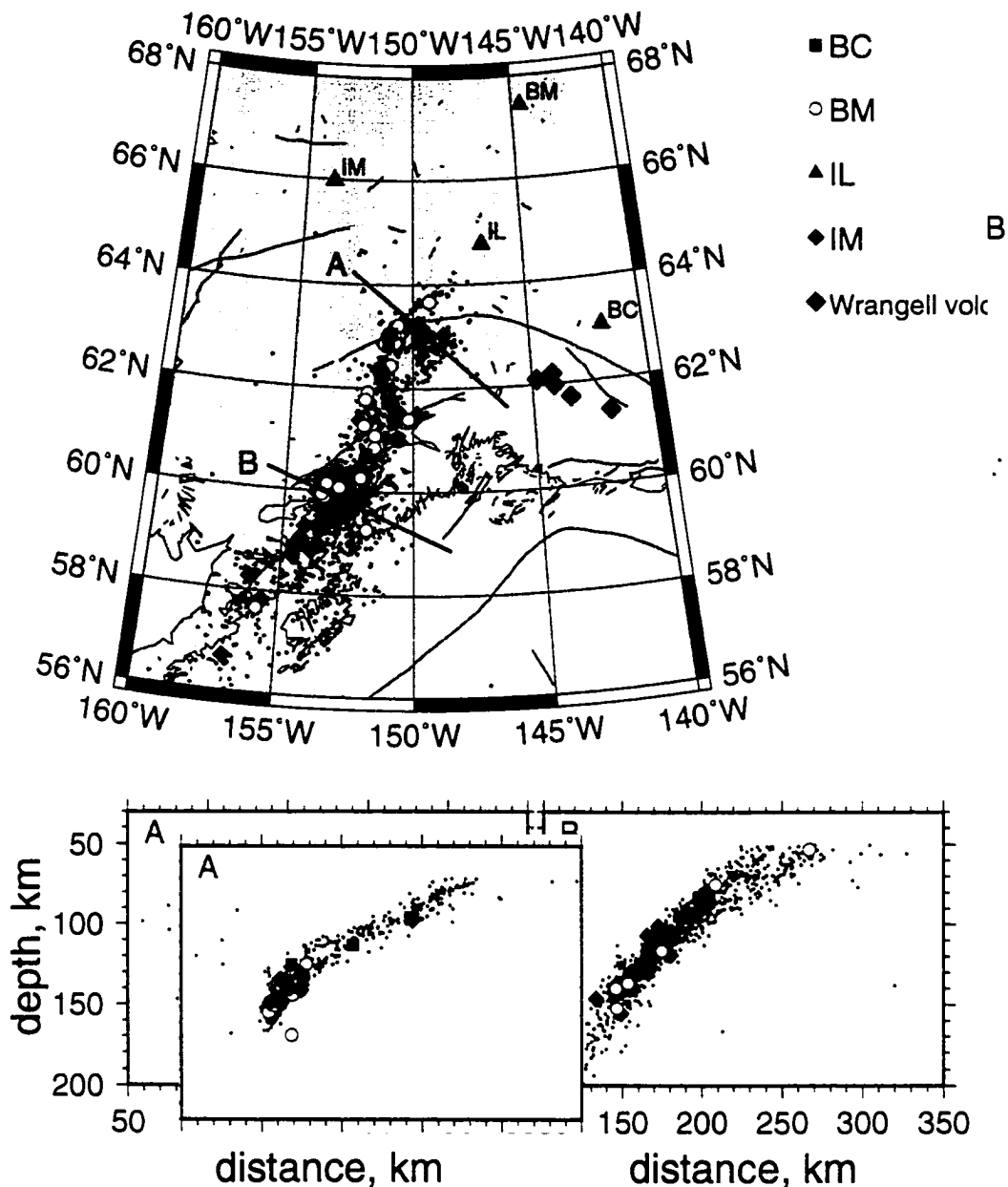
Figure 5.4. Location of the earthquakes with the observed anomalous phases Y: blue squares at array BC, yellow circles at array BM, red triangles at array IL, and green diamonds at array IM. Two cross-sections are also shown, each is 150 km thick. Background seismicity includes earthquakes from 1988 to 1999 with $M_L \geq 3$ and depths greater than 50 km as cataloged by the Alaska Earthquake Information Center. Black triangles are locations of the seismic arrays. Major faults in the area and the Aleutian trench are shown by red lines.

Figure 5.5. Examples of the anomalous phases X (upper panel) and Y (lower panel) observed at array IL. Upper panel is a record of the earthquake that occurred beneath Iliamna volcano (depth 117.24 km, M_L 3.7), lower panel is a record of M_L 4.2 earthquake that occurred at 92.04 km depth and 3.2° epicentral distance.

Figure 5.6. Estimated parameters of the anomalous phases X (crosses) and Y (circles) observed at array IL. Differences in traveltimes, back azimuths, apparent velocities, and amplitudes between the first P arrival (t1, az1, vel1, amp1) and phases X or Y (t2, az2, vel2, amp2) versus latitude or depth of the source are shown. Back azimuths and apparent velocities are determined from FK analysis of the array data.
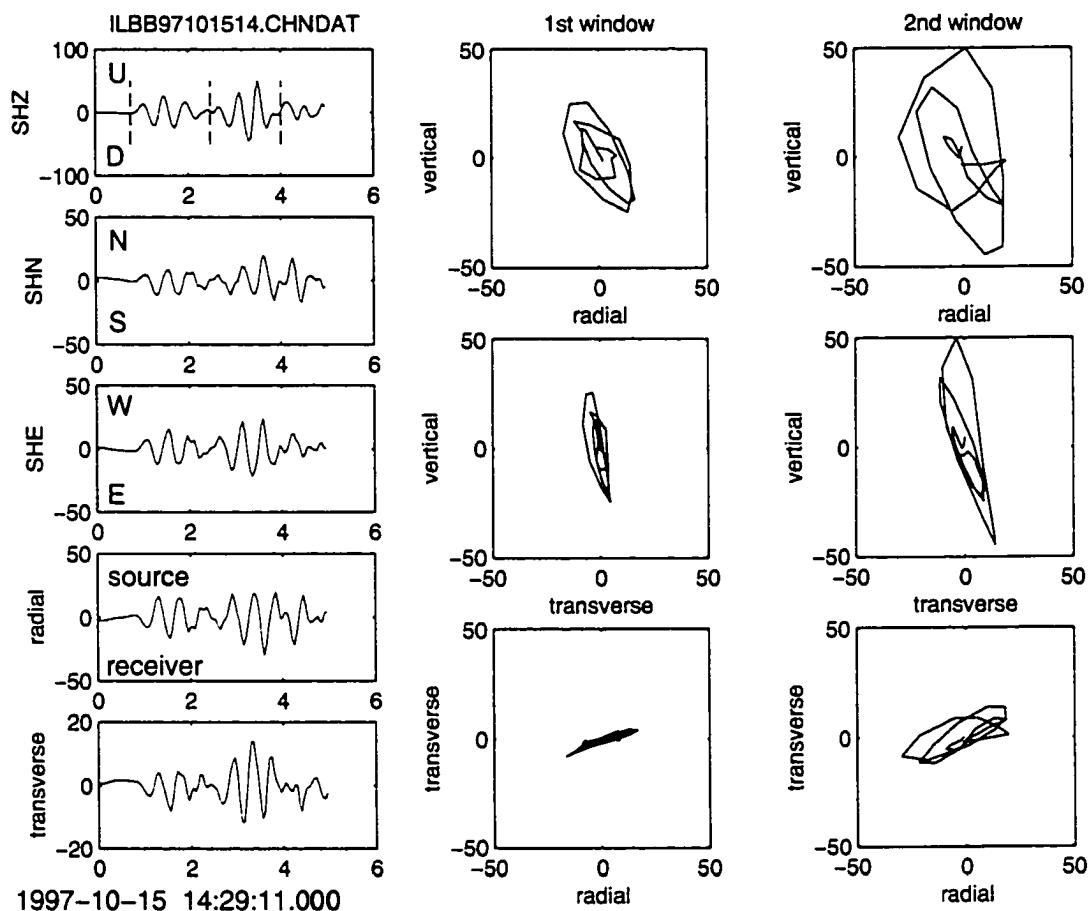
Figure 5.7. Particle motion analysis of the Iliamna event of 97/10/15 shown in Figure 5.3. Left panel displays records of the three original components recorded at station ILBB (vertical, NS and WE) with rotated radial and transverse components below. Dashed lines show time windows selected for the analysis. Middle and right panels are particle motions for the 1st and 2nd windows, respectively.

ferences between back azimuths, apparent velocities, traveltimes and amplitudes of the first P-wave arrival and phase X_{IL}. Based on the analysis of 73 earthquakes with this phase, its distinct characteristics are: (1) higher amplitude and (2) higher apparent velocity than those of the first P-wave arrival. Particle motion analysis of available three-component records shows that phase X_{IL} has a P-wave sense of motion, although with less recti-linearly (Figure 5.7).

There are two important observations regarding phase X_{IL}. First, as the epicentral distance increases, the azimuthal difference between the first P-wave arrival and phase X_{IL} systematically changes (Figure 5.6(c)). At closer epicentral distances the first P arrival comes from a larger back azimuth than phase X_{IL} (positive azimuthal difference), while for more distant events this trend reverses, i.e. the first P-wave arrival has a smaller back azimuth than phase X_{IL} (negative azimuthal difference). The second observation is that the differences between the apparent velocities of phase X_{IL} and the first P-wave arrival are larger for the deeper events (Figure 5.6(f)).

We also observe a rare second anomalous phase at array IL (herein referred to as Y_{IL}). It arrives with a 8 s delay after the first P-wave arrival (Figure 5.5, lower panel). There are only 3 earthquakes with this phase. They are clustered at 62.2°N latitude between 79 and 92 km depth (Figure 5.4). Characteristics of phase Y_{IL} are illustrated in Figure 5.6. The amplitude of this phase is comparable to, or smaller than, that of the first P-wave arrival. Apparent velocities are on average smaller by 0.4 km/s than those of the first P arrival.

Array BM. Array BM is located on continuation of the strike of the Alaskan WBZ and is about 400 km away from its northern termination. At this array we observe two anomalous phases between the first P- and S-wave arrivals. One arrives with a 2-3 s delay (herein referred to as X_{BM}) and another with a 8-9 s delay (herein referred to as Y_{BM}) after the first P-wave arrival. For this array, the later phase is observed more commonly (32 events) than the earlier one (13 events). Examples of the records of these phases are shown in Figure 5.8. Differences between traveltimes, back azimuths, apparent velocities and amplitudes of the first arrival and the anomalous phases are illustrated in Figure 5.9.

The consistent characteristics of phase X_{BM} are: (1) the amplitude is larger than amplitude of the first arrival in a majority of the cases, and (2) the apparent velocities are in general smaller than those of the first arrival, but within 0.5 km/s. In general, the back azimuth of arrival X_{BM} is smaller than that of the first P-wave arrival for closer events and
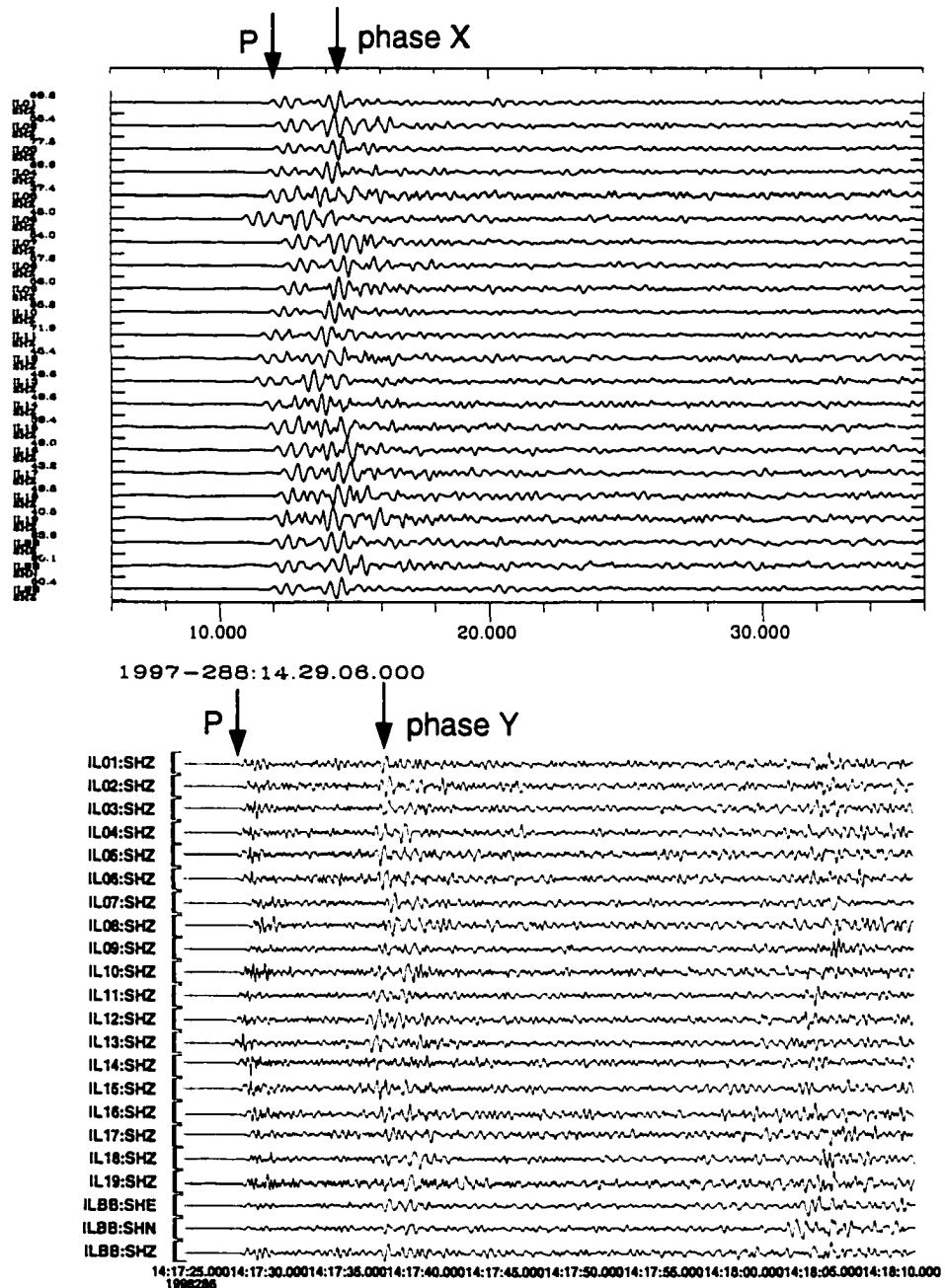
Figure 5.8. Example of the anomalous phases X (upper panel) and Y (lower panel) observed at array BM. Upper panel is a record of M_L 3.9 earthquake that occurred at 64.30 km depth and 7.6° epicentral distance. Lower panel is a record of M_L 4.4 earthquake that occurred at 88.78 km depth and 5.7° epicentral distance.

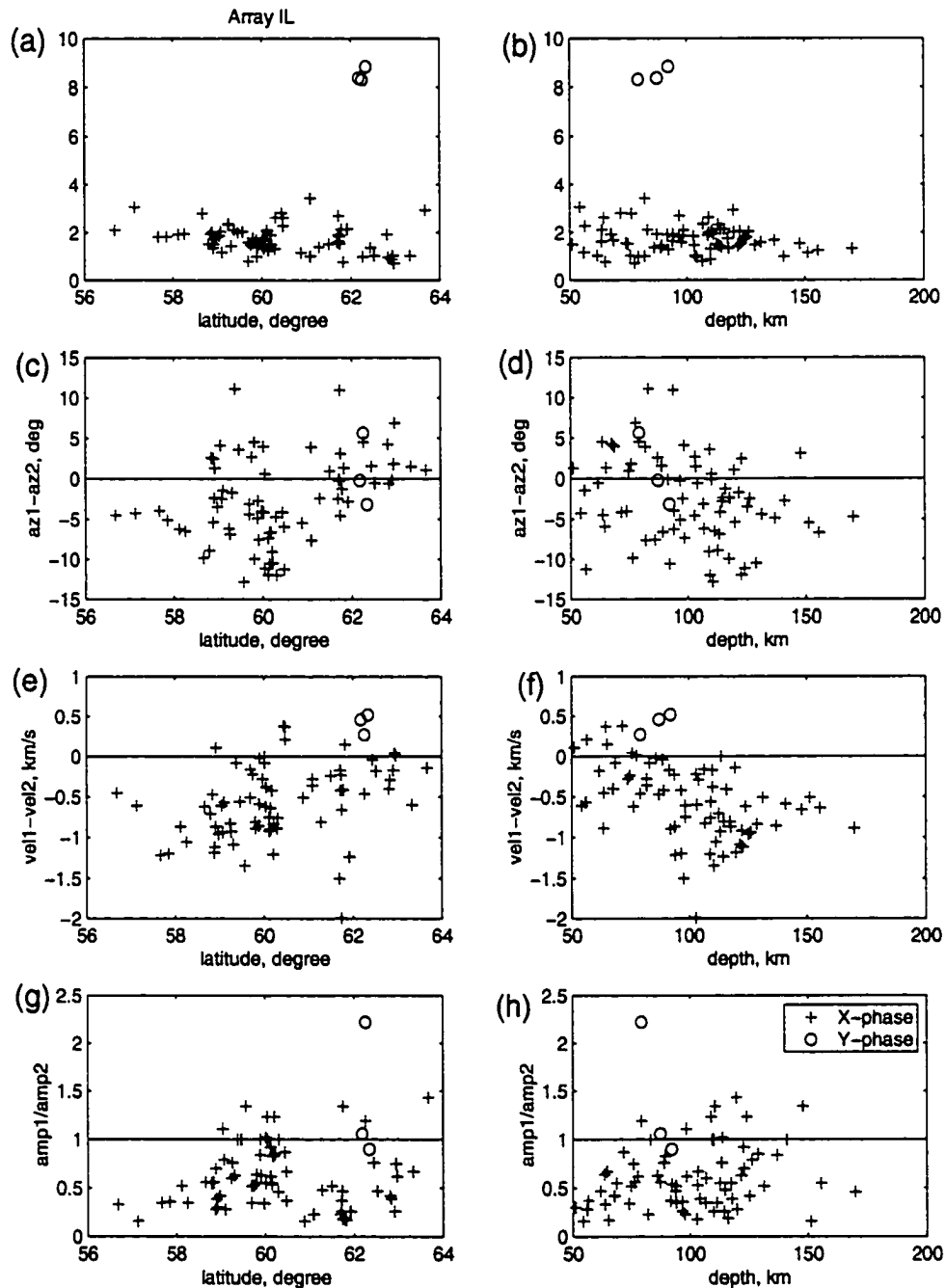**Figure 5.9.** Estimated parameters of the anomalous phases X (crosses) and Y (circles) observed at array BM. Differences in traveltimes, back azimuths, apparent velocities, and amplitudes between the first P arrival (t1, az1, vel1, amp1) and phases X or Y (t2, az2, vel2, amp2) versus latitude or depth of the source are shown. Back azimuths and apparent velocities are determined from FK analysis of the array data.

it is larger for more distant events (Figure 5.9(c)). This characteristic is common with phase X_{II}.

The distinct characteristics of phase Y_{BM} are: (1) low frequency content, (2) the amplitude in general is smaller than that of the first arrival, and (3) the apparent velocities are less than the velocities of the first arrival by 0.7 km/s on average. Azimuthal differences between the first arrival and phase Y_{BM} are between -10° and 7° with no clear trend (Figure 5.9(c)).

The phase Y_{BM} is observed more frequently than phase X_{BM}. It is also seen at much closer epicentral distances and from events that occur in the McKinley block, while no events with phase X_{BM} are found from this source area (Figures 5.3 and 5.4).

Array IM. Array IM is located on the northwest side of the subducted slab. The closest distance to the Alaskan WBZ is about 300 km. At array IM we observe two anomalous phases, one arriving with a 1.5-2.5 s delay (herein referred to as X_{IM}) and another with a 7-9 s delay (herein referred to as Y_{IM}) after the first P-wave arrival. Twice as many events are found with the later phase Y_{IM} than with the earlier phase X_{IM}. Examples of the records of these phases are shown in Figure 5.10. A comparison of characteristics between the first arrival and the anomalous phases is presented in Figure 5.11.

The consistent characteristics of phase X_{IM} are: (1) the amplitude is comparable to or larger than the amplitude of the first arrival and (2) the apparent velocities are within 1 km/s of those of the first arrival. In general, apparent velocities of phase X_{IM} are smaller than those of the first arrival for the shallower events, but are larger for the deeper events (Figure 5.11(f)).

The consistent characteristics of phase Y_{IM} are: (1) the amplitude in general is smaller than the amplitude of the first arrival and (2) the apparent velocities are smaller than the velocities of the first arrival by 0.9 km/s on average.

Comparison of the geographic and depth distribution of the events with phases X_{IM} and Y_{IM} shows that at around 59.3°N (location of the Iliamna earthquake cluster) and
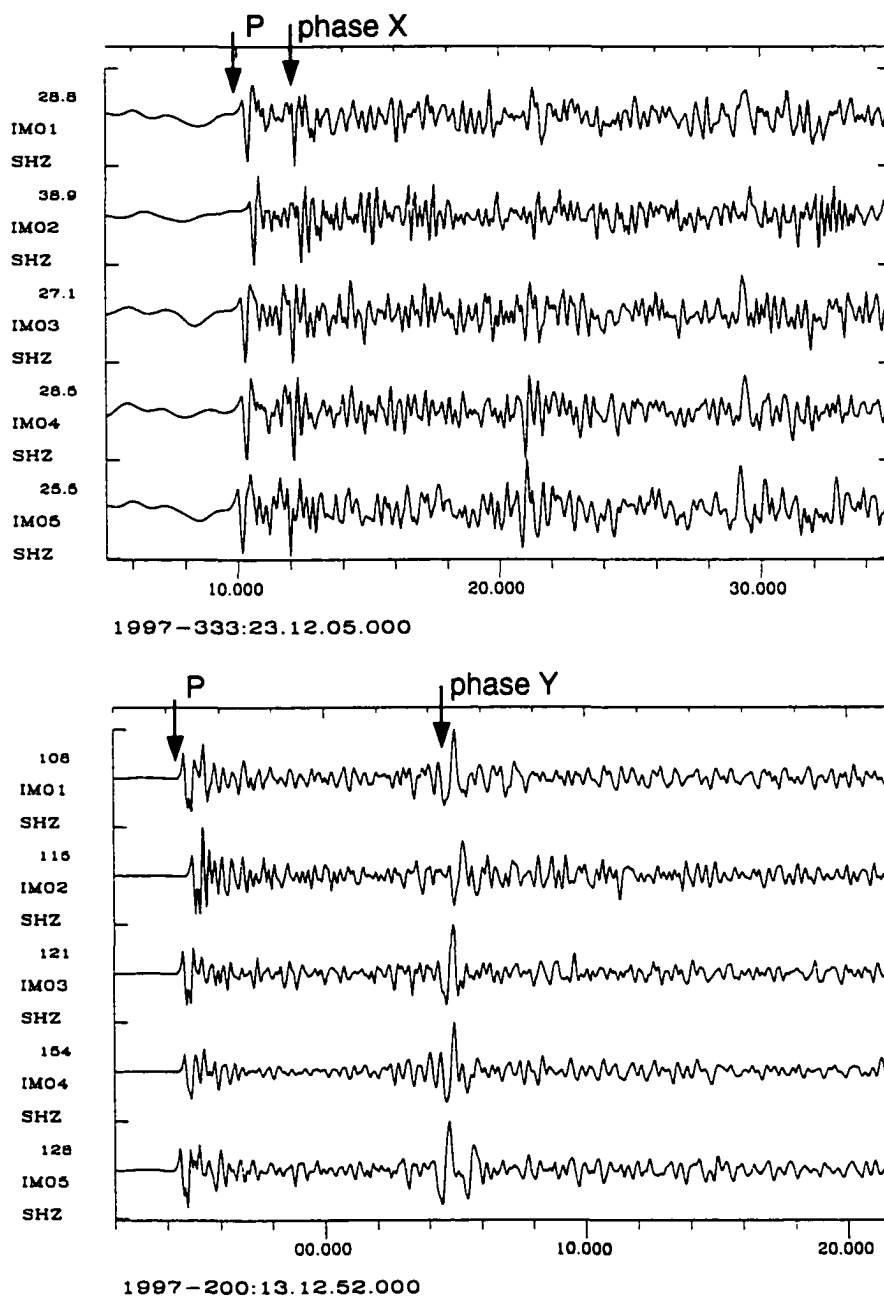
Figure 5.10. Example of the anomalous phases X (upper panel) and Y (lower panel) observed at array IM. Upper panel is a record of M_L 3.2 earthquake that occurred at 61.57 km depth and $4.0°$ epicentral distance. Lower panel is a record of M_L 3.1 earthquake that occurred at 119.50 km depth and $3.0°$ epicentral distance.
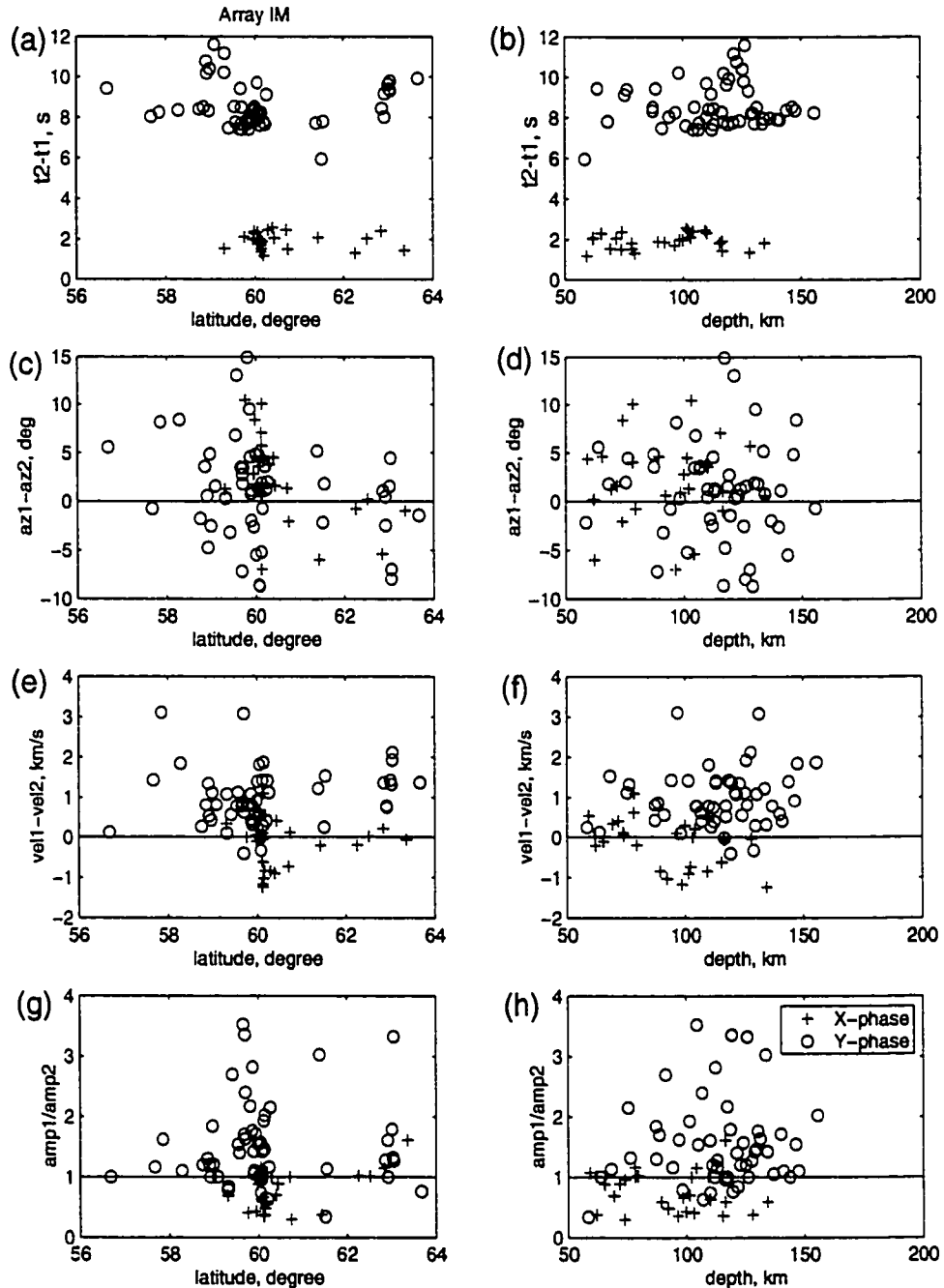
Figure 5.11. Estimated parameters of the anomalous phases X (crosses) and Y (circles) observed at array IM. Differences in traveltimes, back azimuths, apparent velocities, and amplitudes between the first P arrival (t1, az1, vel1, amp1) and phases X or Y (t2, az2, vel2, amp2) versus latitude or depth of the source are shown. Back azimuths and apparent velocities are determined from FK analysis of the array data.

farther south we stop seeing events with phase X_{IM} but continue seeing events with phase Y_{IM} (Figures 5.3 and 5.4). Also, phase X_{IM} is generated in general by shallower earthquakes than phase Y_{IM}.

Array BC. Array BC is located north-east of the surface projection of the northern termination of the Alaskan WBZ and on its up-dip side. At this array, we also observe two anomalous phases arriving between direct P- and S-waves. The earlier phase (herein referred to as X_{BC}) arrives with a 2-3 s delay and the second phase (herein referred to as Y_{BC}) arrives with an 11-12 s delay after the first P-wave arrival. The later arrival Y_{BC} is observed less frequently (6 events) than the earlier arrival X_{BC} (25 events). Examples of these phases are shown in Figure 5.12. Differences between traveltimes, back azimuths, apparent velocities and amplitudes of the first arrival and the anomalous phases are illustrated in Figure 5.13.

The consistent characteristics of phase X_{BC} are: (1) the amplitude is larger than amplitude of the first arrival, and amp(P)/amp(X) is smaller for the shallower or more distant events and (2) the apparent velocities in the majority of the cases are less than those of the first arrival and are within 1 km/s of them. Azimuthal residuals between the first and X_{BC} arrivals are mostly negative, i.e. the back azimuth of the first arrival is less than that of phase X_{BC}. Moreover, events with the most negative azimuthal residuals are located to the north of 62°N parallel, where the strike of the WBZ exhibits a turn (Figure 5.13(c)).

Phase Y_{BC} has the following distinct characteristics: (1) the amplitude in general is a little larger than the amplitude of the first arrival, (2) a low frequency content, and (3) the apparent velocities are slower by 1.4 km/s on average than apparent velocities of the first arrival.

The time delays between the first P-wave arrival and phases X_{BC} and Y_{BC} are larger than those of the analogous phases observed at the three other arrays, which are located to the north and west of the subducted slab.
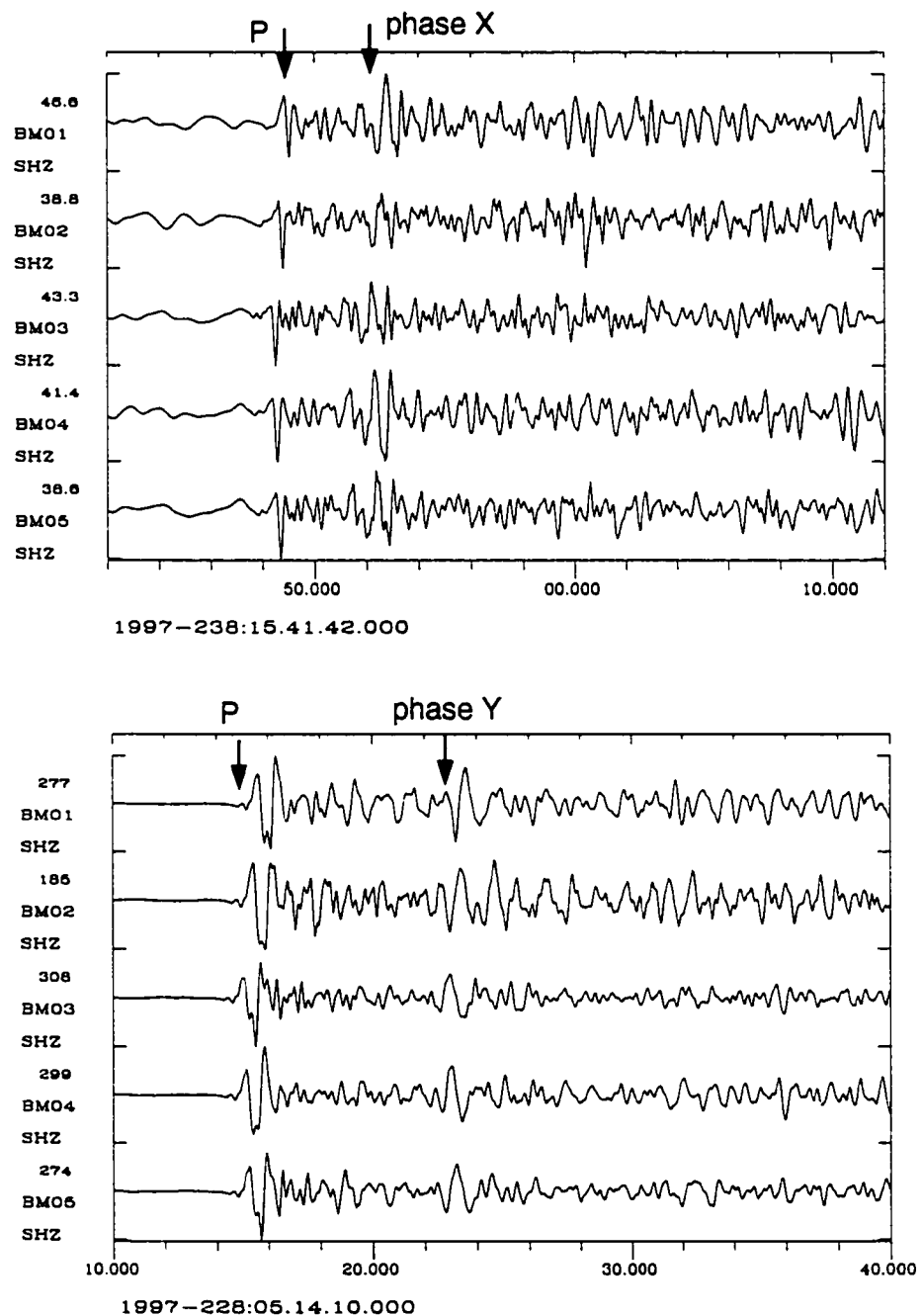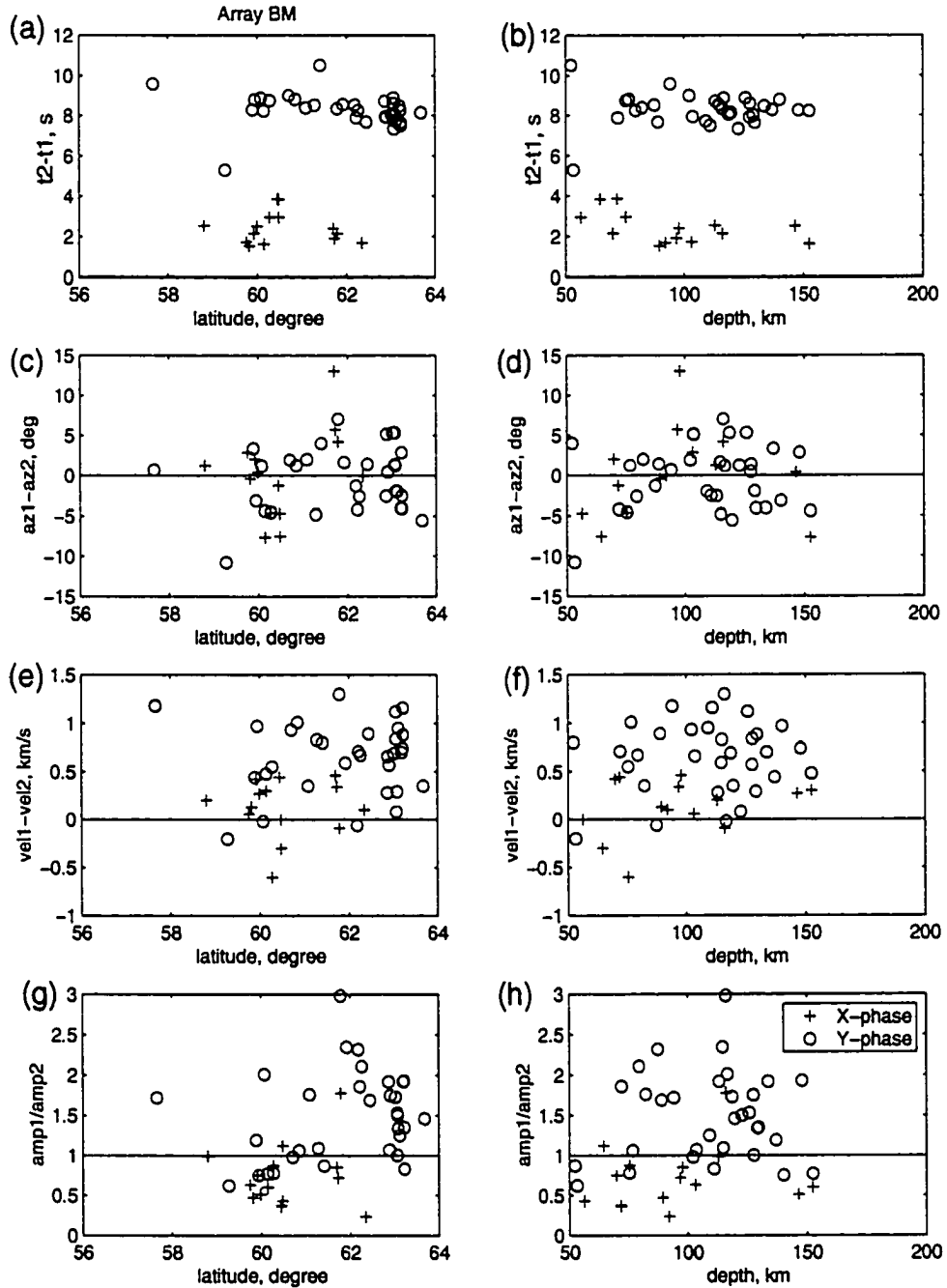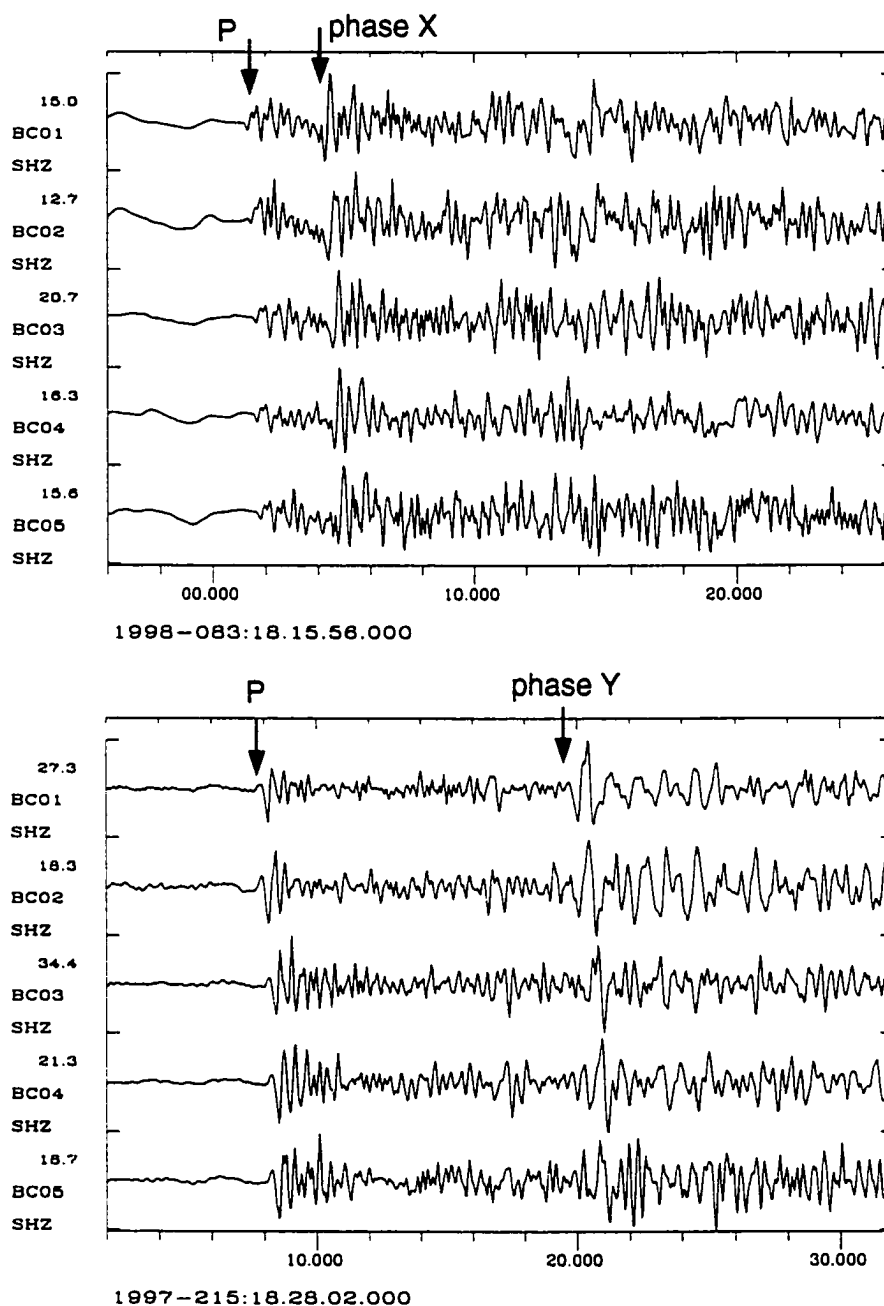
Figure 5.12. Example of the anomalous phases X (upper panel) and Y (lower panel) observed at array BC. Upper panel is a record of M_L 3.0 earthquake that occurred at 117.24 km depth and 4.0° epicentral distance. Lower panel is a record of M_L 3.7 earthquake that occurred at 102.05 km depth and 5.3° epicentral distance.
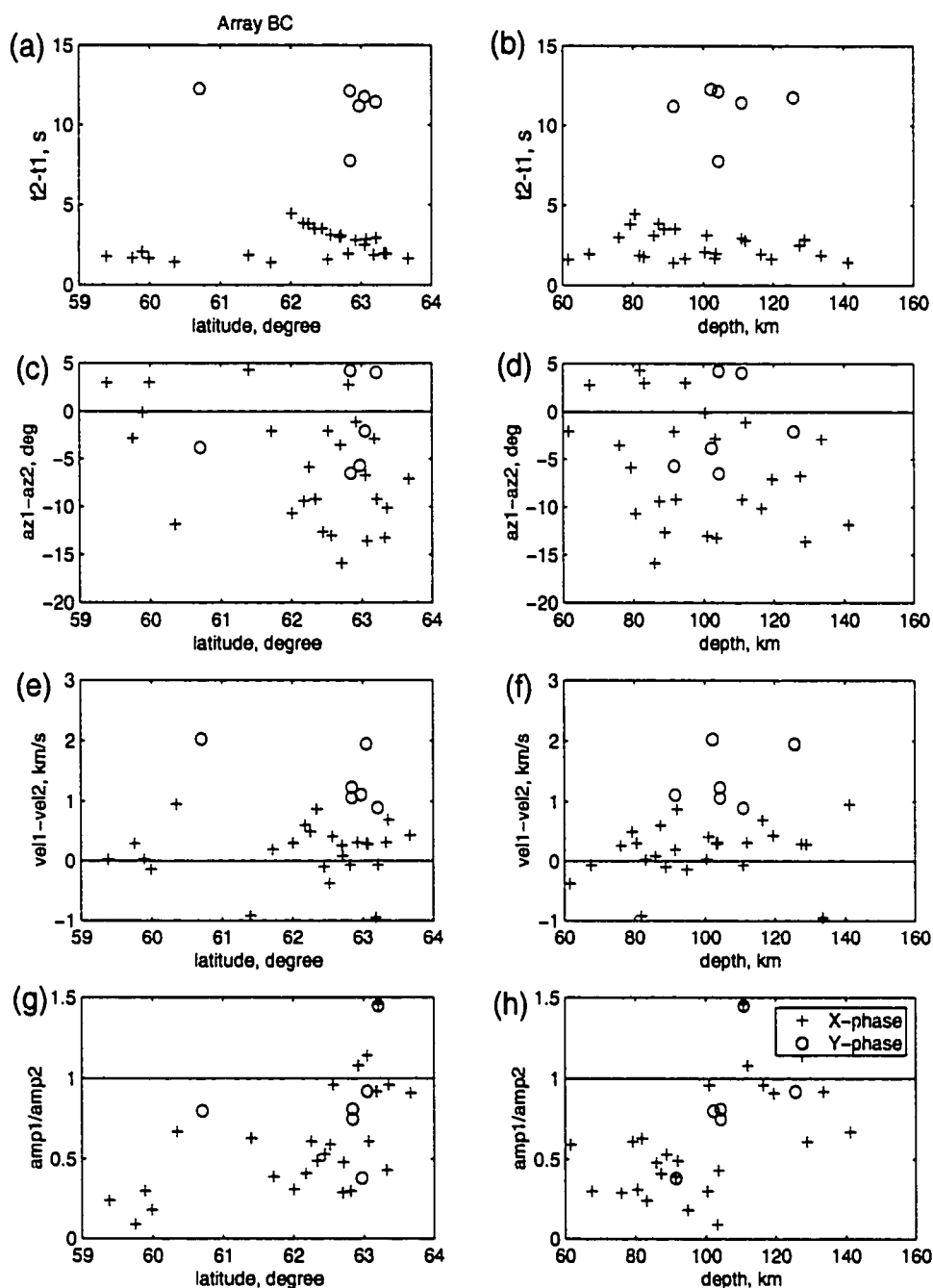
Figure 5.13. Estimated parameters of the anomalous phases X (crosses) and Y (circles) observed at array BC. Differences in traveltimes, back azimuths, apparent velocities, and amplitudes between the first P arrival (t1, az1, vel1, amp1) and phases X or Y (t2, az2, vel2, amp2) versus latitude or depth of the source are shown. Back azimuths and apparent velocities are determined from FK analysis of the array data.
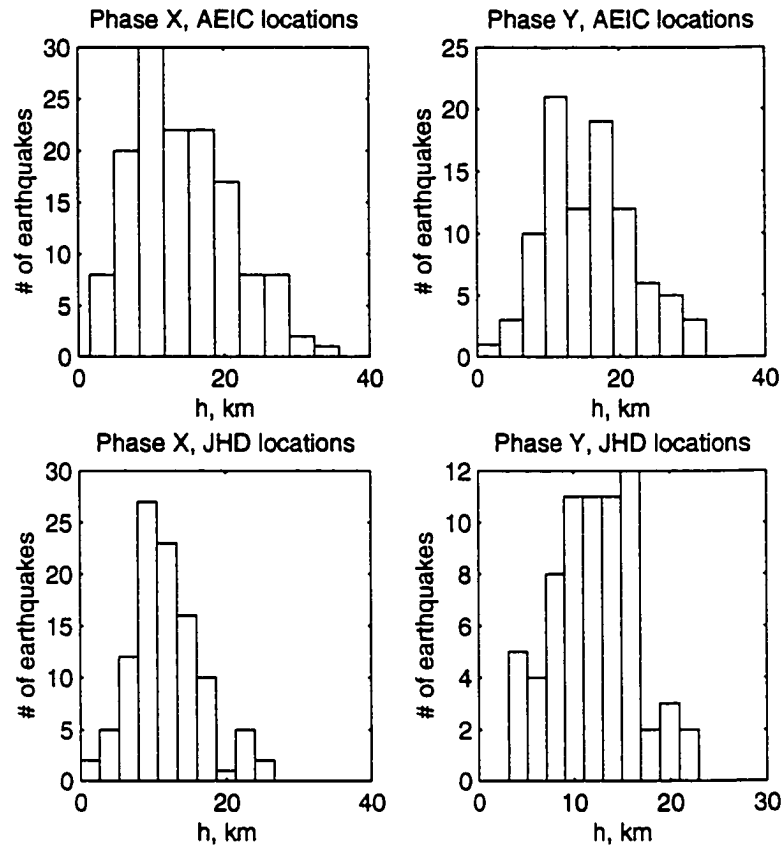
Figure 5.14. Histograms of the normal distance from the source location to the upper surface of the WBZ for all the earthquakes with observed phases X and Y. Two sets of the hypocentral locations are used: the AEIC (Alaska Earthquakes Information Center) catalog and the JHD (joint hypocenter determination) relocated hypocenters.

After identifying anomalous phases and their characteristics, we examined the position of the earthquakes with the observed anomalous phases within the WBZ. We used two different sets of hypocentral locations. One is taken from the Earthquake Catalog produced by the AEIC and the other is the JHD (Joint Hypocenter Determination method) relocated hypocenters (Ratchkovski and Hansen, 2000; see also Chapter 2). It has been shown that the relocated hypocenters provide better relative locations for the earthquakes. In the AEIC catalog, earthquakes with observed anomalous phases are located 13-16 km below the upper surface of the WBZ, ranging between extreme locations of very near the surface of the WBZ and 30 km below it (Figure 5.14). The JHD hypocentral locations are

<div align="center">

Table 5.1: Characteristics of anomalous phase X.

</div>

Array	IL	BM	IM	BC
# of events	72	14	26	25
traveltime delay	0.71-3.43 s mean=1.73 s	1.52-3.86 s mean=2.41 s	1.18-2.57 s mean=1.92 s	1.4-4.43 s mean=2.49 s
latitudinal distribution	56.7-63.7°N	58.8-62.3°N	59.3-63.4°N	59.4-63.7°N
focal depth	51-170 km mean=100 km	56-152 km mean=96 km	59-134 km mean=91 km	62-141 km mean=99 km
distance to upper surface of the WBZ	2-32 km mean=15 km	3-30 km mean=13 km	3-36 km mean=16 km	6-26 km mean=14 km
back azimuth difference with the first arrival	az.diff. becomes increasingly negative with distance; mean(az_P-az_X)=-2.7° (-12.8 to 11.1)	az. diff. changes from positive to negative with distance; mean(az_P-az_X)=0.2° (-7.7 to 13.0)	no clear trend; mean(az_P-az_X)=2.2° (-7 to 10.5)	az. diff. is predominantly negative; mean(az_P-az_X)=-6° (-15.9 to 4.3)

apparent velocity (km/s)	v_P<=v_X;
	
	mean(v_P)=8.09;
	mean(v_X)=8.65;
	mean(v_P-v_X)=-0.56
		v_P>=v_X;
		
		mean(v_P)=7.98;
		mean(v_X)=7.86;
		mean(v_P-v_X)=0.12
			trend changes from v_P>=v_X to v_P<=v_X with depth;
			mean(v_P)=9.79;
			mean(v_X)=9.92;
			mean(v_P-v_X)=-0.14
				v_P>=v_X;
				
				mean(v_P)=8.28;
				mean(v_X)=8.11;
				mean(v_P-v_X)=0.17

amplitude	amp(P)<=amp(X)	amp(P)<=amp(X)	amp(P)<=amp(X)	amp(P)<=amp(X)

better constrained, placing the hypocenters 11-14 km on average below the upper surface of the WBZ. However, for some of the earthquakes JHD locations are not available. Thus we can conclude, that the earthquakes with the observed anomalous phases tend to be located in the middle of the seismic zone.

Earthquakes with both X and Y phases are rare. More earthquakes with phase X are observed at shallower depths, while at deeper depths earthquakes with phase Y are more common. This is especially true for the region beneath the central Cook Inlet.

In summary, at all four arrays we observe two anomalous phases arriving with 1-3 s (phase X) and 7-12 s (phase Y) delays after the first P-wave. Characteristics of the identified anomalous phases are summarized in Tables 5.1 and 5.2. The locations of earthquakes with the observed phases are shown in Figures 5.3 and 5.4. The apparent velocities of all identified arrivals are summarized in Figure 5.15.

Table 5.2: Characteristics of anomalous phase Y.

Array	IL	BM	IM	BC
# of events	3	32	51	6
traveltime delay	8.31-8.84 s mean=8.51 s	5.29-10.52 s mean=8.30 s	5.95-11.61 s mean=8.58 s	7.76-12.29 s mean=11.11 s
latitudinal distribution	62.2-62.3°N	57.7-63.7°N	56.7-63.7°N	60.7-63.2°N
focal depth	79-92 km mean=86 km	52-152 km mean=108 km	58-155 km mean=114 km	92-126 km mean=106 km
distance to upper surface of WBZ	6-17 km mean=11 km	6-27 km mean=15 km	0-32 km mean=16 km	8-27 km mean=15 km
back azimuth difference with the first arrival	no trend; mean(az_P-az_Y)=0.7° (-3.2 to 5.6)	no trend; mean(az_P-az_Y)=-0.1° (-5.57 to 7.05)	az.diff. changes from negative to positive with distance; mean(az_P-az_Y)=1.0° (-8.69 to 14.95)	no trend; mean(az_P-az_Y)=-2.8° (-6.5 to 4.06)

apparent velocity (km/s)	v_P>v_Y;
	mean(v_P)=7.89;
	mean(v_Y)=7.48;
	mean(v_P-v_Y)=0.42
		v_P>v_Y;
		mean(v_P)=8.05;
		mean(v_Y)=7.38;
		mean(v_P-v_Y)=0.68
			v_P>v_Y;
			mean(v_P)=10.22,
			mean(v_Y)=9.27;
			mean(v_P-v_Y)=0.97
				v_P>v_Y;
				mean(v_P)=8.11;
				mean(v_Y)=6.68;
				mean(v_P-v_Y)=1.44

amplitude and frequency	amp(P)>=amp(Y)	amp(P)>=amp(Y) lower frequencies	amp(P)>=amp(Y)	amp(P)<=amp(Y) lower frequencies

The distinct characteristics of phase X are:

(1) a P-wave sense of the particle motion,

(2) in the majority of the records, the amplitude is larger than that of the first arrival,

(3) the apparent velocity is within 1 km/s of that of the first arrival, and

(4) for each array, the X-P time is almost constant, regardless of the location of the event; the X-P time is larger for array BC located to the northeast of the subducted slab.

Phase Y has the following characteristics:

(1) the amplitude is less than the amplitude of the first P-wave or comparable to it,

(2) the apparent velocity is slower than that of the first P-wave by up to 2 km/s,

(3) it has a low frequency content,

(4) the particle motion is predominantly longitudinal rather than transverse, and

(5) at each of the four arrays, the Y-P time is practically constant; the Y-P times are larger at array located to the northeast of the subducted slab.

Earthquakes with the observed secondary phases are located 13-16 km below the upper surface of the WBZ on average.
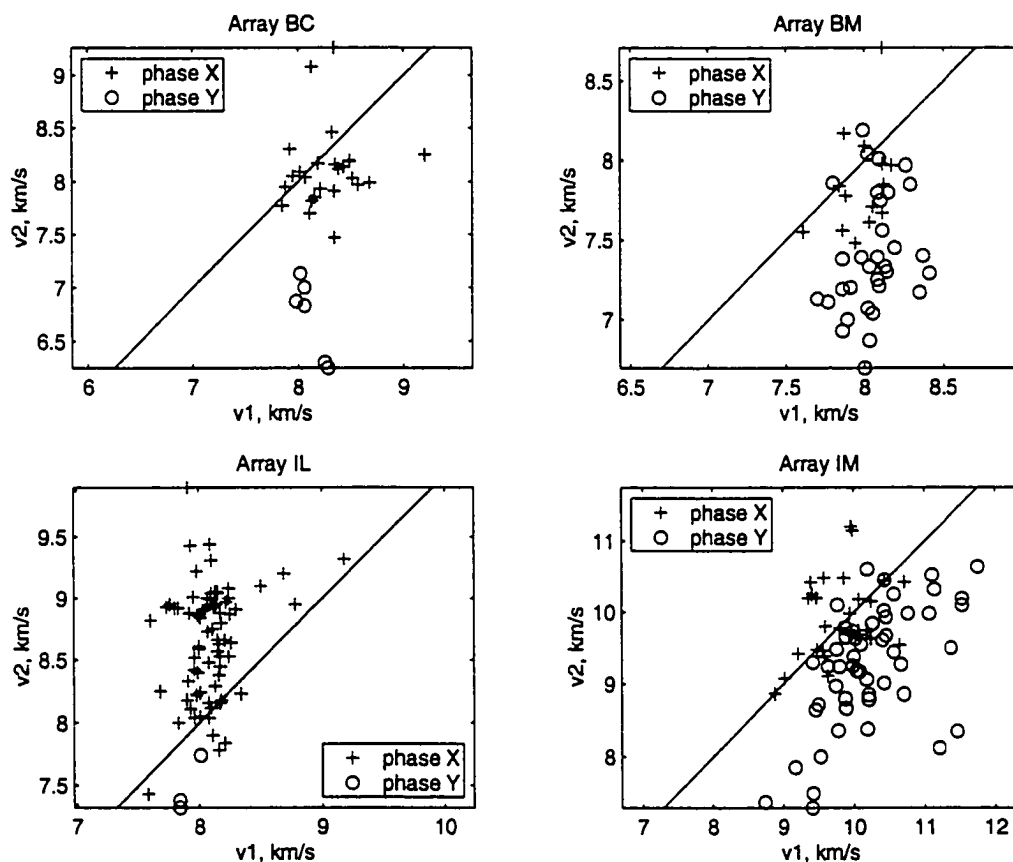
Figure 5.15. Apparent velocities of the anomalous phases X (crosses) and Y (circles) versus apparent velocities of the corresponding first arrivals as estimated from FK analysis.

One may think that additional constraints on the nature of the observed secondary phases can be obtained if we check the relative polarity of the direct and secondary phases. Given short-period vertical recordings, this is nearly impossible to do, however, because the onset of the secondary phases is hard to identify. In addition, well constrained focal mechanisms are available for only a handful of the earthquakes. We made an attempt to

measure S-X and S-Y times. This was impossible to do due to the fact that three of the four arrays have only vertical component sensors.

Based on the apparent velocities, particle motions and frequency content we interpret the X arrival to be a P-wave and the Y arrival to be an SV-wave.

5.4. INTERPRETATION AND DISCUSSION.

There are several possible explanations for the occurrence of the observed anomalous phases:

(1) conversion or refraction at crustal discontinuities beneath or near the receiver;

(2) conversion, reflection, refraction or diffraction at the upper, lower surfaces or at interior interfaces of the subducted slab;

(3) dispersion, or other wave-guide effect, of the inhomogeneous slab (phase X only).

We used a three-dimensional ray tracing algorithm (Lee and Stewart, 1981) to calculate traveltimes and propagation paths of the direct P- and S-waves, P-to-S and S-to-P converted waves at the upper and lower surfaces of the slab, and P-to-S and S-to-P converted waves at the Moho discontinuity. This ray tracing algorithm utilizes a ray shooting approach. The reference velocity model for the crust and upper mantle was adopted from Morelli and Dziewonski (1993), which is a modified version of the IASP91 velocity model. The Conrad and Moho discontinuities are placed at 15 and 40 km depth, respectively. The slab geometry is constrained using seismicity in the WBZ for the past 10 years as cataloged by the AEIC. Based on the tomographic study of P-wave velocity in Alaska of Zhao et al. (1995), the slab thickness is set to 50 km; the velocity contrast at the upper surface of the slab with respect to the mantle is 6%. The velocity inside the slab decreases towards the lower surface of the slab.

There is an uncertainty in the slab geometry in the north-eastern portion of the Alaska subduction zone between 62°N and 63°N. The subducted slab is believed to be discontinuous in that area (Ratchkovski and Hansen, 2000; Chapter 2). Also, there are few constraints on the geometry of the Wrangell subducted slab and its relation to the Alaskan slab. This area is important for modeling incoming ray paths to array BC, which is located

up-dip of the Alaska and down-dip of the Wrangell subduction zone. For the purpose of simplification, the subducted slab is represented as a continuous structure throughout that region and the Wrangell slab is not included in the model at all.

Rays are traced from equally spaced source locations between the 58°N and 64°N parallels. Each source location is represented by four hypocenters positioned 10, 20, 30, and 40 km below the 6% velocity contrast, which in our model represents the upper surface of the subducted slab. In addition to four receivers corresponding to the array locations, we placed additional receivers between each array and the slab, which do not represent locations of the real seismic stations but allow us to investigate the models in more detail.

Unfortunately, the three-dimensional ray tracing method we used is not well suited for models with strong velocity gradients, such as those produced by S-to-P and P-to-S conversions at the slab/mantle interface. In some difficult cases we did not succeed in hitting a target receiver with a high enough accuracy. Therefore, while we are able to compare ray paths of different phases, the calculated traveltimes are not reliable for testing different velocity structure models. This is especially true for modeling P-to-S converted rays at the slab interfaces.

Results of the ray tracing show that the direct P-wave closely follows the great circle path. For arrays IL and BM, the ray refracts up-dip into the high velocity slab near the source, propagates inside the slab along its strike and exits it after the strike bend, in the middle of the McKinley block (Figure 5.16(a)). The deeper the source is located beneath the upper surface of the slab, the longer the ray stays inside the slab.

First, we consider dispersion as a possible cause of phase X. In order to observe dispersion, or waveguide effects of the slab on body waves, a wavetrain should travel a relatively long path along the channel structure. Therefore, we can consider the waveguide effect of the slab as a possible cause of phase X only for arrays IL and BM, which are located on continuation of the slab strike. Abers and Sarker (1996) examined P waveforms for Alaska slab events deeper than 100 km recorded at the Global Seismic Network station COLA, located 50 km to the north-west of array IL. For events with a long slab path, they
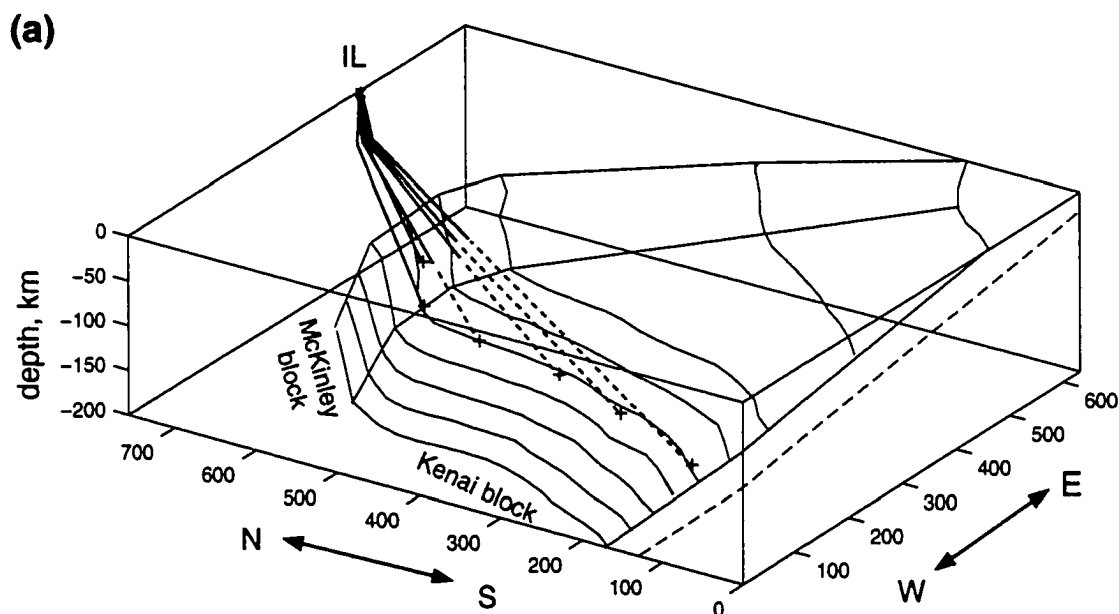
Figure 5.16. Schematic representation of the ray tracing results. Shown is the geometry of the subducting plate as used in the three-dimensional ray tracing modeling. Depth contours of the leading edge of the WBZ are drawn with 25 km intervals, the deepest contour is at 200 km depth. Thin dashed lines is location of the lower surface of the slab for 50-km-thick plate. X- and Y-axis indicate distance in WE and SN direction, respectively, measured in kilometers from 58°N 155°W origin.

(a) Direct P-wave ray paths from representative source locations to array IL are shown. Dashed and solid lines correspond to the ray segments inside and outside the slab, respectively. Rays from the sources located in the Kenai block propagate inside the slab for considerable time and exit it through the upper surface of the plate in the McKinley block. Rays from the sources located in McKinley block do not have essential "slab" components in the path.

found 0.5-1.5 s delays between the low-frequency energy and high-frequency energy. Indeed, at array BM we observe phase X only from events that originate south of 62°N and therefore have a relatively long slab path. However, at array IL, we also observe phase X in the records of earthquakes that do not have an essential slab component in their travelpath (Figure 5.3). In addition, at both arrays traveltime delays between phase X and the first arrival are on average larger, than those reported by Abers and Sarker. The higher apparent velocity of phase X at array IL contradicts the waveguide explanation, since we would expect the later phase to travel through a low-velocity layer and to have a slower

velocity than the first arrival. The high amplitude of phase X is also difficult to explain by the dispersion phenomenon. In addition, it has been observed in Japan (Hori et al., 1985; Oda et al., 1990), that the earthquakes with dispersed first arrivals originate in the low-velocity layer near the top of the slab and the dispersion is observed only at the stations, where a contact between the overriding and subducting plates is present. In our case, earthquakes with phase X are located on average 13-15 km beneath the upper surface of the WBZ. If there is a low-velocity layer at the top of the subducted slab in southern and central Alaska, then most of the earthquakes with phase X are not located in it. Therefore, we think that phase X mush have a different origin than the dispersion phenomenon reported by Abers and Sarker (1996).

An alternative possible explanation for phase X at arrays IL and BM is that the first arrival represents a wave diffracted at the leading slab/mantle interface while phase X is the direct P-wave. This phenomenon has been observed in the Tonga and Kermadec subduction zones (Smith et al., 1994; van der Hilst and Snieder, 1996). This explanation would be consistent with the low amplitude of the first arrival. However in this case, we would expect the direct P-wave represented by phase X to have a back azimuth close to the back azimuth of the epicentral location of the earthquake. However, at array IL, the back azimuth of phase X is less consistent with the AEIC epicentral locations than the back azimuth of the first arrival (Figure 5.2). Therefore, the data support the suggestion that the first arrival is indeed the direct P-wave, while phase X is an anomalous arrival caused by three-dimensional inhomogeneities of the subsurface structure. In addition, the wave-field modeling results of van der Hilst and Snieder (1996) showed that the diffracted wave can be explained as propagating in a thin high-velocity layer (HVL) and does not survive interruptions or strong lateral variations of the HVL. As we mentioned before, there is a strong indication that the subducted slab beneath central Alaska is discontinuous. Moreover, the study of Abers and Sarker (1996) indicates that a low-velocity layer is present in the slab beneath Alaska, rather than a high-velocity layer. Therefore, phase X observed at arrays IL and BM can not be a diffracted wave in the slab.

If we assume that phase X is a PP-wave reflected off the upper surface of the subducted slab or other interior interface, we should expect it to have a lower amplitude than the direct P-wave. However, this is not the case. Therefore, we can reject P-wave reflections at the slab interfaces as a likely cause of phase X at all four arrays.

The small traveltime delays of phase X suggest that it may be a refracted P-wave. P-waves refracted at the bottom or top surfaces of the subducted slab or interior interfaces are quite difficult to trace in practice and their existence strongly depends on details of the velocity model and the position of the source. In Vanuatu arc, Chiu et al. (1985) observed small amplitude first arrivals and an impulsive secondary arrivals 2-3 s later. They interpreted the first arrival to be a P-wave refracting into the deeper portion of the slab and traveling with a higher velocity, while the second P-wave was traveling through the outer (upper) portion of the slab. For this to be possible, the earthquake source must be located in an upper layer of lower velocity above the central zone of the highest velocities. An earthquake within the high-velocity zone would probably not produce two refracted arrivals. In our case, however, earthquakes that generate phase X are located in the high-velocity core of the slab. Therefore, we reject refractions in the slab as a cause of phase X.

The observed anomalous phases may be generated by crustal inhomogeneities. The ray tracing results show that the P-to-S converted waves at the Moho discontinuity arrive 5.5-6.5 s after the direct P-waves. This time delay is considerably lower than the observed time delay of phase Y at any of the four arrays. P-to-S conversion at the Conrad discontinuity, or other crustal interfaces, would have even smaller time delays. S-to-P waves converted at the Moho would arrive around 7 s before the direct S-wave. Next, we expect P-waves refracted or reflected near the receiver to have a smaller amplitudes than the direct P-wave. On the contrary, phase X is characterized by larger amplitudes than the first P-wave arrival. The long time delays of phase Y makes it an unlikely candidate for a near-receiver origin. Therefore, we think near-receiver reflections and conversions are not the cause of the observed secondary arrivals.

Therefore, the last possible cause of phases X and Y remains, which is conversions at the slab interfaces. Waves converted from P to S and from S to P near the top of the sub-

ducting slab have been observed in Japan (Matsuzawa et al., 1986, 1990; Iidaka et al., 1990), in New Hebrides (Chiu et al., 1985), in the Tonga-Kermadec arc (Mitronovas and Isacs, 1971), and in the Eastern Aleutian arc (Helffrich and Abers, 1997). These conversions would require a strong velocity contrast within a relatively narrow layer at the boundary between the subducted slab and the overlying mantle wedge. According to tomographic studies of the Alaska-Aleutian subduction zone (Zhao et al., 1995), the velocity in the slab is 3-6% higher than that in the surrounding mantle. How sharp the boundary is, however, is not clear.
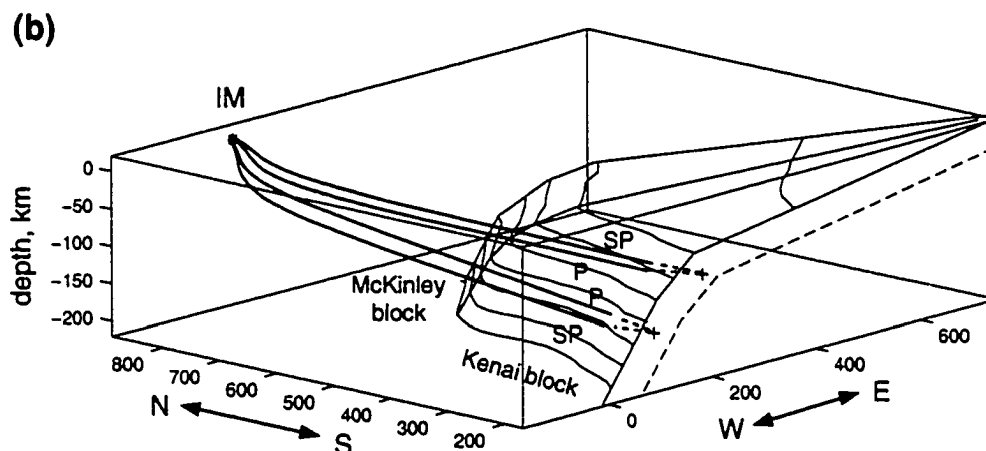
Figure 5.16. (b) Ray paths of the direct P and converted S-to-P waves from two sources to array IM are shown. The sources are located in the Iliamna cluster. Dashed and solid lines correspond to the ray segments inside and outside the slab, respectively. For deeper sources, the S-to-P converted wave has a steeper angle of emergence beneath the receiver than the direct P-wave, while for shallower source the direct P-wave comes to the receiver with a steeper angle of emergence than the S-to-P converted wave.

Ray tracing results for S-to-P converted waves at the top of the high velocity slab are schematically shown in Figure 5.16(b-c). Modeled S-to-P converted waves at arrays BM, IL and IM arrive 0.2-3 s after the direct P-wave, delays are larger for sources located deeper below the slab/mantle interface. The main factors controlling the propagation path in this case are the distance and azimuth to the receiver, the dip of the slab (or dip of the conversion interface), and the position of a hypocenter inside the high-velocity slab. For

the sources located below 100 km and receivers located on a continuation of the strike or down-dip of the slab, ray paths of the S-to-P converted waves deflect deeper near the source, then exit the slab and propagate through the mantle wedge above the slab. This path results in a steeper angle of emergence of the incoming converted wave beneath the receiver locations. Ray tracing results also show that the difference in the angle of emergence between the direct P-wave and the S-to-P converted wave is greater for larger epicentral distances and deeper sources. This is confirmed by the observations at array IL, where differences between the apparent velocities of the first arrival and phase X are greater for the deeper or more distant earthquakes (Figure 5.6(e-f)). Ray paths of S-to-P converted waves from shallower sources (above 100 km) deflect into the outer part of the slab above the source and enter the lower crust soon after exiting the slab. Therefore, S-to-P converted rays from shallower sources have a smaller angle of incidence and have a longer portion of the path in the crust than the direct P-waves. This results in a lower apparent velocity of the converted wave generated by the shallower earthquakes compared to that of the direct P-wave. The dependence of the apparent velocity on the depth of the source is most clearly observed at array IM where apparent velocities of phase X for deeper earthquakes are larger that those of the first arrival, while for shallower earthquakes velocities of phase X are smaller that those of the first arrival (Figure 5.11(f)).

Comparison of the back azimuths of the direct arrival and phase X at arrays located on the continuation of the slab strike indicate that there is a systematic dependence between the azimuthal difference and location of the source along the WBZ strike (Figures 5.6(c) and 5.9(c)). The back azimuth of phase X is in general smaller than the azimuth of the direct arrival for earthquakes located in the McKinley block. The phase X back azimuth becomes larger than the azimuth of the first arrival for more distant sources, especially those located in the Iliamna cluster. The WBZ strike change plays a major role in this factor. The ray tracing results for array IL suggest that the point of S-to-P conversion for sources in the McKinley block tends to be located eastward of the direct P-wave path, while for the sources located in the Iliamna cluster, the conversion point can be located westward of the direct path. This is illustrated in Figure 5.16(c). Therefore, the ray tracing

results for S-to-P converted waves at the upper surface of the slab correlate well with the observations of differences in apparent velocities and back azimuths between the first P-wave arrival and phase X at arrays BM, IL and IM.
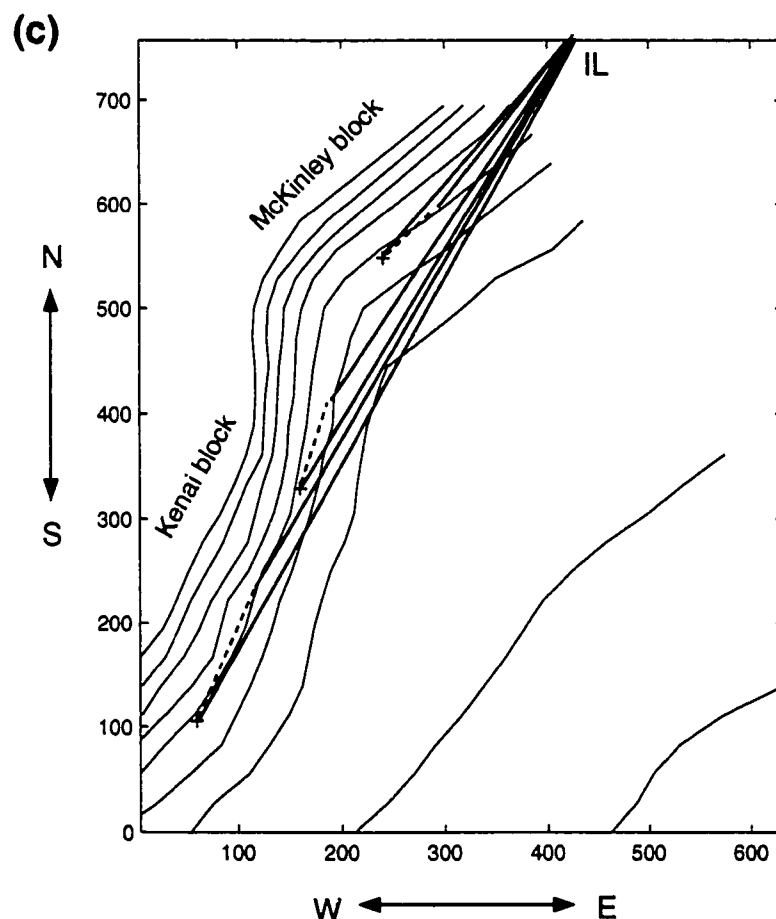
Figure 5.16. (c) Ray paths of the direct P and converted S-to-P waves from three sources to array IL are shown. Direct P-waves are shown by solid lines. Converted rays are shown by dashed (travels as S-wave) and solid (travels as P-wave) lines. For sources located in the McKinley block, the conversion point tends to be located eastward of the direct ray path. For more distant sources the conversion point tends to be located westward of the direct ray path.

Next, we consider the possible causes of phase Y which is most commonly observed at arrays BM and IM, not so frequently at array BC, and very rarely at array IL. Time delays of these phases are within the range of P-to-S conversion phases observed elsewhere in the subduction zones (Mitronovas and Isacs, 1971; Matsuzawa et al., 1986;

Helffrich and Abers, 1997). In addition, this phase has much slower apparent velocity than the first arrival (up to 2 km/s slower) and low frequency content. Our ray tracing results for P-to-S converted waves at the top of the high-velocity slab are least successful of all. We could not obtain a reliable estimate of the time delay of this converted wave with respect to the direct P-wave. Two-dimensional ray tracing results of Helffrich and Abers (1997) show that for a slab model without a low-velocity layer at the top, the P-to-S converted waves have a constant delay (approximately 8 s) with respect to the direct P-wave for epicentral distances greater than 150 km (Figure 7 of Helffrich and Abers (1997)). Based on the fact that we eliminated all other possibilities for the causes of phase Y and that its characteristics are similar to the P-to-S converted waves observed elsewhere in the world, we interpret phase Y observed at arrays BM, IL and IM to be a P-to-S converted wave at the top of the subducted slab.

Array BC is the only one located to the east of the subducted Alaskan slab. In addition, it is located north of the Wrangell subduction zone. Both phases X_{BC} and Y_{BC} have longer time delays with respect to the first arrival than the analogous phases observed at the three other arrays. Due to uncertainty in the relationship between the Alaska and Wrangell slabs in the region between 62°N and 63°N, as well as the geometry of the Wrangell WBZ itself, we can only speculate on how rays propagate through this region. If the Wrangell and Alaska slabs are discontinuous in that area, then the ray paths from the earthquakes located as far as the Iliamna cluster would avoid interaction with the Wrangell slab and propagate through the mantle beneath the subducted Pacific plate until they enter the crust beneath the array. However, if the Wrangell slab extends below 100 km or is connected to the Alaska slab below 50 km depth, then the ray paths would encounter this high velocity anomaly before entering the crust beneath the station. In my opinion however, the Alaska and Wrangell slabs are not connected in the area between 62°N and 63°N. In this case, as the ray tracing results show, the ray paths from the Alaska subduction zone earthquakes exit the high velocity slab through its lower boundary, propagate in the mantle beneath the Pacific plate without interaction with the Wrangell slab, and then enter the crust beneath the array location (Figure 5.16(d)). This ray path geometry would allow the

possibility of converted waves to be generated at the lower boundary of the subducted Pacific plate as the ray exits behind the source.
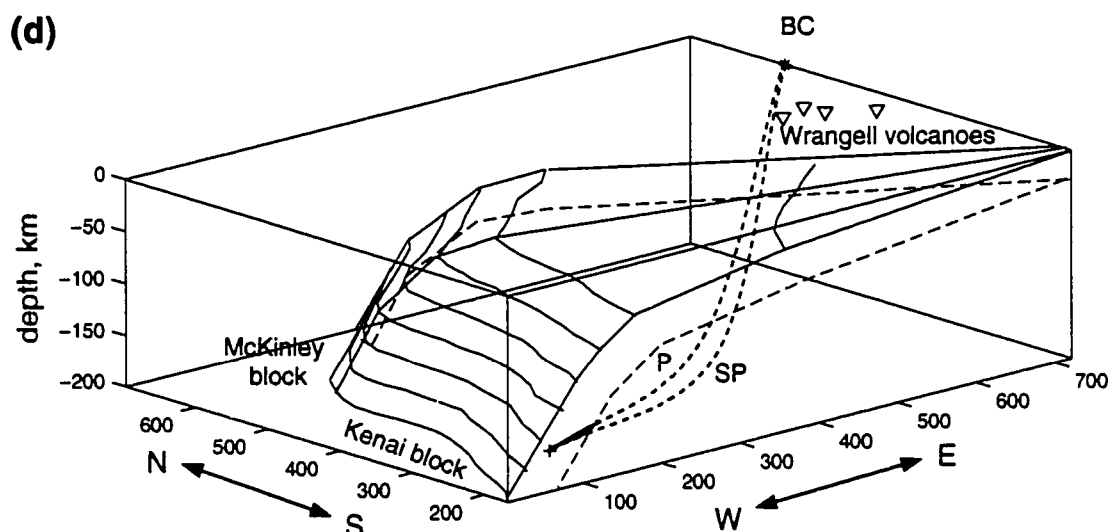
Figure 5.16. (d) Direct P and S-to-P converted wave travelpaths from the source located beneath Iliamna volcano to array BC are shown. Solid and dashed lines correspond to the ray segments inside and outside the slab, respectively. Wrangell volcanoes approximately mark surface projection of 100 km depth contour of the Wrangell subduction zone.

Nakamura et al. (1992) observed anomalous arrivals from earthquakes in the Izu slab 13 s after the direct P-wave. They interpreted them to be P-to-S conversions from a boundary below the source. Suyehiro and Sacks (1979) suggested the possibility of a reflection off the bottom of the slab to explain anomalous phases observed in the Honshu region of Japan. These observations provide evidence for the existence of a sharp lower boundary of the slab. Since we know little about the location of the lower boundary of the Alaska slab and the velocity contrast across it, we can not draw definite conclusions from the results of the ray tracing with regards to the observations at array BC. S-to-P converted waves at the lower boundary of the high-velocity slab with a 3% velocity contrast across it are delayed 3-4 s with respect to the direct P-wave. These delays are in the range of the observed traveltime delays of phase X_{BC}. The apparent velocity of phase X_{BC} is within 1 km/s of the first arrival, and the velocity of phase Y_{BC} is slower by up to 2 km/s than that

of the first P arrival. Therefore, the characteristics of phases X_{BC} and Y_{BC} are consistent with those produced by S-to-P and P-to-S converted waves across the lower boundary of the slab.

In summary, we interpret the secondary phases X and Y observed at arrays BM, IL and IM to be S-to-P and P-to-S converted phases at the top of the slab, respectively. Phases X and Y observed at array BC are most likely S-to-P and P-to-S converted waves at the bottom of the subducted slab.

5.5. CONCLUSIONS AND SUGGESTIONS FOR FUTURE RESEARCH.

The purpose of this study was to search for, and identify, anomalous phases in the seismic array recordings of the Alaskan subduction zone earthquakes. After analyzing data from July, 1997 to March, 1998, we identified two secondary phases arriving with 1-3 s and 7-12 s delays after the direct P-wave. We analyzed the apparent velocities, back azimuths, time delays, and amplitude ratios of the observed secondary phases and direct arrivals as well as locations of the earthquakes with the observed anomalous phases. We used three-dimensional ray tracing to calculate travelpaths and traveltimes of different arrivals. Based on this analysis, we interpret the phases with 1-3 s and 8-9 s delays observed at the arrays located on a continuation of the strike and down-dip of the slab to be S-to-P and P-to-S conversions at the upper surface of the slab, respectively. We interpret the phases with 2-4 s and 11-12 s delays observed at the array located to the north-east of the subducted slab to be S-to-P and P-to-S converted waves at the lower boundary of the Pacific plate.

Converted phases have a great potential for providing direct information on the structure of the subduction zone. Use of P-PS or S-SP times is an effective way of locating the boundaries of the subducted slab since the use of converted waves is not sensitive to the hypocenter locations (Matsuzawa et al., 1986, 1990). A systematic collection of high-resolution data (e.g., three-component digital data) from intermediate depth earthquakes recorded at several stations at various azimuths in Alaska is highly recommended for

future studies in this direction. It would provide an opportunity for a more complete polarization and frequency analysis of the observed anomalous slab phases. A better three-dimensional ray tracing algorithm and waveform modeling should also be used in addressing the question of the origin of the observed anomalous slab phases in Alaska in the future.

Appendix A. Joint Hypocenter Determination method.

Determination of hypocentral locations of local earthquakes recorded by a local network relies in most cases on the use of a flat-layer velocity model. Because the Earth is more complicated than this simple model, its use introduces unavoidable errors in the process of earthquake location. These errors are a combination of deviations from the model near the hypocenter, near the station and along the path from the source to the station. With a single earthquake it is impossible to discriminate between these effects. One way to solve this problem is to perform a three-dimensional simultaneous inversion of earthquake location and velocities. This approach, however, is difficult due to some limiting factors, such as data quality and excessive computer time. There is, however, a simpler way to look at the problem. Assuming a cluster of earthquakes. In this case, for each earthquake-station pair, the effect of model deviations near the hypocenter will be nearly the same, so that they can be ignored. The other two effects can be lumped together into a single effect, which may be termed "station correction".

The joint determination of hypocentral parameters and station corrections was originally proposed by Douglas (1967). The problem was solved by using a least-squares method. A major disadvantage of this technique was that for a large number of earthquakes the size of the matrices involved was very large. This problem was overcome by Herrmann et al. (1981), who simplified the normal equations in such a way that the problem was reduced to the solution of one 4x4 system for each earthquake, plus the solution of a system of equations for the station corrections. However, since the joint determination of hypocenters and station corrections is nonunique because of the trade-off between origin times and station corrections, and additional constraint has to be imposed. This is done by using a well-located event, known as a "master event", which remains fixed during the inversion procedure. Alternatively, one of the station corrections can be set to some fixed

value, say zero. One difficulty with the least-squares method is that the condition number of the original system of linearized equations is squared when forming the normal equations, and numerical errors may result when the condition number is large. An alternative solution to the joint determination of hypocenters and station corrections that does not make use of the normal equations was proposed by Pavlis and Booker (1983). Their method relies on the orthogonality of the matrices that enter into the singular value decomposition of a given matrix.

The method of Pavlis and Booker was later utilized by Pujol (1988) to locate regional earthquakes using local networks. This method is summarized below and follows the presentation in Pujol (1988). Let us consider the problem of determining N station corrections and the hypocenters of M earthquakes recorded by all of the stations. For the jth earthquake and the ith station, we have:

$$r_{ij} = dT_j + \frac{\partial t}{\partial x}dx_j + \frac{\partial t}{\partial y}dy_j + \frac{\partial t}{\partial z}dz_j + ds_i \; ; \; i = 1, N; j = 1, M \tag{A1}$$

where:

$$r_{ij} = t_{ij}^{\,0} - t_{ij} = t_{ij}^{\,0} - (T_j + \tau_{ij} + s_i) \quad .$$

$t_{ij}^{\,0}$ is the observed arrival time, t_{ij} is the computed arrival time, T_j and (x_j, y_j, z_j) are the initial estimates of origin time and hypocenter coordinates, τ_{ij} is the computed travel time, and s_i is the station correction. In matrix form, we can write equation (A1) as

$$\vec{r}_j = A_j d\vec{X}_j + S_j d\vec{s} \; ; j = 1, M \tag{A2}$$

where $\vec{r}_j$ contains the residuals r_{ij}, A_j is an Nx4 matrix of derivatives, $d\vec{X}_j$ is the vector of origin time and hypocenter adjustments, S_j is an NxN diagonal matrix with ones for the stations that recorded the earthquake and zeros otherwise, and $d\vec{s}$ is the vector of adjustments to the s_i's. Equation (A2) clearly shows that the earthquakes are coupled to each other only through the station corrections. The system implied by equation (A2) can be

written as a single matrix equation. This new equation can be solved by forming the normal equations and simplifying them in the following way. Let us write the singular valued decomposition of A_j as

$$A_j = U_j \Lambda_j V_j^T = U_{jp} \Lambda_{jp} V_{jp}^T . \qquad (A3)$$

U_{jp} is obtained from the partition $U_j = (U_{jp} | U_{j0})$, where p is the number of nonzero singular values. A similar partition applies to V_j. In this application, only earthquakes with $p=4$ are used to avoid nonuniqueness in the earthquake locations. After premultiplying equation (A2) by U_{j0}^T and using equation (A3) and properties of the partitioned matrices, we obtain

$$U_{j0}^T S_j d\vec{s} = U_{j0}^T \vec{r}_j ; j = 1, M. \qquad (A4)$$

Therefore, the station corrections are isolated from the earthquake parameters. The M equations implied by equation (A4) can be written as a single matrix equation

$$Sd\vec{s} = \vec{R} \qquad (A5)$$

where

$$S = (S_1 U_{10} | S_2 U_{20} | \dots | S_M U_{M0})^T \text{ and } \vec{R} = (\vec{r}_1 U_{10} | \vec{r}_2 U_{20} | \dots | \vec{r}_M U_{M0})^T.$$

The matrix S is very large having N columns and MN rows. Pavlis and Booker solved this equation by using the generalized inverse of S. The approach taken by Pujol is to solve (A5) by least squares as follows

$$S^T S d\vec{s} = S^T \vec{R}. \qquad (A6)$$

Making use of properties of the partitioned matrices, we can write equation (A6) as

$$\left(\sum_{j=1}^{M} S_j U_{j0} U_{j0}^T S_j \right) d\vec{s} = \sum_{j=1}^{M} S_j U_{j0} U_{j0}^T \vec{r}_j \qquad (A7)$$

therefore solving equation (A6) by forming the normal equations without ever explicitly forming the matrix S.

The last step required to close one iteration loop is to solve for the $d\vec{X}_j$'s. From (A2) we get

$$A_j d\vec{X}_j = \vec{r}_j - S_j d\vec{s}\,; j = 1, M. \tag{A8}$$

After solving equation (A8) by least squares, the origin time, hypocenter coordinates, and station corrections are updated and a new iteration is started. The process stops when some cut-off criterion is satisfied, usually after 5 to 7 iterations.

Appendix B. Seismic moment tensors and waveform inversion for source parameters.

B1. INTRODUCTION.

A major research interest in seismology is the description of the physics of seismic sources. A common approach is the approximation of seismic sources by a model of equivalent forces that corresponds to the linear wave equation neglecting non-linear near-field effects (Aki and Richards, 1980). Equivalent forces are defined as producing displacements at the earth's surface that are identical to those from actual forces of the physical processes at the source. The classical method of describing seismic sources is by their strength (magnitude) and their fault plane solution. In the last two decades seismic moment tensors have been used routinely for describing point sources (when source dimensions are small compared to the wavelengths of interest). Seismic moment tensors are important because they completely describe in a first order approximation the equivalent forces of general seismic point sources. The equivalent forces can be correlated to physical source models such as sudden relative displacement on a fault surface. The equivalent forces representing such displacement form a double couple, the most commonly used description of a seismic source. It should be remembered, that seismic moment tensor is a general concept, describing a variety of seismic source models, the shear dislocation (double-couple source) being just one of them.

Gilbert (1970) introduced moment tensors for calculating the displacement at the free surface, which can be expressed as a sum of moment tensor elements times the corresponding Green's functions. A Green's function is a displacement field due to an unit impulse, i.e. the Green's function describes how the medium modifies an impulse response between source and receiver. The response of the medium to any other time function is the

convolution of that time function with the impulse response. The Green's function depends on the earth model and is a tensor. The linearity between the moment tensor and Green's function elements was first used by Gilbert (1973) for calculating moment tensor elements from observations. The concept of seismic tensors was further expanded by a variety of researches. The moment tensor can be determined from free oscillation of earth, surface waves or body waves (see Jost and Herrmann (1989) for references).

B2. MOMENT TENSOR FORMULATION FOR A GENERAL ELAS-TODYNAMIC SOURCE AND A DOUBLE-COUPLE SOURCE.

The following description of the moment tensor representation follows Jost and Herrmann (1989). The observed displacement d_n at a location $\vec{x}$ at the time t due to a distribution of equivalent body force densities f_k in a source region is (Aki and Richards, 1980):

$$d_n(\vec{x},t) = \int_{-\infty}^{\infty} \int_V G_{nk}(\vec{x},t;\vec{r},\tau) f_k(\vec{r},\tau) dV(\vec{r}) d\tau, \tag{B1}$$

where G_{nk} are the components of the Green's function, V is the source volume and the f_k are non-zero. Summation over repeated subscripts is implied.

By assuming that the Green's functions vary smoothly within the source volume, they can be expanded into a Taylor series around a reference point $\vec{r} = \xi$:

$$G_{nk}(\vec{x},t;\vec{r},\tau) = \sum_{m=0}^{\infty} \frac{1}{m!} (r_{j_1} - \xi_{j_1}) \ldots (r_{j_m} - \xi_{j_m}) G_{nk,j_1 \cdots j_m}(\vec{x},t;\xi,\tau), \tag{B2}$$

where comma between indices indicates partial derivatives with respect to the coordinates after the comma. The components of the time-dependent moment tensor are defined as:

$$M_{kj_1 \cdots j_m}(\xi,\tau) = \int_V (r_{j_1} - \xi_{j_1}) \ldots (r_{j_m} - \xi_{j_m}) f_k(\vec{r},\tau) dV. \tag{B3}$$

With the Taylor expansion (B2) and definition of the time-dependent moment tensor (B3), the displacement (B1) can be written as a sum of terms

$$d_n(\vec{x}, t) = \sum_{m=1}^{\infty} \frac{1}{m!} G_{nk, j_1 \cdots j_m}(\vec{x}, t; \xi, \tau) \bullet M_{kj_1 \cdots j_m}(\xi, \tau), \qquad (B4)$$

where the bold dot denotes temporal convolution. By using a point source approximation we need to consider only the first term in (B4) (first-order approximation). Assuming the same time dependence $s(\tau)$ for all components of the time dependent moment tensor and neglecting higher order terms, we get

$$d_n(\vec{x}, t) = M_{kj}[G_{nk, j} \bullet s(\tau)], \qquad (B5)$$

where M_{kj} are constants representing the components of the second order seismic moment tensor $\mathbf{M}$. The conservation of angular momentum for the equivalent forces leads to the symmetry of the seismic moment tensor. The displacement d_n is a linear function of the moment tensor elements and the terms in the square brackets. If the source time function $s(\tau)$ is a delta function, the only term left is $G_{nk,j}$, describing nine generalized couples. The derivative of a Green's function component with respect to the source coordinate ξ_j is equivalent to a single couple with arm in the ξ_j direction.

For a double-couple source moment tensor components are given by

$$M_{kj} = \mu A(u_k v_j + u_j v_k), \qquad (B6)$$

where μ is the shear modulus, A is the fault area, $\mathbf{u}$ is the slip vector on the fault surface and $\mathbf{v}$ is the vector normal to the fault plane. Contributions of $\mathbf{u}$ and $\mathbf{v}$ are symmetric and can be interchanged without affecting the displacement field. The term in parenthesis forms a tensor describing a double couple. This tensor is real and symmetric, giving real eigenvalues and orthogonal eigenvectors. The eigenvalues are proportional to $(1, 0, -1)$ and the eigenvectors give directions of the principal axes. The eigenvector corresponding to the eigenvalue zero gives the null-axis, the eigenvector corresponding to the positive values gives the tension axis, and the eigenvector corresponding to the negative value gives

the pressure axis. These axes can be related to the corresponding axes of the fault plane solution.

If the source can not be described by a pure double-couple mechanism, the moment tensor can be decomposed into an isotropic part, which describes volume changes in the source, double couple and remaining non-double couple components or another combination of those terms (Jost and Herrmann, 1989). In the moment tensor inversion algorithm used in this study we decompose the moment tensor into a major double couple and a compensated linear vector dipole (CLVD). The isotropic part is constrained to be zero. This is the most commonly used seismic moment tensor decomposition.

In addition to the orientation of the principal axes and the values of principal moments, an important parameter of the moment tensor is the scalar moment M_o

$$M_o = \frac{|m_1| + |m_2|}{2}, \tag{B7}$$

where m_1 and m_2 are the largest eigenvalues (in the absolute sense). The scalar moment M_o is related to the moment magnitude M_W through a relation (Kanamori, 1977):

$$M_W = \frac{\log M_o}{1.5} - 10.73, \tag{B8}$$

There are various methods of inversion of the system of linear equation (B6) for the moment tensor elements. The inversion can be done in frequency or time domain. Different seismic data can be used separately or combined. Certain a priori constraints can be imposed to stabilize inversion. The first difficulty, however, is calculation of the synthetic Green's functions.

B3. GREEN'S FUNCTIONS.

The Green's functions are dependent on the earth model, source location and receiver position. A number of different approaches can be used to calculate Green's functions. They can be subdivided into empirical, analytical and numerical. In empirical method (Hartzell, 1978; Dreger, 1994), a small earthquake is used as a Green's function

for a larger event in the same location. Analytical methods, such as ray tracing, can be useful in synthesizing particular phases, but are cumbersome to use when trying to compute complete solution, because they require a priori specification of a large number of ray-paths. Numerical methods are by far the most extensively used. Among them are the reflectivity methods. The reflectivity methods can be used to compute complete seismic codas for arbitrary frequency bandwidths and source depths, and for vertically inhomogeneous models (Kennett, 1980; Cormier, 1980). The major disadvantage of the reflectivity method is the computational expense, which is proportional to the product of frequency bandwidths and maximum distance range.

The other alternative is a modal representation of seismic waves. It combines features of both the analytical methods and the reflectivity method. The advantages of the modal method over the reflectivity method are that it is more accurate since one of the numerical integrals is eliminated, and it is more computationally efficient, since the number of residues within some wavenumber bandwidth will be less than the necessary number of numerical integration points within the same bandwidth. A summary of the theory for normal mode superposition can be found in Aki and Richards (1980) or other seismology textbooks.

We compute Green's functions using the locked mode approximation of the normal mode superposition method (Harvey, 1981). The essence of this method is to place an unrealistically high velocity half-space (or a layer) at the bottom of the velocity model, so called "cap layer". It has the effect of converting so called "leaking" modes (Gilbert, 1964) to trapped, or locked, modes. The requirement is that this cap layer be placed at a depth such that the earliest P-wave reflection from the top of the cap layer arrives after the seismic coda of interest. Phase velocity filters in the form of a mode truncation can also be used to avoid cap layer reflection problem. For distances less than 1000 km, the locked mode method is more practical in a computational sense than the reflectivity method or the various ray theories. Comparison of the locked-mode superposition to analytical solutions (Harvey, 1981) and reflectivity method synthetics (Harvey, 1993) showed that the approx-

imations made in the normal mode method had no appreciable negative effect on the calculated synthetic seismograms.

B4. MOMENT TENSOR INVERSION.

The inversion method used here is similar to the method presented in Gomberg and Masters (1988) and fully described in Harvey (1993). The process is iterative and each iteration contains two steps. First, the least-squares solution for equation (B5), i.e. moment tensor components, is found using a generalized inversion approach. Then, an inversion for the structure inversion is done with fixed source parameters. The damped steepest descent approach is used for the determination of local performance gradients. The inversion parameters are P- and S-wave velocities in each layer. Different constraints can be specified, including v_p/v_s ratio, and any of the velocities can be fixed or freed. The source depth, source-receiver distance and layer thickness are fixed during the inversion. An average variance reduction between the synthetic data and the observations is calculated in each iteration. The process stops after a predefined number of iterations is completed.

B5. SOURCE PARAMETERS FROM A SINGLE STATION.

Finally, we discuss inversion for the source parameters using a single station recording. As mentioned above, slip on a fault can be represented by an equivalent double-couple force system. The displacement field from a given double couple is unique, which means that if we can model the entire transient displacement field at a single point, we should be able to recover the source orientation. In other words, complete waveform inversion at a single station is enough to recover source parameters. In practice, uncertainties in the Green's functions and source time function, limited bandwidth of recording instruments, and noise make it difficult. However, at local and near-regional distances the effects of structure are easily accounted for, and the new generation of very broadband, high-dynamic-range instrument makes it possible to use sparse networks to determine accurately the source parameters of small to moderate-sized earthquakes.

Appendix C. Catalog of seismic moment tensors for central Alaska earthquakes.

Moment tensors are presented for 38 earthquakes that occurred in central Alaska from 1989 to 2000. For each earthquake, results of the inversion are presented in three panels. The panel on the left displays the initial (thin line) and final (thick line) P- (right lines) and S-wave (left lines) velocities. The title above this panel indicates the date of the earthquake and the name of the station used in the inversion. The panel on the right displays the recorded (thin) and synthetic (thick) filtered waveform data. Time along the x-axis is from the origin time of the earthquake. The lower hemispheric projection of the focal sphere is shown in the middle panel. First motion data is indicated by the closed squares (compression) and open circles (dilation). Strike, dip and slip values of the fault planes are printed below the focal sphere, as well as percentage of the double couple and CLVD components in the solution.

Figure C1. Event 5/22/89 3:16:14.59 63.34°N 150.34°W 18.12 km M_L 4.0.
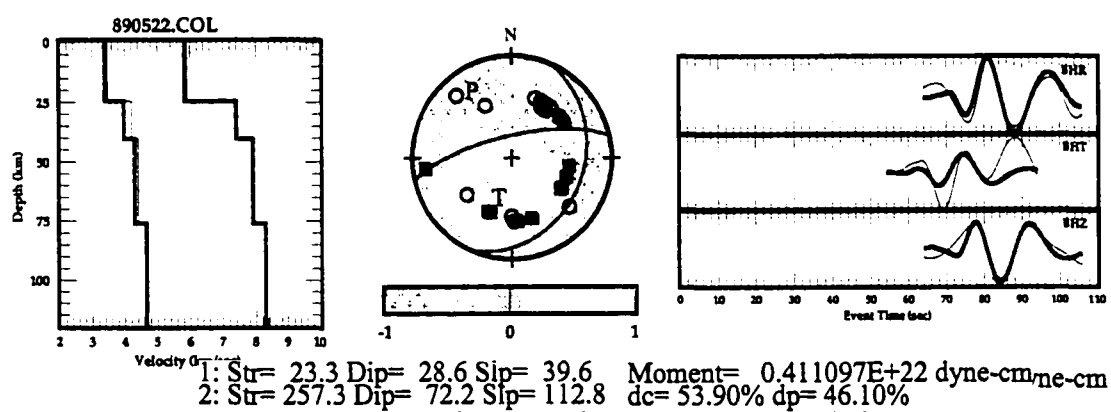
Figure C2. Event 7/28/89 5:48:20.13 64.15°N 151.71°W 9.99 km M_L 4.3.

1: Str= 282.4 Dip= 71.4 Slp= -165.9   Moment= 0.490865E+22 dyne-cm
2: Str= 187.8 Dip= 76.6 Slp=-19.1   dc= 66.73% dp= 33.27%
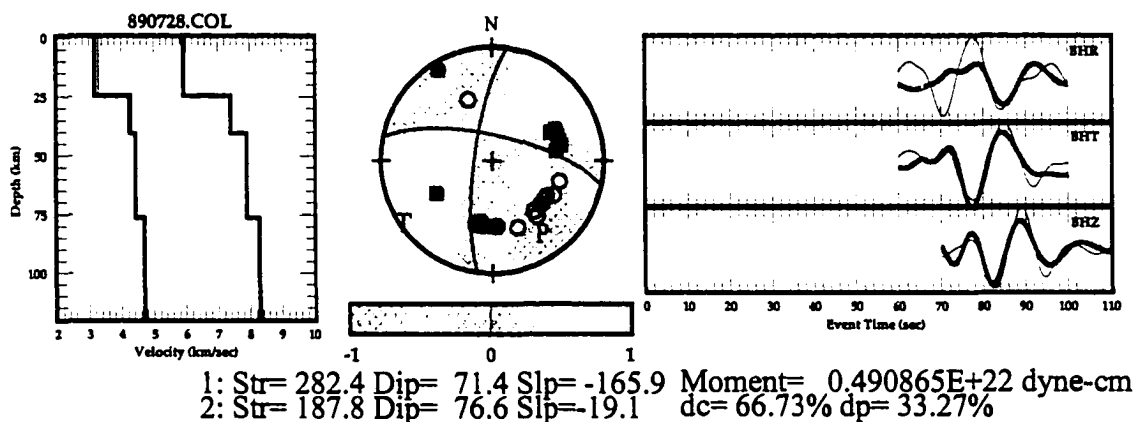
Figure C3. Event 2/17/90 2:11:32.43 63.56°N 150.11°W 10.58 km M_L 4.0.

1: Str= 195.8 Dip= 23.7 Slp=61.10   Moment= 0.657298E+25 dyne-cm
2: Str= 46.9 Dip= 69.4 Slp= 102.0   dc= 67.86% dp= 32.13%
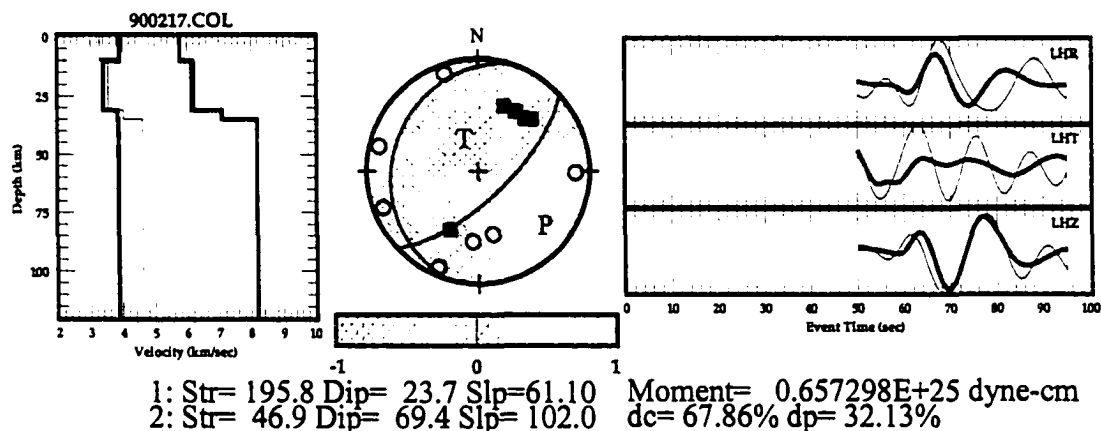
Figure C4. Event 10/1/90 9:02:34.95 63.50°N 151.21°W 14.47 km M_L 4.4.

1: Str= 285.7 Dip= 75.3 Slp= 168.1   Moment= 0.553062E+24 dyne-cm
2: Str= 18.8 Dip= 78.5 Slp= 15.0   dc= 77.33% dp= 22.67%
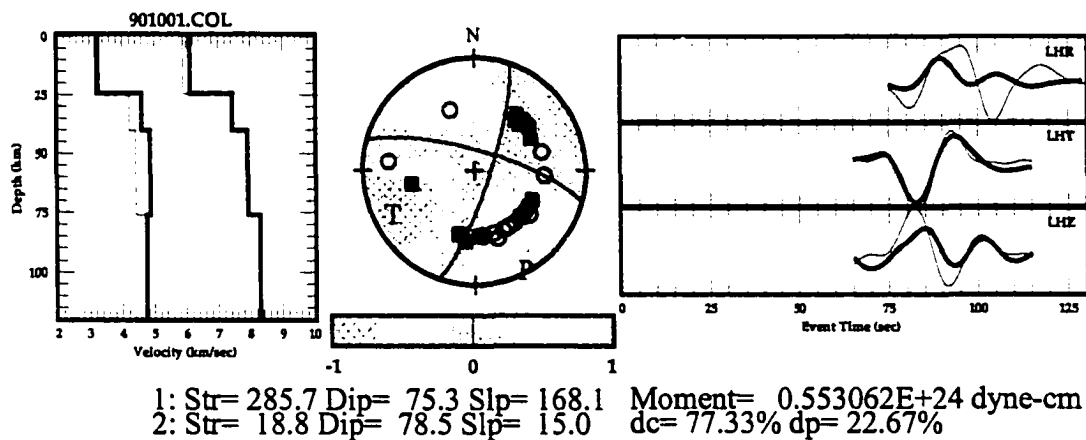
Figure C5. Event 2/7/91 6:04:20.47 66.37°N 147.94°W 10.00 km M_L 5.5.

1: Str= 313.0 Dip= 84.6 Slp= 160.4 Moment= 0.110891E+26 dyne-cm
2: Str= 45.0 Dip= 70.4 Slp= 5.7 dc= 85.15% dp= 14.85%
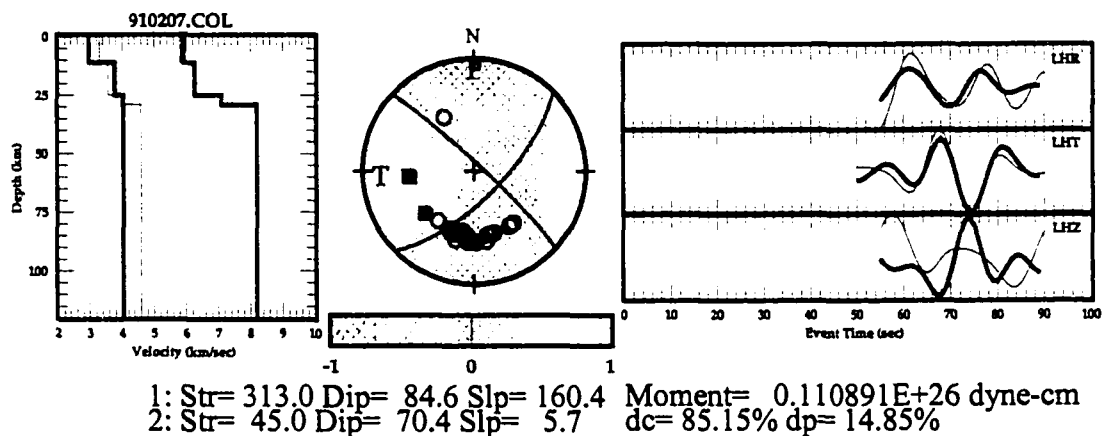
Figure C6. Event 3/11/91 5:54:16.13 64.86°N 149.13°W 19.30 km M_L 4.3.

1: Str= 123.2 Dip= 84.2 Slp= 155.6 Moment= 0.108264E+23 dyne-cm
2: Str= 215.8 Dip= 65.8 Slp= 6.4 dc= 78.56% dp= 21.44%
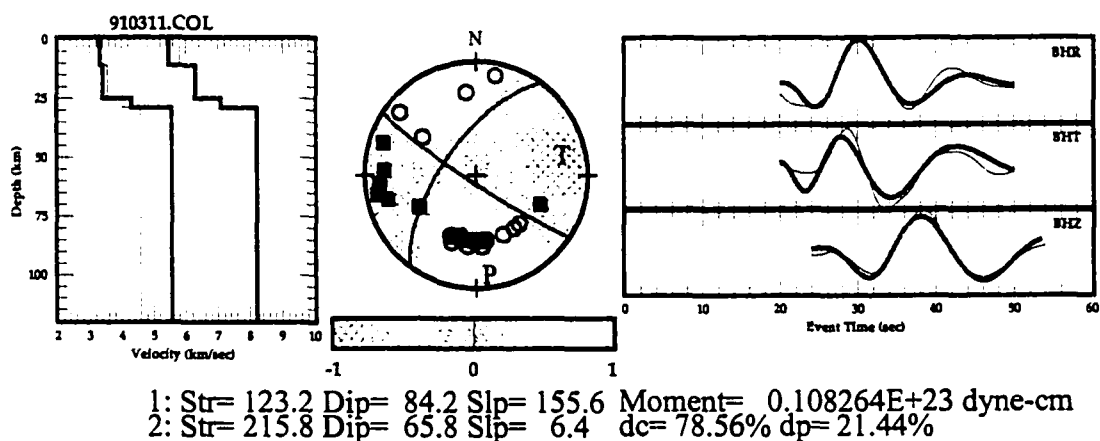
Figure C7. Event 8/14/91 20:44:19.66 63.19°N 151.06°W 14.40 km M_L 4.6.

1: Str= 351.9 Dip= 40.6 Slp= 3.1 Moment= 0.132672E+23 dyne-cm
2: Str= 259.6 Dip= 88.0 Slp= 130.5 dc= 66.13% dp= 33.87%
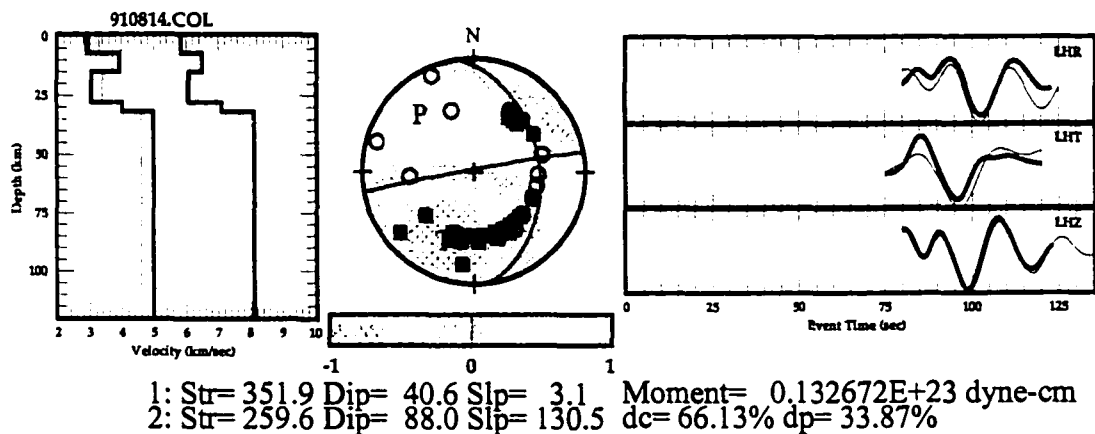
Figure C8. Event 10/2/91 14:02:32.47 63.21°N 149.52°W 18.43 km M_L 4.6.

1: Str= 206.7 Dip= 32.6 Slp= 110.0 Moment= 0.462356E+23 dyne-cm
2: Str= 3.3 Dip= 59.6 Slp= 77.6   dc= 85.04% dp= 14.96%
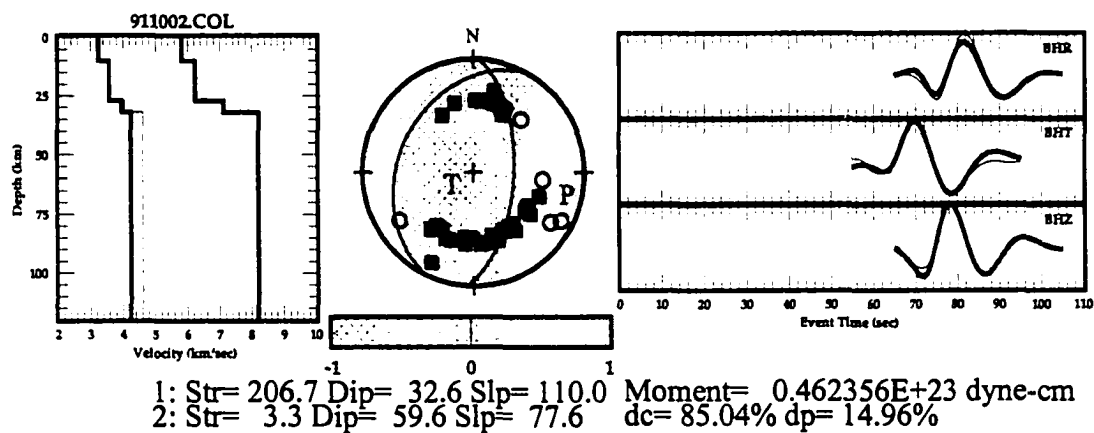
Figure C9. Event 1/27/92 5:22:32.27 64.24°N 150.94°W 22.32 km M_L 4.6.

1: Str= 172.9 Dip= 51.4 Slp= 11.4 Moment= 0.620874E+22 dyne-cm
2: Str= 75.7 Dip= 81.1 Slp= 140.9 dc= 98.60% dp= 1.40%
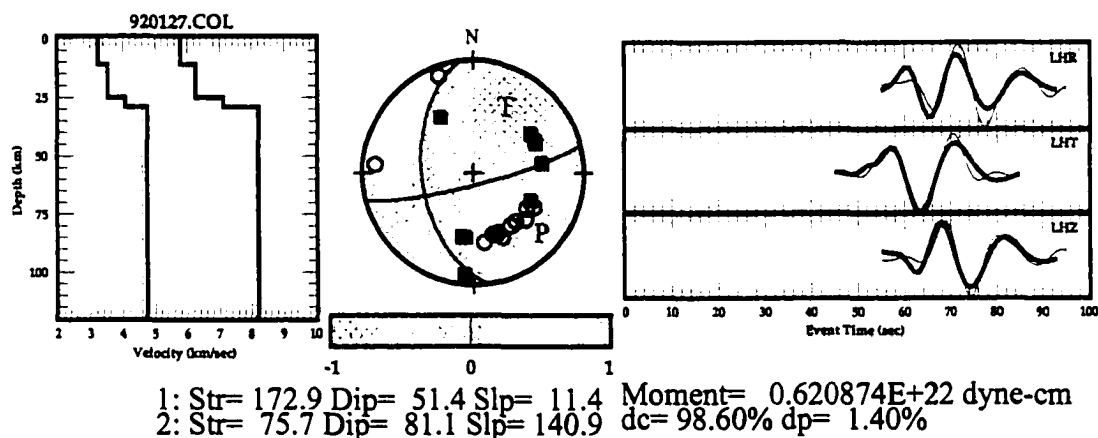
Figure C10. Event 3/25/92 15:14:57.98 66.25°N 146.83°W 1.47 km M_L 4.2.

1: Str= 111.4 Dip= 66.8 Slp= -175.9 Moment= 0.723952E+23 dyne-cm
2: Str= 19.8 Dip= 86.2 Slp= -23.2   dc= 80.54% dp= 19.46%
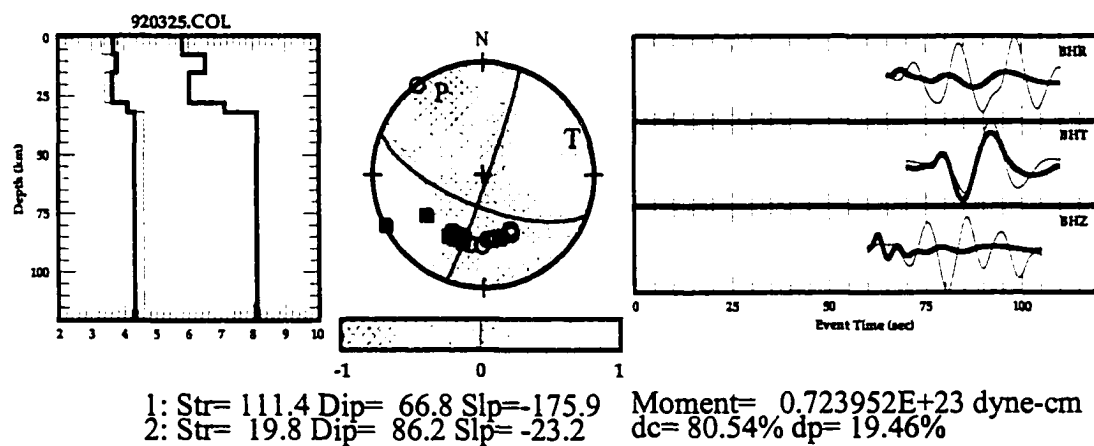
Figure C11. Event 7/31/92 17:07:54.77 63.32°N 151.33°W 16.68 km M_L 4.3.

1: Str= 30.3 Dip= 40.3 Slp=36.1   Moment= 0.255008E+22 dyne-cm
2: Str= 271.2 Dip= 67.6 Slp=124.5 dc= 56.24% dp= 43.76%
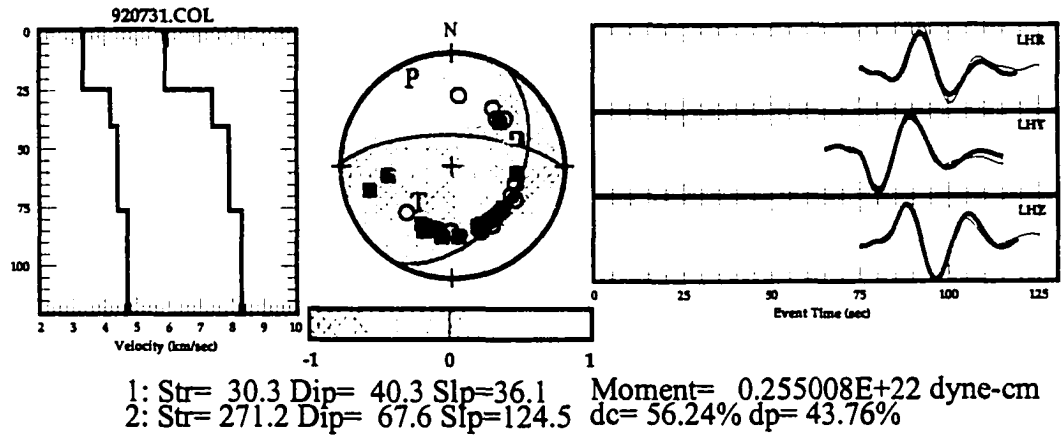
Figure C12. Event 1/17/93 10:25:33.78 64.97°N 149.19°W 19.37 km M_L 4.7.

1: Str= 123.7 Dip= 67.8 Slp= 169.1 Moment= 0.502312E+23 dyne-cm
2: Str= 217.9 Dip= 79.9 Slp= 22.5   dc= 67.18% dp= 32.82%
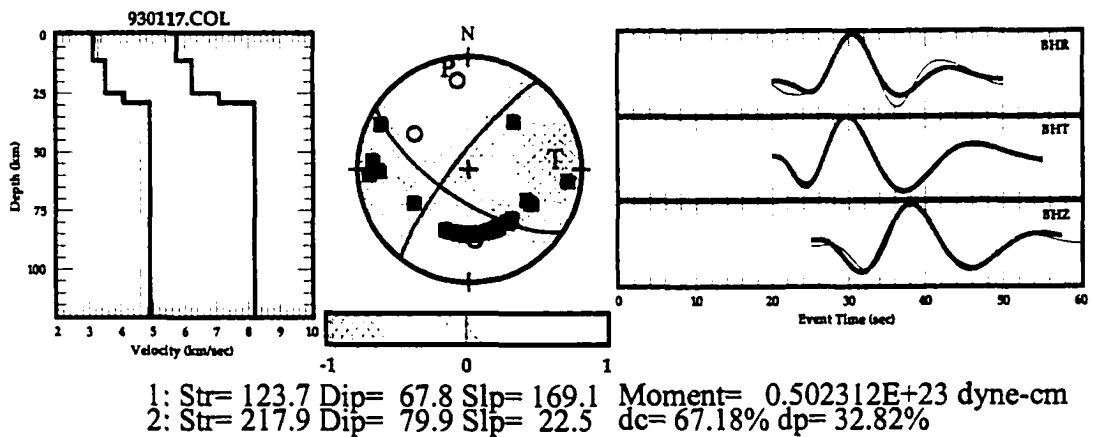
Figure C13. Event 12/19/93 8:03:16.19 63.31°N 151.28°W 15.31 km M_L 4.6.

1: Str= 94.5 Dip= 89.9 Slp=-135.0 Moment= 0.406544E+22 dyne-cm
2: Str= 4.4 Dip= 45.0 Slp= -0.2   dc= 97.46% dp= 2.54%
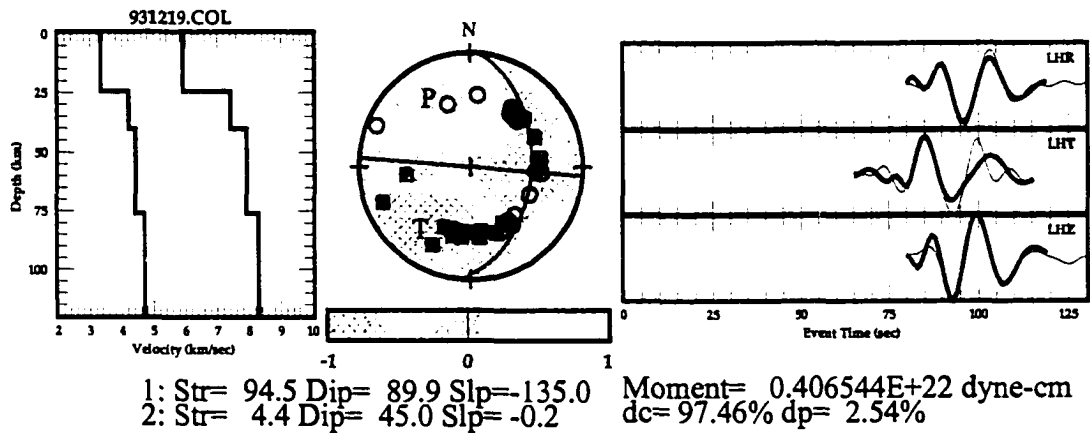
Figure C14. Event 12/29/93 9:34:38.27 64.44°N 146.83°W 10.75 km M_L 4.6.

1: Str= 71.5 Dip= 51.8 Slp=35.4   Moment= 0.878043E+23 dyne-cm
2: Str= 317.8 Dip= 62.9 Slp= 136.0 dc= 33.48% dp= 66.52%
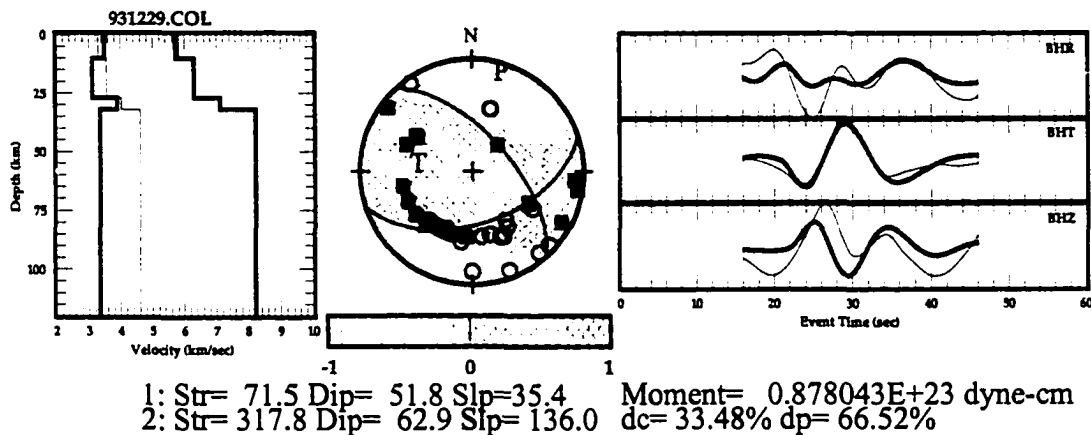
Figure C15. Event 3/30/94 17:42:43.50 66.52°N 148.09°W 9.66 km M_L 5.0.

1: Str= 287.2 Dip= 53.5 Slp= 175.1 Moment= 0.152396E+24 dyne-cm
2: Str= 20.1 Dip= 86.0 Slp= 36.6   dc= 67.30% dp= 32.70%
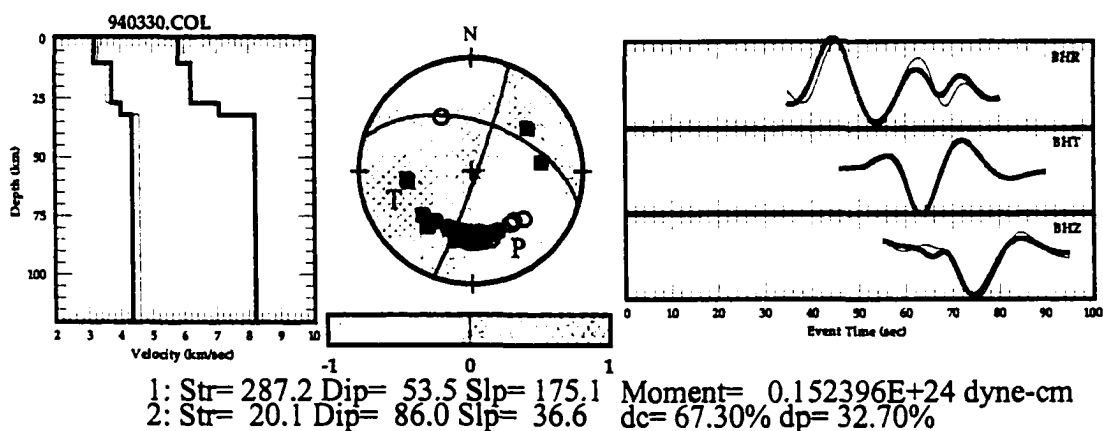
Figure C16. Event 10/17/94 14:12:03.46 63.88°N 146.11°W 6.84 km M_L 4.0.

1: Str= 328.1 Dip= 46.6 Slp=-177.7 Moment= 0.682513E+21 dyne-cm
2: Str= 236.6 Dip= 88.4 Slp= -43.4 dc= 74.65% dp= 25.35%
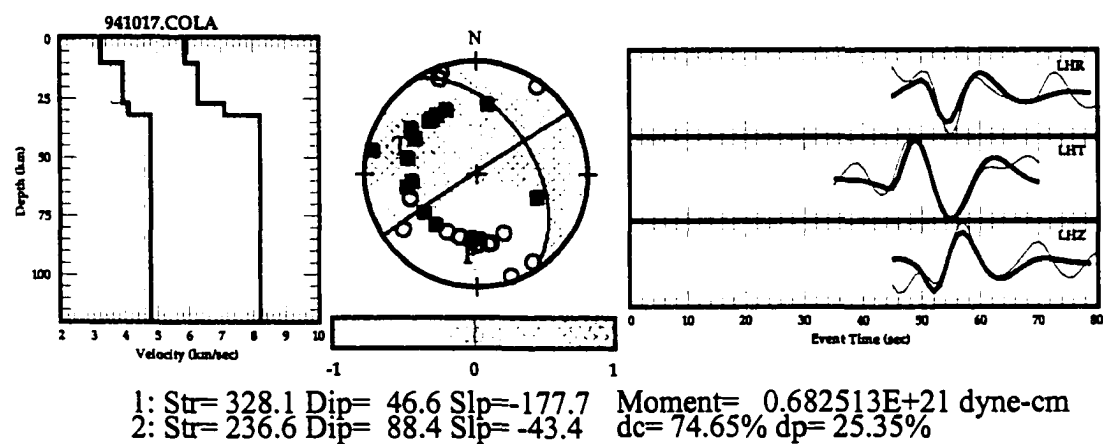
Figure C17. Event 11/7/94 9:39:58.45 63.52°N 151.13°W 11.67 km M$_L$ 4.4.

1: Str= 350.2 Dip= 75.5 Slp= 6.0 Moment= 0.173195E+23 dyne-cm
2: Str= 258.7 Dip= 84.2 Slp= 165.4 dc= 89.04% dp= 10.96%
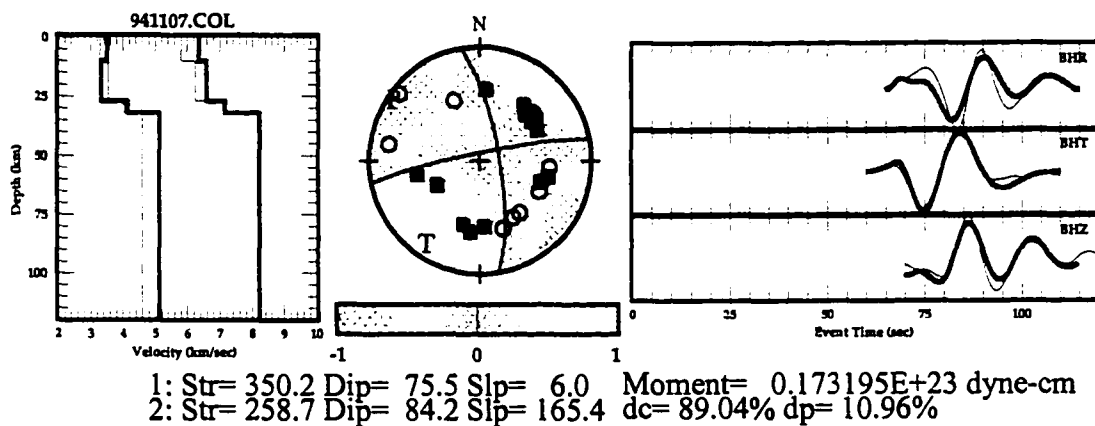
Figure C18. Event 11/17/94 2:40:39.79 63.54°N 151.25°W 10.39 km M$_L$ 4.3.

1: Str= 78.0 Dip= 48.5 Slp= 111.2 Moment= 0.224390E+23 dyne-cm
2: Str= 227.6 Dip= 45.8 Slp= 67.8 dc= 98.52% dp= 1.48%
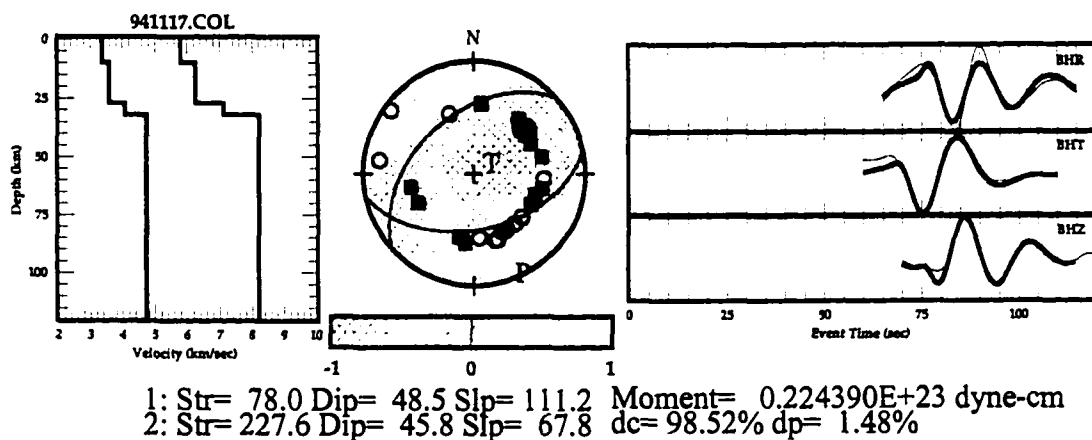
Figure C19. Event 12/17/94 2:07:35.53 65.09°N 150.48°W 10.63 km M$_L$ 4.1.

1: Str= 294.8 Dip= 84.9 Slp= 175.6 Moment= 0.144659E+22 dyne-cm
2: Str= 25.2 Dip= 85.6 Slp= 5.2 dc= 65.73% dp= 34.27%
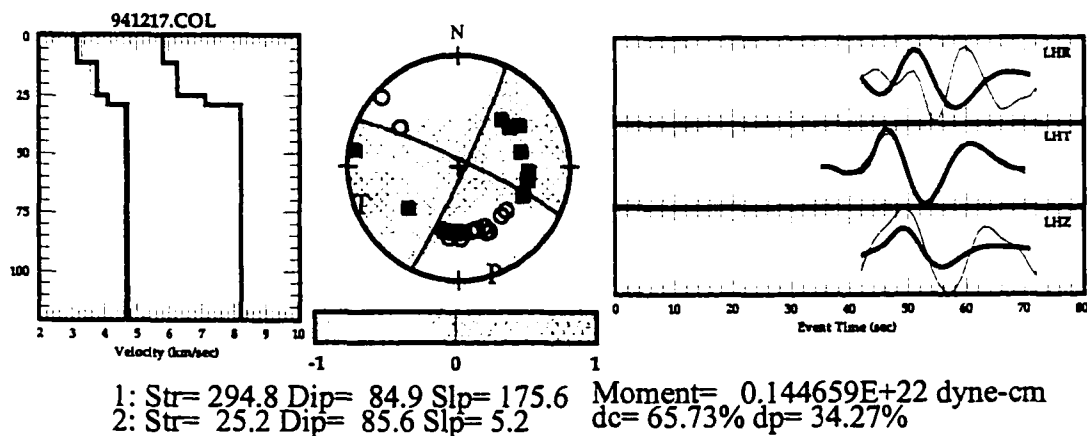
Figure C20. Event 8/25/95 11:57:12.12 64.67°N 148.33°W 16.87 km M_L 4.5.

950825.COL

1: Str= 274.1 Dip= 83.3 Slp=-178.4 Moment= 0.158584E+23 dyne-cm
2: Str= 184.0 Dip= 88.4 Slp= -6.7   dc= 98.68% dp= 1.32%
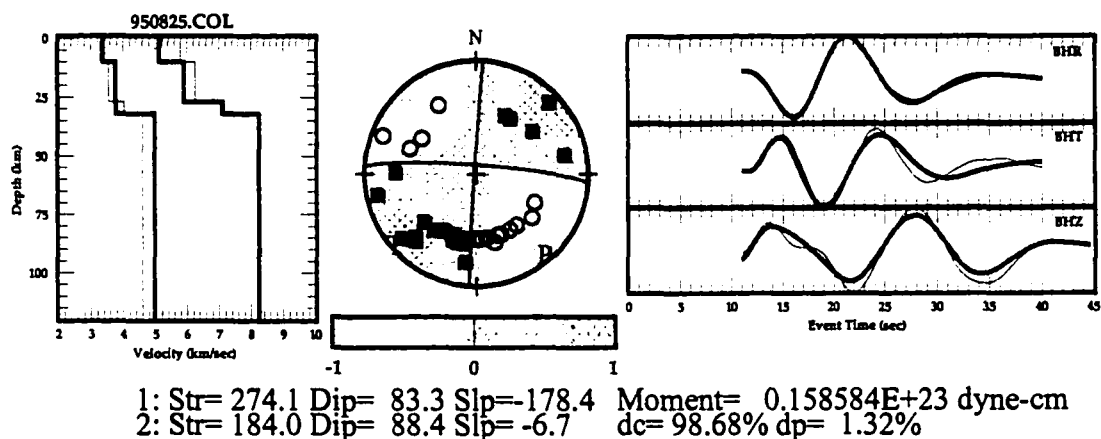
Figure C21. Event 9/21/95 9:06:14.55 64.98°N 149.05°W 15.88 km M_L 4.1.

950921.COL

1: Str= 138.0 Dip= 52.9 Slp= -95.9 Moment= 0.948296E+22 dyne-cm
2: Str= 327.8 Dip= 37.5 Slp= -82.2 dc= 49.24% dp= 50.76%
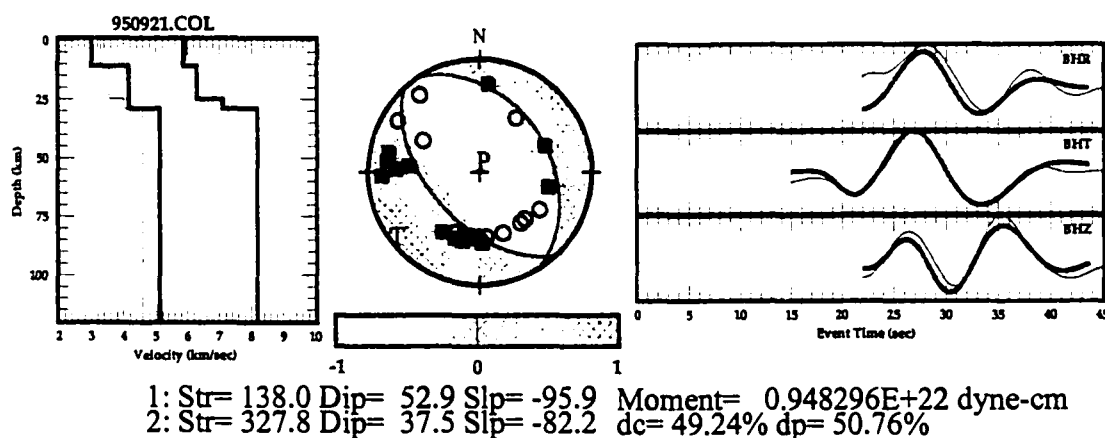
Figure C22. Event 10/6/95 5:23:18.96 65.16°N 148.54°W 12.18 km M_L 6.2.

9510060523.COL

1: Str= 115.9 Dip= 83.6 Slp= 163.6 Moment= 0.462276E+25 dyne-cm
2: Str= 207.7 Dip= 73.7 Slp= 6.6   dc= 86.12% dp= 13.88%
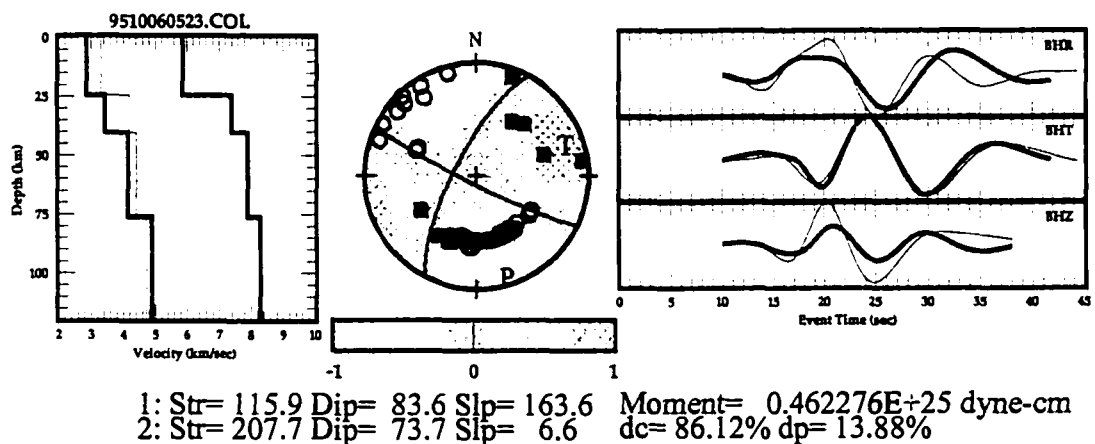
Figure C23. Event 10/6/95 5:40:09.41 65.14°N 148.55°W 12.77 km M$_L$ 4.3.

1: Str= 283.1 Dip= 88.0 Slp=-170.1   Moment= 0.144192E+24 dyne-cm
2: Str= 192.8 Dip= 80.1 Slp= -2.0   dc= 40.77% dp= 59.23%
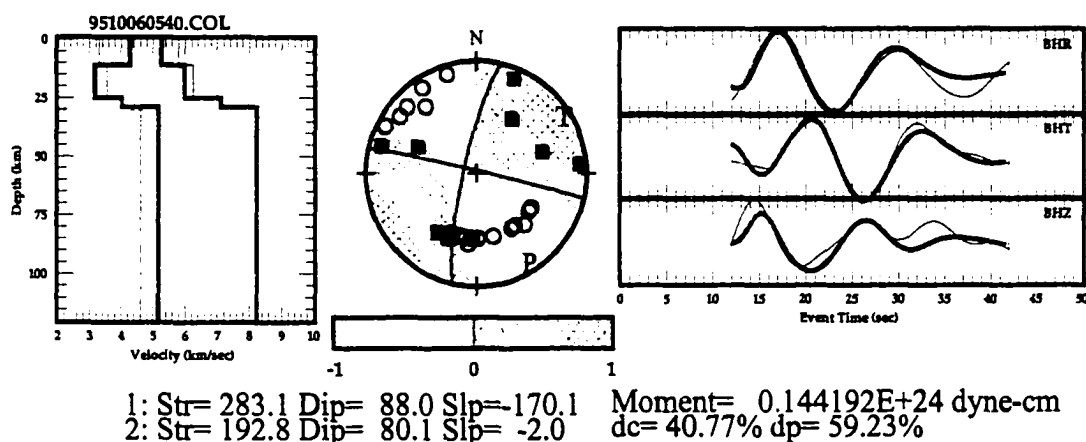
Figure C24. Event 10/6/95 15:48:47.99 65.12°N 148.62°W 18.26 km M$_L$ 4.3.

1: Str= 110.2 Dip= 90.0 Slp= 169.4   Moment= 0.631281E+22 dyne-cm
2: Str= 200.2 Dip= 79.4 Slp= 0.0   dc= 99.96% dp= 0.04%
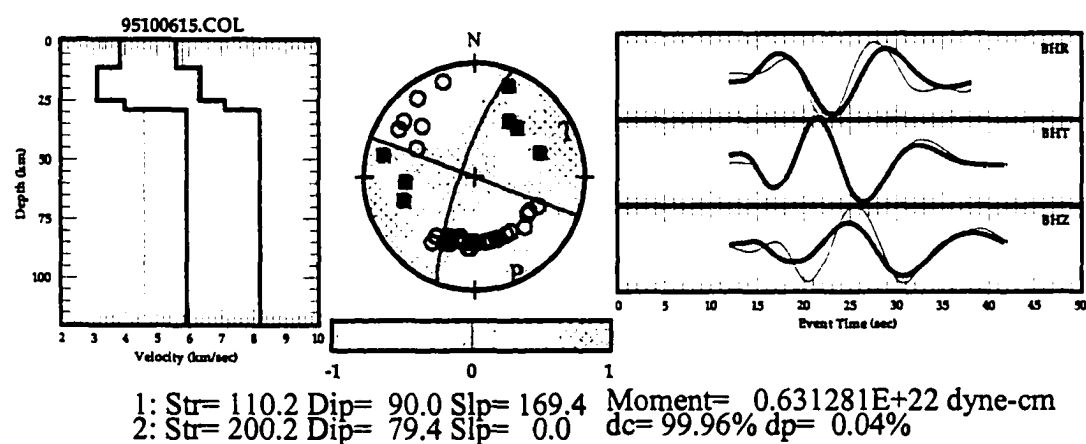
Figure C25. Event 10/12/95 18:47:02.38 65.18°N 148.55°W 10.80 km M$_L$ 4.1.

1: Str= 100.1 Dip= 89.0 Slp= 173.7   Moment= 0.299735E+22 dyne-cm
2: Str= 190.2 Dip= 83.7 Slp= 1.0   dc= 81.28% dp= 18.72%
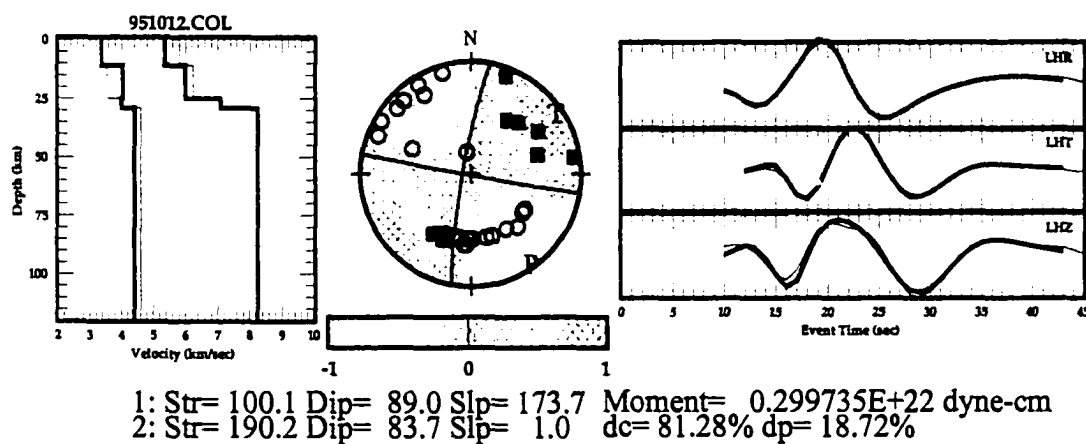
Figure C26. Event 10/16/95 21:31:10.15 65.14°N 148.58°W 12.66 km M$_L$ 4.5.

1: Str= 127.6 Dip= 80.2 Slp= 173.2 Moment= 0.288345E+23 dyne-cm
2: Str= 218.8 Dip= 83.3 Slp= 9.8 dc= 91.67% dp= 8.33%
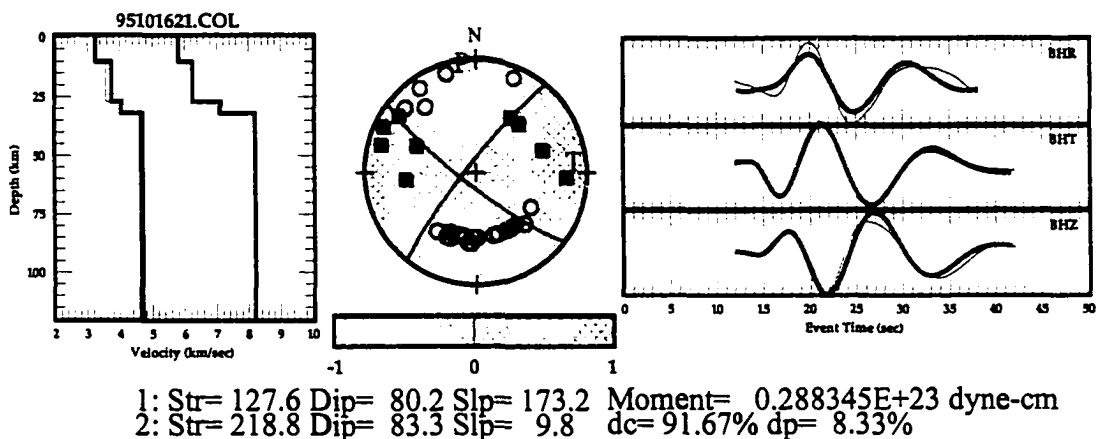
Figure C27. Event 10/16/95 23:29:23.12 65.84°N 151.16°W 9.52 km M$_L$ 4.9.

1: Str= 103.4 Dip= 88.5 Slp= 132.5 Moment= 0.182233E+23 dyne-cm
2: Str= 195.0 Dip= 42.5 Slp= 2.2 dc= 61.96% dp= 38.04%
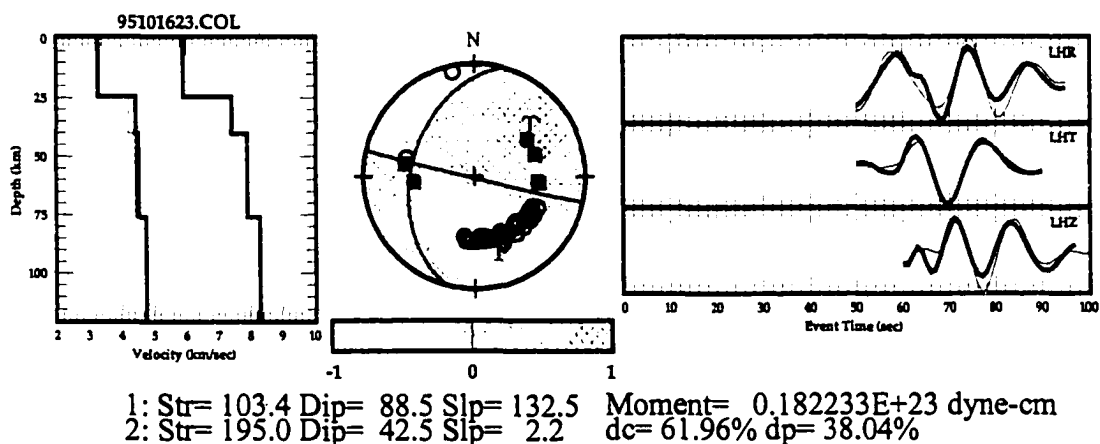
Figure C28. Event 10/25/95 1:27:25.34 63.28°N 151.12°W 14.87 km M$_L$ 4.0.

1: Str= 95.5 Dip= 69.3 Slp=135.3 Moment= 0.701179E+22 dyne-cm
2: Str= 204.7 Dip= 48.9 Slp= 28.0 dc= 94.29% dp= 5.71%
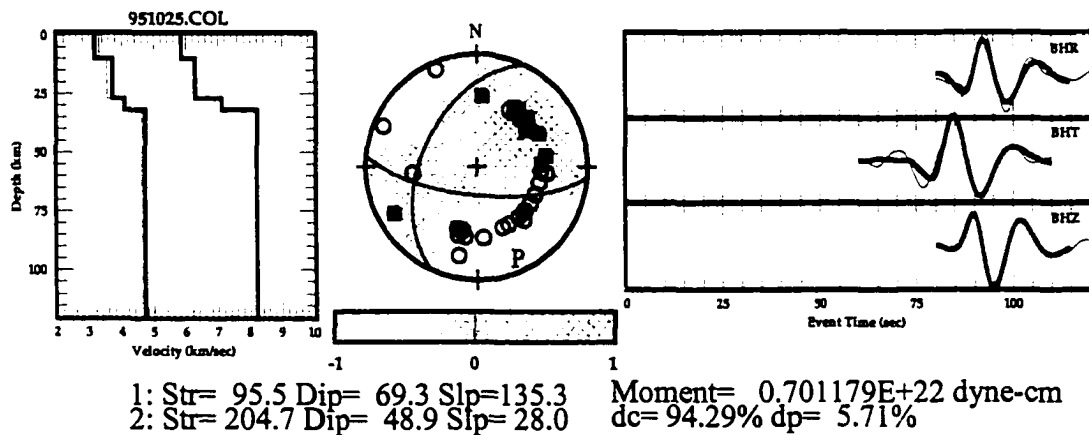
Figure C29. Event 10/22/96 22:15:02.77 63.36°N 145.29°W 2.76 km M_L 5.5.

1: Str= 128.2 Dip= 90.0 Slp= 124.9   Moment= 0.313038E+25 dyne-cm
2: Str= 218.2 Dip= 34.9 Slp=0.1   dc= 72.53% dp= 27.47%
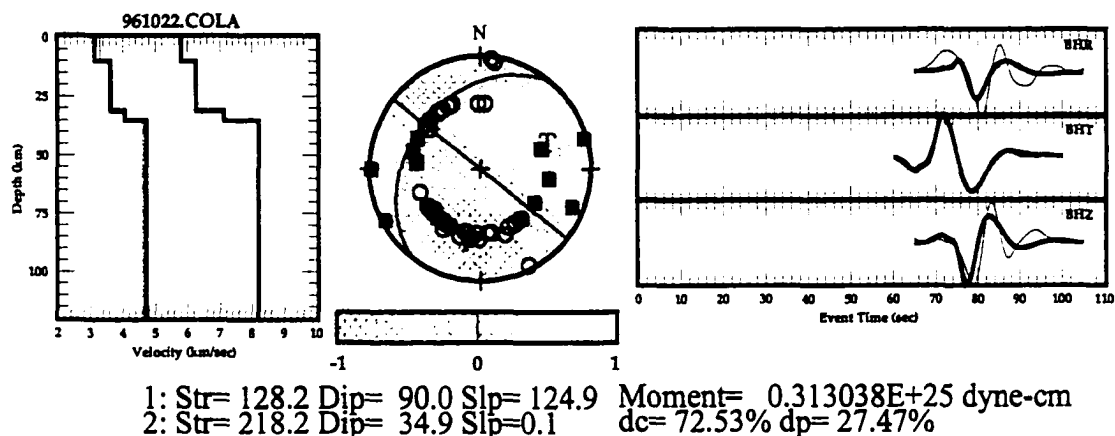
Figure C30. Event 11/14/98 1:04:57.72 63.42°N 151.28°W 15.71 km M_L 4.1.

1: Str= 131.4 Dip= 17.3 Slp= 158.1   Moment= 0.112802E+24 dyne-cm
2: Str= 242.4 Dip= 83.6 Slp= 73.8   dc= 37.28% dp= 62.72%
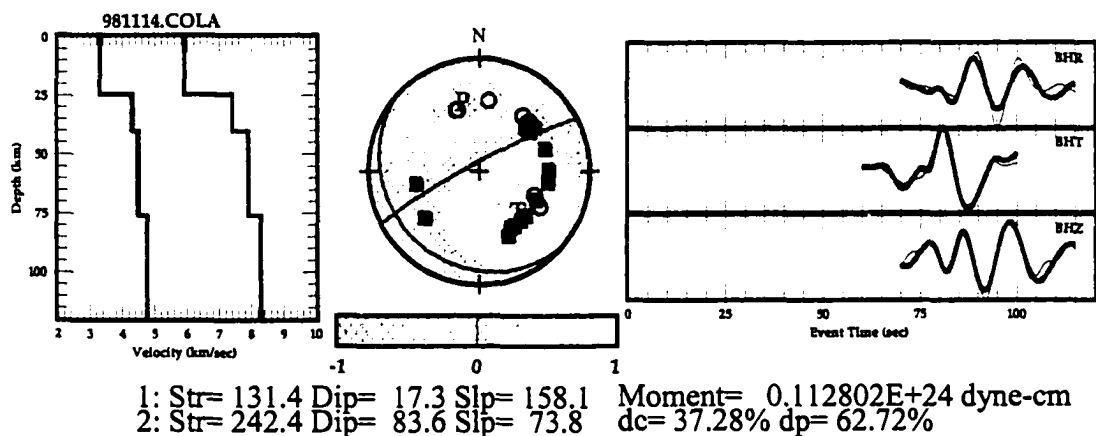
Figure C31. Event 6/25/99 11:34:30.74 63.44°N 151.43°W 11.18 km M_L 4.0.

1: Str= 94.8 Dip= 80.8 Slp=-176.7   Moment= 0.401532E+24 dyne-cm
2: Str= 4.3 Dip= 86.7 Slp= -9.2   dc= 96.23% dp= 3.77%
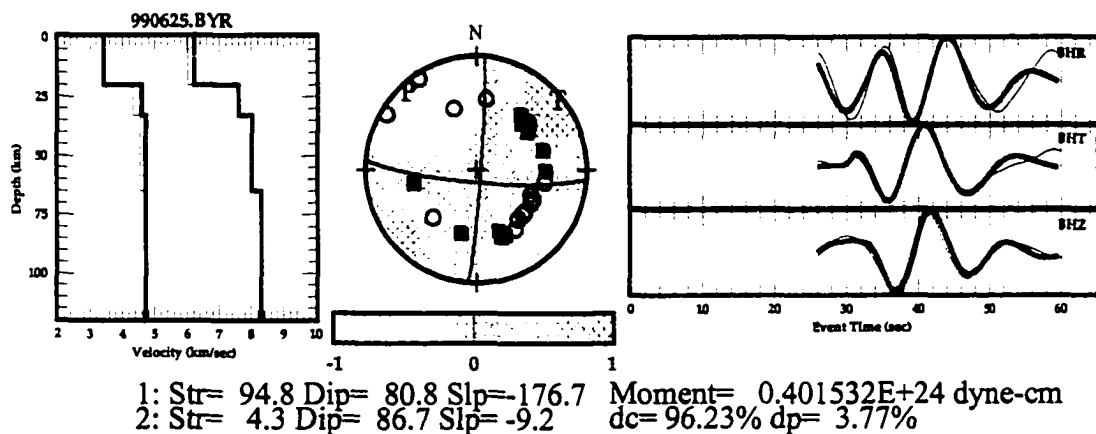
Figure C32. Event 8/5/99 9:06:44.47 63.22°N 151.41°W 8.86 km M_L 4.0.

1: Str= 153.7 Dip= 71.2 Slp= 0.0   Moment= 0.168215E+23 dyne-cm
2: Str= 63.7 Dip= 90.0 Slp= 161.2 dc= 99.89% dp= 0.11%
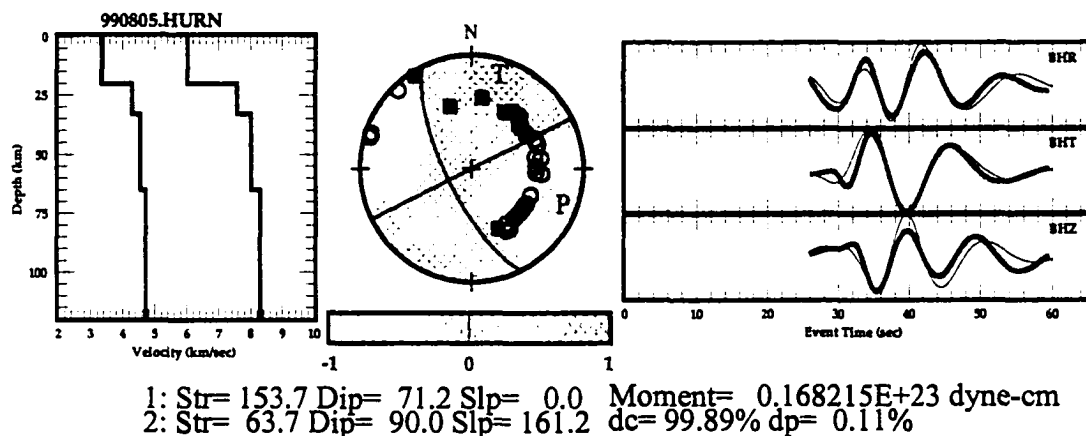
Figure C33. Event 12/12/99 22:15:35.33 62.85°N 148.98°W 7.83 km M_L 4.1.

1: Str= 178.3 Dip= 32.3 Slp= 42.6   Moment= 0.178871E+23 dyne-cm
2: Str= 50.4 Dip= 68.8 Slp= 115.0   dc= 84.51% dp= 15.49%
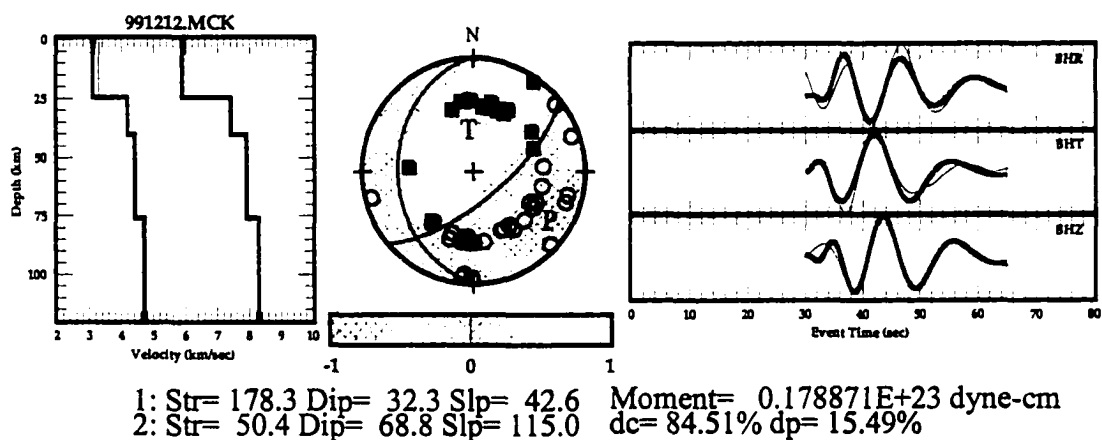
Figure C34. Event 2/25/00 6:37:38.59 63.19°N 151.25°W 3.87 km M_L 4.1.

1: Str= 160.8 Dip= 81.4 Slp= 43.0   Moment= 0.139704E+23 dyne-cm
2: Str= 62.9 Dip= 47.6 Slp= 168.4   dc= 63.73% dp= 36.27%
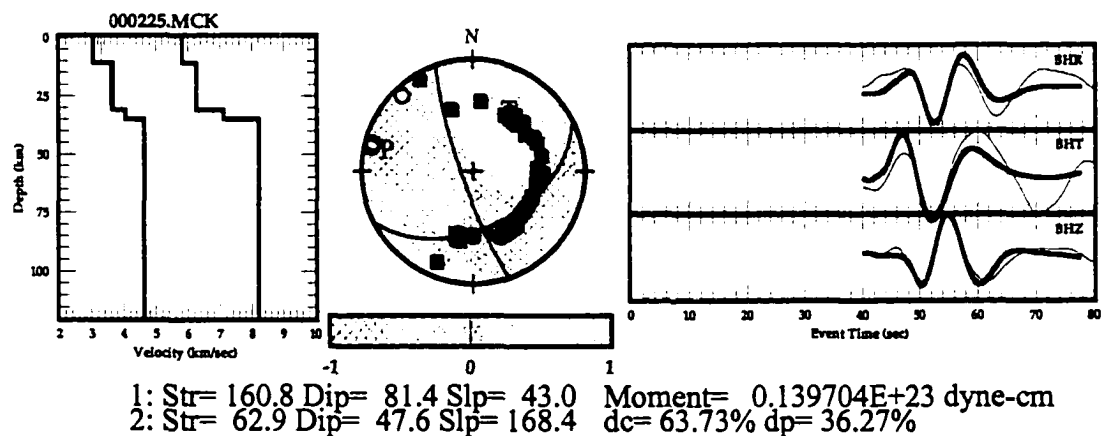
Figure C35. Event 3/15/00 9:10:08.52 63.58°N 151.97°W 7.95 km M_L 4.3.

1: Str= 274.7 Dip= 69.4 Slp= 144.8 Moment= 0.261860E+23 dyne-cm
2: Str= 18.6 Dip= 57.3 Slp= 24.7 dc= 67.88% dp= 32.12%
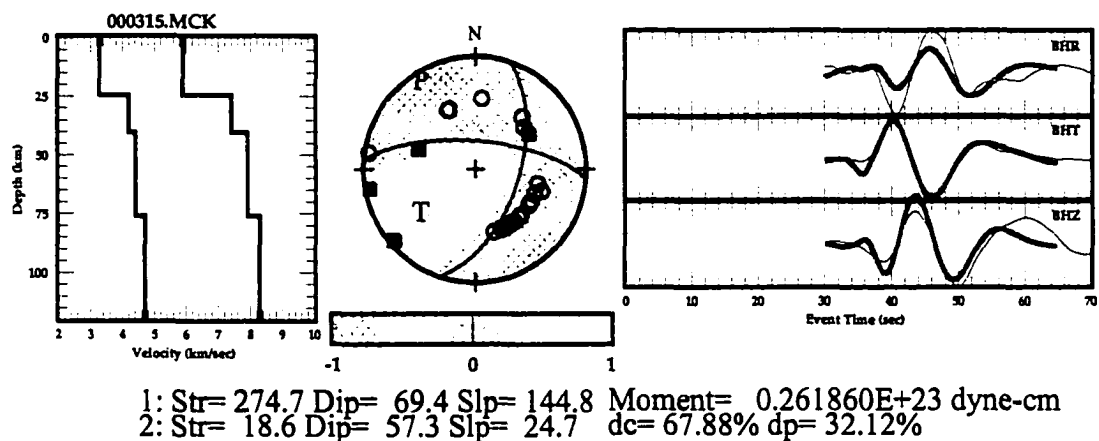
Figure C36. Event 11/9/00 16:25:13.76 64.63°N 152.47°W 10.00 km M_L 4.7.

1: Str= 107.9 Dip= 78.5 Slp= 104.0 Moment= 0.869960E+23 dyne-cm
2: Str= 236.5 Dip= 18.1 Slp=40.0 dc= 47.37% dp= 52.63%
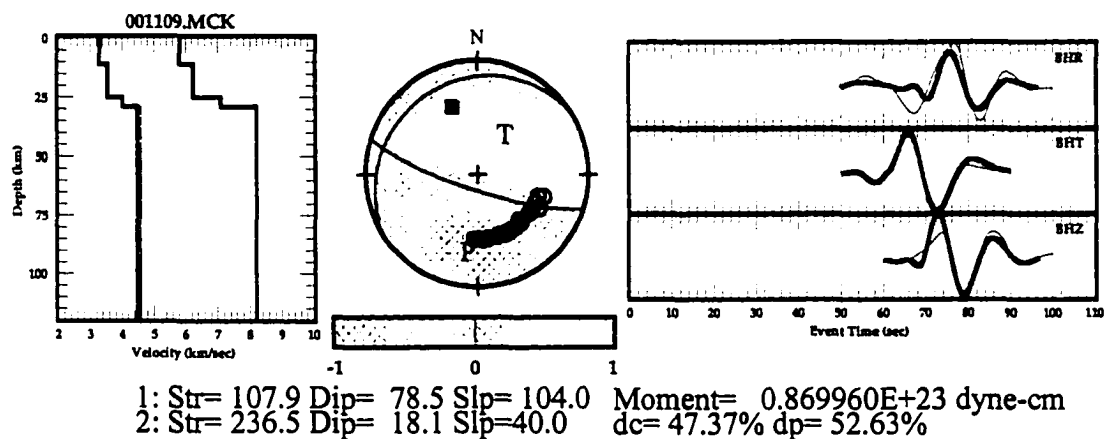
Figure C37. Event 11/29/00 10:35:47.88 63.85°N 150.26°W 19.60 km M_L 5.6.

1: Str= 105.5 Dip= 69.7 Slp= -168.4 Moment= 0.264448E+25 dyne-cm
2: Str= 11.5 Dip= 79.1 Slp= -20.7 dc= 68.40% dp= 31.60%
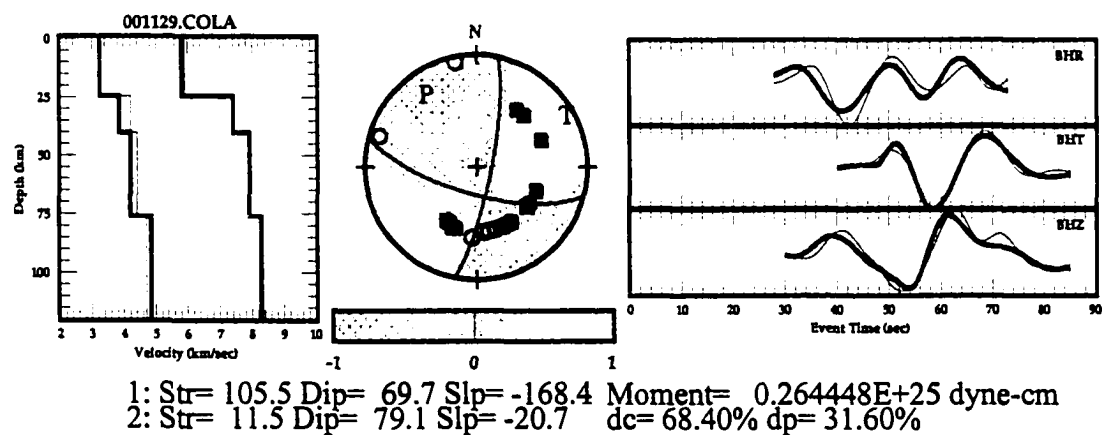
Figure C38. Event 12/06/00 18:40:26.59 63.86°N 150.32°W 13.77 km M_L 5.0.

1: Str= 170.6 Dip= 66.4 Slp= -2.8   Moment= 0.421414E+24 dyne-cm
2: Str= 261.7 Dip= 87.4 Slp= -156.4   dc= 90.65% dp= 9.35%
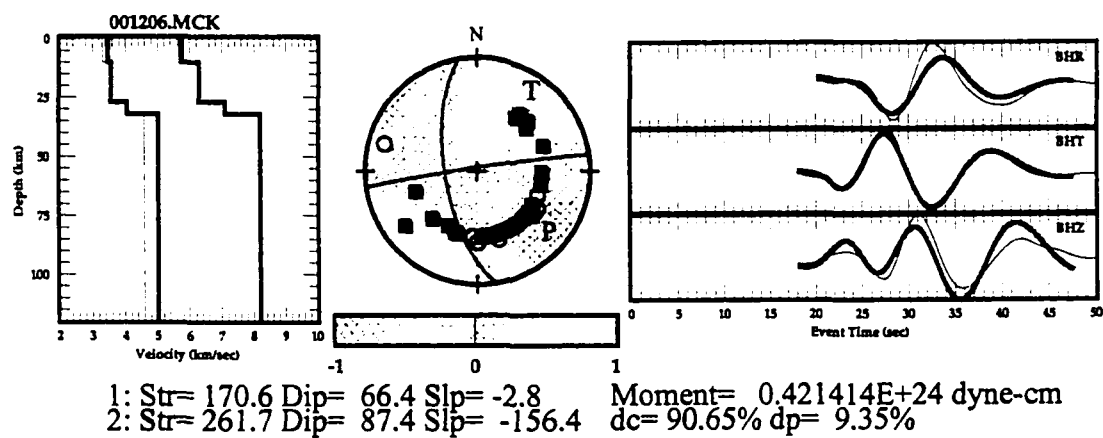
Appendix D. Apparent velocity and back azimuth estimates from analysis of seismic array data.

Seismic arrays are superior to single three-component stations for detecting and indentifying signals from earthquakes and explosions. The superior signal detection capability is obtained by suppression of noise using a beamforming technique, thus enhancing the signal to noise ratio. Standard beamforming assumes that the seismic signal arriving at the array is coherent from station to station, while the noise is not. The arrival times of the seismic signal at each station are delayed relative to each other. In order to form a coherent beam, the waveforms are shifted to line up a coherent seismic signal and then summed. This procedure enhances the signal at expense of the noise.

In order to compute the time delays for each station it is assumed that the incoming wavefront is a plane wave. In this case, two angles are needed to specify the orientation of the wavefront relative to the array. They are an angle of approach called back azimuth (in a horizontal plane) and an angle of incidence (in a vertical plane). The angle of incidence ϕ along with the propagation velocity v under the array determine the apparent velocity $v_{app} = v/\sin(\phi)$. The beamforming technique, therefore, allows the estimation of apparent velocity and back azimuth of the incoming seismic signal by finding those parameters that enhance the signal the most.

The following description of a beamforming technique follows the presentation of Fyen (1996). Let $y(\vec{r}_j, t)$ be a time series from the ith site at time t. Then the beam is

$$b(t) = \frac{1}{N} \sum_{i=1}^{N} y(\vec{r}_i, t + \vec{r}_i \cdot \vec{u}),$$ (D1)

where N is the number of sites, $\vec{r}_i = (x_i, y_i, z_i)$ is the position of an instrument within the array, and $\vec{u} = (u_x, u_y)$ is the apparent slowness vector with inverse apparent velocity components. Assuming that the incoming wave is a harmonic plane wave of frequency f, we have:

$$b(t) = \frac{1}{N} \sum_{i=1}^{N} A e^{j\omega(t + \vec{r}_i \cdot \vec{u} + \vec{r}_i \cdot \vec{u})} = \frac{1}{N} \sum_{i=1}^{N} A e^{j\omega t} \tag{D2}$$

where $\omega = 2\pi f$ is angular frequency. Equation (D2) describes procedure of beamforming. If the seismic waves were harmonic waves with no noise, then this equation would estimate the signal accurately. In real life, of course, the observation $y(t)$ is a sum of signal $S(t)$ and noise $n(t)$. Assuming that S(t) is a harmonic plane wave as in (D2) and the noise has zero mean value, we have

$$b(t) = \frac{1}{N} \sum_{i=1}^{N} y(\vec{r}_i, t + \vec{r}_i \cdot \vec{u}) = \frac{1}{N} \sum_{i=1}^{N} (S(\vec{r}_i, t + \vec{r}_i \cdot \vec{u}) + n(\vec{r}_i, t + \vec{r}_i \cdot \vec{u})) = S(t),$$

i.e. the beam is identical to the signal if the noise has a normal amplitude distribution with zero mean value and zero correlation between array elements. If the signal is coherent, then the delay-sum operator (D2) will be an optimal estimator of the signal. In this case the noise standard deviation will be reduced by a factor of $\sqrt{N}$ (Mykkeltveit et al., 1988).

Another approach to beamforming is to do it in a frequency domain and is called fk-analysis. A time shift in the time domain is equivalent to a phase shift in the frequency domain. The beams are formed in frequency domain for a number of predefined different slowness values. A grid-search process is used to find maximum power, and the corresponding slowness and back azimuth are the resulting observed values.

References

Abe, K. (1981). Magnitudes of large shallow earthquakes from 1904 to 1980, *Phys. Earth Planet. Int.* **27**, 72-92.

Abers, G.A. and G. Sarker (1996). Dispersion of regional body waves at 100-150 km depth beneath Alaska: In situ constraints on metamorphism of subducted crust, *Geophys. Res. Lett.* **23**, 1171-1174.

Aki, K. and P.G. Richards (1980). *Quantitative Seismology: Theory and Methods*, W.H. Freeman and Co., New York, San Francisco, 932 pp.

Beaudoin, B.C., G.S. Fuis, W.D. Mooney, W.J. Nokleberg, and N.I. Christensen (1992). Thin, low-velocity crust beneath the southern Yukon-Tanana terrane, east central Alaska: Results from Trans-Alaska Crustal Transect refraction/wide-angle reflection data, *J. Geophys. Res.* **97**, 1921-1942.

Berg, E., S. Kubota, and J. Kienle (1967). Preliminary determination of crustal structure in the Katmai National Monument, Alaska, *Bull. Seism. Soc. Am.* **57**, 1367-1392.

Boyd, M.T. and A.L. Lerner-Lam (1988). Spatial distribution of turn-of-the-century seismicity along the Alaska-Aleutian arc, *Bull. Seism. Soc. Am.* **78**, 636-650.

Burbach, G.V. and C. Frohlich (1986). Intermediate and deep seismicity and lateral structure of subducted lithosphere in the Circum-Pacific region, *Rev. Geophys.* **24**, 833-874.

Capon, J. (1969). High-resolution frequency-wavenumber spectrum analysis, *Proc. IEEE* **57**, 1408-1418.

Chiu, J.-M., B.L. Isacks, and R.K. Cardwell (1985). Propagation of high-frequency waves inside the subducted lithosphere from intermediate-depth earthquakes recorded in Vanuatu Arc, *J. Geophys. Res.* **90**, 12741-12754.

Christensen, D.H. and S.L. Beck (1994). The rupture process and tectonic implications of the Great 1964 Prince William Sound earthquake, *PAGEOPH* **142**, 29-53.

Cormier, V.F. (1980). The synthesis of complete seismograms in an earth model specified by radially inhomogeneous layers, *Bull. Seism. Soc. Am.* **70**, 691-716.

Davies, J.N. (1975). Seismological investigations of plate tectonics in south-central Alaska, *Ph. D. Thesis*, Univ. of Alaska, Fairbanks, 193 pp.

Davies, J.N. and L. House (1979). Aleutian subduction zone seismicity, volcano-trench separation, and their relation to great thrust-type earthquakes, *J. Geophys. Res.* **84**, 4583-4591.

Dewey, J.W. and W. Spence (1979). Seismic gaps and source zones of recent large earthquakes in Coastal Peru, *PAGEOPH* **117**, 1148-1171.

Douglas, A. (1967). Joint epicentre determination, *Nature* **215**, 47-48.

Dreger, D.S. (1994). Empirical Green's function study of the January 17, 1994 Northridge, California earthquake, *Geophys. Res. Lett.* **21**, 2633-2636.

Engdahl, E.R., J.W. Dewey, and K. Fujita (1982). Earthquake location in island arcs, *Phys. Earth Planet. Int.* **30**, 145-156.

Estabrook, C.H. and K.H. Jacob (1991). Stress indicators in Alaska, in: Slemmons, D.B., E.R. Engdahl, M.D. Zoback, and D.D. Blackwell, eds., *Neotectonics of North America*, Boulder, Colorado, Geological Society of America, Decade Map Volume 1, 387-399.

Fletcher, J.H. and J.T. Freymueller (2000). Using GPS to unravel the tectonics of interior Alaska, *EOS Transactions* **81**, F1126.

Foster, H.L., T.E.C. Keith, and W.D. Menzie (1994). Geology of the Yukon-Tanana area of east-central Alaska, in: Plafker, G. and H.C. Berg, eds., *The geology of Alaska*, Boulder, Colorado, Geological Society of America, Geology of North America, Volume G-1, 205-240.

Frohlich, C. (1992). Triangle diagrams: ternary graphs to display similarity and diversity of earthquake focal mechanisms, *Phys. Earth Planet. Int.* **75**, 193-198.

Fyen, J. (1996). *NORSAR array data processing: Draft reference guide*, NORSAR, Kjeller, 37 pp.

Gedney, L. and J.N. Davies (1986). Additional evidence for down-dip tension in the Pacific plate beneath central Alaska, *Bull. Seism. Soc. Am.* **76**, 1207-1214.

Gephart, J.W. and D.W. Forsyth (1984). An improved method of determining the

regional stress tensor using the earthquake focal mechanism data: Application to the San Fernando earthquake sequence, *J. Geophys. Res.* **89**, 9305-9320.

Giampiccolo, E., C. Musumeci, S.D. Malone, S. Gresta, and E. Privitera (1999). Seismicity and stress-tensor inversion in the central Washington Cascade Mountains, *Bull. Seism. Soc. Am.* **89**, 811-821.

Gilbert, F. (1964). Propagation of transient leaking modes in a stratified elastic wave-guide, *Rev. Geophys.* **2**, 123-154.

Gilbert, F. (1970). Excitation of the normal modes of the Earth by earthquake sources, *Geophys. J. R. Astron. Soc.* **22**, 223-226.

Gilbert, F. (1973). Derivation of source parameters from low-frequency spectra, *Phil. Trans. R. Soc. A* **274**, 369-371.

Gomberg, J. and T. Masters (1988). Waveform modelling using locked-mode synthetic and differential seismograms: application to determination of the structure of Mexico, *Geophys. J. R. Astr. Soc.* **94**, 193-218.

Guttenberg, B. and C. Richter (1954). *Seismicity of the Earth*, 2nd ed., Princeton University Press, Princeton, New Jersey, 310 pp.

Hansen, R.A., H. Bungun, and A. Alsker (1989). Three recent larger earthquakes offshore Norway, *Terra Nova* **1**, 284-195.

Hansen, R.A. and D.J. Harvey (1989). Surface wave modeling for source and structure inversion, *NORSAR Annual Technical Rep.*, 3-14.

Hardebeck, J.L. and E. Hauksson (2001). Stress orientations obtained from earthquake focal mechanisms: What are appropriate uncertainty estimates?, *Bull. Seism. Soc. Am.* **90** (in press).

Hartzell, S. (1978). Earthquake aftershocks as Green's functions, *Geophys. Res. Lett.* **5**, 1-5.

Harvey, D.J. (1981). Seismogram synthesis using normal mode superposition: the locked mode approximation, *Geophys. J. R. Astr. Soc.* **66**, 37-61.

Harvey, D.J. (1993). Full waveform inversion for structure and source parameters using regional data recorded in eastern Kazakhstan, *Final Rep. PL-TR-92-2138, Phillips*

Laboratory, Hanscom AFB, 41 pp.

Helffrich, G. and G.A. Abers (1997). Slab low-velocity layer in the eastern Aleutian subduction zone, *Geophys. J. Int.* **130**, 640-648.

Herrmann, R., Ś. Park, and C. Wang (1981). The Denver earthquakes of 1967-1968, *Bull. Seism. Soc. Am.* **71**, 731-745.

van der Hilst, R. and R. Snieder (1996). High-frequency precursors to P wave arrivals in New Zealand: Implications for slab structure, *J. Geophys. Res.* **101**, 8473-8488.

Hori, S., H. Inoue, Y. Fukao, and M. Ukawa (1985). Seismic detection of the untransformed 'basaltic' oceanic crust subducting into the mantle, *Geophys. J. R. Astr. Soc.* **83**, 169-197.

Huppert, L.N. and C. Frohlich (1981). The P velocity within the Tonga Benioff Zone determined from traced rays and observations, *J. Geophys. Res.* **86**, 3771-3782.

Iidaka, T. and M. Mizoue (1991). P-wave velocity structure inside the subducting Pacific plate beneath the Japan region, *Phys. Earth Planet. Int.* **66**, 203-213.

Iidaka, T., M. Mizoue, I. Nakamura, T. Tsukuda, K. Sakai, M. Kobayasi, T. Haneda, and S. Hashimoto (1990). The upper boundary of the Philippine Sea plate beneath the western Kanto region estimated from S-P-converted wave, *Tectonophysics* **179**, 321-326.

James, D.E. and J.A. Snoke (1990). Seismic evidence for continuity of the deep slab beneath central and eastern Peru, *J. Geophys. Res.* **95**, 4989-5001.

Jost, M.L. and R.B. Herrmann (1989). A student's guide to and review of moment tensors, *Seism. Res. Lett.* **60**, 37-57.

Kanamori, H. (1977). The energy release in great earthquakes, *J. Geophys. Res.* **82**, 2981-2987.

Katsumata, K., M. Ichiyanagi, M. Miwa, and M. Kasahara (1995). Aftershock distribution of the October 4, 1994 M_W 8.3 Kurile Islands earthquake determined by a local seismic network in Hokkaido, Japan, *Geophys. Res. Lett.* **22**, 1321-1324.

Kennett, B.L.N. (1980). Seismic waves in a stratified half space - II. Theoretical seismograms, *Geophys. J. R. Astr. Soc.* **61**, 1-10.

Kienle, J., S.E. Swanson, and H. Pulpan (1983). Magmatism and subduction in the eastern Aleutian arc, in: Shimozuru, D. and I. Yokoyama, eds., *Arc Volcanism: Physics and Tectonics*, Terra Scientific Publishing Company, Tokyo, 191-224.

Lahr, J.C. (1975). Detailed seismic investigation of Pacific-North American plate interaction in southern Alaska, *Ph. D. Thesis*, Columbia University, New York, 88 pp.

Lahr, J.C. (1989). HYPOELLIPSE/version 2.00: A computer program for determining local earthquakes hypocentral parameters, magnitude, and first motion pattern, *U.S. Geol. Surv. Open-File Rep. 89-116*, 89 pp.

Lahr, J.C. and others (1978). Catalog of Earthquakes in South Central Alaska, *U.S. Geol. Surv. Open-File Rep.*

Lay, T., L. Astiz, H. Kanamori, and D.H. Christensen (1989). Temporal variation of large intraplate earthquakes in coupled subduction zones, *Phys. Earth Planet. Int.* **54**, 258-312.

Lee, W.-H. K. and S.W. Stewart (1981). *Principles and applications of microearthquakes networks*, Academic Press, New York, 293 pp.

Lindquist, K.G. (1998). Seismic array processing and computational infrastructure for improved monitoring of Alaskan and Aleutian seismicity and volcanoes, *Ph.D. Thesis*, Univ. of Alaska, Fairbanks, 255 pp.

Lindquist, K.G. and R.A. Hansen (2001). Near-real-time Alaskan regional seismic network monitoring with the Iceworm system, *Bull. Seism. Soc. Am.* (submitted).

Louat, R., B.L. Isacks, and J. Dubois (1979). Anomalous propagation of seismic waves through the zone of shearing contact between the converging plates of New Hebrides arc, *Nature (London)* **281**, 293-295.

Lu, Z. and M. Wyss (1996). Segmentation of the Aleutian plate boundary derived from stress direction estimates based on fault plane solutions, *J. Geophys. Res.* **101**, 803-816.

Lu, Z., M. Wyss, and H. Pulpan (1997). Details of stress directions in the Alaska subduction zone from fault plane solutions, *J. Geophys. Res.* **192**, 5385-5402.

Matsuzawa, T., T. Kono, A. Hasegawa, and A. Takagi (1990). Subducting plate boundary beneath the northeastern Japan arc estimated from SP converted waves, *Tectonophysics* **181**, 123-133.

Matsuzawa, T., N. Umino, A. Hasegawa, and A. Takagi (1986). Upper mantle velocity structure estimated from PS-converted wave beneath the north-eastern Japan Arc, *Geophys. J. R. Astr. Soc.* **86**, 767-787.

Matsuzawa, T., N. Umino, A. Hasegawa, and A. Takagi (1987). Estimation of thickness of a low-velocity layer at the surface of the descending oceanic plate beneath the Northeastern Japan Arc by using synthesized PS wave, *Sci. Rep. Tohoku Univ., Ser. 5*, **31**, 19-28.

Matumoto, T. and R.A. Page (1969). Microaftershocks following the Alaska earthquake of 28 March 1964: Determination of hypocenters and crustal velocities in the Kenai Peninsula-Prince William Sound area, in: *The Prince William Sound, Alaska, Earthquake of 1964 and Aftershocks*, Volume 2B&C, U.S. Coast and Geodetic Surv. Publ. 10-3, U.S. Govt. Printing Office, Washington, 157-173.

Meyers, E.V., D.H. Christensen, G.A. Abers, and M.C. Pollock (1999). Preliminary results from BEAAR (Broadband Experiment Across the Alaska Range), *EOS Transactions* **80**, F711.

Meyers, E.V., D.H. Christensen, G.A. Abers, J.C. Stachnik, A.R. Holland and K.B. Beebe (2000). Broadband (Seismic) Experiment Across the Alaska Range (BEAAR) to determine the crustal and upper mantle structure beneath central Alaska, *EOS Transactions* **81**, F877.

Mitronovas, W. and B. Isacks (1971). Seismic velocity anomalies in the upper mantle beneath the Tonga-Kermadec Island Arc, *J. Geophys. Res.* **76**, 7154-7180.

Moore, J.C., J. Diebold, M.A. Fisher, J. Sample, T. Brocher, M. Talwani, J. Ewing, R. von Huene, C. Rowe, D. Stone, C. Stevens, and D. Sawyer (1991). EDGE deep seismic reflection transect of the eastern Aleutian arc-trench layered lower crust reveals underplating and continental growth, *Geology* **19**, 420-424.

Morelli, A. and A.M. Dziewonski (1993). Body wave traveltimes and a spherically

symmetric P- and S-wave velocity model, *Geophys. J. Int.* **112**, 178-194.

Mykkeltveit, S., J. Fyen, F. Ringdal, and T. Kvaerna (1988). Spatial characteristics of the NORESS noise field and implications for array detection processing, *Phys. Earth Planet. Int.* **63**, 277-283.

Nakamura, K. and S. Uyeda (1980). Stress gradient in arc-back arc regions and plate subduction, *J. Geophys. Res.* **85**, 6419-6428.

Nakamura, M., M. Ando, and T. Ohkura (1992). Reflected waves from the lower plate boundary, *Abstracts, Annual Meeting Seism. Soc. Jpn.*

Oda, H., T. Tanaka, and K. Seya (1990). Subducting oceanic crust on the Philippine Sea plate in Southwest Japan, *Tectonophysics* **172**, 175-189.

Page, R.A., N.N. Biswas, J.C. Lahr, and H. Pulpan (1991). Seismicity of continental Alaska, in: Slemmons, D.B., E.R. Engdahl, M.D. Zoback, and D.D. Blackwell, eds., *Neotectonics of North America*, Geological Society of America, Decade Map Volume 1, 47-68.

Page, R.A., G. Plafker, and H. Pulpan (1995). Block rotation in east-central Alaska: A framework for evaluating earthquake potential?, *Geology* **23**, 629-632.

Page, R.A., C.D. Stephens, and J.C. Lahr (1989). Seismicity of the Wrangell and Aleutian Wadati-Benioff zones and the North American plate along the Trans-Alaska crustal transect, Chugach mountains and Cooper River basin, southern Alaska, *J. Geophys. Res.* **94**, 16059-16082.

Pavlis, G. and J. Booker (1983). Progressive multiple event location (PMEL), *Bull. Seism. Soc. Am.* **73**, 1753-1777.

Power, J.A., S.C. Moran, S.R. McNutt, S.D. Stihler, and J.J. Sanchez (2001). Seismic response of the Katmai volcanoes to the December 6, 1999 magnitude 7.0 Karluk Lake earthquake, Alaska, *Bull. Seism. Soc. Am.* **90** (in press).

Provost, A.-S. and H. Houston (2000). State of stress in northern and central California: Evolution from a young to a mature strike-slip plate boundary, *EOS Transactions* **81**, F919.

Pujol, J. (1988). Comments on the joint determination of hypocenters and station

corrections, *Bull. Seism. Soc. Am.* **78**, 1179-1189.

Pujol, J. (1992). Joint hypocenter location in media with lateral velocity variations and interpretation of the station corrections, *Phys. Earth Planet. Int.* **75**, 7-24.

Pujol, J., J.-M. Chiu, A. Johnston, and B.-H. Chin (1989). On the relocation of earthquake clusters. A case history: the Arkansas earthquake swarm, *Bull. Seism. Soc. Am.* **79**, 1846-1862.

Pujol, J., J.-M. Chiu, R. Smalley Jr., M. Regnier, B. Isacks, J.L. Chatelain, J. Vlasity, D. Vlasity, J. Castano, and N. Puebla (1991). Lateral velocity variations in the Andean foreland and in Argentina determined with the JHD method, *Bull. Seism. Soc. Am.* **81**, 2441-2457.

Pulpan, H. and C. Frohlich (1985). Geometry of the subducted plate near Kodiak Island and lower Cook Inlet, Alaska, determined from relocated earthquake hypocenters, *Bull. Seism. Soc. Am.* **75**, 791-810.

Ratchkovski, N.A. and R.A. Hansen (2000). New evidence for segmentation of the subducted plate in Alaska, *Seism. Res. Lett.* **71**, 238-239.

Ratchkovsky, N.A., R.A. Hansen, and J.L. Orrey (1999). Anomalous phases in the records of Alaskan subduction zone earthquakes: Observations and modeling, *Seism. Res. Lett.* **70**, 258.

Ratchkovsky, N.A., J. Pujol, and N. Biswas (1997). Relocation of earthquakes in the Cook Inlet area, south central Alaska using the Joint Hypocenter Determination method, *Bull. Seism. Soc. Am.* **87**, 620-636.

Ratchkovsky, N.A., J. Pujol, and N. Biswas (1998). Relocation of shallow earthquakes in southern Alaska using Joint Hypocenter Determination method, *J. Seis.* **2**, 87-102.

Reasenberg, P.A. and D. Oppenheimer (1985). FPFIT, FPPLOT and FPPAGE: Fortran computer programs for calculating and displaying earthquake fault-plane solutions, *U.S. Geol. Surv. Open-File Rep. 85-739*, 109 pp.

Reyners, M. and K.S. Coles (1982). Fine structure of the dipping seismic zone and subduction mechanics in the Shumagin islands, Alaska, *J. Geophys. Res.* **87**, 356-366.

Sanchez, J.J. (2000). Inversion of focal mechanism data for the directions of stress near

Redoubt volcano, Alaska, *M.S. Thesis*, Univ. of Alaska, Fairbanks, 100 pp.

Savage, J.C., J.L. Svarc, and W.H. Prescott (1999). Deformation across the Alaska-Aleutian subduction zone near Kodiak, *Geophys. Res. Lett.* **26**, 2117-2120.

Searcy, C.K., D.H. Christensen, and G. Zandt (1996). Velocity structure beneath College station, Alaska from receiver functions, *Bull. Seism. Soc. Am.* **86**, 232-241.

Shor, G.G. and R. von Huene (1972). Marine seismic refraction studies near Kodiak, Alaska, *Geophysics* **37**, 691-700.

Singh, S.K., M. Ordaz, L. Alcantara, N. Shapiro, V. Kostoglodov, J.F. Pacheco, S. Alcocer, C. Gutierrez, R. Quaas, T. Mikumo, and E. Ovando (2000). The Oaxaca earthquake of 30 September 1999 (M_W=7.5): A normal-faulting event in the subducted Cocos plate, *Seism. Res. Lett.* **71**, 67-78.

Smith, G., D. Gubbins, and W. Mao (1994). Fast P wave propagation in subducted Pacific lithosphere: refraction from the plate, *J. Geophys. Res.* **99**, 23787-23800.

Stephens, C.D., K.A. Fogleman, J.C. Lahr, and R.A. Page (1984). Wrangell Benioff zone, southern Alaska, *Geology* **12**, 373-376.

Stephens, C.D., R.A. Page, and J.C. Lahr (1990). Reflected and mode-converted seismic waves within the shallow Aleutian subducting zone, southern Kenai Peninsula, Alaska, *J. Geophys. Res.* **95**, 6883-6897.

Suyehiro, K. and I.S. Sacks (1979). P- and S-wave velocity anomalies associated with the subducting lithosphere determined from travel-time residuals in the Japan region, *Bull. Seism. Soc. Am.* **69**, 97-114.

Wiemer, S. (1996). Analysis of seismicity: New techniques and case studies, *Ph.D. Thesis*, Univ. of Alaska, Fairbanks, 120 pp.

Wiemer, S. and R. Zuniga (1994). ZMAP V 5.0. A software package to analyze seismicity, *EOS Transactions* **75**, F456.

Woollard, G.P., N.A. Ostenso, E. Thiel, and W.E. Bonini (1960). Gravity anomalies, crustal structure, and geology in Alaska, *J. Geophys. Res.* **65**, 1021-1037.

van Wormer, J.D., J. Davies, and L. Gedney (1974). Seismicity and plate tectonics in south central Alaska, *Bull. Seism. Soc. Am.* **64**, 1467-1475.

Wyss, M., B. Liang, W.R. Tanigawa, and X. Wu (1992). Comparison of orientations of stress and strain tensors based on fault plane solutions in Kaoiki, Hawaii, *J. Geophys. Res.* 97, 4769-4790.

Zhao, D., D. Christensen, and H. Pulpan (1995). Tomographic imaging of the Alaska subduction zone, *J. Geophys. Res.* 100, 6487-6504.